CALIPSO

Final Report

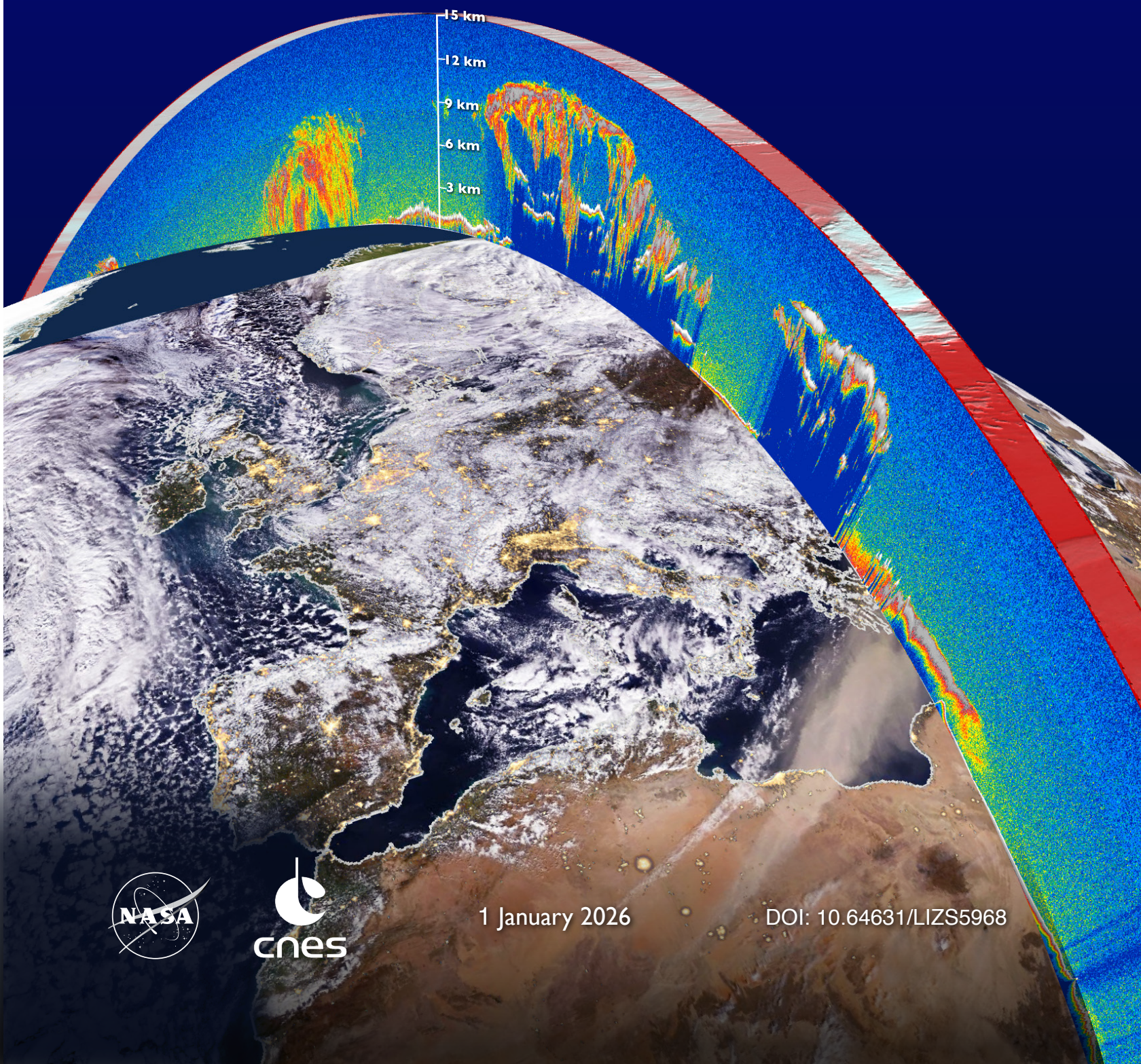

NASA

cnes

1 January 2026

DOI: 10.64631/LIZS5968

NASA/TP–2026000771

CALIPSO Final Report

Compiled By: Charles Trepte
Langley Research Center, Hampton, Virginia

National Aeronautics and
Space Administration

Langley Research Center
Hampton, Virginia 23681-2199

January 2026

Available from:

NASA STI Program / Mail Stop 050

NASA Langley Research Center

Hampton, VA 23681-2199

Table of Contents

1. Executive Summary.

The Cloud-Aerosol Lidar and Infrared Pathfinder Satellite Observation (CALIPSO) mission was a pioneering international partnership between NASA and the French Space Agency, CNES. Launched on 28 April 2006 into the A-Train's 705 km orbit altitude, CALIPSO's measurements filled a crucial, well-recognized need for high-resolution atmospheric profiles, and proved essential in reducing the uncertainties that limit our understanding of the roles of aerosols and clouds in the Earth's global climate system. The 3-year nominal mission was completed on 28 April 2009, and the project was granted mission extensions following NASA Earth Science Division (ESD) Senior Reviews in 2009, 2011, 2013, 2015, 2017, and 2020. CNES held similar mission reviews, known as REvue D'Extension de Mission (REDEM), and participated in and concurred with all ESD mission extension decisions.

The CALIPSO instrument suite consisted of CALIOP (i.e., the Cloud-Aerosol Lidar with Orthogonal Polarization), a two-wavelength, polarization-sensitive elastic backscatter lidar, a three-channel Imaging Infrared Radiometer (IIR), and a single-channel Wide Field-of-view Camera (WFC). Since routine science operations began on 12 June 2006, data were collected almost continuously and all instruments performed exceptionally well. The lidar's primary laser delivered over 1.6 billion shots before a slow pressure leak in the laser canister left the laser susceptible to anomalous electrical discharges that caused unacceptable reductions in laser pulse energies. The primary laser was taken out of service on 16 February 2009. The backup laser was activated on 12 March 2009, and performed superbly, generating over 8 billion shots in 14+ years of operation. The canister for the backup laser also had a slow pressure leak that eventually caused intermittent low energy laser pulses. While these low energy pulses had the potential to seriously degrade science data quality, the development and application of innovative data handling methods largely minimized their effects.

In September 2018, CALIPSO exited the A-Train and descended to its disposal orbit at 688 km to resume matched lidar/radar cloud profile measurements with CloudSat. All spacecraft and platform subsystems continued to operate nominally in the new C-Train orbit. Because fuel reserves were depleted, CALIPSO's orbit slowly drifted to later local ascending node crossing times, leading to compromised power margins. The science phase of the mission was terminated in June 2023 while end of mission activities for the spacecraft continued until December 2023 when the platform was passivized.

The CALIPSO project routinely produced and archived a comprehensive catalog of standard and expedited data products that were distributed to scientific researchers worldwide through data centers in the United States and France. The expedited products were designed to meet the near-real-time data delivery requirements of active field campaigns and operational forecast centers. To date there have been five comprehensive releases of the standard data products, with each new release offering substantial improvements in retrieval accuracies and uncertainty characterization. These products have been extensively validated and reported in peer-reviewed literature. The CALIPSO data have been embraced throughout the science community, as evidenced by the publication ~5000 studies in peer-reviewed journals.

CALIPSO's co-aligned lidar and IIR measurements and robust retrieval techniques led to significant advances in retrieving cloud and aerosol distributions and optical properties, both by themselves and in synergy with CloudSat and the other A-Train instruments. Observationally-based estimates of all-sky aerosol direct radiative effect were made possible by CALIPSO's unique ability to measure aerosols in cloudy skies. CALIPSO directly observed cloud altitude and thermodynamic phase, providing key new insights in understanding the feedbacks between Arctic cloud cover, sea ice extent and life cycle, and the thinning of Greenland's ice sheets. CALIPSO's vertical profile measurements

DOI: 10.64631/LIZS5968

of clouds and aerosols provided an unprecedented resource for evaluating weather and climate models, air quality models, and models used to forecast the dispersion of volcanic and fire plumes.

CALIPSO was truly a pathfinder spaceborne lidar mission. Not only did its measurements open doors to new scientific discoveries and applications that benefit society, but the team also created innovative techniques and tools to analyze a new class of Earth science observations. The mission learned that lidar profile observations are highly valued by operational weather centers for improving the skill of their forecasts and can uniquely address a broad spectrum of scientific questions. The mission also demonstrated that lasers could operate in space for long periods and that the measurement technique is stable and resilient – if proper preparations are taken. Indeed, the 17-year climate data record established by CALIPSO's continuous global measurements now provides an invaluable reference dataset that is widely used by the science community to better understand the processes that influence climate. In many ways, the knowledge and wisdom gained from CALIPSO paved the way forward for other space-based lidar missions: International Space Station (ISS)/CATS lidar and the European Space Agency (ESA) EarthCare/ATLID as two successful missions to date. Future missions such as Italian Space Agency (ASI) Luce and the German Aerospace Center (DLR)/CNES MERLIN are also leaning heavily on the experiences learned from CALIPSO.

2. Mission Science Objectives and Accomplishments

2.1. Introduction and Report Road Map

In the 1990s, the disparate roles played by clouds and aerosols in Earth's climate, weather, and air quality were considered the most significant sources of uncertainties in achieving reliable and accurate short- and long-term weather and climate forecasts (IPCC, 1995; National Research Council, 1996). To address these uncertainties, the science community asked for comprehensive and co-located global observations to answer basic questions such as: 1) what is the temporal and spatial distribution of high-altitude cirrus clouds, and do these clouds warm or cool the Earth's atmosphere?; 2) how frequently do multilayered clouds occur?; 3) what fraction of clouds contain ice, water, or some combination of both phases?; 4) what are the primary sources of natural and human-made aerosols and how are they regionally and/or globally transported?; and 5) how do different aerosol types and concentrations affect Earth's radiation balance?

The NASA Earth Observing System (EOS) satellite constellation (Aqua, Aura, and Terra) was developed, to a large degree, to help answer these questions. The sophisticated Aqua and Terra instruments (e.g., MODIS, CERES, AIRS, MISR) depended on passive sensor techniques that measured scattered sunlight or upwelling infrared radiation at discrete wavelengths. Despite numerous technological advances, these instruments still lacked the ability to detect faint clouds, identify multilayer clouds, recognize mixed scenes containing clouds above or below aerosols, and to unambiguously determine the vertical structures of clouds and aerosols in the Earth's atmosphere. Nevertheless, in-depth knowledge of the altitudes and properties clouds and aerosol layers remains crucial for accurately determining their impacts on the many complex synergies between the Earth's atmosphere, oceans, and land masses.

The Cloud-Aerosol Lidar and Infrared Pathfinder Satellite Observation (CALIPSO) mission concept was designed to fill this measurement gap with profile measurements from a very sensitive atmospheric elastic backscatter lidar. Lidars transmit short pulses of laser light and measure the intensity of the light reflected back to the receiver as a function of elapsed time. These return times can be directly translated into highly accurate measurements of the distance between the lidar and the atmospheric volume from which the reflected light originated. The first ground-based lidars were

built in the 1960s (e.g., Fiocco and Smullins, 1963; Megie et al., 1978; McCormick et al., 1978) and were later integrated onto aircraft in the 1970s (e.g., McCormick and Swissler, 1983). In 1994, the successful 10-day Lidar In-space Technology Experiment (LITE) onboard the Space Shuttle STS-64 demonstrated that a spaceborne lidar was a viable measurement technique for advancing Earth System sciences and that the technology was ready for a sustained space mission (Winker et al., 1996).

The CALIPSO concept evolved directly from the LITE experience (Winker et al., 2010). CALIPSO's Cloud-Aerosol Lidar with Orthogonal Polarization (CALIOP) was designed to acquire profile observations over the globe at two wavelengths (532 nm and 1064 nm) to gain insight into the relative size of suspended atmospheric matter (e.g., cloud droplets, ice crystals, or aerosols. At 532 nm, CALIOP also measured the degree to which the transmitted linearly polarized laser light was depolarized by the scattering processes. Depolarization provides information about the shape of the particles being measured (e.g., multifaceted irregular cloud ice crystals vs. smooth, round cloud droplets). CALIPSO's NASA and French Space Agency (CNES) collaboration included a French-contributed three-channel Imaging Infrared Radiometer (IIR) that was co-aligned with the lidar to provide observations of cirrus ice crystals and help answer questions on how they are formed. A single channel Wide Field-of-view Camera (WFC) was also included to provide contextual images of clouds in the area observed by CALIOP and the IIR.

During this same period, 94 GHz (W-band) cloud profiling radar capabilities reached a level of maturity that offered a feasible path for spaceborne microwave observations of clouds and light precipitation. It was realized in the late 1980s that combined lidar and radar observations are highly complementary and that having both capabilities simultaneously viewing the same scene would significantly advance knowledge of cloud vertical structure, thermodynamic phase, and water content. Two ensuing mission concepts (CALIOP/IIR/WFC aboard CALIPSO and a cloud profiling radar aboard CloudSat (Stephens et al., 2002; 2018) were proposed separately to the NASA's 2nd Earth System Science Pathfinder (ESSP) Announcement of Opportunity for new missions in 1998, and both were selected to fly in close coordination with each other and with the Aqua satellite in what became the Afternoon or A-Train satellite constellation. The missions were launched together on 28 April 2006 and helped usher in a new era of unprecedented advances in understanding the Earth's radiation balance, hydrological cycle, atmospheric composition.

Four primary science objectives were formulated for the CALIPSO mission.

- Provide measurements to improve observationally-based estimates of aerosol forcing and its uncertainty.
- Provide global observations to improve assessments of aerosol indirect radiative forcing.
- Improve the accuracy of observational estimates of longwave radiative fluxes at Earth's surface.
- Improve assessments of cloud feedback in the climate system.

The success of CALIPSO in meeting these objectives is reflected in the 5th Assessment Report (AR5) of the Intergovernmental Panel on Climate Change (IPCC) (IPCC, 2013) which extensively references the advances in our understanding of aerosol and cloud enabled by CALIPSO. CALIPSO's collocated lidar and IIR measurements acquired within the A-Train constellation, together with innovative and robust retrieval techniques, have led to significant advances in cloud retrievals by other A-Train instruments. Observation-based estimates of all-sky aerosol Direct Radiative Effect (DRE) are now made possible by CALIPSO's unique ability to measure aerosols in cloudy skies. Further, the 2017 Decadal Survey (National Academies, 2018) called for development of a CALIOP-like lidar to extend the CALIPSO record, to better address cloud-climate feedbacks (cloud occurrence, height, phase), to

characterize aerosol-cloud interactions, and to characterize the impact of future volcanic eruptions on the stratosphere.

Organizational Structure of this Report. The CALIPSO final report provides a summary of the mission from its origin through its completion. Section 2 reviews the most significant of the many scientific discoveries and accomplishments that are directly attributed to CALIPSO in concert with other measurements and modeling capabilities. The highlights provided in subsections 2.1-2.3 illustrate the depth and breadth by which CALIPSO measurements satisfied its primary mission objectives, and they also touch on many unexpected accomplishments and findings enabled by CALIPSO. Although CALIPSO was designated as a research mission, many operational weather forecast, air quality, and aviation flight planning organizations embraced the CALIPSO observations to enhance the quality of their products and services. These are highlighted in subsection 2.4. Subsection 2.5 briefly enumerates some of the significant retrieval techniques that were forged during the mission and enhanced the science value beyond the original intentions proposed in 1998. While these lists are not exhaustive, the selected examples provide a balanced overview of the many applications in which the CALIPSO data set has been used for scientific research and benefits to society. The references in this report are also only a small sampling of the complete bibliography; nevertheless, they provide a rich source of information for readers to find additional details.

Section 3 provides a timeline of the mission to provide context on the events the occurred. Section 4 of this report provides a comprehensive overview of the implementation of the mission, highlighting its design, development, execution and deliverables. A description of the instrument payload and the French provided spacecraft are presented. Overviews of the project's joint NASA-CNES organizational structure are given for both the development phase and the on-orbit operational phase. The Implementation section reviews CALIPSO's major flight and ground systems and identifies the major events that impacted instrument performance and science data quality throughout the mission.

Appendices are provided that provide a comprehensive description of the CALIPSO data products (Appendix A); a list of all acronyms used (Appendix B); a comprehensive list of references cited in this report (Appendix C); a set of trending charts that track important instrument parameters throughout the mission lifetime (Appendix D); a brief analysis of the peer-reviewed publications that cite CALIPSO data products (Appendix E), and a list of relevant international field campaigns (Appendix F).

2.2. Relevance to NASA Goals and Programs

Since launch, CALIPSO measurements made an increasing number of increasingly valuable contributions to NASA's atmospheric and climate science goals. The 2017 Decadal Survey for Earth Science and Applications from Space (National Academies, 2018) identified an extensive list of research priorities to be pursued by the NASA Earth Sciences program. Table 1 maps relevant peer-reviewed journal papers published since CALIPSO's launch, along with the CALIPSO science objectives discussed in section 2.3, to the priorities identified in the Decadal Survey report.

Table 1. CALIPSO Peer-Reviewed Publications that are directly relevant to the science priorities called out in the 2017 Decadal Survey for Earth Science. Priorities deemed 'most important' by the survey panel are identified in the table as (MI); similarly, priorities 'very important' are identified as (VI).

Decadal Survey Science Priorities	Relevant CALIPSO Publications
C-2a. Reduce uncertainty in low and high cloud feedback by a factor of 2 (MI).	Guzman et al., 2017; Vaillant de Guélis et al., 2017a, 2017b, 2018; Winker et al., 2017; Chepfer et al., 2018; Frey et al., 2018; Cesana et al., 2019a; He et al., 2019; Wang, X. et al., 2022; McKim et al., 2024; Cesana et al., 2024; Tan, I. et al., 2025.
C-2h. Reduce the IPCC AR5 total aerosol radiative forcing uncertainty by a factor of 2 (MI).	Chen et al., 2017; Tsikerdekis et al., 2017; Oikawa et al., 2018; Bagtasa et al., 2019; Kacenelenbogen et al., 2019; Matus et al., 2019; Bellouin et al, 2020; Mallet et al., 2021; Shi et al., 2022; Peng et al., 2023; Vescovini et al., 2024; Kacenelenbogen et al., 2025.
C-2g. Quantify the contribution of the upper troposphere and stratosphere to climate feed--backs and change (VI).	Khaykin et al., 2017 Martinsson et al., 2017; Schoeberl et al., 2018; Ueyama et al., 2018; Fromm et al., 2019; Johansson et al., 2019; Snels et al., 2019; Bian et al., 2020.
C-5a. Improve estimates of the emissions of natural and anthropogenic aerosols and their precursors via observational constraints (VI)	Govardhan et al., 2017; Lee et al., 2018; Sun et al., 2018; Barkley et al., 2019; Jia et al., 2019; Sokolik et al., 2019; Kalluri et al., 2020; Shukurov et al., 2023.
C-5c. Quantify the effect that aerosol has on cloud formation, cloud height, and cloud properties including semi-direct effects (VI).	Penner et al., 2018; Allen et al., 2019; Fadnavis et al., 2019; Xie et al., 2019; Zhao, B. et al., 2019; Douglas and L'Ecuyer, 2020; Painemal et al., 2020; Ding et al., 2021; Zhang, J. et al., 2022; Zhang, M. et al., 2025; Zhu, H. et al., 2025.
W-1a. Determine the effects of key boundary layer processes on weather, hydrological, and air quality forecasts (MI).	Wall et al., 2017; Ahlgrimm et al., 2018; O et al., 2018; Su et al., 2018; Zhu, Z. et al., 2018; Smalley et al., 2019; Abel et al., 2020.
W-2a. Improve the observed and modeled representation of natural, low-frequency modes of weather/climate variability (e.g. MJO, ENSO) (MI).	Masunaga and Bony, 2018; Morrison et al., 2018; Cesana et al., 2019b; Kato et al., 2019; Pan et al., 2019; Voigt et al., 2019; Wall et al., 2022.
W-5a. Improve the understanding of the processes that determine air pollution distributions and aid estimation of global air pollution impacts on human health and ecosystems (MI)	Gao et al., 2017; Gong et al., 2017; Sun et al., 2018; Bauer et al., 2019; Mahapatra et al., 2019; Toth et al., 2019; Wang, L. et al., 2020; Toth et al., 2022.

2.3. Meeting CALIPSO's Mission Science Objectives

During the mission, CALIPSO observations and data products were widely used throughout the international scientific community and were used in ~5000 peer-reviewed publications. These publications include 135 Master's theses and >330 Ph.D. dissertations. Each year, CALIPSO data were used in increasingly sophisticated ways as the international community became more skilled at utilizing this new type of satellite data. There were increasing use of merged data products that combined CALIPSO and CloudSat measurements with A-Train passive sensor data, such as 2B-FLXHR-LIDAR (Matus et al., 2019), DARDAR (Listowski et al., 2019), SODA (Painemal et al., 2019),

and C3M (Thorsen et al., 2018). CALIPSO observations were widely adopted by the modeling community, particularly by the Cloud Feedback Model Intercomparison Project (CFMIP) cloud-climate feedback community (e.g., Koshiro et al., 2018). More than a dozen published papers used CALIOP cloud observations to evaluate the representation of clouds in climate models (https://www.earthsystemcog.org/projects/cfmip).

2.3.1. Provide measurements to improve observationally-based estimates of aerosol forcing and its uncertainty.

Aerosols scatter and absorb solar and terrestrial radiation, contributing to atmospheric heating and surface cooling. CALIOP provided the first global observations of aerosol vertical distributions and the first global partitioning of extinction by aerosol type. CALIOP's unprecedented ability to observe aerosols beneath optically thin clouds and above low clouds and bright surfaces such as deserts led to substantially improved estimates of aerosol DREs than available from passive satellite sensors alone (e.g., MODIS and MISR). Figure 2-1 shows CALIOP observations of a dense dust layer lying between the surface and ~5 km altitude (yellow, red and gray colors), being transported over an opaque marine stratus deck (white) in the Indian Ocean with transparent cirrus clouds above. In contrast to passive sensor capabilities, CALIOP can retrieve the spatial and optical properties of aerosols both above dense lower clouds and below optically thin higher clouds.

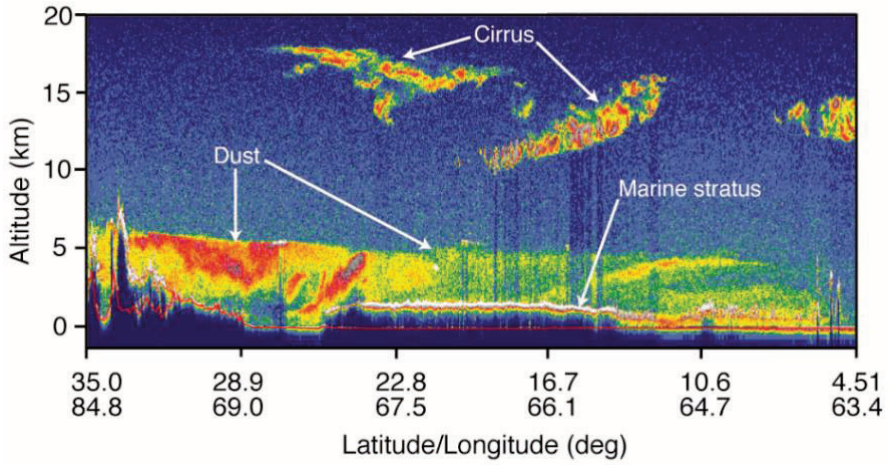

Figure 2-1. Dust elevated above opaque marine stratus and lying below transparent cirrus observed by CALIOP in the Indian Ocean off the coasts of Pakistan and India (Source credit: NASA).

Table 2 lists several publications that rely on CALIOP aerosol information, in combination with collocated cloud data, to derive improved estimates of global mean DRE at the Top Of Atmosphere (TOA). Oikawa et al. (2018) and Korras-Carraca et al. (2019) combined CALIOP aerosol products with cloud properties obtained from either MODIS or ISCCP (International Satellite Cloud Climatology Project). Notably, Matus et al. (2019) uses the CloudSat 2B-FLXHR-LIDAR product, which computes radiative fluxes from merged CloudSat, CALIOP, and MODIS data. These studies made different assumptions about aerosol intrinsic optical properties (single scattering albedo and asymmetry parameter) and used different methods to compute TOA radiative fluxes. Global mean estimates from Oikawa et al. (2018) and Korras-Carraca et al. (2019) agree rather well, while the all-sky DRE estimate in the Matus et al. (2019) study is somewhat stronger and the clear-sky DRE is significantly weaker. The clear-sky DRE estimates in the two first studies are about 20% weaker than the DRE derived from MODIS alone (Yu et al., 2006). Although the geographic sampling and cloud-screening used in deriving MODIS aerosol products are different from those used by CALIOP,

differences in the global mean DRE are consistent with the differences in MODIS and CALIOP global mean Aerosol Optical Depth (AOD) estimates. Observation-based all-sky results currently require the use of CALIOP data, since only CALIOP can retrieve both below-cloud and above-cloud AOD.

Table 2, Summary of Global Mean TOA Shortwave (SW) Aerosol DRE Estimates Published since 2017.

	Aerosol/Cloud Products	All-Sky DRE	Clear-Sky DRE
Oikawa et al. (2018)	CALIOP V3 / MODIS C5	-2.1 W/m^2	-4.0 W/m^2
Korras-Carraca et al. (2019)	CALIOP V4 / ISCCP D2	-1.9 W/m^2	-3.9 W/m^2
Matus et al. (2019)	2B-FLXHR-LIDAR R5	-2.4 W/m^2	-2.6 W/m^2

Because models do a poor job of simulating the vertical distribution of aerosols (Koffi et al., 2016), estimates of the amount of aerosol found above clouds are highly uncertain. Similarly, the radiative effects of Aerosols Above Clouds (AAC) are a highly uncertain component of aerosol radiative forcing estimates. Kacenelenbogen et al. (2019) assessed AAC radiative effects by retrieving above-cloud AOD using a highly accurate technique pioneered by the CALIPSO team (Hu et al., 2007; Liu Z. et al., 2015). This study was the first global characterization of the radiative effects of AAC, finding half a dozen regions around the globe where AAC occurs frequently (Figure 2-2). The global mean radiative effect was found to be a small net warming of 0.20 W/m^2, although this result is sensitive to assumptions on aerosol absorption. Results from this study were used in a major review of aerosol forcing (Bellouin et al., 2020) as the only available observational constraint on above-cloud DRE.

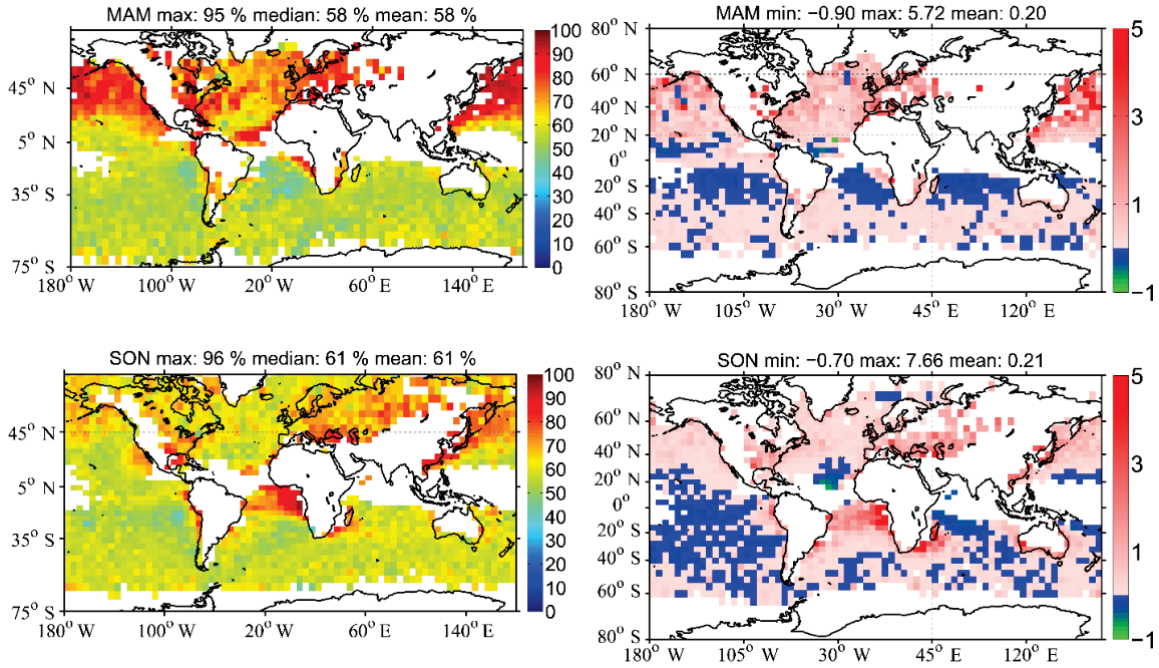

Figure 2-2. Left) Seasonal occurrence of Aerosols Above Clouds (AAC) (%); (Right) SW direct aerosol radiative effect from AAC at TOA (W/m2). Upper panels: March, April and May (MAM); lower panels: September, October and November (SON) (adapted from (Kacenelenbogen et al., 2019; Used under CC BY 4.0).

Motivated by concerns about the effects of wildfire smoke on the mass balance of northern hemisphere ice sheets, researchers used CALIOP data to estimate aerosol impacts on snow surfaces.

Thomas et al. (2017) combined CALIOP observations with model outputs to investigate the emission, transport, and deposition of smoke from Canadian forest fires onto the Greenland ice sheet. The WRF-Chem model was found to severely underestimate aerosol deposition, due both to errors in modeling emissions and in the parameterization of wet scavenging. Bali et al. (2017) performed a similar study, looking at potential increases in snowmelt due to smoke aerosols transported into the glaciated regions of the upper Himalayas during a period of anomalously high burning in India.

2.3.2. Provide global observations to improve assessments of aerosol indirect radiative forcing

The indirect effects of aerosols on various cloud properties dominate uncertainties in estimates of anthropogenic climate forcings (Bellouin et al., 2020). For example, aerosol above stratocumulus can alter the radiative effects of the cloud, whereas clouds embedded in aerosol layers are subject to both radiative and microphysical interactions. CALIOP provided the only global observations that could establish the relative locations of aerosol and cloud layers. Amiri-Farahani et al. (2017) used CALIOP profile data to characterize aerosol effects on cloud albedo (Twomey effect vs. radiative interaction) off the coast of northwest Africa, a region heavily influenced by transported Saharan dust. The authors found a strong semi-direct effect during boreal winter, when the stratocumulus off the coast tends to be embedded in the dust layer, and heating of the cloud layer by ambient dust tends to reduce cloud cover, providing a weakly positive radiative forcing. These aerosol-cloud radiative interactions appear to dominate the potential aerosol-cloud microphysical interactions. During other seasons, however, the dust layers tend to be elevated above the clouds in this region and a strong negative radiative forcing was seen. In these cases, the elevated dust layers produced a radiative cooling at cloud top which tends to stabilize the cloud layer and enhance the cloud deck.

Aerosol indirect effects have potentially large impacts on the surface energy budget of the Arctic Ocean but estimates of aerosol indirect effects from models are highly uncertain and poorly validated by observations. Zamora et al. (2017) combined CALIOP and CloudSat observations with transport modeling to quantitatively estimate aerosol indirect effects on a regional scale. Focusing on Arctic stratus and aerosol-induced longwave cloud forcing, the authors investigated the microphysical mechanisms responsible for the aerosol impacts on the stratus. They found that shallow, optically thin, predominantly liquid clouds over open waters are less susceptible to aerosol effects than similar clouds lying over extended sea ice, indicating that meteorological forcing dominates aerosol microphysics when these types of clouds occur over the Arctic Ocean.

While aerosol interactions with liquid clouds are complicated, aerosol impacts on ice clouds are even more complex and uncertain. A number of different mechanisms contribute to the formation of ice particles, which depend on temperature, supersaturation, updraft velocity, and the concentration of ice nuclei, among other things (Krämer et al., 2016). Ice crystal number concentration (Ni) is a key property of ice clouds, for both cloud radiation and microphysics, but factors which control Ni remain difficult to determine. CALIPSO measurements and retrievals provided the empirical foundations required to guide development of improved model parameterizations. Gryspeerdt et al. (2018) used Ni retrievals from the joint CALIPSO-CloudSat DARDAR product to identify variations in cloud top Ni that are consistent with both homogeneous and heterogeneous nucleation processes. This study also found relationships between aerosol and Ni at cloud top that vary depending on the prevailing meteorological situation and aerosol type. Mitchell et al. (2018) developed a new retrieval technique that used co-located observations from CALIOP and the IIR 10.6 and 12.05 μm channels to estimate cirrus cloud Ni, effective diameter (De), and Ice Water Content (IWC). Using this method, the authors conducted a two-year study that focuses on single-layered semi-transparent ice clouds for which the cloud base temperatures are ≤ 235 K. For this specific subset of cirrus, they established the global

variability of Ni and De according to temperature, cloud thickness, latitude, season, and underlying surface topography (i.e., land vs. ocean). Figure 2-3 illustrates results from these two Ni studies. Although the retrieved values are different, most likely depending on instrument-specific crystal size sensitivities, similar patterns of Ni from these two completely different approaches can be seen – low concentrations in the tropics and concentrations tending to be higher in regions of high surface relief – supporting a dependence of homogeneous ice nucleation in cirrus clouds on topography and latitude. The retrieval technique was improved recently (Mitchell et al., 2025) and an innovative approach based on these observations was proposed to identify cirrus clouds affected by homogeneous nucleation (Mitchell and Garnier, 2025).

Merged CALIPSO-CloudSat data products such as DARDAR (Sourdeval et al., 2018) and 2C-ICE (Deng et al., 2015) also provide estimates of ice particle concentrations, offering new opportunities for global-scale investigations into ice nucleation processes using active remote sensing.

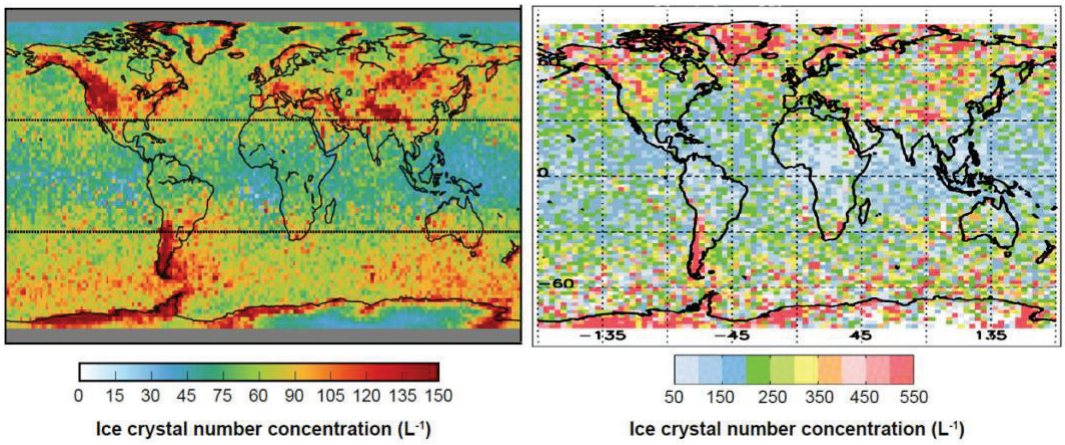

Figure 2-3. Comparison of the global distribution of relative Ni. (Left) cloud top Ni for clouds with top temperature equal to 223 K (adapted from Fig. 1b, Gryspeerdt et al., 2018). (Right) Ni in clouds of radiative temperature between 218 and 228 K (adapted from Fig. 12a, Mitchell et al., 2018; Used under CC BY 4.0).

2.3.3. Improve the accuracy of observational estimates of longwave radiative fluxes at Earth's surface

Fundamentally, Earth's climate is determined by the energy flows between the TOA and Earth's surface. Collocated CALIOP and CloudSat profiles provide an unprecedented three-Dimensional (3D) view of clouds and cloud structures and their impacts on radiative fluxes. CALIOP detects layers such as thin cirrus and shallow water clouds that lie well below the detection sensitivity of CloudSat's Cloud Profiling Radar (CPR), whereas CPR can penetrate to the base of optically thick clouds, well beyond where the CALIOP signal is completely attenuated, and detect precipitation. Figure 2-4 shows the vertical profile of monthly zonal mean volume cloud fractions estimated by CALIPSO-CloudSat (left) and MODIS (right) (Kato et al., 2019). Perhaps the most prominent of the many differences between these two estimates are that, in the MODIS data, the altitudes of high clouds are biased low, low clouds are under-reported, and mid-level clouds are over-reported. Passive sensor estimates of cloud base tend to be too high, and thus too cool, leading to an underestimate of downwelling longwave radiation at the surface. The close relationship between cloud radiative heating profiles and the general circulation has long been established (e.g., Slingo and Slingo, 1988, 1991; Raymond, 2000) and now accurate knowledge of the vertical structure of clouds is the key to further advancing our understanding of the radiative coupling between clouds and circulation. Improved knowledge of the

vertical distribution of aerosols is also required. CALIOP profile data provided important observational constraints in deriving global estimates of atmospheric heating due to aerosols and the subsequent 'semi-direct' aerosol radiative forcing via the response of clouds to this heating (Allen et al., 2019). Similarly, the combination of CALIPSO and CloudSat measurements has been highly used influential in evaluating vertical variations in cloud radiative heating. For example, Voigt et al. (2024) CALIPSO data products as a benchmark in a wide-ranging performance assessment of model predictions of cloud radiative heating profiles using 20 CMIP6 models (i.e., 20 different models from phase 6 of the Coupled Model Intercomparison Project (CMIP)).

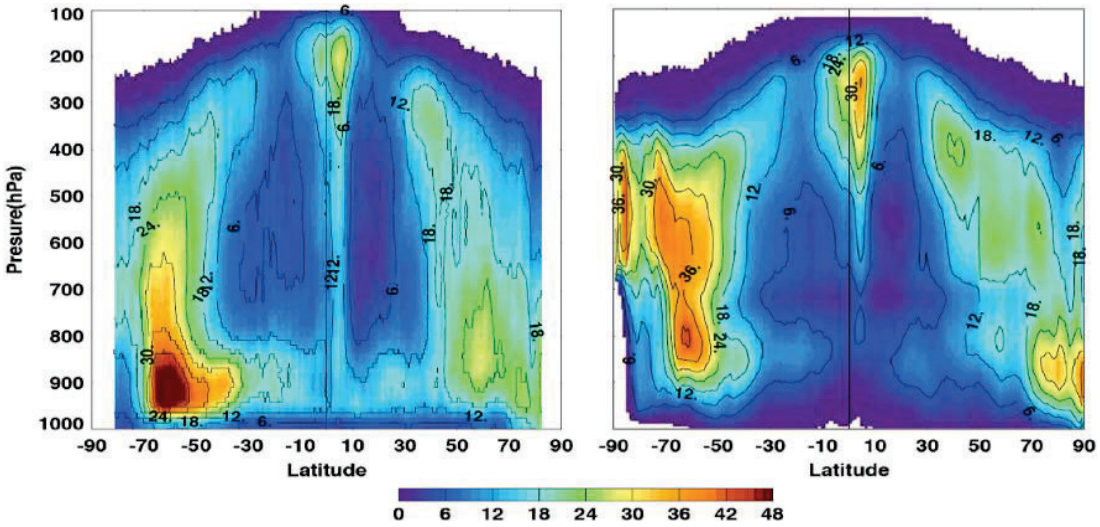

Figure 2-4. (Left) Zonal-mean vertical volume cloud fraction in percent derived from CALIPSO and CloudSat for April 2010 as a function of latitude. (Right) The same, but from Aqua MODIS. (Fig. 1, Kato et al., 2019; © American Geophysical Union, Used under CC BY-NC-ND 4.0).

Combined with passive sensor A-Train data, CALIPSO-CloudSat cloud profiles provide greatly improved observational constraints on the surface and atmospheric radiation budgets, leading to the first rigorous estimates of the global energy budget (Kato et al., 2012; L'Ecuyer et al., 2015). Making use of accurate cloud base height and vertical structure from CALIPSO-CloudSat for both single and multi-layer clouds, L'Ecuyer et al. (2019) evaluated global cloud radiative effects as a function of cloud type and estimate the annual mean net cloud radiative effect at the surface with an uncertainty less than ± 10 W m^{-2}.

The radiative impact of clouds strongly depends on how cloud water is partitioned between liquid and ice phases. Models must represent this phase partitioning correctly to accurately simulate the energy budget and the flows of energy within the present-day climate, and to estimate cloud feedbacks in simulations of future climate. CALIOP accurately determines cloud-top thermodynamic phase and, together with CloudSat, yields unprecedented insights into the vertical partitioning of ice and water that provide important observational constraints on global estimates of cloud radiative effects. Matus and L'Ecuyer (2017) used the merged CALIPSO-CloudSat 2B-FLXHR-LIDAR product to document seasonal and regional variability of cloud radiative effects as a function of cloud phase, with implications for global heat transport (Figure 2-5). This improved knowledge of Earth's radiation budget and global heat transport is leading to continued new insights into fundamental mechanisms of our climate (Stephens and L'Ecuyer, 2015; Thompson et al., 2017).

DOI: 10.64631/LIZS5968

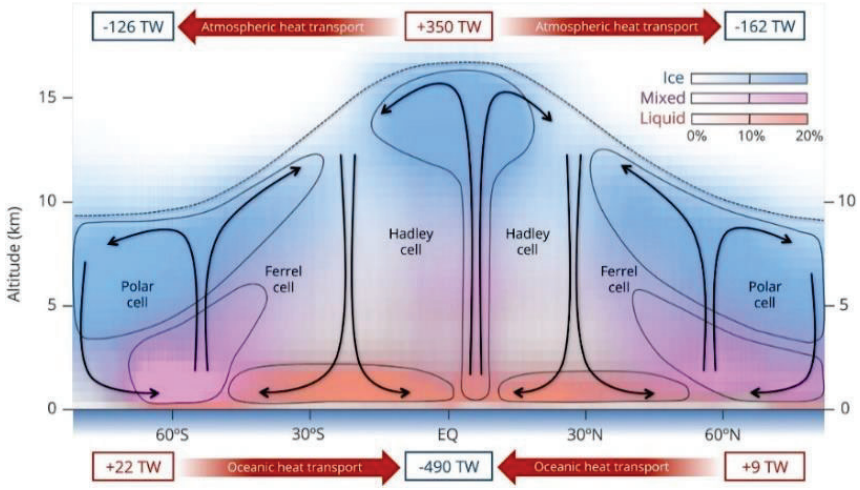

Figure 2-5. Annual occurrences of liquid (red), ice (blue), and mixed-phase clouds (pink), based on 2B-CLDCLASS-LIDAR cloud phase classification data from 2007 to 2010. Boxed values indicate the contribution of annual heat flux from mixed-phase clouds within the atmosphere and at the surface. For illustrative purposes, gray outlines indicate the boundaries of idealized cloud structures and canonical atmospheric flow patterns are indicated by black arrows (Fig. 12, Matus and L'Ecuyer, 2017; © American Geophysical Union, Used under CC BY 4.0).

An especially critical question is the impact of clouds on the Arctic surface radiation budget and the melting of sea ice. Passive retrievals of Arctic clouds are problematic due to frequent presence of snow and ice, seasonal darkness, and the dominance of shallow clouds associated with strong temperature inversions. Clouds can influence the melting and growth of sea ice and, conversely, clouds may respond to changes in sea ice. The ability of CALIOP to accurately characterize the presence, altitude, opacity, and ice/water phase of Arctic clouds illuminated the interactions of clouds, radiation, and sea ice (Morrison et al., 2018).

An unexpected achievement was the development of a retrieval of the influence of clouds on longwave surface radiative fluxes from CALIOP data alone (Arouf et al., 2022). Monthly zonal means from this technique compare well with estimates based on joint CERES, CALIPSO, CloudSat, and MODIS observations (C3M, Kato et al. 2010; 2B-FLXHR-Lidar) and extends the active-sensor record of surface longwave (LW) fluxes beyond the 2006-2010 period when diurnal CloudSat observations were available.

2.3.4. Improve assessments of cloud feedback in the climate system

Cloud-radiation-climate feedback processes are the largest source of uncertainty in climate change predictions (IPCC, 2013). These feedback uncertainties arise from complex interactions between radiative, dynamical, and microphysical processes. Many of these processes are unresolved in global models and must be parameterized. Combined CALIPSO-CloudSat observations provide a unique resource for addressing these uncertainties. Initial studies used joint CALIPSO-CloudSat observations to evaluate cloud vertical structure and overlap (Barker, 2008a, 2008b). Since then, many merged CALIPSO-CloudSat products were developed, with some focusing on cloud radiative properties (Kato et al., 2010; Henderson et al., 2013) and others on vertically resolved cloud microphysical properties (Deng et al., 2015; Cazenave et al., 2019). These merged products were key in advancing our understanding of mixed phase and super-cooled liquid clouds, using CALIOP to identify cloud-top thermodynamic phase. Supercooled liquid clouds strongly modulate cloud albedo and play an

important role in Arctic climate change (Tan, I. and Storelvmo, 2019). Analysis of CALIOP data showed that models underestimate the occurrence of these clouds, leading to biases in the radiation budgets predicted by both weather and climate models (Stephens et al., 2018). New parametrizations, derived from joint CALIPSO-CloudSat observations and tested at European Center for Medium-range Weather Forecasting (ECMWF), showed that modifying cloud formation processes to allow more water at cloud top can reduce biases in shortwave (SW) radiation (Forbes et al., 2016). More recently, CALIPSO-CloudSat data were used in several other studies of supercooled boundary layer clouds, including in the Indian Ocean (Vérèmes et al., 2019), the Arctic (Mioche and Jourdan, 2018; Morrison et al., 2018), and the Antarctic (Listowski et al., 2019).

The merged CALIPSO-CloudSat products also delivered the only global, observationally-based retrievals of cloud vertical heating profiles. Voigt et al. (2019) examined impacts of cloud radiative heating on large scale circulation, finding robust effects across a model ensemble, but with the magnitude of the changes varying significantly across models. Comparisons with the CALIPSO-CloudSat 2B-FLXHR-LIDAR product showed the models significantly misrepresent the vertical profile of cloud radiative heating in the present day, and these errors propagate into predictions of future scenarios. Figure 2-6 shows a cloud heating profile based on the ERA-Interim reanalysis, which constrains a global model with observations of the atmospheric state. This profile also shows large differences with CALIPSO-CloudSat, demonstrating the inability of even constrained models to simulate realistic cloud heating profiles, and the continued need for direct cloud profile observations.

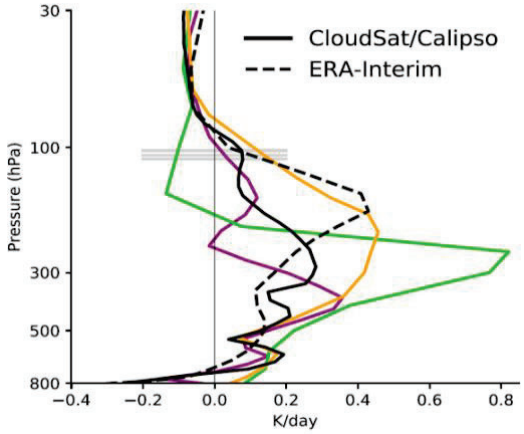

Figure 2-6. Present-day tropical cloud radiative heating profiles from three CMIP5 models (colored lines) and as derived from CloudSat/CALIPSO and the ERA-Interim reanalysis (Fig. 8c from Voigt et al., 2019, © American Meteorological Society. Used with permission).

As another example of the insights into cloud-radiation-climate processes derived from CALIPSO-CloudSat, Masunaga and Bony (2018) study tropical convective-radiative interactions by examining variability at the hourly to daily scale over the convective lifecycle. Vertical profiles of cloud cover and radiative heating from CALIPSO-CloudSat are sorted into a lagged time series around the hour of convective occurrence identified by the TRMM precipitation radar. Compiling tropical statistics over 2006-2009, the authors find evidence for rapid coupling of cirrus-induced radiative effects to convective dynamics. They present a simple conceptual model which explains this coupling in terms of cirrus radiatively promoting moistening of the atmosphere via congestus-mode dynamics which precondition the atmosphere to favor deep convection.

DOI: 10.64631/LIZS5968

Cloud radiative feedbacks arise from changes in cloud cover, cloud altitude, and cloud optical thickness in response to rising surface temperatures, but these feedbacks are poorly constrained by existing passive satellite observations due to sensitivities to calibration drifts (Shea et al., 2017) and incomplete knowledge of the vertical structure of clouds. Active profiling instruments (e.g., lidars) are essential for overcoming the latter obstacle. Furthermore, CALIOP's calibration has remained exceptionally stable throughout the mission lifetime (e.g., see Figure D1 and Kar et al., 2018).

When measuring opaque ice clouds, the 12 μm cloud emissivity approaches a black body at the geometric altitude where the CALIOP signals becomes fully attenuated (Winker et al., 2017). This fact is exploited in a series of papers that develop a method of estimating cloud LW feedbacks from the CALIOP total attenuation altitude. Estimates of outgoing LW radiation from the CALIOP opacity altitude are well-correlated with LW Cloud Radiative Effects (LWCRE) from CERES (Vaillant de Guélis et al., 2017a). This method not only characterizes the contribution of clouds to the LWCRE but also quantifies the cloud property variations responsible for the variability (Vaillant de Guélis et al., 2018).

The technique is extended to estimates of cloud feedbacks in Vaillant de Guélis et al. (2018). Figure 2-7 shows interannual cloud LW feedbacks from CALIOP compared to interannual and long-term feedbacks from the LMDZ climate model. Feedback due to rising cloud heights is a robust feature among climate models and Figure 2-7 shows observations and simulations agree well for opaque clouds, which dominate the components of the LW feedback. Changes in cloud amount are less constrained by fundamental physics, producing more diversity between models. The large difference in observed and simulated opaque cloud cover feedback results in opposite signs of the observed and simulated total feedback, pointing to variability of high cloud cover as an area requiring focused research. This new technique for observation-derived cloud feedbacks is completely independent of the current approach based on radiative kernels and the ISCCP cloud top pressure vs. optical depth diagram (Zelinka et al., 2012a, 2012b, 2016).

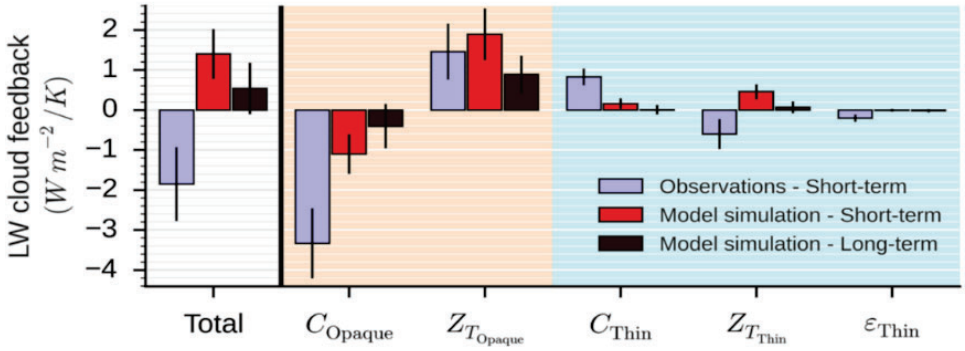

Figure 2-7. Decomposition of longwave cloud feedback from CALIOP observations into 5 components: opaque cloud cover and altitude, thin cloud cover, altitude, and emissivity, and comparisons with short-term and long-term simulations from the LMDZ climate model (Fig. 2, Vaillant de Guélis et al.,2018; Used under CC BY 4.0).

Shallow marine clouds are at the heart of uncertainties in the cloud-climate feedbacks simulated by models. Models often fail to correctly simulate both the amount and type of shallow clouds and the cloud types produced by models are often inconsistent with the ambient meteorological environment (Nam, C. et al., 2012). An independent data product created by Cesana et al. (2019c) documents the spatial distributions and vertical profiles of 5 different varieties of stratocumulus and shallow cumulus using CALIOP and/or CloudSat cloud heights and vertical/horizontal variabilities. This product

identifies shallow clouds by type more accurately than previous methods and allows more detailed evaluation of the type of shallow cloud being simulated and the tracking of cloud type evolution during climate model runs.

In a recent analysis on the surface energy budget using CERES/MODIS, Loeb et al. (2024) showed that the surface radiation imbalance could be attributed to the decrease of low-level clouds in the subtropical regions. The comparison between cloud fraction trends from MODIS and from CALIPSO-CloudSat showed a global coherence between both analyses of cloud fraction change but evidenced significant differences more particularly for clear air frequency (Figure 2-8). The study emphasized that the surface energy imbalance had recently increased after the El Nino transition of 2012, explaining sea surface temperature (SST) increase. Hakuba et al. (2025) and Allan and Merchant (2025) reconciled this observation with Ocean Heat uptake. Allan and Merchant (2025) concluded that "*A doubling of Earth's energy imbalance from 0.6±0.2 Wm^{-2} in 2001–2014 to 1.2±0.2 Wm^{-2} in 2015–2023 is primarily explained by increases in absorbed sunlight related to cloud-radiative effects over the oceans. Observed increases in absorbed sunlight are not fully captured by ERA5 and determined by widespread decreases in reflected sunlight by cloud over the global ocean.*"

Clouds are aerosols are main actors of the ocean-atmosphere system and monitoring their properties is of first importance for understanding climate change. The role of aerosols and the way they are accounted for in models, however, remains controversial (Hansen et al., 2025). Further work is clearly necessary using all climate datasets, including new data provided by EarthCARE.

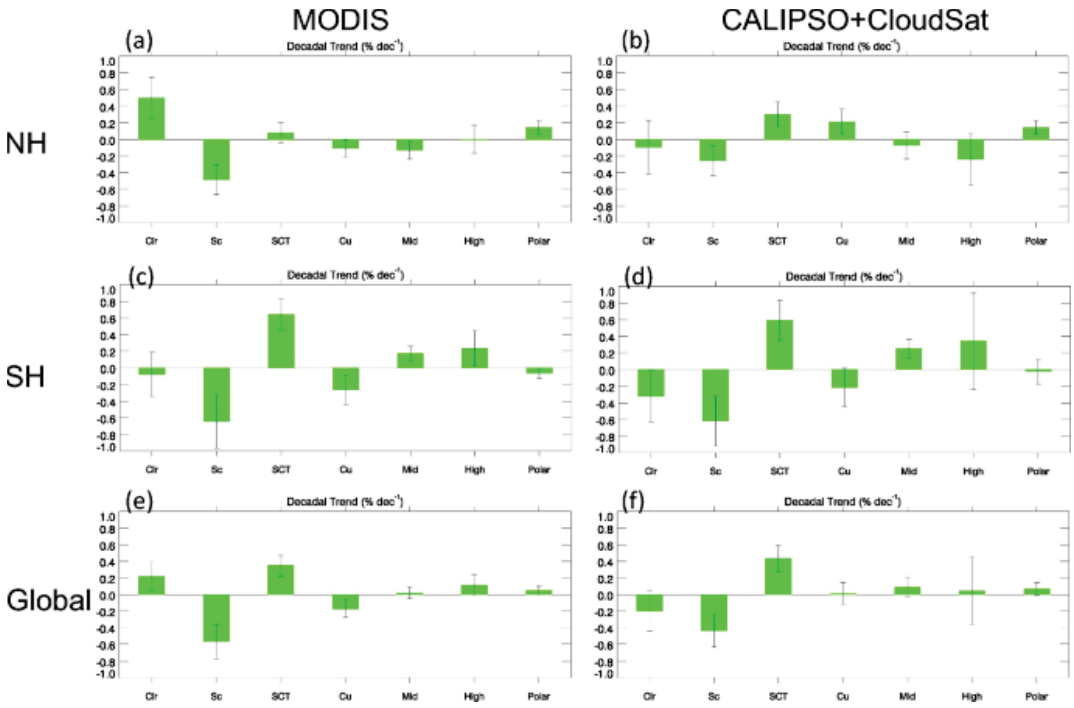

Figure 2-8. Clear-sky frequency and cloud fraction trends by cloud type from: a MODIS for NH, b CALIPSO-CloudSat (CC) for NH, c MODIS for SH, d CC for SH, e MODIS for globe, and f CC for globe using coincident measurements from January 2008 to December 2017 (Loeb et al., 2024; Used under CC BY 4.0). Clr: clear sky, Sc: stratocumulus, SCT: scattered clouds, Cu: cumulus, Mid: mid-layer clouds, High: high-layer clouds, Polar: polar clouds.

Moreover, there are many theories on how high tropical clouds will respond to climate warming and the response of thunderstorm anvil clouds to climate warming as a leading source of uncertainty in recent climate assessments. Saint-Lu et al. (2020) analyzed 10 years of CALIOP observations, finding evidence of anvil rise and a decrease in anvil coverage in response to tropical warming. Two recent papers (Sokol et al. 2024; McKim et al. 2024) used data from CALIPSO and CloudSat to place constraints on the type and magnitude of changes in anvil clouds under climate warming. The combined result of these studies was to bound the potential magnitude and nature of cloud feedbacks and provided observational evidence that could be used to evaluate and improve climate model predictions.

2.4. Beyond the Original Science Objectives

Even at the end of the mission, CALIPSO data continued to be applied in a broad range of pioneering research investigations that extend far beyond the original mission objectives. This section describes how CALIPSO data were used to evaluate and improve models and passive sensor data products, to better understand stratospheric aerosols, and to evaluate aerosol effects on human health and improve air quality forecasts.

2.4.1. Evaluation of Other Satellite Retrievals

With high vertical resolution, high detection sensitivity, and direct measurement of cloud altitude and cloud top thermodynamic phase, CALIOP is an invaluable resource for evaluating passive sensor cloud retrievals. CALIPSO observations were heavily used over the years to validate cloud products in MODIS Collection 5 (Holz et al., 2008) and Collection 6 (Platnick et al., 2017), quantifying not only uncertainties and biases but also examining the underlying reasons for retrieval failures and guiding algorithm improvements (e.g., Holz et al., 2016).

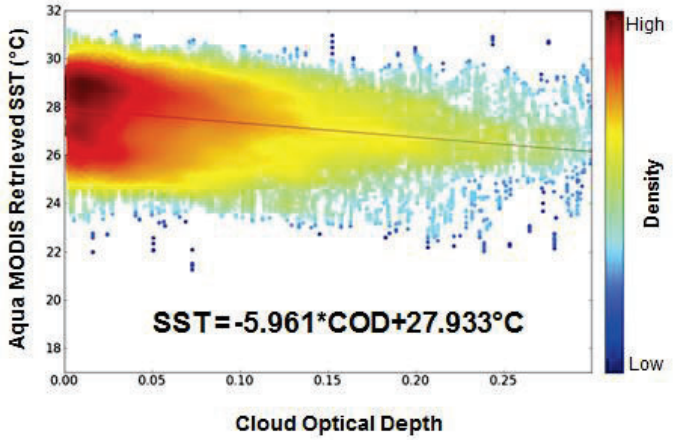

Figure 2-9. CALIOP COD vs Aqua-MODIS SST for cirrus-contaminated retrievals for August-October 2012 over the Maritime Continent (from Marquis et al., 2017; © American Meteorological Society, Used with permission).

Figure 2-9 displays one example for how CALIOP data provided improved insight into difficulties MODIS has with detecting faint clouds (optical depths less than about 0.3); yet they are easily detected by CALIOP (Ackerman et al., 2008). Marquis et al. (2017) looked at the impact of these missed clouds on retrievals of SST from MODIS, AVHRR, and VIIRS. They found that a high occurrence of these optically thin clouds are in the tropics. The figure shows cloud-biased SSTs from MODIS vs.

collocated cirrus optical depths from CALIOP. These biases in retrieved SSTs hinder the accurate forecasting of tropical cyclones and the impacts of El Niño on global weather patterns.

CALIOP observations continued to be used for validation of MODIS products such as cloud fraction and height, thermodynamic phase, cirrus optical depth and IWC (Xia et al., 2018; Tan S. et al., 2019; Trepte et al., 2019; Minnis et al., 2021; Yost et al., 2021), as well as validation of new algorithms applied to MODIS data (Minnis et al., 2019). Heidinger et al. (2019) used CALIOP cloud height data to validate improvements in VIIRS cirrus height retrievals obtained by merging VIIRS with collocated observations from the Cross-track Infrared Sounder. CALIOP observations were also used to validate the 35-year cloud data set built from the AVHRR record (Stengel et al., 2020) and algorithms for detection of optically thin clouds by the Geostationary Ocean Color Imager (Yeom et al., 2020). CALIOP cloud data were further used extensively to validate cloud height retrievals from new geostationary sensors such as Advanced Himawari Imager (AHI) on the Himawari-8 geostationary satellite (Huang, Y. et al., 2019; Qin et al., 2019; Min et al., 2020), dust layer top height from IASI (Clarisse et al., 2019), and cloud information from SEVIRI (de Laat et al., 2017).

2.4.2. Use of CALIPSO Data to Test and Improve Models

Aerosol and clouds play key roles in Earth's climate system but are among the most difficult aspects to properly simulate. CALIPSO provided new measurements and metrics to evaluate and improve the representation of aerosol and clouds in a variety of models. CALIOP's vertically resolved observations of aerosol loading provided uniquely important capabilities for analyzing emission and transport processes. Aerosol modeling groups worldwide used CALIOP to evaluate and improve the performance of both regional and global models. Konsta et al. (2018) evaluated the ability of the Spanish BSC-DREAM8b regional model to simulate the 3D distribution and transport pathways of Sahara dust using the LIdar climatology of Vertical Aerosol Structure (LIVAS) dust climatology, a third-party level 3 (L3) data product based on CALIOP profile data (Amiridis et al., 2015). Bou Karam et al. (2017) used CALIOP aerosol profile data and a regional model to study the mobilization of dust in Iraq by the Shamal low-level jet.

Ocko and Ginoux (2017) compared CALIOP aerosol profile data with the seasonal distributions simulated at 7 polluted and biomass burning sites around the world by two Geophysical Fluid Dynamics Laboratory (GFDL) global climate models: CM2.1 and CM3, used in CMIP-3 and CMIP-5, respectively. While the two models have many similarities, their treatments of aerosols are quite different, leading to significant differences in the simulated 3D seasonal distributions. Comparison of the two models to CALIOP aerosol profiles showed that some aspects were better simulated by the more advanced CM3 while other aspects are better simulated in the earlier CM2.1 model. In particular, an aerosol injection height parameterization in CM3 performed more poorly than the older scheme used in CM2.1. These comparisons provided insights into the underlying aerosol physics and provided guidance for model improvements.

Modeling the long-range transport of Sahara dust has been confounded by a persistent puzzle. Observations consistently show weaker removal of large super-micron dust particles during transport across the Atlantic than expected from the gravitational settling velocities predicted by Stokes theory. Removal rates are relevant to the role played by Sahara dust either in ocean fertilization, if removed during trans-Atlantic transport, or in fertilization of the Amazon basin if sedimentation is suppressed. Gasteiger et al. (2017) used CALIOP dust profile data, airborne in situ measurements, and modeling to examine two hypotheses on the processes controlling the removal of super-micron dust during transport. The study suggested that vertical mixing within the lofted Sahara dust layer, likely due to in situ heating of the dust by absorption of sunlight, can allow large particles to stay airborne longer.

Additional studies have used CALIPSO data to assess the vertical lofting of dust in the MACC-II and WRF-Chem models (Cuevas et al., 2015; Nabavi et al., 2017), and to replicate dust outbreaks in the meso-NH model (Bou Karam Francis et al., 2017). While dust models are widely used to forecast the occurrence and impacts of dust storms, model estimates of dust storm intensity and the amount of dust emitted are highly uncertain. In an attempt to reduce these uncertainties, Todd and Cavazos-Guerra (2016; see Figure 2-10) developed a method to use CALIOP profile data to quantify dust emissions across the Sahara. The method has advantages over previous efforts using TOMS (Prospero et al., 2002), which is limited to daytime data only, and the geostationary SEVIRI infrared sensor, which has only limited capabilities to identify dust at night. Analysis of geographic and diurnal emission patterns, in conjunction with weather analyses, allows the identification of atmospheric processes responsible for dust mobilization, pointing to a path for improving parameterizations of dust mobilization processes in models.

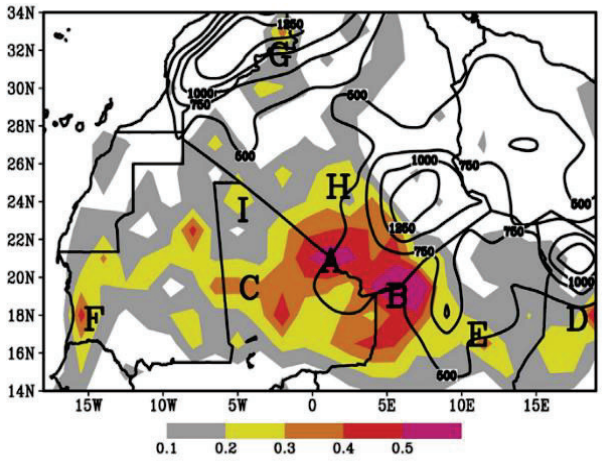

Figure 2-10. Long-term mean dust emission intensity (shaded) derived from analysis of CALIOP data for June-September 2006-13 (from Todd and Cavazos-Guerra, 2016; © Elsevier Ltd, Used under CC BY 4.0).

CALIPSO observations are also critical to improvements in model representations of clouds. Due to the spatial heterogeneity of clouds relative to the size of model grids and the large span of cloud properties, it is difficult to meaningfully compare satellite observations with model simulations. Instead, 'instrument simulators' were developed which create synthetic cloud observations from model output data (Bodas-Salcedo et al., 2011). The algorithm used to simulate CALIOP detection of climate model cloud layers was also applied to CALIOP level 1 (L1) data and used to produce the General Circulation Models (GCM) Oriented CALIPSO Cloud Product (GOCCP), providing an observational cloud data set comparable to the simulated cloud detections (Chepfer et al., 2008, 2010). The CALIPSO simulator and GOCCP product were widely accepted and had proven invaluable for evaluating the representation of clouds in GCMs (Cesana et al., 2019a; Po-Chedley et al., 2019; Zhang, Y. et al., 2019). Only the ISCCP and CALIOP simulators were recommended for all of the core experiments that were run within CFMIP in support of the next IPCC climate assessment.

It is well known that most climate models underestimate marine stratiform cloud fraction in tropical subsidence regions. These clouds are maintained by a balance between competing processes of production and break-up and are very sensitive to how these processes are parameterized in the model. Koshiro et al. (2018) used CALIPSO observations from GOCCP to diagnose factors related to model

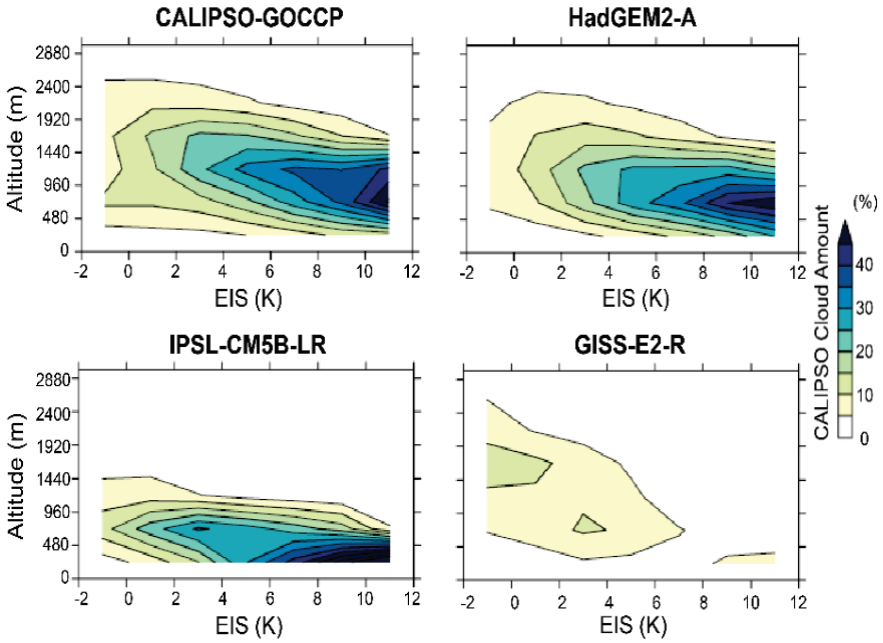

Figure 2-11. Low cloud occurrence as a function of EIS. The top left show CALIPSO-GOCCP observations; the remaining panels show predictions by global circulation models (adapted from Fig. 4, Koshiro et al., 2018; Used under CC BY 4.0).

underestimates of shallow cloud amounts. Bodas-Salcedo et al. (2019) further showed that the introduction of new model schemes related to cloud microphysics reduces the bias in the SW feedback due to low-level clouds over the southern Indian Ocean. The estimated temperature inversion strength (EIS, Wood and Bretherton, 2006) at the top of the marine boundary layer exerts a strong control on low cloud cover. EIS was found to be well-simulated in the models, with little inter-model diversity, but there was a large model diversity in the simulated stratiform cloud cover (Figure 2-11). Comparisons with CALIPSO vertically resolved cloud cover show that the marine boundary layers simulated by models are too shallow. To gain insight into cloud responses to climate warming, Cesana et al. (2019b) use the GOCCP data set to investigate cloud changes in response to interannual SST changes. They evaluate monthly changes in the vertical structure of low cloud cover in 12 CMIP5 models and two versions of the Goddard Institute for Space Science (GISS) climate model against the changes observed in 10 years of the GOCCP data set. While the models are found to capture the sign and shape of the profile of monthly low-cloud cover changes in response to SST changes, the magnitude of cloud changes is underestimated, and varies considerably between models. Results from these studies help identify paths to model improvement. Moist processes within the Planetary Boundary Layer (PBL) appear to be critical to model performance, and the inability of models to simulate the observed relationship between cloud cover and EIS may be linked to the processes which lead to unrealistic vertical structure of the marine boundary layer.

2.4.3. Stratospheric Aerosol

Although not an original mission science objective, CALIPSO had provided a continuous record of the vertical distribution and evolution of stratospheric aerosols over the globe since 2006 (Vernier et al., 2009; Khaykin et al., 2017; Thomason et al., 2018). While a series of SAGE solar occultation instruments had been delivering accurate measurements of stratospheric aerosol optical depths since the 1980s, the CALIOP data bridged a critical gap in this long-term record that occurred between the

demise of SAGE II in 2005 and the activation of SAGE III-ISS in 2017. These two data sets are highly complementary. CALIOP observed aerosol in the stratosphere with higher spatial and temporal resolution than SAGE, while the SAGE retrievals of aerosol extinction are more accurate. SAGE III-ISS data were used extensively in the initial validation the CALIOP stratospheric aerosol product (Kar et al., 2019).

CALIOP observations during the gap between SAGE II and SAGE III-ISS document an increase in stratospheric aerosol loading since the mid-2000s due to a number of moderate volcanic eruptions and wildfire activities. Friberg et al. (2018) used Version 4 (V4) L1 data to construct a time history of aerosol optical depths from the tropopause to the mid-stratosphere from 2006 through 2015 and used this to estimate the climate forcing from stratospheric aerosol. Increases in stratospheric aerosol forcing as large as 40% are traced to a series of moderate volcanic eruptions, which generated an increased cooling of ~0.2 W/m^2 over the study period.

The improved calibration introduced in CALIPSO's V4 and Version 5 (V5) data releases led to significant improvements in stratospheric aerosol retrievals from CALIOP and the subsequent development of an official L3 stratospheric aerosol product (Kar et al., 2019). This product came at an opportune moment for assessing stratospheric change and diagnosing the effects from the massive eruption from Hunga Tonga in 2022 (see Figure 2-12). The increasing frequency and intensity of wildfires spreading over large areas has injected significant amounts of smoke into the stratosphere, in some cases equivalent in mass to a moderate volcanic eruption (Peterson et al., 2018). These injections, which are closely linked to pyrocumulonimbus activity (Peterson et al., 2014), could contribute to a substantial increase in radiative heating of the stratosphere, as smoke is more absorbing than typical volcanic aerosols. (Christian et al., 2019).

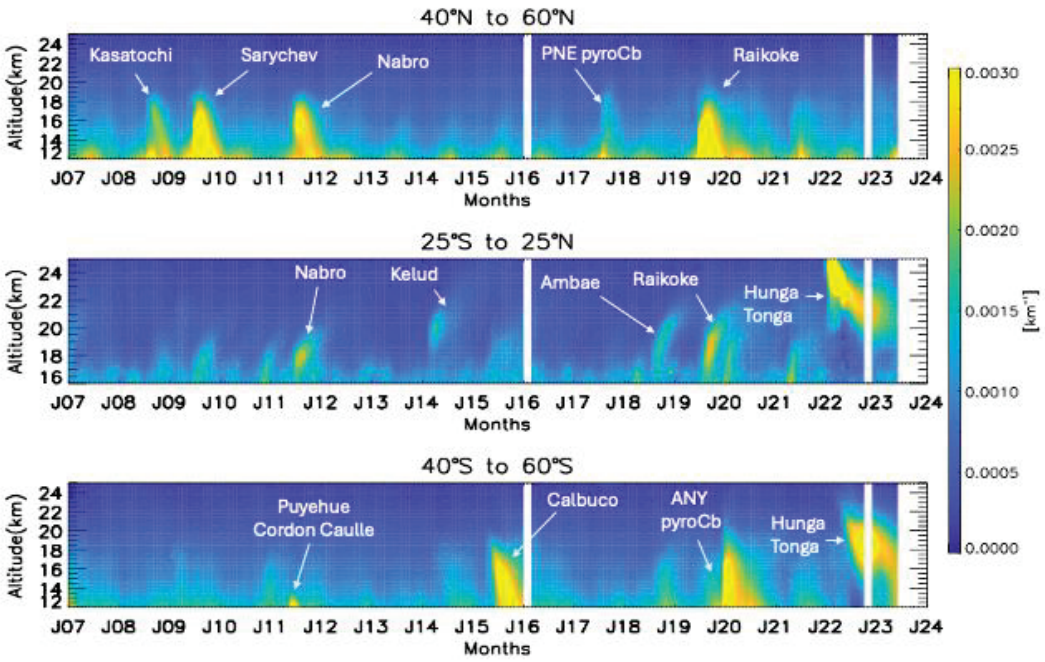

Figure 2-12: CALIOP 17-year record of stratospheric extinction that displays the loading and decay of volcanic ash and sulphate aerosol in three latitudinal bands following major eruptions highlighted in the figure. The impact on the stratosphere from major injections of smoke from pyrocumulonimbus systems from devastating wildfires in the Pacific Northwest Event (PNE) in 2017 and the Australian New Year's (ANY) in 2020 (Source credit: NASA).

2.4.4. Polar Stratospheric Clouds

CALIPSO's unparalleled 17-year dataset on Polar Stratospheric Clouds (PSCs) provides a valuable resource to the science community for studies of the roles PSCs play in stratospheric chlorine activation and ozone depletion. The roles of PSCs differ depending on particle composition, with chlorine activation primarily occurring on Supercooled Ternary Solution (STS) droplets, denitrification driven by Nitric Acid Trihydrate (NAT) particles, and dehydration by sedimentation of ice. The long-term CALIOP PSC dataset stimulated a new era in research aimed at bridging the gaps in our understanding of PSC processes, all of which are crudely parameterized in global models. An example of the unique data provided by CALIOP is given by Figure 2-13, which shows the mean and standard deviation of the spatial coverage of Antarctic PSCs over the first 12 years of CALIOP observations (panel a), along with a breakdown of the observations by composition. The renewed interest in PSCs also motivated a new PSC initiative (PSCi) led by members of the CALIPSO PSC team.

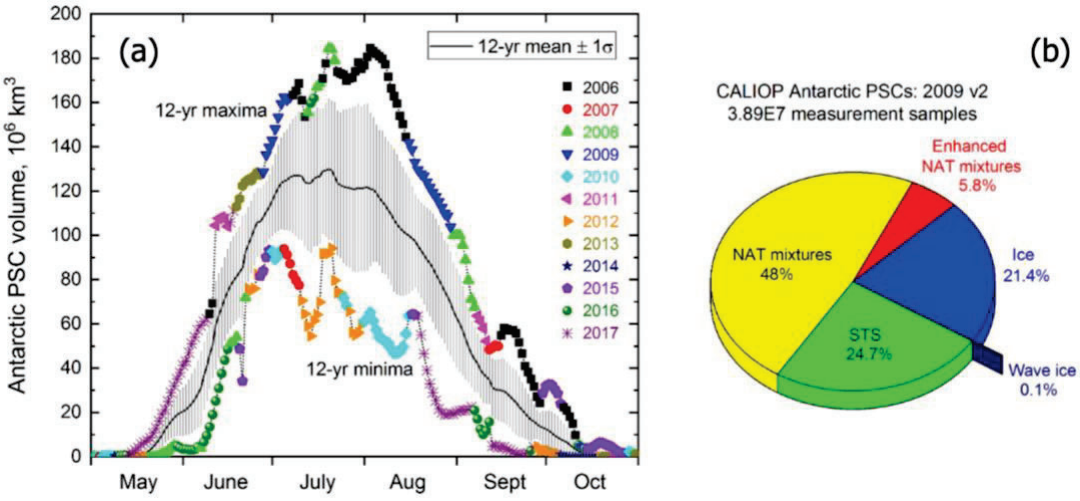

Figure 2-13. (a) time series of monthly mean Antarctic PSC spatial volume computed for 2006-2017; the black solid line shows monthly means; gray bars show ±1 standard deviation for each month; for each month, minimum and maximum values are shown with symbols color-coded by occurrence year (b) mean PSC compositions observed over the same period (images from Pitts et al., 2018; Used under CC BY 4.0).

2.4.5. Exploiting Surface Measurements

Though largely ignored prior to launch, the signals from CALIOP surface returns have since been mined for a wealth of unanticipated new discoveries (Lu and Hu, 2014; Lu et al., 2016). Lu et al. (2017) developed a technique that uses surface depolarization ratios and surface backscatter color ratios to discriminate between four Arctic surface types: open ocean, bare land, snow/ice, and surface melt ponds. As illustrated in Figure 2-14, surface returns from snow/ice are characterized by high depolarization and color ratios, whereas returns from open oceans show markedly lower values for both quantities. In May, surface returns from bare land and from melt ponds forming on sea ice are characterized by low and high values of color ratio, respectively, and intermediate values of depolarization ratio. Results from this classification scheme show good correlation with surface products from MODIS and AMSR-E. Snow/ice cover and melting exhibit large interannual variability. This new CALIOP technique complements existing satellite capabilities, providing high spatial resolution, insensitivity to lighting conditions, and an ability to characterize the surface even when obscured by optically thin cloud.

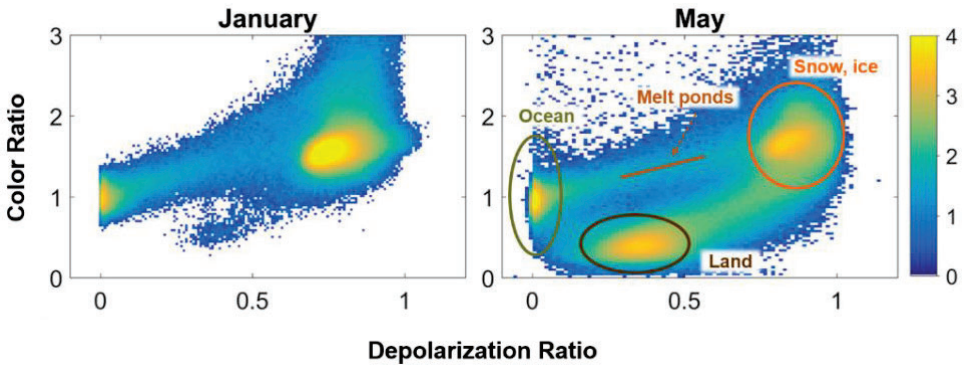

Figure 2-14. Monthly 2D histogram of Arctic depolarization ratio and color ratio in January (left) and May (right) (from Lu et al., 2017; © Copyright Elsevier, Used under CC BY-NC-ND 4.0).

Over oceans, CALIOP's ability to extract scientifically useful information increases significantly. In principle, given knowledge of the surface wind speed, the ocean backscatter signals from a well-calibrated space-based lidar can be inverted to obtain estimates of the total column optical depth between the lidar and the ocean surface (Reagan and Zielinskie, 1991). CALIOP's 532 nm calibration accuracy is well-established (Getzewich et al., 2018; Kar et al., 2018) and suitable wind speed estimates are available from collocated MERRA-2 (Modern-Era Retrospective analysis for Research and Applications, Version 2) reanalysis data and AMSR retrievals (Ryan et al., 2024). Unfortunately, transient response artifacts in the 532 nm detectors (Hunt et al., 2009) introduce persistent overestimates of ocean surface backscatter that impede unbiased column optical depth retrievals. To circumvent this obstacle, Ryan et al. (2024) leveraged prior work by Venkata and Reagan (2016) to fully characterize and compensate for these detector artifacts, leading to a robust, fully automated retrieval that now delivers high-quality estimates of total column optical depth from CALIOP's ocean surface signals. The lack of bias in this retrieval is demonstrated by Figure 2-15, which shows global, multi-year comparisons to collocated MODIS aerosol optical depths. The data products generated by this method have since been comprehensively validated using global AERONET AOD measurements (Thorsen et al., 2025) and have been used to make substantial contributions in nighttime estimates of the liquid water content of thin clouds observed by CloudSat and CALIPSO (Schulte et al., 2024) and in using multi-sensor satellite observations to quantify aerosol direct radiative effects (Kacenelenbogen et al., 2025).

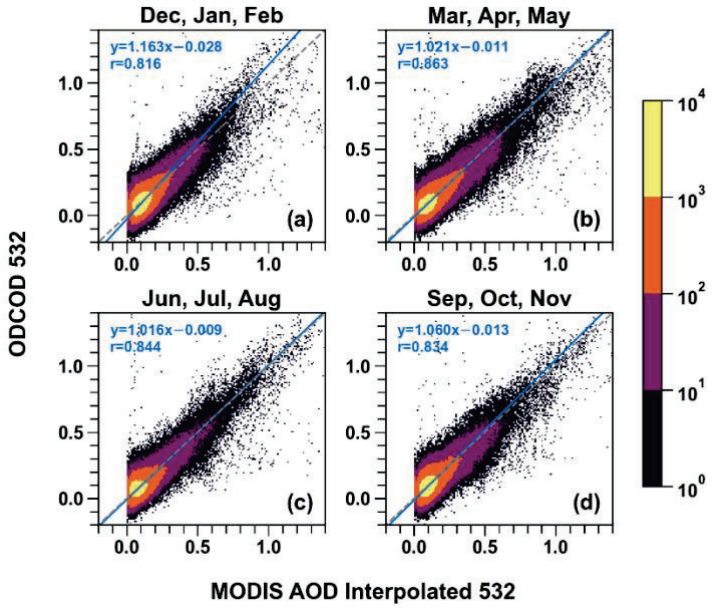

Figure 2-15. Comparison of CALIOP Ocean-Derived Column Optical Depths (y-axis) to collocated MODIS AOD retrievals for all measurements between March 2008 and February 2011. Image from Ryan et al., 2024. Comparisons are for daytime data only. Because the MODIS algorithm uses sunlight as a light source, MODIS does not retrieve optical depths during the nighttime portions of its orbit. On the other hand, because CALIOP's light source is an onboard laser, CALIOP delivers estimates of column optical depths over global oceans for nighttime and daytime (Source credit: NASA).

2.4.6. Ocean Subsurface Retrievals

CALIPSO began its on-orbit lifetime as a dedicated atmospheric sensor capable of delivering a wealth of new discoveries about the vertical structure of clouds and aerosols. By the end of its lifetime, its atmospheric observational prowess had been augmented by a revolutionary extension of its scientific measurement's capability. In a ground-breaking paper published in 2013 (Behrenfeld et al., 2013), CALIPSO Lidar Science Working Group (LSWG) members first introduced the use of CALIOP backscatter coefficients measured beneath the ocean surface to estimate global ocean phytoplankton biomass and total particulate organic carbon stocks. Figure 2-16 shows global distributions of subsurface particulate backscattering coefficients (b_{bp}) retrieved from CALIOP 532 nm perpendicular channel measurements acquired between 2006 and 2012. The stark seasonal changes seen in high-latitude backscatter intensities correspond perfectly with well-documented seasonal changes in phytoplankton abundances. Relative to passive sensors, the disadvantage of CALIOP's zero-width swath is offset by its ability to acquire both daytime and nighttime observations (passive sensor phytoplankton retrievals are only possible during daytime) and to make reliable measurements below dense aerosol layers and semi-transparent clouds. CALIOP ocean subsurface data have since been used to characterize the "annual boom–bust cycles of polar phytoplankton biomass" (Behrenfeld et al., 2017) and to provide a first global survey of the diurnal cycles in feeding patterns for ocean-dwelling animals (Behrenfeld et al., 2019a). Subsequent investigations have used CALIOP ocean sub-surface retrievals to improve the accuracy of ocean color estimates derived from collocated passive sensors (Bisson et al); validate improved MODIS retrievals of chlorophyll-a (Zhang, K. et al., 2024); map krill distributions in the southern oceans (Zhong et al., 2024); and estimate the flux of CO_2 between the atmosphere and the oceans (Huang, H. et al., 2024; Zhang, S. et al., 2024).

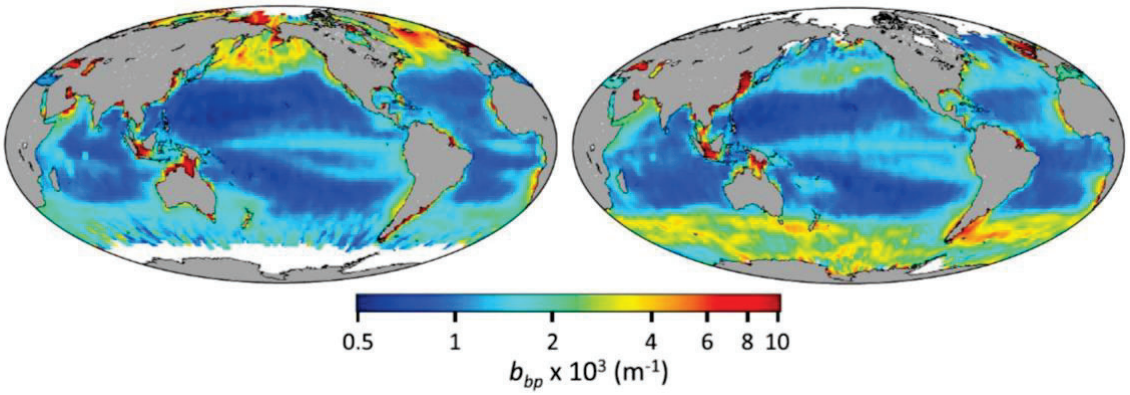

Figure 2-16: Seasonal changes in subsurface particulate backscattering coefficients (b_{bp}). The left panel shows boreal summer (June–August) while the right panel shows boreal winter (December–February). Data are CALIOP-based b_{bp} seasonal average climatologies for the 2006–2012 period binned into 2° latitude × 2° longitude pixels. (Figure and caption adapted from Figure 3 in Behrenfeld et al., 2013; © American Geophysical Union, Used under CC BY 4.0).

2.4.7. Air Quality, Health and Hazards

CALIPSO observations were increasingly used to monitor and evaluate forecasts of aerosol impacts on air quality and human health. In a proof-of-concept study, Toth et al. (2019) derived $PM_{2.5}$ over the continental USA from near-surface CALIOP aerosol retrievals and model-based aerosol hygroscopicity for two years (2008-2009). CALIOP aerosol types were used to constrain estimates of the scaling coefficients necessary to convert extinction to mass. In a follow-on study, Toth et al. (2022) applied this $PM_{2.5}$ derivation technique over the continental USA for an extended portion of the CALIPSO record (2007-2018). Twelve-year means and trends of $PM_{2.5}$ concentrations derived using CALIOP observations were found to capture the spatial variability of those computed using surface *in situ* $PM_{2.5}$ datasets from the U.S. Environmental Protection Agency (EPA) (Figure 2-17; Toth et al., 2022). Toth's technique could potentially deliver $PM_{2.5}$ estimates to underserved regions throughout the nation. In other applications, CALIOP aerosol profiles are used to initialize transport models to quantify the impact of long-range aerosol transport on regional air quality (Zhang, Z. et al., 2017; Wang, S.-C. et al., 2018; Ray et al., 2019); are combined with AOD from MODIS or other passive sensors to estimate surface $PM_{2.5}$ (Gao et al., 2017; Chowdhury et al., 2018; Li, Y. et al., 2018; Nam, J. et al., 2018; Bauer et al., 2019; Beig et al., 2019; Li, W. et al., 2019a; Li, W. et al., 2019b); are assimilated into forecast models; and are used to check numerical simulation results that assimilate AODs from other satellites (Jung et al., 2019). Simulations of spring dust outbreaks leading to PM_{10} exceedances have also been validated using CALIPSO aerosol data products (Bessagnet et al., 2017; Ma et al., 2019).

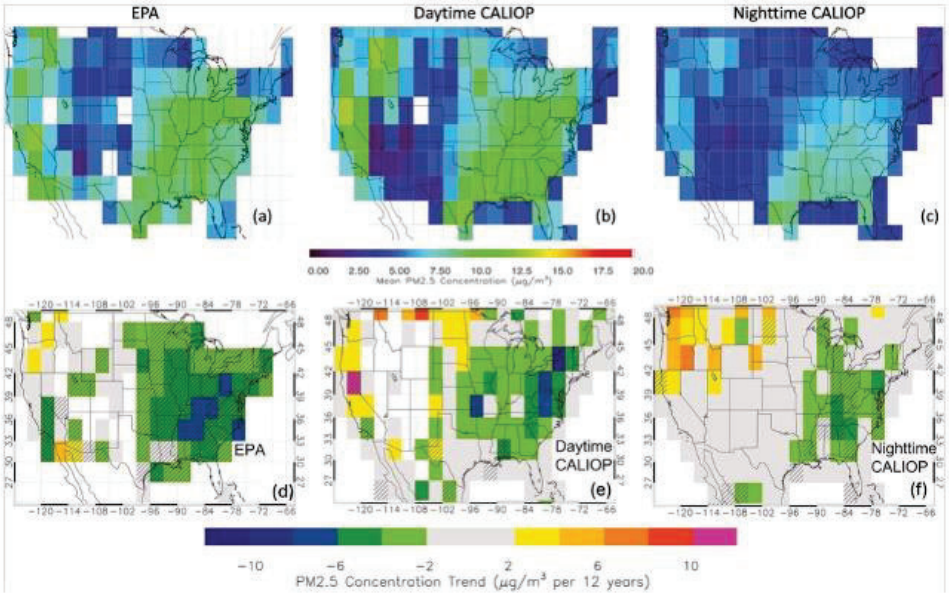

Figure 2-17. Twelve-year (2007-2018) mean $PM_{2.5}$ concentrations (a) at EPA stations and those derived from (b) daytime and (c) nighttime CALIOP near-surface aerosol extinction (gridded at 3°x3° latitude/longitude resolution). Also shown are the corresponding twelve-year (2007-2018) $PM_{2.5}$ concentration trends at (d) EPA stations and those computed from CALIOP measurements for (e) daytime and (f) nighttime conditions (gridded at the same resolution). Hatched grid boxes indicate trends that are significant at the 95% confidence interval, calculated using the Mann-Kendall Test. From Toth et al. (2022;).

2.5. Advances in the analyses of elastic backscatter lidar measurements

CALIPSO's three sensors generated ~3.5 gigabytes of highly compressed raw data that was telemetered daily back to Earth. Each day, the CALIPSO science data processing facility converted this ~3.5 gigabytes of input into ~64 gigabytes of expedited L1 and level 2 (L2) data products built using the most recently available ancillary inputs and made available to the global data user community in near real time. As soon as high-resolution ephemeris and accurate coincident ancillary data were available (e.g., time-matched meteorological model data from the NASA's Global Modeling and Assimilation Office (GMAO), this processing cycle was repeated to produce another ~64 gigabytes of standard data products suitable for rigorous scientific analyses. The engine driving this high-speed, high-volume data production was a collection of advanced, fully automated science retrieval algorithms developed and implemented by the CALIPSO project. The subsections below highlight the most important of these algorithms.

2.5.1. Calibration

Space-based elastic backscatter lidars are typically calibrated at very high altitudes using the well-known molecular normalization technique (Osborn et al., 1998; Palm et al., 2004). Implementing this technique for CALIOP measurements presented two thorny instrument-related problems: very low Signal-to-Noise Ratio (SNR) in the high-altitude calibration regions and thermal beam steering that caused calibration changes by ~30% during the course of a single orbit (see Figure 4-15). To overcome these challenges, the French and American members of the LSWG jointly developed innovative noise rejection techniques (Powell et al., 2009) and data averaging schemes (Kar et al., 2018; Getzewich et al., 2018) that delivered near-continuous sampling throughout both nighttime and

daytime segments of the orbits and 532 nm calibration coefficients with validated uncertainties of ~1.5%. These very low calibration uncertainties are essential for obtaining high-quality retrievals of extinction coefficient profiles in the follow-on L2 analyses.

Calibrating the 1064 nm channel presented addition challenges because the molecular backscatter signal at 1064 nm is more than 16 times weaker than at 532 nm. To surmount this difficulty, the LSWG devised a sophisticated calibration transfer scheme that used the spectrally independent back-scatter and extinction from carefully selected ice clouds to scale the 532 nm calibration for use at 1064 nm (Vaughan et al., 2019). In the process, the LSWG empirically established the theoretically posited spectral independence of laser backscatter from ice clouds using measurements made by NASA's Cloud Physics Lidar (Vaughan et al., 2010).

To calibrate the relative gain of CALIOP's 532 polarization-sensitive channels science data acquisition was periodically interrupted to insert an onboard pseudo-depolarizer into the optical path of the receiver (Powell et al., 2009). While this worked exceedingly well at night, solar background during daytime operations made this approach prohibitively costly in terms of lost science data. When a wholly unanticipated diurnal variability was discovered in Polarization Gain Ratio (PGR), the project quickly turned to an innovative approach first proposed prelaunch by LSWG members (Liu Z. et al., 2004). Using an LSWG-developed vector radiative transfer model (Zhai et al., 2009), the LSWG rapidly developed an integrated PGR calibration scheme that fully accounts for diurnal changes (Vaughan et al., 2023a).

The IIR was calibrated in flight using images of a temperature-monitored warm blackbody source and of the cold deep space. Gains for each pixel of an image in each channel were produced every 40 s to account for intra-orbit variations. This worked very well except around day-to-night terminators where the gains were slightly biased in a portion of the images with biases of different amplitude in each channel, which caused a stripping effect and systematic biases with respect to MODIS/Aqua (Garnier et al., 2017). The project revisited the calibration procedure and defined semi-empirical corrections (Garnier et al., 2018).

2.5.2. Layer Detection

The targets of scientific interest retrieved from CALIOP's global profiling measurements span enormous variations in signal strength and vertical location, from highly reflective opaque water clouds low in the atmosphere (Zeng et al., 2025) to diffuse subvisible aerosol plumes in the stratosphere (Friberg et al., 2023). To reliably detect all of these features, the LSWG created a highly flexible layer detection method that harnesses a sophisticated profile scanning engine to an iterated, multi-resolution averaging scheme, enabling CALIOP to detect the very strongest of scattering species at single shot resolution while subsequently using extensive along-track averaging to detect extremely tenuous features, all within the same scene (Vaughan et al., 2009). The original CALIOP feature finder has since spawned a family of follow-on algorithms that continue advancing the state of the art with new detection schemes that reduce false positives while offering improved sensitivity to even the faintest atmospheric features (Mao et al., 2021; Vaillant de Guélis et al., 2021; Herzfeld et al., 2025).

The climatology of cloud and aerosol layer boundaries now available in the CALIOP data products is spearheading a revolution in cloud detection in passive sensor measurements. By using CALIOP's highly accurate layer heights as training sets in machine learning algorithms, researchers have begun to mine the wealth of previously inaccessible information stored in existing passive sensor data sets, including cloud detection and thermodynamic phase classification in VIIRS and AHI imagery (Wang, C. et al., 2020; Min et al., 2020); detection of low clouds in multi-layer scenes observed by AHI and

GOES ABI (Tan Z. et al., 2022; Haynes et al., 2022); and highly confident cloud detections in the decades-long AVHRR data set (Heidinger et al., 2012).

2.5.3. Layer Type Identification

Layer detection is limited to identifying regions of suspended particulate matter that give rise to backscatter signals that significantly exceed the magnitudes expected from clear skies. Once layers are detected, determination of layer type is essential for quantifying its optical and radiative properties. To accomplish the first step in this process, the LSWG constructed a unique set of five-dimensional Probability Distribution Functions (PDFs), that, when queried using a subset of the CALIOP observables, classifies any layer as either cloud or aerosol and returns a quantitative evaluation of classification confidence (Liu Z. et al., 2009; Liu Z. et al., 2019). For clouds, thermodynamic phase is determined using an innovative lidar-only algorithm that directly partitions ice clouds from water cloud without relying on temperature but instead based on layer-integrated measured optical properties (Hu, 2007). Results derived from this technique have led to an entirely new understanding of the occurrence frequency of super-cooled water cloud and their effects on Earth's radiation budget (Hu et al., 2010; Bodas-Salcedo et al., 2016). For aerosols, a pair of decision trees are used to separately classify tropospheric aerosols and stratospheric aerosols according to subtype (e.g., dust, smoke, volcanic, etc.; Omar et al., 2009; Kim M.-H. et al., 2018; Tackett et al., 2023). CALIOP is the first space-based sensor to identify height-resolved aerosol subtypes, and this capability has garnered an enormous amount of research interest. All of the layer type identification algorithms were designed and developed prelaunch by the CALIPSO LSWG and subsequently refined repeatedly as the mission progressed.

2.5.4. Parameterizations of Multiple Scattering

Retrievals of layer spatial and optical properties can be badly confounded by the multiple scattering of photons within the lidar field of view. In extreme cases, space-based lidar signals from dense stratus can appear to penetrate several kilometers below the Earth's surface (Miller and Stephens, 1999). Due to significant advances in systems design, this aberration does not occur in CALIOP measurements. Nevertheless, disentangling single scattered photon from their multiply scattered companions remains one of the most challenging problems in lidar data analysis.

2.5.4.1. Multiple Scattering in Water Clouds

In dense water clouds, multiple scattering rapidly overwhelms the single scattered component of the measured backscatter, making the retrieval of height resolved profiles of optical properties extremely uncertain. However, due to the pioneering work of the LSWG, CALIOP measurements of these clouds can be confidently mined to obtain numerous important optical properties. Early in the mission, the LSWG formulated a theoretical relationship between multiple scattering and direct measurements of the volume depolarization ratios in water clouds (Hu et el., 2006, 2007a). The implications of this relationship lead directly to the generation of several first-of-their-kind data products, e.g., to accurate retrievals of water cloud lidar ratios (Young et al., 2018; Zeng et al., 2025) and to the first ever estimates of particulate optical depths above opaque water clouds, now routinely reported in the CALIOP data products (Hu et al., 2007b; Liu Z. et al., 2015). This latter achievement is now making major contributions toward a much-improved empirically based accounting of Direct Aerosol Radiative Effects (DARE; Kacenelenbogen et al., 2019; Kacenelenbogen et al., 2025).

2.5.4.2. Multiple Scattering in Ice Clouds

While multiple scattering in ice clouds is somewhat more tractable than in water clouds, failing to account for its effects can lead to significant underestimates in height-resolved extinction coefficients and optical depths. By leveraging simultaneous, perfectly collocated observations of transparent ice clouds by both CALIOP and the IIR, the LSWG developed a temperature-dependent parameterization of multiple scattering that was instrumental in resolving biases in ice cloud optical depths that plagued early comparisons between CALIOP and MODIS (Garnier et al., 2015; Holz et al., 2016). Because ice clouds are significant modulators of the Earth's radiation budget, this highly accurate accounting of ice cloud multiple scattering is a prerequisite for retrieving the profiles of extinction coefficients used to validate and correct climate models (Gasparini et al., 2018).

2.5.5. Calculating Particulate Extinction Profiles

Passive sensors provide a two-Dimensional (2D) view of the Earth that extends both along track and across track but does not provide any information in the vertical dimension. The across track dimension, known as the swath, and varies substantially for different sensors, from ~64 km for the CALIPSO IIR to ~3,060 for VIIRS. In contrast, active sensors also provide a 2D view of the Earth that extends along track, but with a second dimension that extends vertically above the ground track rather than horizontally across the track so that, relative to passive sensors, active sensors such as CALIPSO and CloudSat have a zero-width swath. Consequently, gaining 3D insights into the Earth's atmosphere requires the combination of passive and active measurements.

A key parameter delivered by passive sensors is the optical depth of the atmospheric column (i.e., within each image pixel), which is often measured or retrieved at multiple wavelengths. To do these retrievals, passive sensors must first determine whether the particulates in each scene are vertically homogeneous. As illustrated in Figure 2-18, vertical homogeneity is not guaranteed. The atmosphere often contains a chaotic mix of different feature types, and in these cases current passive sensor retrievals are incapable of teasing out the optical depths of the individual layers. However, these multi-layer scenes present no impediment to the powerful extinction retrieval algorithm designed and developed by the LSWG. When faced with multiple layers in a column, the extinction algorithm processes them sequentially, starting with the uppermost layer and progressing downward (Young and Vaughan, 2009). Informed by the classifications of layer types conducted earlier in the analyses, the extinction algorithm calculates vertical profiles of particulate extinction coefficients at both 532 nm and 1064 nm. These profiles are subsequently integrated between layer top and base to derive optical depths. Although optical depths cannot be computed in opaque layers (because the signal becomes totally attenuated before reaching layer base), CALIOP's extinction retrieval remains stable and calculates accurate extinction estimates even when retrieving values from deep within opaque ice clouds (Young et al., 2018).

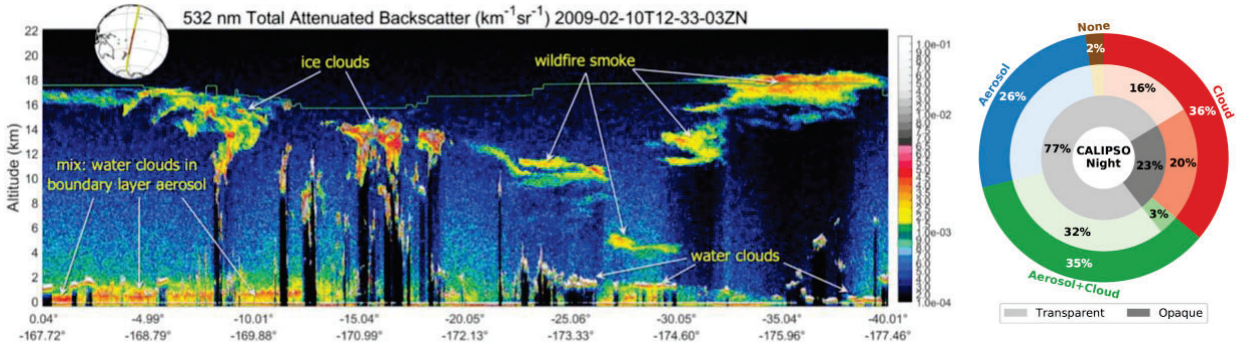

Figure 2-18: The left panel shows a scene measured over the western south Pacific shortly after the eruption of the 2009 "Black Saturday" bush fires in Australia. The solid green horizontal line between ~15 km and ~18 km shows the local tropopause height. In this scene there are no vertically homogeneous columns, making it entirely intractable for passive sensor retrievals. The right panel uses multiple years of nighttime CALIOP measurements to partially quantify the relative occurrence frequencies of multi-layer observations such as seen in the left panel. A vertical mix of clouds and aerosols are detected in 35% of all cases. However, because no distinction is made between ice clouds and water clouds this diagram underrepresents the occurrence frequency of multi-layers scenes (Source credit: NASA).

2.5.6. Data Fusion I: Implementation of the LIRAD Method from Space

Space-based application of the venerable LIdar+RADiometer technique (LIRAD), first proposed for ground-based instruments in the early 1970s (Platt, 1973) was made possible only because CALIOP flew in tandem with the IIR (Garnier et al., 2018). By applying the LIRAD method to CALIPSO's multi-sensor measurements, the LSWG delivered significant advances in the knowledge of ice cloud optical depths (Garnier et al., 2012; Garnier et al., 2021a; Garnier et al., 2021b). Furthermore, because IIR-derived optical depths are only weakly sensitive to scattering and to the microphysical assumptions required for the conversion from the thermal infrared to the visible spectrum, they provided a critically important reference to assess and greatly improve the accuracies of the CALIOP optical depth retrievals. This CALIPSO-specific synergy also paid dividends for other A-Train sensors, as it was instrumental in resolving cirrus optical depth biases between CALIOP and the MODIS-Aqua visible/near infrared retrievals (Holz et al., 2016).

2.5.7. Data Fusion II: Retrieving Aerosol Lidar Ratios Using CALIOP+MODIS

The overriding scientific motivation for the A-Train satellite constellation was the promise of multi-sensor data fusion. Collocated, near-simultaneous measurements of Earth's atmosphere and oceans from both passive and active sensors would deliver "comprehensive information about various key components and processes of the Earth system" (Maring, 2007) and thus yield science insights that could not otherwise be retrieved from any single instrument. In a notable example of this promised A-Train synergy, the LSWG paired MODIS AOD retrievals with CALIOP attenuated backscatter profiles to derive empirically based estimates of the extinction-to-backscatter ratios (i.e., lidar ratios) of marine aerosols in cloud-free skies (Toth et al., 2025). The global maps of regionally and seasonally varying lidar ratios generated by this effort were fully integrated into the CALIPSO V5 data release, thereby markedly improving the correspondence between CALIOP and MODIS marine AOD estimates and ensuring highly reliable estimates of the vertical structure of aerosol optical properties.

2.5.8. Cloud microphysical properties

The three IIR channels at 8.65, 10.6 and 12.05 μm were chosen specifically for retrieving cirrus microphysical properties. Ice crystal size information is contained in the 12.05-to-10.6 and 12.05-to-

8.65 ratios of effective absorption optical depths, called, respectively, the $\beta_{eff}12/10$ and $\beta_{eff}12/08$ microphysical indices. These indices are very sensitive to the presence of small particles. By leveraging CALIOP's layer detection sensitivity, LSWG developers derived and implemented sophisticated IIR-based algorithms that retrieved ice crystal effective diameters and ice water path in thin cold cirrus with optical depths smaller than 0.3 over oceans (Garnier et al., 2013, 2021a, 2021b). This accomplishment fills an important void in the ice crystal size retrievals previously derived from the CloudSat radar and from passive sensors such as MODIS.

The LSWG further advanced the state-of-the-art in characterizing cirrus microphysical properties by developing innovative and entirely new retrievals of ice crystal number concentration, thereby offering new insights into cirrus cloud formation through heterogeneous and/or homogeneous nucleation (Mitchell and Garnier, 2025). This new technique uses in situ measurements from numerous field measurements campaigns in the tropics and mid-latitudes to formulate relationships between the IIR $\beta_{eff}12/10$ microphysical index and relevant microphysical quantities (Mitchell et al., 2018; Mitchell et al., 2025).

2.5.9. Extending the Boundaries of Lidar Data Analyses

When CALIPSO launched in April 2006, the primary mission science objectives (section 2.3) were focused exclusively on goals that could be attained by measuring vertical profiles of clouds and aerosols in the Earth's atmosphere. During 17 years on orbit, the CALIPSO LSWG extended the wealth of knowledge that could be retrieved from space-based elastic backscatter lidar measurements into previously inconceivable arenas. The subsections below provide brief synopses of these algorithmic and data product accomplishments.

2.5.9.1. Optical Depths from Ocean Surface Measurements

Retrieval synergies across different sensors was the raison d'être of the A-Train. Early in the mission, LSWG members realized this goal with a surprising revelation: particulate optical depths in the atmospheric column could be accurately inferred by combining ocean surface measurements from CALIPSO and CloudSat (Josset et al., 2008). This discovery led to the development and distribution of the Synergized Optical Depths of Aerosols (SODA) data product (Josset et al., 2011), which subsequently found numerous uses in aerosol and cloud research (Josset et al., 2012; Dawson et al., 2015; Painemal et al., 2019; Li, Z. et al., 2022). Unfortunately, plans to incorporate SODA retrievals into CALIOP's standard data product offerings were torpedoed by a CloudSat battery anomaly in April 2011 that thereafter limited CloudSat's data collection to daytime orbit segments only (Nayak et al., 2012). The LSWG's fallback position was to develop a lidar-only algorithm that used prelaunch laboratory measurements to fully characterize the non-ideal instrument response of the CALIOP photomultipliers to extremely strong signals (Venkata and Reagan, 2016). Substantial efforts were focused on the design and development of the new Ocean Derived Column Optical Depths (ODCOD) algorithm, which, beginning with the V4.51 data release, now provides CALIOP data users with column optical depth estimates both day and night over global oceans (Ryan et al., 2024).

2.5.9.2. Wind Speeds

While the ocean surface was never envisioned as a target of interest in the prelaunch CALIPSO science plans, it has nonetheless played a prominent role in the development of multi-sensor retrieval methods that take advantage of CALIOP measurements. In 2008, LSWG members published an influential paper that uses coincident AMSR-E measurements to derive an empirical correlation between sea surface wind speeds and CALIOP ocean surface backscatter (Hu et al., 2008). This development opened the door for the use of space-based lidar to probe ocean-atmosphere interactions

(Neukermans et al., 2018) and helped usher in the totally unprecedented use of space lidar to characterize the ocean subsurface environment (e.g., Behrenfeld et al., 2013). The inverse of this relationship – that is, ocean surface backscatter as a function of wind speed – is now being used extensively in ocean studies that rely on measurements from NASA's ICESat-2 satellite (Lu et al., 2020; Lu et al., 2021; Li, X. et al., 2025).

2.5.9.3. Probing Beneath the Ocean's Surface

From the earliest days of the mission, CALIPSO LSWG members pioneered to use of CALIOP measurements to extract unanticipated geophysical parameters from beneath the ocean surface (Hu et al., 2006; Hu, 2009; Lu et al., 2014). Refinements of these algorithms are the bedrock for extended ocean subsurface studies conducted by researchers worldwide (Dionisi et al., 2020; Behrenfeld et al., 2023; Zhong et al., 2024). The LSWG has since developed innovative signal processing algorithms that extend CALIOP's ocean subsurface retrieval capabilities to shallow water bathymetry (Lu et al., 2022). By parameterizing the shape of CALIOP's non-ideal detector response relative to the observed surface peak signal, the LSWG method retrieves a vertical precision of ~1.4 m from CALIOP's nominal 30 m vertical resolution at the Earth's surface (Lu et al., 2014). Because the 532 nm perpendicular signal is largely insensitive to the ocean surface, applying this technique to the perpendicular channel measurements in shallow waters yields both sea floor depths and an initial characterization of sea floor surface type.

2.5.9.4. Drizzle Detection

At the beginning of the mission, expectations for CALIOP retrievals from opaque water clouds were very low. While the intense backscatter signals from these clouds meant that top altitudes could be accurately located, true cloud base could not be determined because the signals were totally attenuated within the clouds. Moreover, because range-dependent multiple scattering within these clouds is very poorly parameterized, extracting reliable optical property profiles (e.g., extinction coefficients) is extraordinarily challenging. Nevertheless, as described in section 2.5.4.1, LSWG breakthroughs in characterizing layer-effective multiple scattering now enable reliable lidar ratio retrievals from opaque water clouds. Having these lidar ratios available sparked yet another wholly new retrieval developed by the LSWG. Because lidar ratios are governed by droplet size distributions, CALIOP opaque water cloud data can now be mined to determine if/when the clouds are drizzling (Zeng et al., 2025). While this information is also available from CloudSat (albeit at a coarser spatial resolution), (a) surface clutter often prevents CloudSat detections of very low clouds that are plainly visible in the CALIOP data (Liu, D. et al., 2016) and (b) CloudSat acquired only daytime measurements after April 2011. CALIOP retrievals thus fill in important gaps in the global precipitation data record.

2.5.10. Aggregating Clouds and Aerosols into Level 3 Data Products

CALIPSO L3 data products report monthly averages of key spatial and optical parameters onto 3D spatial grids (i.e., latitude × longitude × altitude). Because they are also the first routinely generated and publicly distributed L3 data products derived from space-based lidar measurements, no previous templates existed to guide the LSWG in the product development design phase. Moreover, because data quality in the lower layers depends critically on retrieval accuracies in the upper layers, the L3 algorithm designers needed to be intimately familiar with the uncertainties associated with the propagation of laser light through an inhomogeneous atmosphere, as these uncertainties dictated the quality screening parameters implemented for each product. The project distributes five L3 lidar data products and one L3 IIR data product: a tropospheric aerosol profile product that reports aerosol type-specific mean extinction profiles (Winker et al., 2013; Tackett et al., 2018); a stratospheric aerosol

profile product that reports extinction profiles for stratospheric aerosols that largely lie below the detection threshold of the L2 retrievals (Kar et al., 2019); a general cloud occurrence product that reports vertical profiles of cloud occurrence frequencies (Cai et al., 2018); an ice cloud-specific product that provides altitude-resolved histograms of extinction and ice-water content distributions (Winker et al., 2024); and two lidar products, one CALIOP-only and the other IIR-only, created specifically for the Global Energy and Water Cycle Experiment (GEWEX) Cloud Assessment (Stubenrauch et al., 2024).

2.6. Societal Benefits

When the CALIPSO concept was developed in the 1990's, the team recognized that CALIOP's high resolution profile information could be very useful to operational forecast centers. Because the mission was classified as a research mission, however, funds were limited for the ground system and the data were transmitted from the spacecraft only once per day. The data latency was often too slow to be ingested into most standard data assimilation systems. In spite of this limitation, CALIOP aerosol and cloud observations were used in multiple ways by operational agencies. A few years into the mission, the CALIPSO team developed 'expedited' versions of the standard data products to provide products to operational users as quickly as possible – usually within 24 hours of their on-orbit acquisition. Since the level 1.5 (L1.5) product was available within typical operational forecast cycles, it was used to evaluate the performance of various types of forecast models and improved the characterization of uncertainties with the satellite data being assimilated into these models.

2.6.1. Clouds and Numerical Weather Prediction

CALIPSO's vertical cloud measurements were highly valued by weather forecasting agencies and groups around the world (e.g., National Oceanic and Atmospheric Administration (NOAA), US Air Force 557th Weather Wing, US Naval Research Laboratory (NRL), ECMWF, Météo-France, UK Met Office, Environment Canada, Japan Meteorological Agency, and the Australian Bureau of Meteorology (BoM)). The data provided unique insight on satellite cloud retrieval accuracy and have played prominent roles in the development and validation of operational algorithms such as those for JPSS-1 VIIRS and NOAA GOES 16/17 observations. CALIPSO measurements combined with CloudSat data further enabled an unprecedented understanding of cloud structure and microphysics that helped advance weather model development, stimulating new data assimilation techniques, and improving forecasting skill.

CALIPSO observations became a prime training data source for increasingly sophisticated probabilistic algorithms now being pursued for cloud mask, ice/water phase and layer height retrievals from Low Earth Orbit (LEO) and geostationary constellations (e.g., Noh et al., 2017). For example, a new Machine Learning (ML) algorithm derives Cloud-Top Heights (CTHs) from combined CALIPSO and AHI observations (Min et al., 2020). This technique shows significant improvements for high altitude and optically thin clouds (reduced CTH errors of 1.5–2 km) relative to traditional algorithms based on passive sensor measurements alone. Similar machine learning CTH algorithms are under development by the NOAA and US Navy that are enhancing forecast skills of weather and visibility (Holz, personal communication, 2025).

DOI: 10.64631/LIZS5968

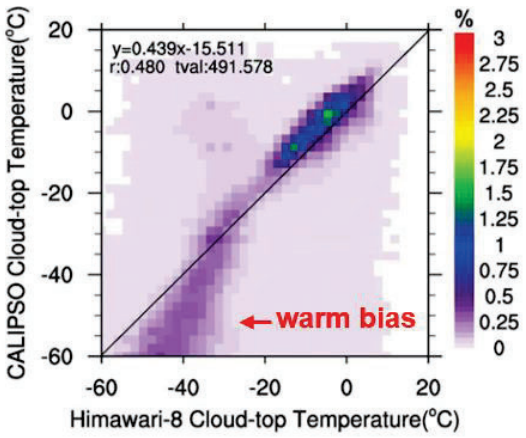

Figure 2-19. Frequency distributions of coincident CALIOP cloud-top temperatures (based on retrieved top altitude) and Himawari-8 retrieved cloud-top temperatures (adapted from Huang, Y. et al., 2019; © American Meteorological Society, Used with permission).

CALIPSO observations were further used to identify biases from undetected, misclassified, or misregistered clouds in operational satellite data products that are routinely ingested into Numerical Weather Prediction (NWP) models such as with NOAA's Rapid Refresh model, or ECMWF's Integrated Forecast System (IFS). One comparison study using coincident retrievals from CALIPSO and Himawari-8, displayed in Figure 2-19, revealed a warm CTH bias in the AHI results for colder (higher) clouds (Huang Y. et al., 2019). A different study found a cold bias of about 0.1°C in tropical SSTs because IR satellite sensors are unable to detect optically thin clouds that are observed by CALIPSO (Marquis et al., 2017).

NWP models use Atmospheric Motion Vectors (AMVs) to provide wind estimates in remote regions where direct measurements are not available. CALIOP cloud detections provide validation information for AMV retrieval algorithms, such as those of Himawari-8 and the Geostationary Korea Multipurpose Satellite GEO-KOMPSAT-2A (Oh et al., 2019; Santek et al., 2019). CALIOP data were used to evaluate the horizontal averaging length of measurements by Aeolus, the ESA wind-profiling satellite mission (Šavli et al., 2019), and to develop the infrastructure for assimilating Aeolus aerosol data into transport models (A. Benedetti/ECMSW, personal communication, 2020).

2.6.2. Aviation Safety

CALIPSO provided critical information for two aviation hazards: volcanic ash and aircraft icing. Volcanic ash is recognized as a major safety concern for the aviation industry (Casadevall, 1994; Guffanti et al., 2010). To alert air traffic controllers to potential threats due to volcanic ash, nine regional Volcanic Ash Advisory Centers (VAACs) prepare forecasts of volcanic ash dispersion using observations from satellites, ground-based sensors, and trajectory models. The Darwin VAAC routinely used the precise vertical information provided by CALIOP expedited data to determine the altitude of volcanic ash within air traffic corridors (A. Tupper/BoM, personal communication, 2020). CALIPSO volcanic ash detections were also used by the Darwin VAAC to verify and calibrate volcanic ash forecasts from the BoM's ACCESS model (Zidikheri et al., 2018).

CALIPSO has proved invaluable for validating volcanic aerosol height retrievals from passive and active satellite instruments. For example, the EUNADICS-AV project, aimed at understanding the data available to European agencies during airborne hazards, used CALIPSO to validate volcanic ash

and dust plume heights retrieved by several operational satellites including IASI, OMI, TROPOMI, SEVIRI, and SLSTR (Virtanen et al., 2019). Similarly, the World Meteorological Organization (WMO)-sponsored SCOPE-Nowcasting Volcanic Ash Algorithm Intercomparison project also relies on CALIPSO for validation data. CALIPSO further provides a key data set for validating near-real time TROPOMI volcanic SO_2 layer height retrievals (Hedelt et al., 2019) and new volcanic ash detection techniques using Global Navigation Satellite Systems (GNSS) radio occultation measurements (Biondi et al., 2017; Cigala et al., 2019).

Aircraft icing is also a significant threat to aviation safety. This includes the freezing of supercooled liquid water as ice on the aircraft which reduces lift and air speed (Smith et al., 2012), and where ice is ingested by the engine, causing power loss (Haggerty et al., 2019). The combined CALIPSO/CloudSat DARDAR product was used to validate retrievals that routinely forecast aircraft icing hazards, such as the Current Icing Product distributed by the National Weather Service (NWS) (Etherton et al., 2014) and the NASA SatCORPS Airframe Icing Product which is delivered to NOAA's Aviation Weather Center and the Alaska Aviation Weather Unit (W. Smith/NASA, personal communication, 2020). DARDAR retrievals were also used to evaluate SEVIRI detections of high ice water content in support of the European High Altitude Ice Crystals project, aimed at improving aviation safety related to aircraft icing (de Laat et al., 2017).

Using CALIOP measurements paired with Copernicus Atmosphere Monitoring Service (CAMS) model reanalysis predictions, Ryder et al. (2024) quantified dust loads ingested into jet aircraft engines over 10 of the world's dustiest airports. The greatest risk for engine abrasion was found to occur during holding patterns on arrival, while planes await clearance to land. CALIOP measurements of the vertical variations of dust loading led the researchers to conclude that the potential damage done is exacerbated when aircraft fly holding patterns at altitudes below 1 km.

2.6.3. Aerosol Forecast and Assimilation Models

The vertical information provided by CALIPSO on aerosol occurrence, type, and extinction is valuable for improving and validating aerosol forecast model accuracy. NOAA used CALIOP profiles to validate simulated plume heights for volcanic ash and smoke by the HYSPLIT dispersion model and to validate the 3D extent of smoke movement within the National Center for Environmental Prediction (NCEP) GEFS-Aerosol model (Crawford et al., 2016; P. Bhattacharjee/NOAA/ESLR, personal communication, 2020).

Accurately modeling smoke plume injection heights is important for predicting air quality downwind of fire events. A study by Baker et al. (2018) used CALIOP profiles to assess the performance of EPA's CMAQ photochemical model in transporting smoke from the 2013 Rim Fire in California. Backward trajectories were used to connect CALIOP smoke observations with upwind MODIS fire detections to independently establish smoke plume injection heights. These were compared to CMAQ injection heights. In another example, Yao et al. (2018) used machine learning and CALIOP smoke observations to create a predictive model for smoke plume injection heights and the subsequent risk of population exposure. CALIOP AOD and aerosol extinction profiles have also been used to evaluate RAMS-CMAQ aerosol dispersion accuracy over China (Wu T. et al., 2017).

Assimilating CALIOP vertical profile observations has been shown to improve the forecasting capabilities of aerosol transport models, including Météo-France (El Amraoui et al., 2020) and the Japanese Meteorological Agency (Sekiyama et al., 2010). A notable example is Cheng et al. (2019) who performed a series of experiments assimilating CALIOP aerosol extinction profiles in addition to MODIS AOD into the NICAM-SPRINTARS atmospheric model hourly aerosol fields. Figure 2-20 shows a decrease in the monthly deviation of forecasted aerosol extinction (simulated extinction minus

CALIOP-retrieved) when CALIOP data are included in the optimization. CALIOP data assimilation has further improved analysis and forecasting of high pollution episodes in global and region models (Quennehen et al., 2016; Pelon et al., 2017; Jung et al., 2019) and corrected underestimates in AODs in Météo-France's MOCAGE chemistry transport model (El Amraoui et al., 2020).

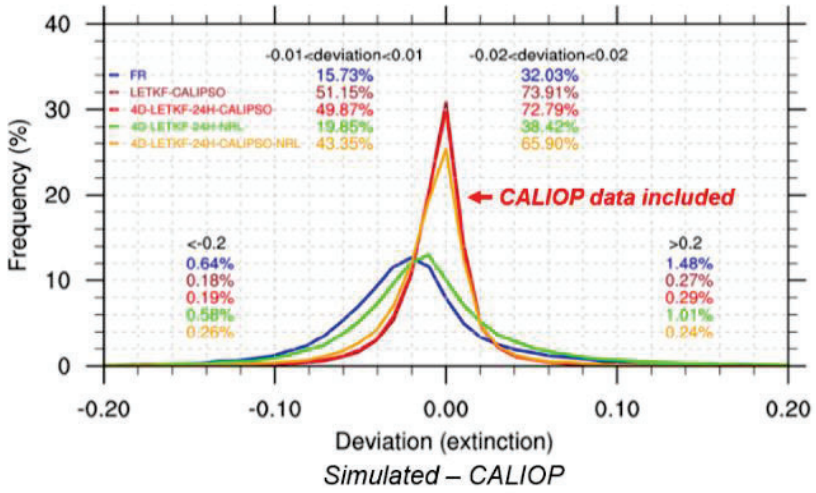

Figure 2-20. Frequency distributions of deviations (model-simulated minus CALIOP level 3 aerosol extinction) over ocean for November 2016. Each curve is a different assimilation experiment; those including CALIOP are red and orange (adapted from Cheng et al., 2019,; Used under CC BY 4.0).

Experiments in assimilating CALIOP L1.5 data conducted at ECMWF (Benedetti et al., 2018) were also used to develop methods of assimilating lidar profiles into the ECMWF global forecast model which are now being used operationally to assimilate aerosol profile data from the ATLID lidar on EarthCare.

2.6.4. Air Quality Assessment

CALIOP aerosol observations were used by state and local air quality monitoring agencies for characterizing 'exceptional events', where local airborne pollution levels exceed the EPA National Ambient Air Quality Standard. Analysts used CALIOP in conjunction with passive satellite and surface measurements to demonstrate compliance with the Clean Air Act by attributing $PM_{2.5}$ and ozone precursors to sources beyond the control of local and state governments (D. Westenbarger/TCEQ and K. Jones/APCB, personal communications, 2020). Routine use of CALIPSO data for air quality analyses was facilitated through expedited browse imagery on the CALIPSO webpage and by the EPA's Remote Sensing Information Gateway (RSIG). The RSIG-3D tool was used for over-plotting CALIOP observations with data from other satellites, models, and in-situ measurements.

3. Mission Timeline

The CALIPSO mission spanned a 27-year period from its initial proposal submission in 1998 to the final processing and archival of its data products in the summer of 2025. Because of the number and variety of events that occurred and influenced the mission, a timeline is presented in Figure 3-1. The figure charts key programmatic and operational reviews, significant platform or payload anomalies, and major solar flares that interrupted science operations. The timeline further documents the release of the major data products and shows how the mission sustained a healthy engagement with the scientific community through its involvement in meetings, workshops and participation in field missions. Individual milestones or events are condensed in the figure, and the reader is advised to magnify sections to more easily view them.

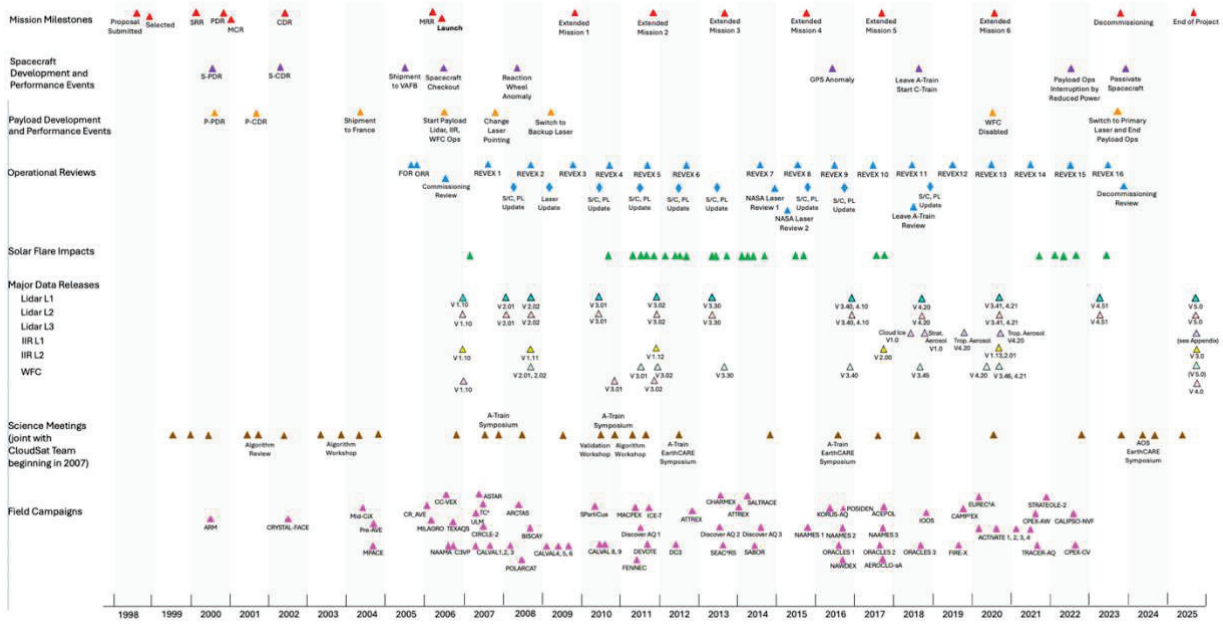

Figure 3-1. Mission Timeline (*a high-resolution version of this chart is attached at the end of the document,* Source credit: NASA)

4. Implementation

CALIPSO and CloudSat were jointly manifested on a Delta II launch vehicle, launched from Vandenberg Air Force Base on 28 April 2006, and inserted into a 705 km sun-synchronous orbit. After their checkout phase, which included a sequence of maneuvers that inserted the spacecraft into formation with the A-Train (Aqua, PARASOL, and Aura in 2006), the CALIPSO instrument payload began collecting science data on 12 June 2006. CALIOP's primary laser produced more than 1.6 billion shots before being turned off on 16 February 2009 due to a pressure leak in the laser canister. The backup laser began science operations on 12 March 2009 and had since produced more than 8.5 billion shots. The IIR and WFC satisfied all of their original performance objectives. The WFC, however, became inoperable in April 2020, but its loss did not impact the primary science objectives of the mission. During 17 years of operations, the satellite and ground systems delivered more than 90% of all possible measurement opportunities. The majority of the lost opportunities were caused by interruptions from solar flares, ground station anomalies, and routine maneuvers.

Following a reaction wheel failure in February 2018, CloudSat left the A-Train to reduce risk to the A-Train in the event of a second failure. In September 2018, CALIPSO descended from the A-Train to its disposal orbit to rejoin CloudSat and resume their matched lidar/radar cloud profile measurements. CALIPSO and CloudSat formed the C-Train at an altitude of 688 km, approximately 17 km below the A-Train. After the descent, the CALIPSO platform had no accessible fuel for orbit maneuvers, so the platform's orbit inclination slowly drifted to a later local crossing time for the ascending node. Predictions indicated that by mid-August 2023, the drift in the Mean Local Time (MLT) of the orbit's ascending node would not allow for adequate charging of the platform batteries to maintain safe operations. In April 2023 the JSG decided to end science operations before August 2023. The mission subsequently conducted engineering assessments of the primary laser and the platform before terminating spacecraft operations in December 2023.

4.1. Project Organization and Oversight

CALIPSO was a highly successful 27-year partnership between NASA and CNES that developed and implemented a pioneering scientific mission for Earth System science. The mission was highly complex with the deployment of the first polarization-sensitive lidar dedicated for atmospheric observations, the coordinated flying of the CALIPSO spacecraft with the CloudSat mission in a multi-satellite constellation and the engagement of international organizations across industry, government, and academia. Overall NASA mission responsibilities were led by the CALIPSO project office. Programmatic interfaces for NASA were managed by the ESSP Program Office. CNES-led responsibilities were managed by the CNES Space Center in Toulouse, France. Mission programmatic oversight and coordination between partners was provided by a Joint Steering Group (JSG) comprised of two senior representatives from NASA (one from Science Mission Directorate (SMD)/Earth Science Division (ESD) and one from Langley Research Center (LaRC)) and two senior representatives from CNES (one from CNES Headquarters (HQ) and another from the Toulouse Space Center). Figures 4-1, 4-2 and 4-3 describe the overarching organizational structure that existed during the operational phase of the mission. The first diagram provides an overarching view of the different levels of communication and oversight (Figure 4-1). Figure 4-2 and Figure 4-3 charts provide a higher level of detail and show the programmatic lines of authority, primary institutional responsibilities for the mission and interfaces between internal and external organizations. A breakdown of specific NASA and CNES contributions and responsibilities are provided further in Table 3.

DOI: 10.64631/LIZS5968

Dr. David Winker (NASA LaRC) was the CALIPSO Principal Investigator (PI) and Dr. Jacques Pelon (Institut Pierre-Simon Laplace, IPSL) was the CALIPSO Co-PI. Together they led the overall mission and were responsible for its science. Mission activities were directed and managed for NASA by the Project Manager/Scientist at LaRC and for CNES by the Project Manager/Mission Coordinator. Day-to-day on-orbit mission operations were led by the LaRC Mission Operations Control Center (MOCC) and CNES Spacecraft Operations Control Center (SOCC) Mission Operations Managers, respectively. The communication and coordination of activities between the PIs, project managers and the MOCC and SOCC occurred through established protocols and were accomplished primarily via weekly teleconferences and email exchanges. Changes to the established flight configuration, including flight software, were reviewed by the responsible institution's technical authority. For NASA, the LaRC Chief Engineer served as the independent Technical Authority. The Technical Authority for CNES was the *Loi sur les Opérations Spatiales* (LOS) office. Expertise with the instrument payload, laser, and platform for nominal and off-nominal conditions was provided by BAE Systems Inc., (previously Ball Aerospace and Technology Corporation during the mission), Fibertek, and Thales Alenia Space (TAS; formerly Aerospatiale and later Alcatel Alenia Space), respectively. Science telemetry data were downlinked through the Swedish Space Corporation (SSC) under a contract to BAE Systems.

The CALIPSO lidar and WFC science data products were designed, developed, and validated by the joint US and French project team with valuable contributions from the CALIPSO science team. The L1 IIR data products were designed and developed in collaboration between CNES and the LaRC project and validated in collaboration with IPSL and AERIS/ICARE. The IIR L2 products were designed by IPSL, developed in collaboration with AERIS/ICARE, and validated in collaboration with the LaRC project. Data production was conducted by the LaRC project, and the data products were archived and distributed by both the Atmospheric Sciences Data Center (ASDC) at LaRC and AERIS/ICARE in Lille, France. Monthly teleconferences were held between parties to review the status of data production and data holdings as well to organize plans for algorithm development and the transfer of data.

The mission's operational status was reviewed by the JSG through quasi-annual 2-day REVEX (REVue d'EXploitation) mission operational reviews and semi-annual updates. Over the mission, 12 REVEX reviews were held and 18 JSG teleconferences were conducted (see the mission timeline in Figure 3-1) for the occurrence of these reviews). Platform and instrument anomalies and resolutions, mission planning, and configuration changes were also reviewed and approved by the JSG.

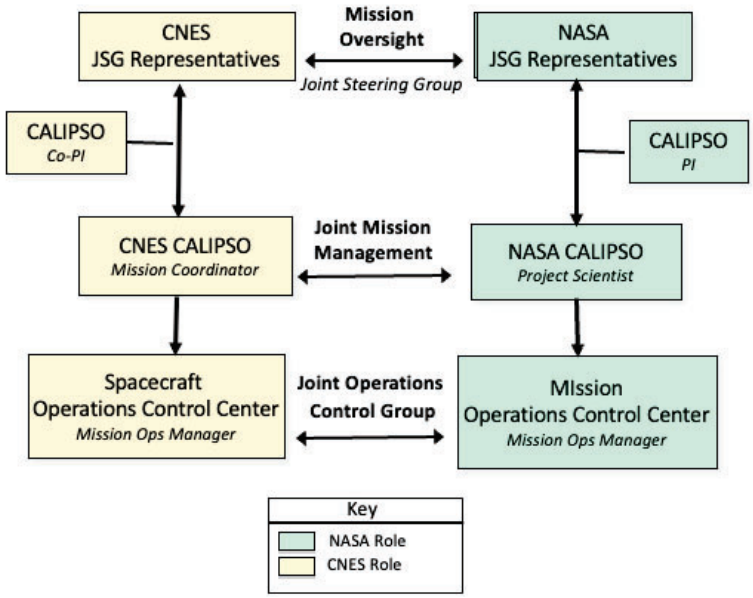

Figure 4-1. The CALIPSO organizational structure for NASA responsibilities with interfaces to CNES and other organizations during the operational phase of the mission (Source credit: NASA).

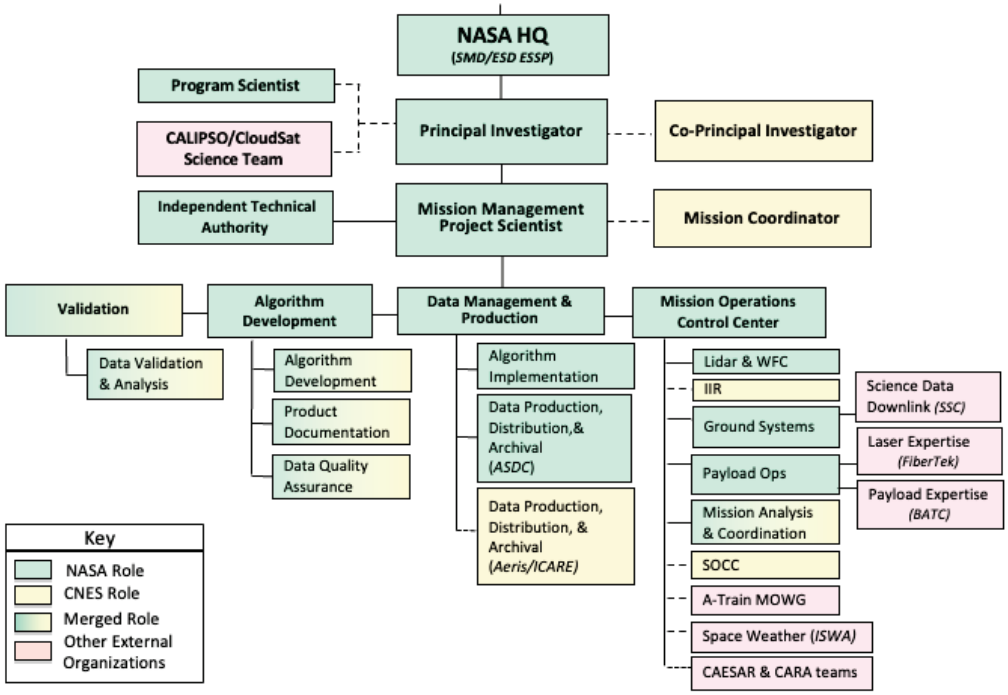

Figure 4-2. The CALIPSO organizational structure for NASA responsibilities with interfaces to CNES and other organizations during the operational phase of the mission (Source credit: NASA).

DOI: 10.64631/LIZS5968

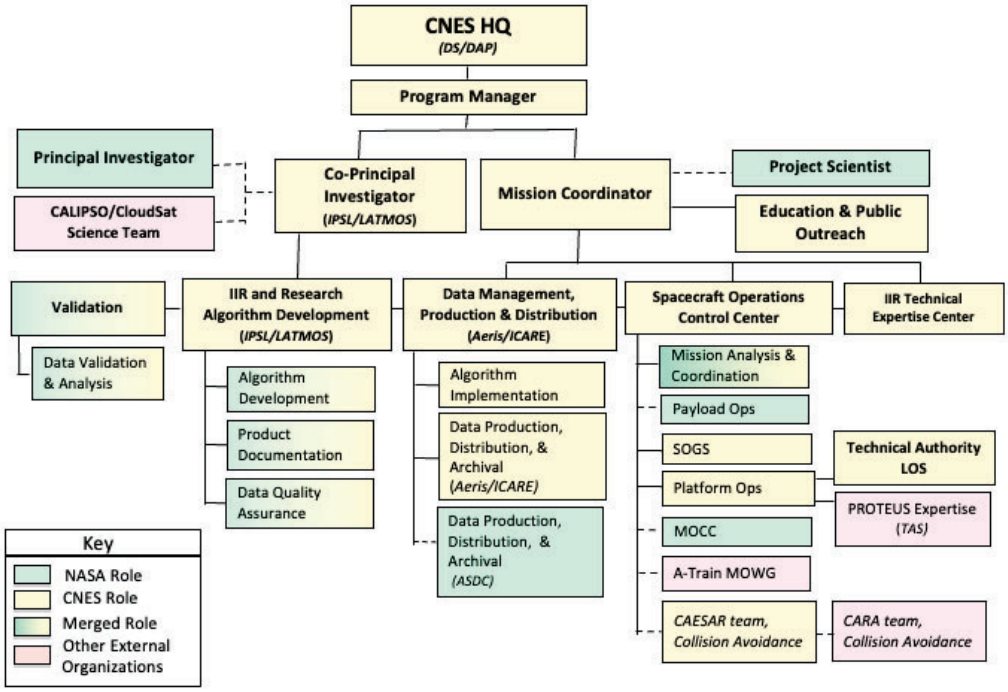

Figure 4-3. The CALIPSO organizational structure for CNES responsibilities with interfaces to NASA and other organizations during the operational phase of the mission (Source credit: NASA).

After CALIPSO completed its 3-year nominal mission in 2009, periodic mission extension reviews were conducted via NASA's Senior Review and CNES's REDEM (REvue D'Extension de Mission) processes. These comprehensive reviews, held in 2- or 3-year intervals, examined science discoveries and achievements accomplished during the mission, reviewed the predicted near-term technical status and reliability of the flight and ground-systems, and balanced the mission measurement opportunities against programmatic priorities. Following the Senior Review/REDEM process, the CALIPSO mission was approved for extended mission operations in 2009, 2013, 2015, 2017, and 2020.

The planning and execution of CALIPSO's spacecraft maneuvers with the A-Train constellation were made through the A-Train Mission Operations Working Group (MOWG). Mission teams shared orbital information through the Constellation Coordination System (CCS) database, and they also met annually to share information on the health and plans for each mission. Because of the close formation flying requirements between CALIPSO and CloudSat, these mission teams developed specific operational protocols and held regular monthly teleconferences. During the mission, CALIPSO participated in 34 MOWG meetings. The Goddard Space Flight Center (GSFC) Conjunction Assessment Risk Analysis (CARA) team, in concert with the CNES Conjunction Analysis and Evaluation Service, Alerts and Recommendations (CAESAR) team, supported the mission by identifying potential collision threats with space debris and other spacecraft.

The CALIPSO mission was highly engaged with the Earth science community throughout the mission. Soon after the mission was selected, the project was supported by a dedicated team comprised of US and French experts in lidar remote sensing and distinguished scientists for the mission's primary four science objectives. Because of the significant synergistic interests with joint lidar and radar retrievals, the CALIPSO and CloudSat Science teams were merged into the CALIPSO-CloudSat

Science Team (CCSTM) shortly after launch. Since this time, the CCSTM was reformed approximately every 3 years through a competitive research proposal and selection process. Meetings were held approximately once per year. Additional meetings with the larger international A-Train and the EarthCare community were held in 2007, 2010, 2015 and 2022. The frequency of the science team meetings and their relationship to important mission milestones and data deliveries is displayed in the mission timeline in Figure 3-1.

Table 3. NASA and CNES Mission Responsibilities and Contributed Activities.

NASA	CNES
○ The Principal Investigator (PI) at LaRC with the Co-PI led the scientific mission and defined science objectives. ○ The Project Manager/Scientist directed and managed NASA's mission responsibilities and activities. ○ The Mission Operations Control Center (MOCC) at LaRC was responsible for overall mission coordination and payload operations. ○ The Atmospheric Sciences Data Center (ASDC) at LaRC processed, archived, and distributed data.	○ The Co-Principal Investigator (Co-PI) defined IIR science goals and provided scientific guidance on overall mission objectives. ○ The Project Manager/Mission Coordinator managed CNES-led responsibilities and activities.
○ The LaRC Algorithm Development Lead spearheaded CALIOP and WFC algorithm development and validation. ○ The CALIPSO Data Manager was responsible for the science data archive, quality control of data processing software, and delivering data products to the ASDC and ICARE.	○ The Satellite Operations Command Center (SOCC) in Toulouse, France, was responsible for operating and maneuvering the spacecraft. ○ Ground station operations were supported from Aussaguel and Kerguelen, France; Hartebeesthoek, South Africa; Kiruna, Sweden; Kourou, French Guyana, and Inuvik, Canada. ○ Spacecraft engineering support was provided through a contract with the spacecraft manufacturer, Thales Alenia Space (TAS). ○ Engineering support, calibration, algorithm development and maintenance, and data quality control was provided for the IIR. ○ The CNES Algorithm Development Lead was responsible for IIR algorithm development and validation.
○ BAE Systems Inc. (previously. BATC during the mission), under contract with LaRC, provided payload engineering support and managed a subcontract with SSC for the acquisition of X-band science data and delivery of level 0 (L0) data to ASDC. ○ Fibertek, under contract to LaRC, provided engineering support for the laser system. ○ The Conjunction Assessment Risk Analysis (CARA) office at GSFC provided satellite and debris conjunction analysis and operations coordination among the satellite teams. For CALIPSO, this work was done in conjunction with CNES CAESAR team. ○ NASA funded telecommunications within the United States and a transatlantic link to CNES.	○ The AERIS/ICARE Data Center in Lille, France received data from ASDC and distributed CALIPSO data to users in France and elsewhere. AERIS/ICARE also supported the development of new joint CALIOP/IIR retrieval algorithms and data products. ○ The Conjunction Analysis and Evaluation Service, Alerts and Recommendations (CAESAR) team provided satellite and debris conjunction analysis for spacecraft operated from CNES Control Centers, in conjunction with the NASA CARA team.

4.2. Mission Overview

The mission was comprised of a Flight Segment and a Ground Segment. The Flight Segment consisted of a payload instrument suite (see 4.3.1) with an independent controller and an X-band transmitter integrated onto a French satellite bus. The Ground Segment consisted of distributed resources to communicate with and control the spacecraft; operate the payload; and collect, process, and archive engineering and scientific data. The functional elements for the mission are depicted in Figure 4-4 and are described in sections below along with notable metrics, events, and anomalies that occurred during the mission.

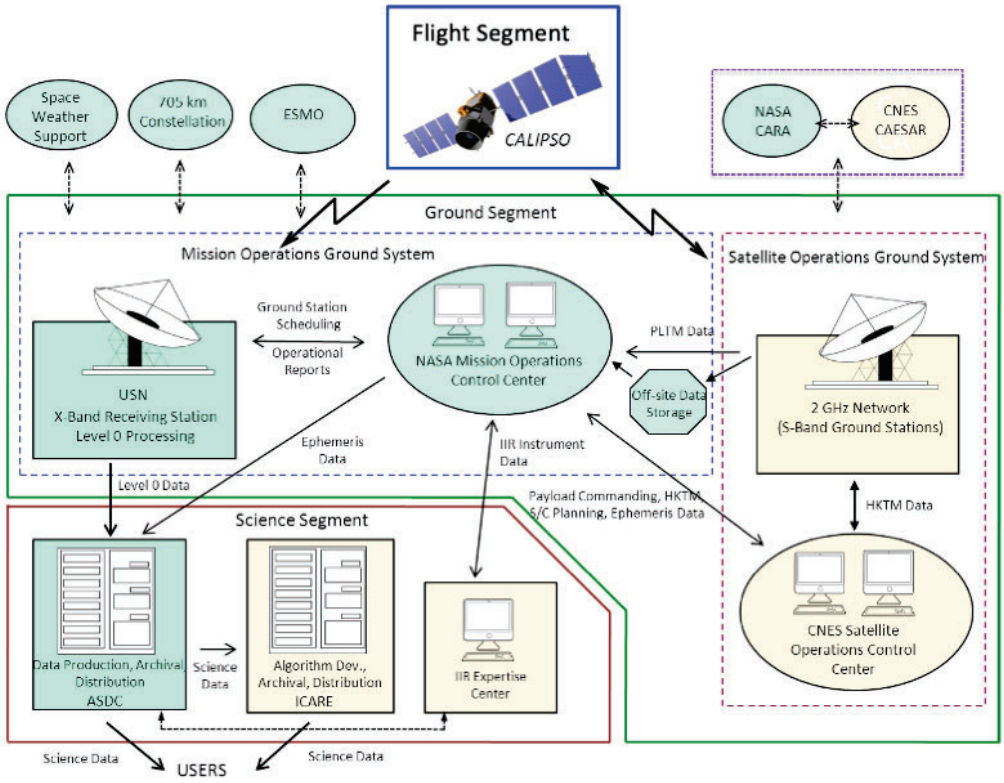

Figure 4-4. The mission concept illustrating the functional elements of the mission. Features highlighted in 'yellow' were roles and responsibilities led by CNES and those highlighted in 'green' were led by NASA. The arrows indicate the flow of information or data (Source credit: NASA).

Mission operations were jointly managed by the CNES SOCC in Toulouse, France and the NASA MOCC in Hampton, VA. Spacecraft command and control telemetry were transmitted through the CNES S-band ground network. Payload commands were generated and verified at the MOCC, transmitted to the SOCC, and uplinked through the S-band transmitter facilities. The on-board payload commands were subsequently passed to the payload computer. Essential payload data needed to monitor the health of critical systems were also downlinked via the S-band network and transferred to the MOCC. Satellite operations with members of the A-Train satellite constellation were facilitated through routine interactions with the international MOWG and with daily reports on spacecraft debris by the CNES CAESAR and NASA CARA organizations.

The CALIPSO payload/science telemetry data were downlinked to an X-band receiving station in Alaska with a backup station in Hawaii operated by the SSC (previously the Universal Space Network).

These data were routed through an SSC data processing facility to the Atmospheric Science Data Center at LaRC for ground data processing. IIR instrument performance evaluation was provided by the CNES IIR expertise center in Toulouse, France. A full catalogue of data products is archived at both ASDC and AERIS/ICARE in Lille, France (see Appendix A).

Details on individual elements of the mission and their performance during the mission are provided in the following sections.

4.3. Flight System

4.3.1. Overview of Spacecraft and Instrument Characteristics

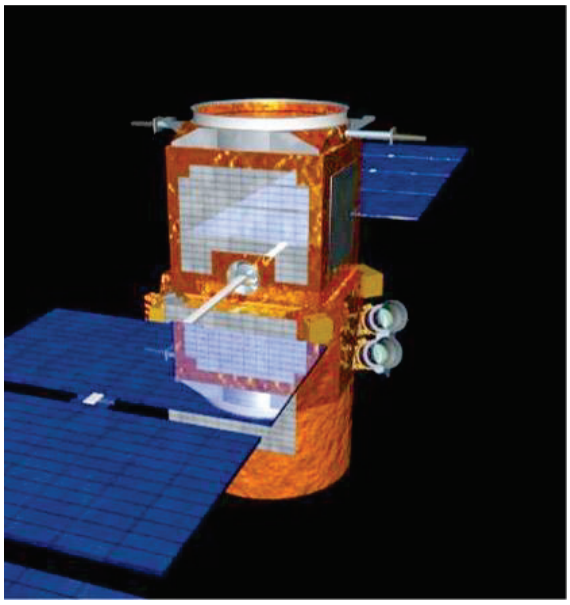

Figure 4-5. Visualization of the CALIPSO Flight System (© CNES, Used with permission).

CALIPSO Payload/Platform Characteristics

Volume	1.9 m x 1.6 m. x 2.46 m
Mass	587 kg, fully fueled
Power Array	550 W from 9.7 m solar

CALIOP

Laser	Nd:YAG
Wavelengths	532 nm and 1064 nm
Pulse energy	110 mJ at each wavelength (BOL)
Repetition rate	20.16 Hz
Pulses per day	1.74 x 106
Pulse width	20 nsec
Polarization purity	532 nm >99 %
Field of view	130 mrad
Dynamic range	2.5 × 106 (>21 bits)
Ground spot size	~80 m
Ground spot spacing	335 m
Vertical resolution	30 m/60 m

IIR

Detector based on an uncooled micro-bolometer array	
Wavelengths	8.65, 10.6, and 12.05 μm
Spectral resolution	0.98, 0.6 and 1.0 μm
NETD, 250 K scene	0.09, 0.14, and 0.11K
Calibration	< 1K
IFOV	1 km
Swath	64 km centered on lidar track

WFC

Wavelength	645 nm
Spectral bandwidth	50 nm
IFOV	125 m within 2.5 km of track 1 km elsewhere
Swath	61 km

4.3.2. Pre-Launch Development Phase

The integrated flight system was developed through a collaboration between NASA and CNES that brought together expertise, skills, services, resources, and mission hardware from France and the US. BAE Systems, Inc. (formerly Ball Aerospace and Technology Corporation in Boulder, CO during the mission) was the prime contractor for the payload and manufactured and assembled the lidar, WFC, and Payload Controller (PLC). Fibertek in Dulles, VA manufactured the primary and backup lasers. LaRC in Hampton, VA developed the lidar detector system. Alcatel in Cannes, France (now TAS)

built the platform and Sodern in Paris, France manufactured the IIR. Details for each of the systems are provided in sections 4.3-4.4. Boeing manufactured the Delta II launch vehicle.

The design, development, fabrication, assembly, integration and testing of these systems required extensive coordination between institutions and facilities with oversight on several levels. NASA oversaw payload responsibilities and launch activities, and CNES oversaw platform development activities and spacecraft integration and testing. IPSL in Paris provided oversight for the IIR. The joint project team developed a comprehensive review schedule that adhered to NASA and CNES guidelines for development. NASA also oversaw spacecraft integration with the CloudSat satellite onto the launch vehicle and oversaw launch responsibilities.

Figure 4-6 provides a schematic layout of the development sequence and illustrates the distribution of activities, shipment of hardware, exchange of information and responsibilities between locations leading to launch. Extensive component and system testing was conducted during the development phase. The dashed line in the figure delineates the transition in responsibilities and components between organizations. The transfer of US based information, hardware and software complied with Export Control regulations and International Traffic in Arms Regulations (ITAR). A listing of the significant mission events and reviews is shown below. These milestones are also highlighted in the overall mission timeline shown in Figure 3-1.

- Mission Selection — Dec 1998
- Prime Contract Awarded — Aug 1999
- Mission System Requirements Review — Jan 2000
- Mission Preliminary Design Review / MDR — Sep 2000
- Mission Confirmation Review (Delta) — Mar 2001
- Mission Critical Design Review — Mar 2002
- Satellite Critical Design Review — Apr 2003
- Payload Pre-Environmental Review — Sep 2003
- Payload Pre-Ship Review — Feb 2004
- Mission Operations Review — Mar 2004
- Satellite Pre-Environmental Review — Apr 2004
- Satellite Pre-Ship Review — Mar 2005
- Mission Readiness Review — Aug 2005 & Mar 2006
- Launch — Apr 2006

DOI: 10.64631/LIZS5968

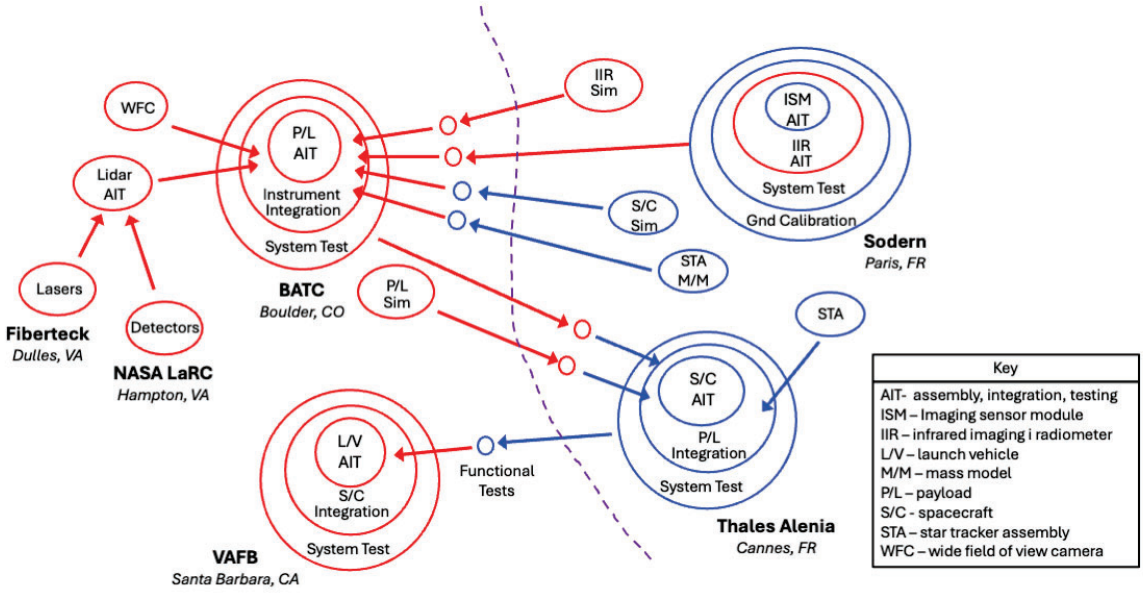

Figure 4-6. Schematic representation of the development, assembly, integration, and testing efforts for the CALIPSO flight system. The dashed line denotes an interface between NASA and CNES responsibilities and where US provided information and materials held appropriate export control and ITAR approvals (Source credit: NASA).

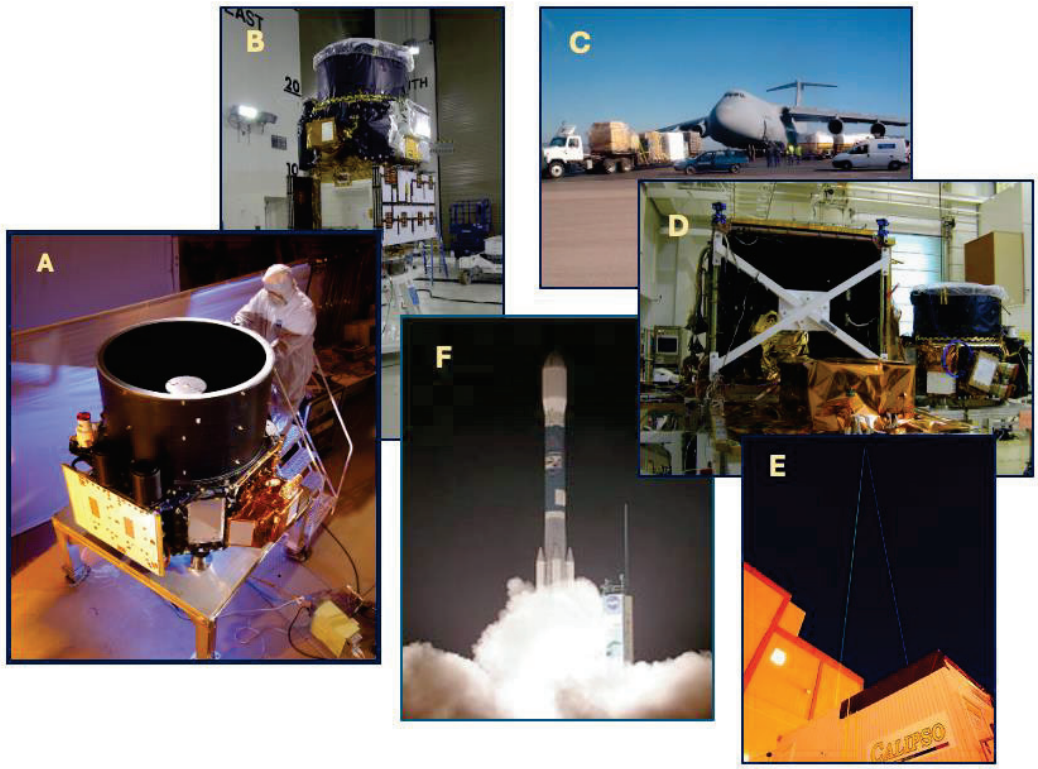

Figure 4-7. Collection of photographs of the CALIPSO payload and platform during development, integration, testing, and launch. (Source credit: Photo A © BAE, used with permission; Photos B-E: NASA).

4.3.3. Platform Performance Overview

The CALIPSO spacecraft was a PROTEUS bus developed in conjunction with CNES and built in France by TAS (formerly Aerospatiale and later Alcatel Alenia Space, Cannes). CALIPSO was the 2nd spacecraft launched from the platform series; the other missions were Jason-1 (2001-2013), Jason-2 (2008-2019), Jason-3 (2016-present), CoRoT (2006-2014), and SMOS (2009-present). For each of these missions, the bus provided power, attitude control, orbit station keeping, command and control, S-band uplink and downlink of telemetry, and telecommands. The bus further provided the payload with GPS spacecraft position, velocity and time information, and with the Star Trackers attitude information. Payload commands and limited engineering data were passed through the platform command and control system. A photograph of the PROTEUS platform and its subsystems is shown in Figure 4-8.

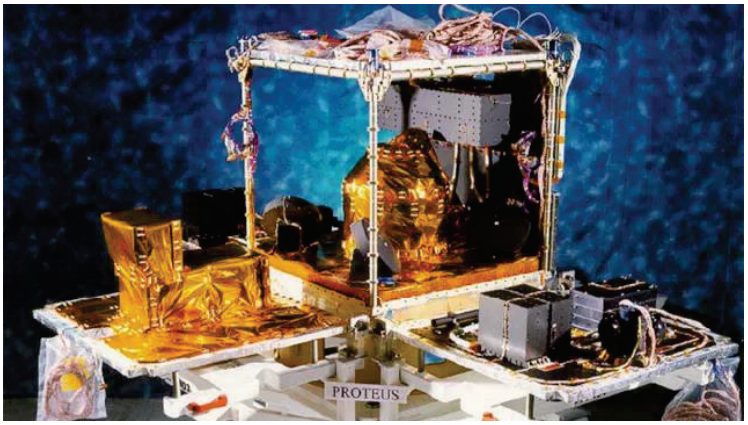

Figure 4-8. PROTEUS platform (© CNES, Used with permission).

Over the course of the mission, the platform provided outstanding performance, and its subsystems were still fully functional at the time that the mission completed its operational science phase in June 2023. Only two noteworthy off-nominal events within the platform interrupted routine measurement operations. A third platform anomaly occurred during the payload engineering close-out assessment phase that prematurely terminated further investigations.

The status of the primary and redundant subsystems at the end of the mission is provided in Table 4. A brief description of the subsystems and how they performed is presented below.

4.3.3.1. Command and Data Handling

All of the platform's computing functions were performed by the Data-Handling Unit (DHU), which ran flight software and controlled the platform through interface electronics. The DHU is analogous to the PLC discussed in the payload section. The DHU also handled platform engineering data recording and playback to Earth using CNES ground stations. The platform had two processor modules. The platform began operations with the A-side half satellite Processor Module (PMA). The platform automatically switched to Processor Module B (PMB) as part of its fault detection and correction function (similar to the payload's Fault Detection Isolation Recovery (FDIR)) in response to a Reaction Wheel (RW) power Single Event Upset (SEU) in March 2008. No damage was incurred during the SEU. The PMB was active through the remainder of the science mission. A major anomaly with the DHU occurred, however, during the laser assessment activities on 1 July 2023 that triggered the platform's 2nd SAFE-hold mode event. The anomaly investigation concluded that the cause was

isolated to the DHU and possibly with the DHU's power supply. It was not linked to the reactivation of the primary laser that occurred three days before the SAFE-hold event, which was the motivating objective of the laser assessment. The platform transitioned to PMA, and PMB was declared inoperable. Other than a PLC status and communications checks carried out for several hours in December 2023, no additional payload activities occurred after this anomaly.

Prior to the DHU anomaly, a minor off-nominal event occurred in January 2016 with the timestamp from the platform's GPS receiver. The problem was traced to the insufficient allocation of memory within a counter that accumulated the number of weeks from a reference setting, which resulted in the value rolling over to an earlier date in 1996. This issue was found across the family of PROTEUS platforms and was corrected with a software patch within a few weeks by the GPS manufacturer, TAS-Italia, and implemented by TAS-France for the PROTEUS fleet. Normal science operations resumed in mid-March 2016.

4.3.3.2. Telecommunications

The platform communicated with Earth ground stations through an S-band transceiver. The platform had two spacecraft transmitters (Tx), Tx1 and Tx2 and two receivers (Rx), Rx1, and Rx2. Tx2 and Rx2 were connected to PMB. Ground stations at Aussaguel and Kerguelen, France; Hartebeesthoek, South Africa; Kiruna, Sweden; Kourou, French Guyana, and Inuvik, Canada supported the mission. Occasional interruptions in the network service or with operations at individual ground stations occurred, but these imposed insignificant impacts to the mission.

4.3.3.3. Attitude and Orbit Control

The platform determined the payload orientation at any given time using a star tracker in combination with two gyroscopes. Fine-tuning of the satellite's attitude was carried out by four reaction wheels. The spacecraft also determined its orientation using eight Coarse Sun Sensors (CSS) and maintained it using three Magneto Torque Bars (MTB).

On 3 March 2008 there was an SEU in the electronics that shut down the power to RW2. The platform FDIR system detected the fault, initiated the 1st platform SAFE-hold mode transition, and switched processors from PMA to PMB. This caused power to be restored to RW2. No permanent degradation occurred. SEU susceptibility in the RW electronics was identified on the Jason-1 mission. A similar anomaly occurred on Jason-1 in RW3 on 8 August 2008.

The 3rd and final platform SAFE-hold mode occurred on 27 August 2023 during the investigation of the DHU anomaly (1 July 2023) that was traced to a malfunction with a Gyro #1. This event occurred within the South Atlantic Anomaly and was likely another SEU. Gyro #1 was reactivated on 6 September 2023 for 4 hours and exhibited normal behavior. Because only two gyros are needed out of a group of three, this unit was held in reserve.

4.3.3.4. Platform Pitch Change

At launch, the CALIPSO lidar operated at 0.3° pitch forward orientation referenced to geodetic nadir. This configuration was selected to minimize specular reflections from surface water bodies. During the mission, however, it was observed that specular returns from horizontally-oriented ice cloud crystals produced anomalously high signal returns that led to significant overestimates in the retrieval of cloud extinction coefficients, and hence, cloud optical depth (Mioche et al., 2010). To mitigate this effect, the spacecraft was commanded on 28 November 2007 to change its orientation to a 3° pitch. This pitch angle remained the nominal flight configuration for the remainder of the mission.

4.3.3.5. Propulsion

Once CALIPSO was inserted into the A-Train, the propulsion system was used only for orbit correction and maintenance, and not for attitude control. CALIPSO adjusted its orbit by firing an appropriate combination of its four onboard thrusters. Propellant was stored in a spherical 42 cm diameter tank, which at launch contained 27.2 kg of hydrazine (including 1.3 kg residuals), pressurized with gaseous nitrogen.

In September 2018, the CALIPSO platform descended out of the A-Train and into the C-Train. A spacecraft thruster anomaly occurred a few weeks later during a minor orbit adjustment maneuver after ~94% of the available propellant had been used. The anomaly was believed to be caused by the presence of gas bubbles inside the fuel line. The nitrogen gas was normally separated from the hydrazine liquid by an elastic membrane. The presence of bubbles implied that the membrane had deteriorated, and the occurrence of more bubbles in the propulsion line was likely. This hypothesis was confirmed during a Risk Mitigation Maneuver (RMM) in April 2019 when a thruster also stopped operating prematurely. Following this event, no further maneuvers were conducted.

As a result of the September 2018 orbit change and the inability to maintain orbit configuration, CALIPSO's mean local crossing time at the equator increased from ~13:50 to ~15:30 by the end of June 2023 as shown in Figure 4-9. No significant thermal effects were observed to the spacecraft or payload; however, there is speculation that minor thermal changes to the backup laser may have occurred and affected the transformation of emitted energy through the doubling crystal between the primary frequency (1064 nm) and its secondary (532 nm) frequency (see Figure D3). The change in the laser energy balance between these two wavelengths is correlated with the change in MLT after the change in orbit altitude. Although there are no reported trends in the laser's pedestal heater temperature or its duty cycle to confirm this hypothesis, it should be noted that location and precision of the laser temperature sensors were not optimized for detecting the minor perturbations that could be responsible.

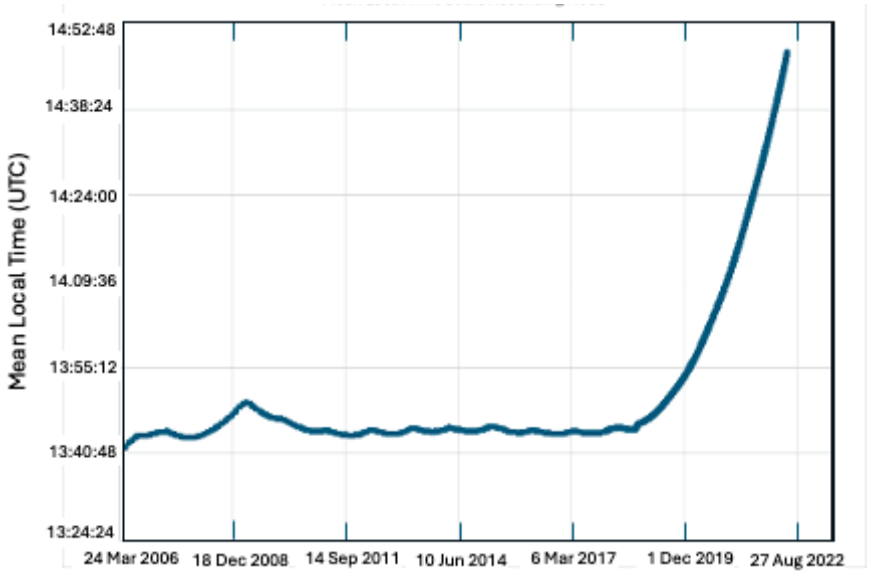

Figure 4-9. CALIPSO's drift of the mean local time (MLT) of the orbit crossing the ascending node. The slight increase in MLT viewed in 2008 occurred because orbit inclination correction maneuvers were postponed until 2009. Typical MLT correction maneuvers occurred annually. After the descent of the platform in September 2018, there were no further correction maneuvers and the MLT drift accelerated (Source credit: NASA).

4.3.3.6. Electrical Power

CALIPSO's power was generated, stored and distributed by the electrical power subsystem. The 28-volt power was supplied by a pair of solar arrays with silicon cells. The arrays were extended on opposite sides of the satellite's main platform and were oriented toward the Sun by two solar array drive motors. Each array consisted of four panels. During periods of solar eclipse, once per orbit, power was provided by a lithium-ion battery. The spacecraft's average power requirements were steady at 460 W (225 W for the platform and 235 W for the payload). There were no major anomalies with the system and the power management system continued to fully recharge the battery with adequate margins prior to the beginning of the next eclipse. The charging margins varied around 7 minutes on average, depending on the solar beta angle. One of the 32 solar array strings was lost in September 2012. The solar arrays degraded at ~0.5% per year, which was much slower than the pre-launch estimate of 1.1%/year. The battery aging rate was stable for most of the mission. In 2020, the total degradation was reported at ~27% after almost 14 years on orbit. The degradation was well below pre-launch predictions (42%) and held ample power reserves to recover from a SAFE-hold mode (~1160 Wh). Since this report, the available power margin decreased markedly as the eastward precession of the C-Train orbit produced larger solar beta angles, resulting in decreased illumination of the solar arrays. Figure 4-10 shows the reduction of the power margins over the last few years and predictions that were periodically provided to the mission operations team. The observations indicated that the predictions were accurate and gave advance notice of the likelihood of insufficient power margins after 1 August 2023. This was a life-limiting constraint for the mission and was the basis for the joint NASA/CNES decision to terminate the science mission in June 2023. All other components of the electrical power system showed nominal performance with little evidence of any degradation.

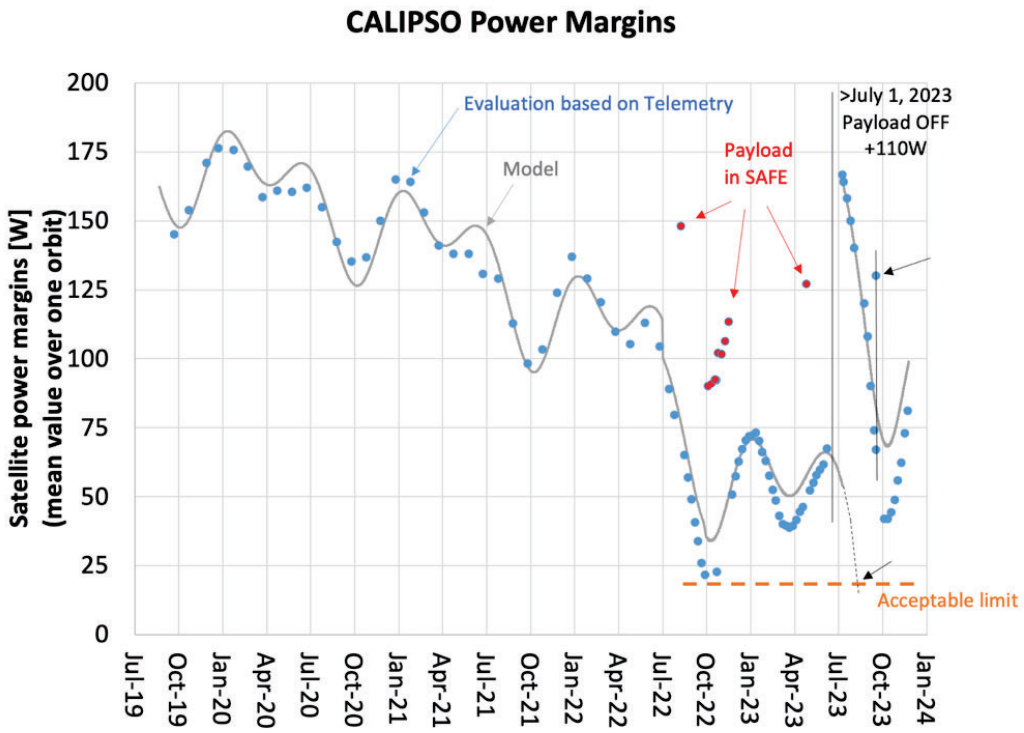

Figure 4-10. The platform orbit-averaged power margin (W) record displayed by blue dots from September 2019 – November 2023 (power margin defined as platform charged-battery capacity minus platform and payload power consumption). The solid grey line represents predicted estimates updated on occasion with platform measurements. The horizontally dashed orange line between fall 2022 and end 2023 represents

the minimum threshold margin required to ensure that platform could recover from a SAFE-hold mode transition. The decreasing power margin trend is anticorrelated with the increase in the orbit MLT (reported in Figure 4-9). The red dots indicate periods when the payload was placed in SAFE-hold mode (with reduced power consumption). The large increase on 1 July 2023 also reflects the increase in power margins following payload being powered off (© CNES, Used with permission).

4.3.3.7. Thermal Control

The thermal control subsystem maintained nominal temperatures for each component on the spacecraft by using a combination of active and passive control elements. The active components were electrical heaters. The passive components were thermal radiators and Kapton-covered Multi-Layer Insulation (MLI) blankets. All heaters and radiators operated within specification and there was no observable degradation of the insulation blankets due to long-term exposure to micro-meteor impacts, atomic oxygen, and/or solar radiation.

4.3.3.8. Flight Software

CALIPSO received commands and control sequences from the CNES SOCC and translated them into spacecraft actions. The platform flight software executed stored time-tagged commands, as well as commands for immediate execution. The flight software controlled a number of autonomous functions, such as spacecraft attitude and internal fault protection. The software FDIR system was used to protect the spacecraft from reasonable, credible faults and automatically performed a number of preset actions to attempt to resolve a problem. Over the mission's life, a total of three FDIRs triggered platform SAFE-hold mode transitions. As reported previously, the first and third events were determined to be triggered by SEU events with the Rx wheel (2008) and a gyro (2023), respectively. The 2nd FDIR event was traced to the failure of a power supply with the DHU unit on PMB (1 July 2023). During the mission, the platform flight software operated nominally; no significant unreported anomalies occurred.

Table 4: Platform Redundancy Status and Capability at End of Platform Operations

	Unit	Final Configuration	Redundancy	Remarks
DHS	Data Handling Unit	PMA	None	Switched on 2023-07-01[1]
	Mass Memories	MM0, MM1, MM2, MM4	MM3 cold redundancy	Shared
TTCS	TT&C Transmitter	Tx1	Tx2	Half-satellite
	TT&C Receiver	Rx1, Rx2	1 Rx loss allowed	Hot redundancy
AOCS	Global Positioning Satellite Receiver	GPS1 4 or more satellites 99% of the time	GPS2	Half-satellite
	Reaction wheels	RW1 to RW4	1 RW loss allowed	Shared; no ageing effects detected
	Magneto-Torques	MTB1 to MTB3 redundant coils	MTB1 to MTB3 nominal coils	Half-satellite
	Solar Array Drive Mechanism	SADM1&2 redundant motor	SADM1&2 nominal motor	Half-satellite
		Potentiometer & REED relays	Potentiometer loss allowed	Shared
	Thrusters	THR1 to THR4	1 THR loss allowed	Shared (not used in NOM)
	Gyrometers	GYR2, GYR3	GYR1 cold redundancy	Removed from AOCS system[2]
	Star Trackers	STR2 Availability ~100%	STR1 cold redundancy	Shared; STR2 checked every 6 months
	Magnetometers	MAG1	MAG2 No anomaly	Half-satellite (not used in NOM; checked every 6 months)
	Coarse Sun Sensors	CSS1 to CSS8	1 CSS loss allowed	Shared (not used in NOM; checked every 6 months), ageing effect < 2%
EPS	Power Conditioning Electronic	12 sections available	1 section loss allowed	Shared
		Redundant TM/TC	Nominal TM/TC	Half-satellite
	Battery Electronic Unit	BEU Redundant	BEU Nominal	Half-satellite
	Solar Array	31 available strings out of 32 with 100 cells each	4 strings loss allowed	Shared (4 strings = 1 Panel section) Aging measurement 0.5% per year versus expected 1.0%
	Battery	9 pack of 3 Li-ion Cells	1 pack loss allowed	Shared

4.3.4. Payload Performance Overview

The CALIPSO payload suite consisted of the dual wavelength (532 nm and 1064 nm) polarization-sensitive elastic lidar (CALIOP), the IIR, the WFC, the PLC, and the X-band transmitter. Figure 4-11 provides a diagram of the payload instrument configuration and Figure 4-12 shows corresponding

photographs of the payload from two perspectives. Descriptions of the payload's major components and their performance are provided in the subsections below. Detailed performance trends are provided in Appendix D.

The performance of the IIR and the receiver portion of the lidar far exceeded prelaunch expectations. The WFC performed admirably until an instrument anomaly in April 2020 rendered it inoperable. The PLC and X-band transmitter were non-redundant components that also performed notably well. The lidar was designed with a primary laser transmitter and a second, fully redundant backup system. The primary laser delivered 'first light' on 7 June 2006. Nominal operations were stopped on 16 February 2009 due to anomalous behavior at low pressure within the laser canister after delivering more than 1.6 billion shots. The anomalous behavior was identified by the increasing occurrence of low energy laser shots. After a brief check out period, the backup system was brought online on 12 March 2009 and subsequently emitted more than 8.47 billon shots. The backup laser performed flawlessly until the end of 2016 when low energy shots began appearing. The backup laser continued to produce valuable measurements until the end of the science phase when it was deactivated on 21 June 2023. While the frequency of low energy shots accelerated as the pressure in the canister decreased, the backup laser was able to function longer and at lower pressures using optimized FDIR settings for the laser. The primary laser was restarted on 28 June 2023 to assess how it performed after being powered-off for 14 years and in near-vacuum conditions.

Throughout the mission, exoatmospheric radiation presented unexpected challenges to the operation of the lasers, to the performance of the lidar detectors, and to the interpretation of the returned lidar signals. The sections below described some of the more significant experiences related to the payload systems, which provide context for changes in the operational configuration of the payload and the need for significant modifications to the scientific data processing algorithms during the mission.

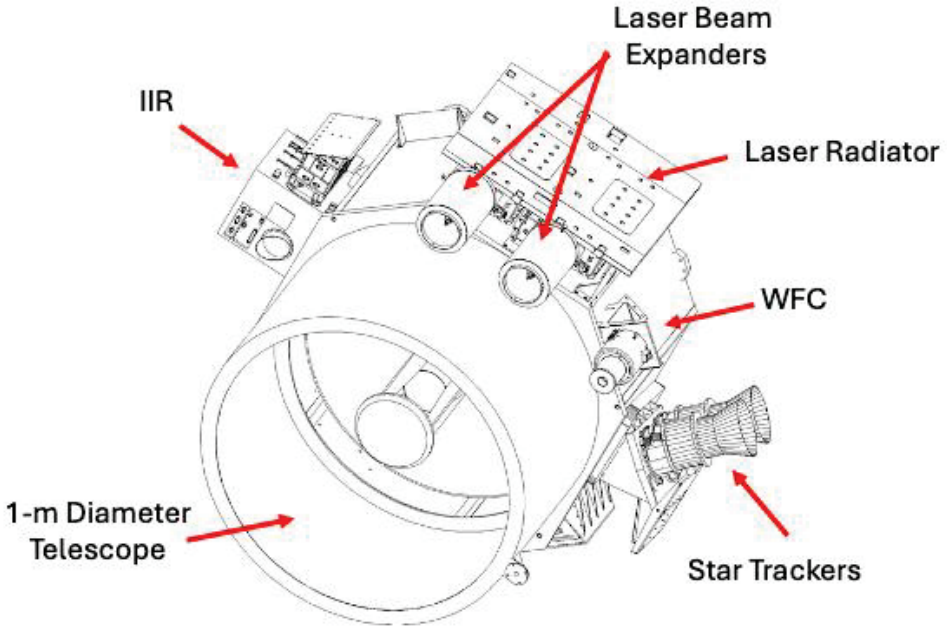

Figure 4-11. Diagram of the CALIPSO payload (© BAE, Used with permission).

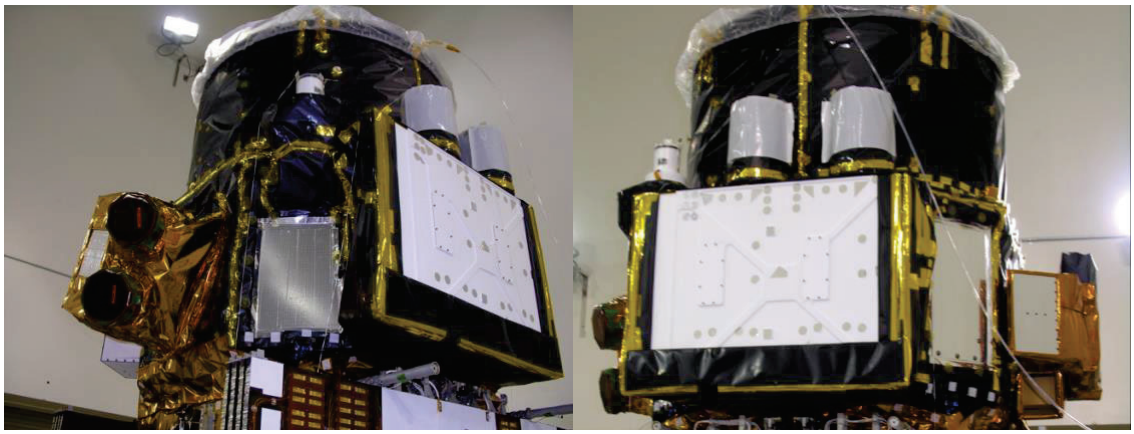

Figure 4-12. The CALIPSO payload in the BAE cleanroom. The white panel is the laser radiator and the two cylinders in the photographs are the laser beam expanders. The telescope diameter is 1 meter (© BAE, Used with permission).

4.3.4.1. CALIOP Lidar

CALIOP had two identical diode-pumped, frequency-doubled, Q-Switched Nd:YAG lasers, only one of which operated at any time. Each unit consisted of an independent laser electronics unit, an optical beam expander, and a laser optical module. The laser modules were hermetically sealed containers and included energy monitors for both wavelengths. Common to both units were a beam steering mechanism, a conducted-emissions filter for the input power line, and a thermal radiator.

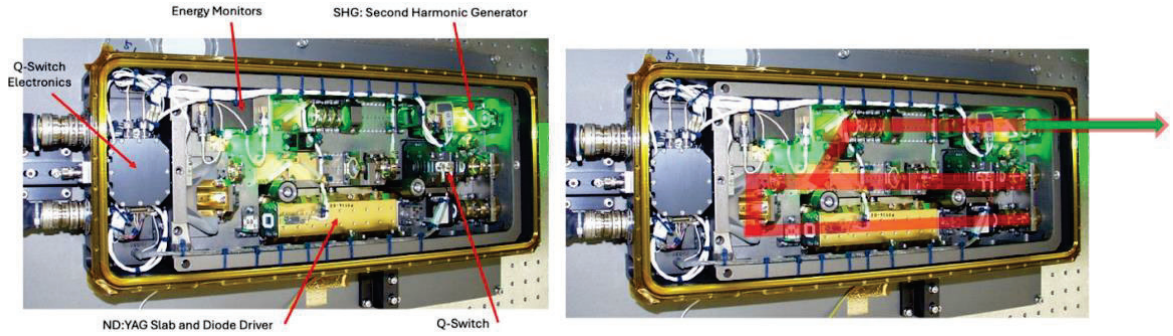

Figure 4-13. Layout of the CALIPSO Laser Flight Unit. The left image is annotated to identify several key components, and the right image provides a ray trace of light within the cavity. (© Fibertek, Used with permission).

The laser canisters for both lasers were pressurized in May 2002 with dry air to 18.7 psia to mitigate possible optical damage from the outgassing of contaminants with high energy light. Laser #2 (2nd unit manufactured) was designated as the *primary* laser, to be used first, because its canister pressure was known prior to launch to be decreasing at a rate that could eventually render it unusable because of corona discharges. Laser #1 was designated as the *backup* laser. A photograph of the one of the flight lasers is shown in Figure 4-13.

Backscatter signals were collected by a 1-meter diameter beryllium telescope, relay optics, and electronics mounted on a carbon composite optical bench. Backscatter signals polarized parallel and perpendicular to the transmitted laser pulse were measured separately by photomultiplier tubes in the

two 532-nm detector channels. An avalanche photodiode was used for detection with a 1064-nm channel.

The instrument was designed to be tuned by adjusting the values of key parameters via ground commanding (e.g., laser pedestal heater temperature, diode pulse width). When activated, the lasers operated continuously at a 20.16 Hz repetition rate and produced laser footprints separated on the Earth's surface by 335 m. The instrument also had its own FDIR system to monitor critical functions and place the laser in a safe state to determine the cause of a fault, correct it and resume normal operations. A detailed description of CALIOP and its early performance is provided by Hunt et al., 2009.

4.3.4.2. Lidar Performance Summary

For most of the mission, the lidar performed superbly. CALIOP's two lasers were designed to satisfy a 3-year mission lifetime, and their combined 17-year performance far exceeded expectations. The quality and stability of the measurements were exceptional for a pathfinder mission as illustrated by the long and consistent SNR record, which surpassed the manufacturer's Statement of Work (SOW) requirements on all channels, day and night, over most of the globe. The SNR of the 532 nm parallel channel at night, which was the basis for all calibrations, remained stable at 50% above the requirements and decreased less than 10 percent since the beginning of the mission (see Figures D1 and D2). The exception to this finding occurred in February 2022 following the extreme volcanic eruption of Hunga Tonga, which injected ash and gases to heights exceeding 40 km. The lidar 532 attenuated backscatter measurements are calibrated against the molecular scattering signal between 34 and 40 km and the highly unusual presence of particles in this layer introduced a significant artifact into calibration record (Figure D1). The relaxation of the stratospheric aerosol perturbation 6 months later demonstrated that the system was robust and continued to provide high levels of SNR up until the end of the mission.

The overall performance of the lidar system belies, however, challenges to the mission by unexpected instrument behavior. To a large degree, many of the more significant problems were addressed with modifications to the data processing algorithms or changes to instrument settings, and the mission successfully satisfied all mission requirements. Despite the issues encountered, independent comparisons of the nighttime backscatter with an airborne High Spectral Resolution Lidar (HSRL) revealed that 532 nm parallel channel calibration uncertainty was ~1.5% and approached the level of uncertainty reported for the molecular scattering model that served as the reference signal (Rogers et al., 2011; Getzewich et al., 2018; Kar et al., 2018). The subsections below provide a brief introduction into the most significant instrument artifacts and concerns identified before or during the mission.

Radiation-Induced Noise: The 532-nm channel PMT detectors were highly sensitive to the detection of cosmic rays and charged particles. The induced noise from these events were as much as two orders of magnitude larger than a pulse signal produced by a single photoelectron from the backscattered laser light. Radiation-induced pulses were common within the South Atlantic Anomaly (SAA) and, to a lesser extent, at high latitudes within the van Allen radiation belts that penetrated down to the satellite's orbit. The intensity of the noise was often correlated with significant solar corona mass ejections. Figure 4-14 shows the geographic distribution of PMT dark noise for a period early in the mission, clearly displaying regions with enhanced noise. Figure D7 shows the dark noise trend over the course of the mission.

The occurrence and impact of radiation-induced noise was significantly higher than anticipated before launch. Special processing steps were taken to isolate and remove noise spikes from the 532-nm nighttime calibration and progressively more sophisticated techniques were employed to deal with the

noise fluctuations inside the SAA and radiation belts. Noise spikes from cosmic rays remained an issue because of the on-board averaging of data from multiple profiles prevented their identification and extraction. Comprehensive descriptions of the 532 nm L1 calibration technique are provided in Powell et al. (2009), Getzewich et al. (2018), and Kar et al. (2018).

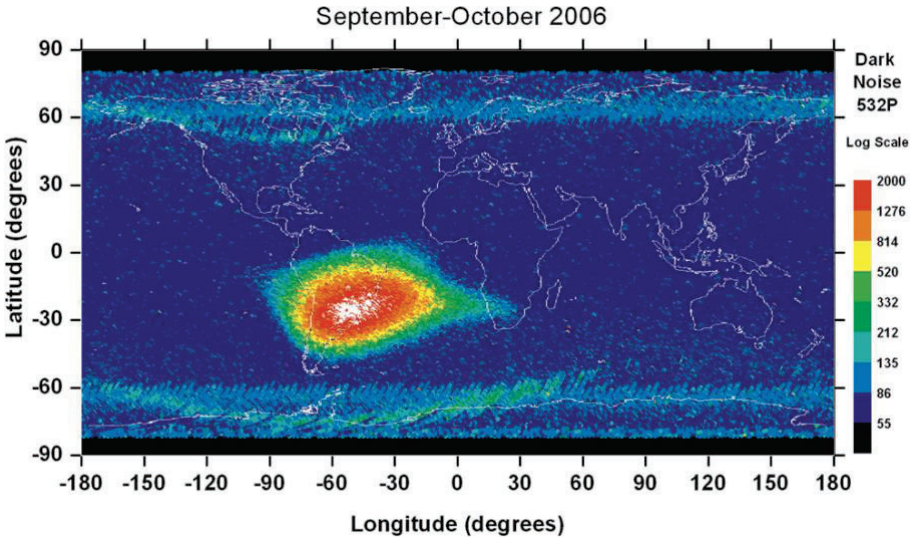

Figure 4-14. Map showing enhanced 532-nm parallel channel dark noise in regions with high radiation for a 16-day period in late September and early October 2006. The SAA stands out distinctly in bright colors near the center of the map. Increased noise is also visible in curve regions in high latitudes. (Image taken from Hunt et al., 2009; © American Meteorological Society, Used with permission).

Thermal Misalignment of Boresight: An Automated Boresight Mechanism (ABM) was installed on the lidar to optimize the beam alignment between the transmitter and receiver. The alignment procedure was conducted at night and at intervals of about 6-8 weeks. More than 100 operations were performed, and over time the nighttime alignment drifted slowly from the initial position set at the activation of each laser. However, analyses of the lidar observations in cloud-free regions in the upper troposphere sampled throughout complete orbits revealed diurnal variations in the boresight alignment of up to 30%. The misalignment also had a seasonal behavior as well as the trend noted from the drift in boresight position that was correlated with decreasing pressure in the laser canisters. The cause of the intra-orbit misalignment was traced to daytime thermal stresses in the ABM structure. Since the lasers were mounted to the ABM, the pressure induced trend is thought to be caused by the flexing of the canister (aka 'oil canning'). Figure 4-15 shows the fluctuation of the 532 nm calibration coefficients, computed by normalizing the backscatter signals between 36 km and 39 km to the expected backscatter derived from a molecular model (Kar et al., 2018; Getzewich et al., 2018). Daytime calibration coefficients near the equator are ~30% lower than the nighttime values in the same region.

The impact of the beam misalignment had far-reaching effects to the quality of the data products. To a first order, the reduced daytime SNR caused by the misalignment was compounded by the elevated detector noise from background sunlight, which notably diminished the ability to detect and characterize faint layers of aerosols and clouds. Of added significance, the daytime 1064-nm calibration approach was greatly complicated. The initial calibration algorithm derived 1064 nm calibration from previously determined 532 nm calibration by assuming (a) the backscatter and extinction coefficients from large ice crystals in cirrus clouds are spectrally independent at the

CALIOP wavelengths and (b) because the 532 nm calibration coefficients remained largely stable throughout the course of an orbit, accurate estimates of the 532-to-1064 calibration scaling factors could be composited using all suitable cirrus clouds measured within each orbit. Assumption (a) has since been validated (Haarig et al., 2016). However, as shown in Figure 4-15, assumption (b) is clearly invalid. The awareness of the thermal misalignment and its possible introduction of artifacts led to a major redesign of the 1064-nm calibration approach that was implemented in the V4 release of the L1 data products. (Vaughan et al., 2019). Comparisons with HSRL observations indicated that the updated CALIPSO 1064 calibration coefficients are accurate to 3%.

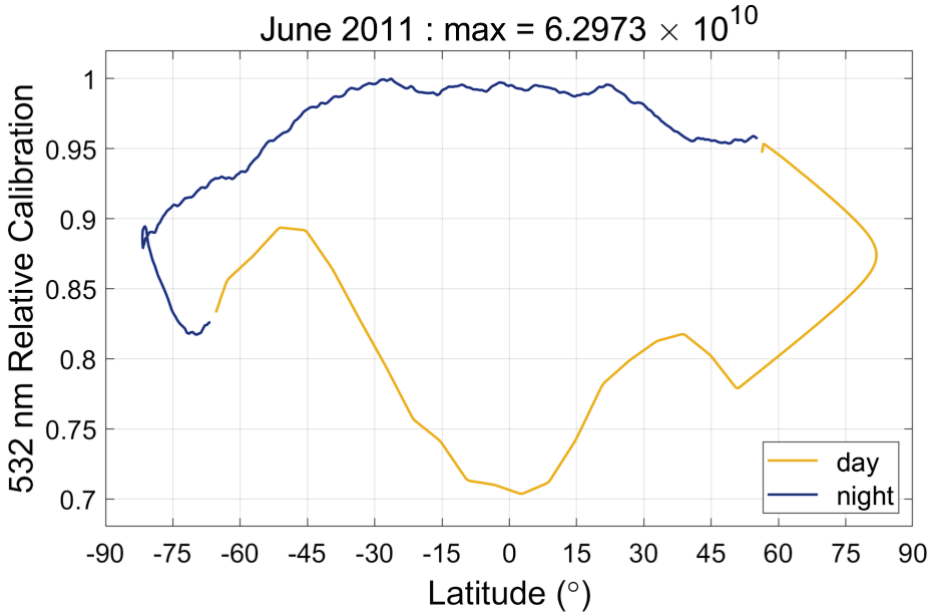

Figure 4-15. Mean diurnal changes in CALIOP's 532 nm parallel channel calibration coefficients for June 2011. The time series for both daytime and nighttime are normalized by the maximum value recorded during nighttime operations (6.2973×10^{10} km^3 sr J^{-1} count). The shape of the calibration curves changes seasonally but is consistent on a monthly basis throughout the mission (Vaughan et al., 2023b; Source credit: NASA).

Laser Diode Reliability: During CALIPSO's development phase, the ICESat lidar altimetry mission (2003-2009) experienced a significant reduction in laser output energy that was traced to the premature failure of its pump diode array (Kichak, 2003; Abshire et al., 2005). An anomaly investigation identified issues with the fabrication technique and the use of flux containing indium as part of the soldering process that progressively eroded gold conductors. The relatively high pulse current requirements for the ICESat laser operations created thermal stressing on the bonds that fractured. The investigation concluded that the detrimental effect of indium contamination was not anticipated nor detected during testing.

Shortly after the ICESat anomaly investigation, a review of the CALIOP laser design noted the presence of indium solder in the manufacture of the CALIOP diodes. A distinguishing difference between the CALIOP and ICESat designs was the lower laser pulse current requirements and lower laser repetition rate. Predictions of thermal fatigue rates for the CALIOP diodes were at least 100 times lower than for the ICESat diodes. An internal project review in 2003 concluded that there was sufficient margin in the laser design for the mission to satisfy its primary 3-year lifetime.

An additional concern raised during the development phase was the growth of tin whiskers from the Pb-Sn solder at the wire bonds that could shunt current and dim or darken a diode array. This concern

was well-known prior to launch and the project anticipated that the occasional loss of a diode bar would occur because of tin whiskers.

Each CALIPSO laser had 192 diodes arrays in two independent banks. For the primary laser, 11 diode bars dimmed or dropped during the first 30 months of operation as inferred by the stepwise reduction in laser output energy (Figure D3) and by changes in the diode voltages. The diode bar losses were random over the operational period of the primary laser. For the backup laser, 27 bars were lost with a greater loss in bank #2. There were also instances of stepwise power increases, which were considered to be the severing of tin-whiskers that had shunted the current for the diode bar. The long-term performance of the diode arrays more than satisfied Level 1 requirements. The project did not find any causal relationship between diode bar drops and either geophysical events or a payload functions.

When restarted in June 2023, the primary laser power levels were similar to those measured in February 2009 (~213 mJ). During the period it was powered off, its temperature was maintained by the survival heaters at around 8° C. The total energy output of ~205 mJ produced after 14 years in hibernation suggests that probably only a few additional diodes dimmed, and the laser was fully capable of resuming operations. Overall, the diodes performed well and did not exhibit the level of degradation that was experienced with ICESat.

Type 1 and Type 2 Low Laser Energy Shot Anomalies: More than 10 billion laser shots were produced during the mission and most of them were within expected performance ranges. Shot-to-shot variations of total output laser energy measured by the two internal energy monitors were typically < 0.4 mJ. Peak averaged total energy variations along the orbit were of about 0.75 mJ, and these were correlated with peak changes in temperature of a few tenths of a degree caused by the external heating and cooling of the payload. This energy shot behavior was similar for both lasers and was considered normal.

Abnormal laser behavior was determined by either large departures in shot energy output from the before mentioned energy distribution or by the violation of instrument threshold-limit settings that were monitored by the laser's FDIR system. Irregular laser shots described in the following sections were rare during their early phase of each laser's operation but occurred with increasing frequency as the lasers operated longer. Anomalous shots are defined by departures from a daily median value by more than 3 mJ. The daily median value is preferred as a metric to track variations because it is less sensitive to large, but infrequent laser energy excursions. Panels a–e in Figure 4-16 show examples of the distribution of total laser energy shots (black dots) acquired over a period of about 4 hours, which corresponds to about 3 orbit passes. These orbits are selected to highlight the significance of laser operations inside and outside the SAA. The selection of the five different dates was also made to highlight laser behavior that was prevalent at different levels of pressure within the laser canisters. The features observed in these examples illustrate the general changes in the laser behavior and are discussed below. Each of these segments display 340,000 individual shots. The red symbols overlayed in each plot represent laser total energy reported through the payload Health and Status (H&S) data that was transmitted separately several times daily in the S-band telemetry. The H&S data were a reduced data set (sampled at 1/5 Hz) and were regularly evaluated by the MOCC team to assess laser performance. Each red symbol is a 120-shot running averaged total energy value that corresponds to the sampling resolution for the laser H&S telemetry data.

Normal and benign laser behavior is illustrated in Figure 4-16, a couple of weeks after the primary laser operations commenced.

Type 1. Small, occasional but persistent abnormalities in the total energy shot output were observed early in the mission with the primary laser, and again later with the backup laser. The first occurrence was noted on the first day the primary laser was fully powered (23 May 2006). The abnormality was discovered in the H&S telemetry, which revealed an upward jump in total energy of a few tenths of a mJ, followed by a slow decay back to normal over a period 10 or more minutes (depicted red symbols in Figure 4-16b). These events were initially designated as 'energy spikes'. When the single shot data were examined, a significantly different picture emerged. The defining feature was an initial lower-than-normal total energy pulse of several mJ followed by successive shots with slightly higher-than-averaged energy. In terms of the 120-shot average, the triggering low energy shot was masked.

These events were later designated as Type 1 anomalies. They tended to occur in radiation prone regions (e.g., SAA and high latitudes) and increased in frequency and magnitude the longer the laser operated. They were not observed with the backup laser until the 2nd half of 2016, approximately 7.5 years after being powered on, and quickly became difficult to identify in the presence of other laser shot anomalies. They were also detected when the primary laser was restarted in late June 2023 and in near-vacuum conditions.

The project conducted a formal study in 2008 to better understand the cause of the Type 1 anomalies. The study included characterization of the anomalous laser shots, development and analysis of fault trees, radiation testing of questionable electrical components, and measured and simulated performance testing of selected circuits. The study team concluded that the most likely cause of the Type 1 low energy shots was an electrical anomaly caused by a diode driver fault, possibly related to the radiation susceptibility of an electrical component.

The impact of Type 1 events to science data processing and data quality was minor. The number of Type 1 events was very modest compared the total number of daily shots at 1.74 million. Moreover, the amplitude of the low energy shot departures were often less than 10 mJ, with only the more extreme losses around 20 mJ. The high energy departures were also typically less than 10 mJ, and both abnormalities were accommodated by the revised L1 calibration procedure.

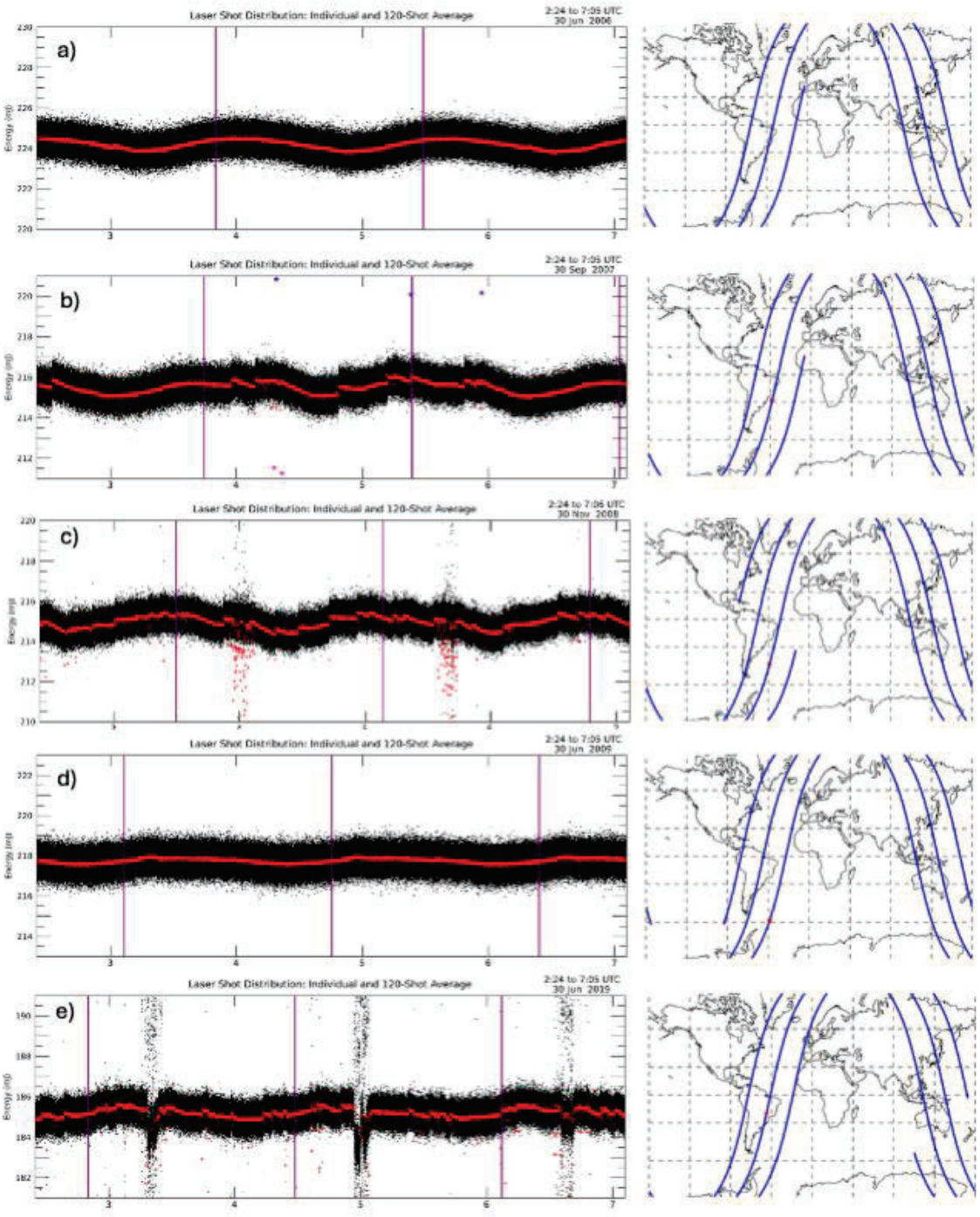

Figure 4-16. A series of charts that show the distribution of total laser energy shots over 3 orbit segments for 5 different periods: a) 30 June 2006, b) 30 September 2007, c) 30 November 2008, d) 30 June 2009, and e) 30 June 2019. Panels a-c are for the primary laser and panels d-e are for the backup laser. Single shot energy is presented by black dots and the 120-shot average is displayed by the red '+' symbols. These figures display the normal shot-to-shot variation of about 0.4 mJ and the intra-orbital variation of ~ 0.75 mJ. Type 1 laser shot anomalies are represented by the jump in averaged energy values (red) and the slow decay in elevated energies (panels b-c). Type 2 laser shot anomalies are represented by the scatter of low energy shots (black) and their averaged value (red) that departed by more than 3 mJ. (Source credit: NASA)

DOI: 10.64631/LIZS5968

Type 2. A second type of laser energy anomaly was associated with the inefficient operation of the laser Q-switch. The high voltage Q-switch acts like a shutter for the laser and when corona or arcing occurs across its terminals, it emits less light. These low energy shots differed from Type 1 anomalies as they had substantially larger departures from nominal averaged values and were isolated and without the subsequent rise and decay of the 120-shot averaged energies.

Prior to launch it was predicted that the primary laser would become unserviceable near the end of the scheduled 3 years of operation because of the threat of corona discharges from the high voltage components inside the canister, and plans were made to change to the backup laser in spring 2009, when the pressure would still be a factor of 2 above the predicted corona region (pre-launch estimate of 1.9 psia). Refer to the pressure trend chart (Figure D4) in Appendix D.

In late 2008, the laser began showing increasingly anomalous behavior with bursts of very low or no energy shots. Eventually the frequency of low energy shots increased to a point that they triggered a FDIR action, placing the payload in SAFE-hold mode. Following multiple FDIR occurrences, it was deemed impractical to continue science operations with the primary laser, and it was decided on 16 February 2009 to suspend operations and use the backup laser. Corona discharges due to the low pressure in the canister were suspected as the cause of the anomalous behavior, even though the pressure was still above the predicted corona region. An investigation of the anomalous behavior revealed a faulty measurement in the gap distance between two high voltage terminals at the laser Q-switch. The measured gap had failed to account for the distance between the lug nuts on the bolt posts and was smaller than had been reported prior to launch. The corona region, hence, occurred at a higher pressure than had been calculated (3.8 psia). It was at this time that the presence of Q-switch related low energy shots was realized (Type 2). Later in the mission, it was determined that Type 2 anomalies appeared in early 2007 at higher pressures and were likely set off by energetic particles that form ionization paths and fostered temporary corona or arcing (Rodriguez et al., 2022). These shot anomalies were first noticed within the SAA and later observed in the radiation belts and elsewhere as pressure decreased and approached the threshold for corona discharges.

The backup laser was activated in March 2009 and operated without significant incident until the first Type 2 anomalies were detected in 2016 at pressures above 6 psia. As observed with the primary laser, the backup laser's Type 2 shots were initially confined within the SAA and later spread to other regions with increasing time (Figure D6). The frequency and magnitude of low energy anomalies also increased significantly as pressure decreased. Discussions with the laser and payload manufacturers and CNES led to relaxation of the FDIR settings for the backup laser, allowing continued operations without endangering the mission. In addition, concern was raised regarding the increased number of very low shots (532 nm < 10 mJ) and their impact to the quality of the data products. Because the processing of L2 products relies on data frames of 15 consecutive profile shots, the loss of several shots within a data frame significantly reduced the averaged SNR that was needed for identifying layers of aerosols and clouds. The project tracked both the number of low energy shots and the number of 15 shot data frames that were impacted. A metric was defined for continued operations with the backup laser that required at least 50% of good data frames be acquired over a week and between 50° N and 50° S, excluding the SAA region. Toward the end of the mission, the percentage of lost data segments increased to a maximum of 4% in February 2023. Trending information on the occurrence of low energy shots is provided in Appendix D with additional discussion (Figure D5).

The primary laser was restarted at the end of June 2023 to assess its performance in near-vacuum conditions (see insert in Figure D4). It was uncertain if it would lase and if it could provide useful energy shots. The laser was reactivated and aligned to its optimal boresight position by the ABM without incident on 28 June 2023. During the more than 24 hours of operation, no Type 2 anomalies

were detected, which added confidence to the belief that these anomalies were caused by corona or arcing discharges. Type 1 anomalies were present and, over the short period of operation, increased in occurrence.

Because the CALIOP instrument simulations did not anticipate this kind of erratic instrument performance, when these events occurred, the quality of the science data retrieved by the CALIPSO L1 and L2 software was adversely affected in unexpected ways. The magnitude of the retrieval problems from Type 2 anomalies was exacerbated by CALIOP's onboard averaging scheme: because no quality screening was done prior to the execution of the onboard averaging scheme, individual low energy shots could potentially contaminate the averaged data downlinked from altitudes above ~8.2 km. While the noise filtering techniques incorporated in the 532 nm nighttime calibration procedures effectively detected and rejected packets containing low energy pulses, new screening techniques were developed for the 532 nm daytime and 1064 nm calibration algorithms. Mitigation strategies for L2 retrievals were also developed to address the large number of low energy shots and were included in the final set of data products (Tackett et al., 2025). A comprehensive discussion of these algorithm modifications, as well as all previous algorithm changes, is included in the data quality summary documents that have accompanied each data release.

Laser Repetition Rate Faults: During the summer of 2008, the primary laser electronics encountered multiple faults in which a Laser Repetition Rate Fault was detected that caused the laser and payload to transition to the Payload SAFE-hold mode. A review of the detection logic design determined that the fault could be caused by either a spurious additional laser firing pulse or a missing firing pulse. The root cause of the fault was not conclusively determined, but similarities suggest that it might be related to a Type 1 laser shot anomaly. Initially these faults required a manual reactivation of the laser using ground commands. Typically, it took 3 or more days to recover from each fault. In an effort to minimize the impact of the faults, a payload flight software modification was developed, tested and uploaded to the payload computer in early October 2008 that allowed the payload computer to reinitialize the laser when a repetition rate fault occurred and if no additional faults were detected within a short period of time. Since the implementation of the software modification, a total of 10 faults had occurred with the primary laser and 2 faults had occurred with the backup laser.

4.3.4.3. Imaging Infrared Radiometer (IIR)

The CALIPSO IIR was built by Sodern in France and provided by CNES. The uncooled Boeing microbolometer array used by the IIR was the first to be deployed for space-based radiometric measurements (see Figure 4-17). The IIR's 3 infrared channels sequentially view the Earth at wavelengths of 8.65, 10.6, and 12.05 μm. The spectral widths of the channels are 0.98, 0.6 and 1.0 μm, respectively, with concomitant noise equivalent temperatures of 0.09, 0.14, and 0.11 K, for a scene temperature of 250 K. In-flight calibration images are obtained by pointing to a blackbody onboard the platform as a warm source (300 K) and to deep space as a cold source (4 K). The pixel resolution is 1 km over a 64 km swath. Dynamic range extends from 200 to 400 K.

The instrument provided high quality science data during the full duration of the mission. The IIR operational power consumption and temperatures remained within expected ranges. No dead or blind pixels were identified.

A small number of anomalies occurred. At the system level, a slow increase in the instrument's focal plane temperature of ~0.65°C has been observed. Analysis of prelaunch data indicated that the drift started prior to launch and is believed to be caused by a part in the measurement circuit.

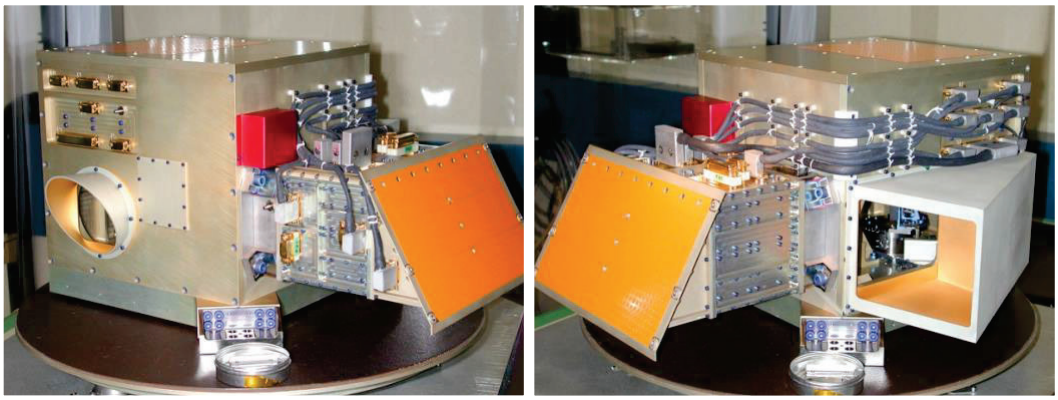

Figure 4-17. Photographs of the IIR flight unit (© CNES, Used with permission).

4.3.4.4. IIR Calibration Performance Record

The instrument's performance in all 3 bands was within specification with an absolute accuracy of <1 K. The day-to-day variations since launch were no more than 0.1 K at 10.6 and 12.05 μm, with no significant drift with respect to MODIS Collection 5 (C5) radiance measurements in comparable channels (Figure D10 in Appendix D). Analyses show that the small drift of 0.02 K/year with respect to MODIS C5 observed at 8.65 μm originates from MODIS C5, with no significant drift within the IIR (Garnier et al., 2017).

While CALIPSO was in the C-Train, co-registered IIR and MODIS observations were sparse (about every 3 weeks for a time-period of 2 to 3 days). On average, the IIR-MODIS differences in the A-Train and in the first 14 months in the C-Train seen in Figure D10 are fully consistent. However, the drift of the CALIPSO orbit was such that matched observations were too sparse after 2020 for meaningful comparisons with MODIS. Therefore, IIR calibration until the end of the mission was carried out through comparisons with SEVIRI/Meteosat similar channels (Figure D11). Data are from SEVIRI on Meteosat 9 to 11. Notwithstanding the noticeable larger day to day variability compared to the one observed when comparing with MODIS, no trend was detected after 2020, showing that IIR continued to be healthy until the end of the mission.

Level 1 Striping 'Tartan' artifact and calibration biases. Small but systematic seasonal calibration biases were discovered in the IIR Version 1 (V1) image data product that held a distinctive striping pattern with intersecting lines, analogous to a fabric 'Tartan plaid' pattern. The artifact was identified from brightness temperature differences between any two channels and was seen north of 30° latitude. An investigation of the calibration procedure revealed calibration biases that were synchronized with the elapsed time since night-to-day transitions. These biases affected about half of the rows of the microbolometer array, were of different amplitude in the three IIR channels, and yielded the striping effect. Comparisons with MODIS collocated observations revealed another type of bias that was affecting all the rows and that could not be identified at instrument level. Both types of biases were occurring only when the temperature of the instrument was increasing, and their amplitude was steadily increasing between the end of the daytime portion of an orbit and the beginning of the following nighttime portion until the instrument was no longer illuminated by the sun light. These biases might be due to parasitic signals in the Earth view images that were not be accounted for during on-board calibration. The season-dependent latitude of the day-to-night terminator yielded seasonal biases at a given latitude north of 30°. These biases, which were smaller than 0.4 K in the worst case, could be detected because of the very large number of IIR-MODIS collocated observations and the stable respective viewing geometries. Correction coefficients for the radiances were generated and

applied to the processing software for Version 2 (V2) that significantly reduced both the striping effect and the biases with respect to MODIS observations (Garnier et al, 2018). The IIR gains and further corrections implemented in V2 are reported in the dedicated IIR L1 calibration products.

4.3.4.5. Wide Field-of-view Camera (WFC)

The WFC was based on a commercial-off-the-shelf BATC Charge-Coupled Device (CCD) star tracker modified to have a single spectral band centered at 645 nm matched to the Aqua MODIS Channel 1 (see Figure 4-18). The WFC operated as a push-broom imager that provided continuous high spatial resolution (125 m) images of radiance and reflectance during the daylight segments of the orbit over a 61 km swath centered on the lidar footprint. The health and functionality of the WFC were evaluated annually. The WFC pointing knowledge was estimated to be better than 50 meters. Its radiometric measurements exhibited excellent agreement with MODIS Channel 1 (Figure D9) with mean radiance difference of <1.5% while CALIPSO was in the A-Train. Since the formation of the C-Train in 2018, comparison opportunities with MODIS were aperiodic as the two sensors were in different orbits. The large difference in radiances seen in late 2018 was believed a sampling artifact and not an instrument issue. On 11 April 2020 the WFC experienced a major anomaly that rendered it inoperable. The investigation noted the loss of communication between the PLC and the WFC as the primary fault.

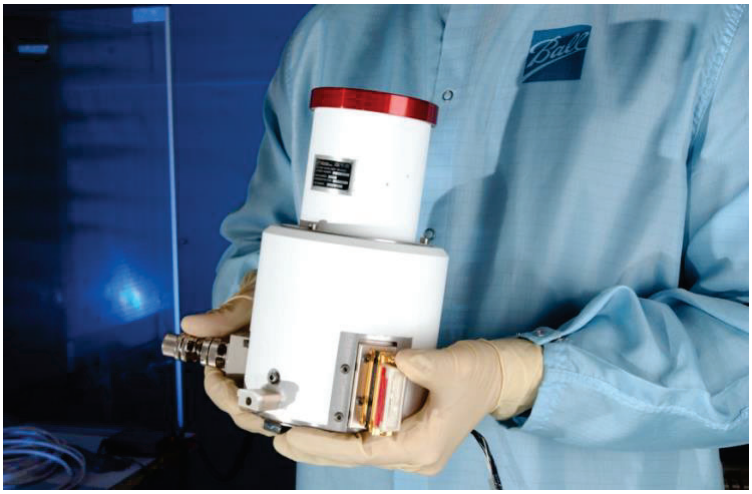

Figure 4-18. The WFC flight unit based on a BATC star-tracker design (© BAE, Used with permission)

4.3.4.6. Payload Controller (PLC)

The PLC consisted of controller electronics, a General Dynamics Single-Board Computer (SBC) with four processors (model unit 6U VME-64), interface electronics, and power converters to control, operate, and power the instrument (see Figure 4-19). Except for two anomalies discussed below, the PLC operated as expected in the on-orbit radiation environment. Mis-comparisons of its 4 synchronized processors were significantly fewer than predicted. The payload controller electronics suffered no on-orbit damage, and the PLC satisfied performance requirements.

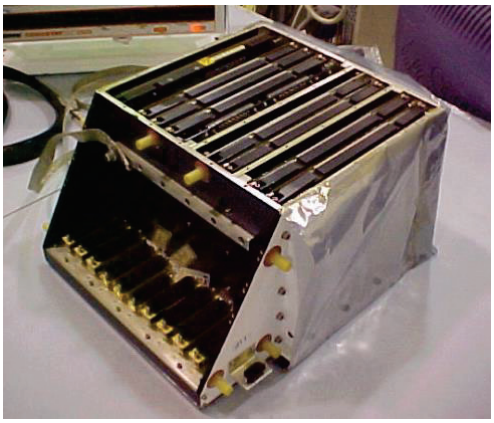

Figure 4-19. The Payload Computer flight unit (© BAE, Used with permission).

An important function of the PLC was to autonomously monitor the health and status of key payload components through a FDIR system. Alerts and mode change actions were issued by the FDIR when status parameters exceeded set threshold values, thereby protecting the payload from unexpected behaviors. Before launch, the FDIR threshold settings were populated in tables using parameters established and verified during ground testing. During on-orbit operations FDIR settings were changed through table updates that did not require flight software revisions. Over the course of the mission, 30 FDIR faults occurred within the payload. For each event the team evaluated the cause and determined a path for its resolution. In many ways, the FDIR system and its flexibility enabled the payload to operate safely long beyond its expected lifetime.

Mass Memory Unit Spurious End of Data Interrupt: In July 2006 an anomaly began to occur in the Mass Memory Unit that caused the X-band science data downlink to occasionally end prematurely resulting in some loss of data. The problem was traced to a status register that erroneously indicated an end of data condition when a memory location error detection and correction interrupt occurred. The problem was mitigated by implementing a flight software change on 11 October 2006 that used an alternate register in the memory unit to determine end of data. No spurious end-of-data interrupts occurred since the change was implemented.

PLC Boot Code Correction: During the latter half of 2010, the CALIPSO payload began to experience a single, intermittent correctable bit error at one location of the payload controller SDRAM memory. Payload operations and science data collection were not disrupted by the errors, which were autonomously corrected by the Error Detection And Correction (EDAC) hardware. The CALIPSO team conducted an anomaly investigation to evaluate health and status of the SDRAM and determined that the boot code memory checks were too stringent and could lead to a boot failure if additional memory errors were present. Through a sustaining engineering contract with BAE and with the SBC vendor, a modified boot code sequence was developed and implemented, which robustly ranks and selects the best viable memory configuration from sixty-six available configurations that contain the least number of correctable bit errors. The new code was uploaded to the payload in November 2010. With this software correction, the PLC rebooted 28 times without issue.

LVPS Power Converter Temperature: The Low Voltage Power Supply (LVPS) temperature in the payload controller was observed to be higher than predicted (see Figure D8). During the peak beta-angle season each fall, the temperatures approach FDIR limits that were established using a conservative threshold value to help track the PLC thermal environment. As a precaution, the mission operations team developed a reduced operational mode for extreme conditions. Fortunately,

temperatures in the PLC did not continue to rise in the later part of the mission and there was no need to implement the alternative mode.

4.3.4.7. X-Band Transmitter

An X-band transmitter was used once or twice a day to transmit the CALIPSO payload science data collected over the previous 24-hour period to an SSC ground station in either Alaska or Hawaii. For redundancy, two downlinks per day were used during the first years of the mission and again during the later years. The reliability of the data capture system was so good that the second transmission was eliminated in 2010 to reduce thermal cycling of the transmitter and extend its lifetime. Each downlink typically lasted ~9 minutes. The transmitter was built by Cincinnati Electronics and was non-redundant. The radio frequency telemetry remained stable, indicating little or no degradation. Mission operations reinstated two downlink sessions per day when scheduling conflicts with other higher priority missions or ground station problems could cause loss of data. Over 7700 transmits were successfully conducted.

4.4. Ground Systems

The Ground Segment consisted of distributed resources to communicate with and control the spacecraft; operate the payload; and collect, process, and archive engineering and scientific data. The Ground Segment is partitioned into satellite and science functional elements, which had split responsibilities between NASA and CNES.

4.4.1. Satellite Control

The CALIPSO spacecraft was operated by CNES from the SOCC located in Toulouse, France. The SOCC provided navigation, telemetry downlink and processing, payload command uplinks, and satellite bus engineering support. Communication with the platform occurred ~4 to 5 times per day through the CNES network of S-band ground stations. Payload health and engineering telemetry were forwarded via secure file transfer over a Wide Area Network architecture to the MOCC located at LaRC. This facility also supported all the other PROTEUS missions. During the mission, more than 30,000 S-band telemetry sessions were accomplished, and more than 800,000 commands were uploaded to the spacecraft.

Within the A-Train constellation, the SOCC maintained CALIPSO in its control box position and successfully executed 232 propulsion burns, including 7 conjunction avoidance maneuvers. While in the A-Train and the C-Train, CloudSat was responsible for maintaining its position relative to CALIPSO.

4.4.2. Mission and Payload Operations

The MOCC was responsible for the operation of the payload and for monitoring its health and performance. It managed overall mission activities, payload commanding, anomaly investigations and recoveries, orbit maneuver coordination, C-Train spacecraft coordination, and engineering and mission assurance support. The MOCC also managed the acquisition of science data through a contract with BAE/SSC. A primary X-band telemetry data downlink session occurred each day to SSC facilities in either Hawaii or Alaska; backup transmits were scheduled to ensure and optimize data retrieval during periods of high-interest atmospheric events, such as wildfires and volcanic eruptions. The level 0 (L0) data were transmitted by SSC to the ASDC located at LaRC for processing, archiving and distribution. Over the mission, data from 90.4% of available measurement opportunities were successfully received by the ground station network and transferred to the ASDC. This exceeded the 85% requirement in mission Level 1 requirements. Of the 9.6% opportunities for

which data were not acquired, Figure 4-20 provides a breakout of the different reasons. In general, interruptions to normal payload operational activities were most impacted by solar weather events (~30%) followed by payload anomalies (~25%), platform operations and anomalies (~23%) and ground station anomalies (~22%).

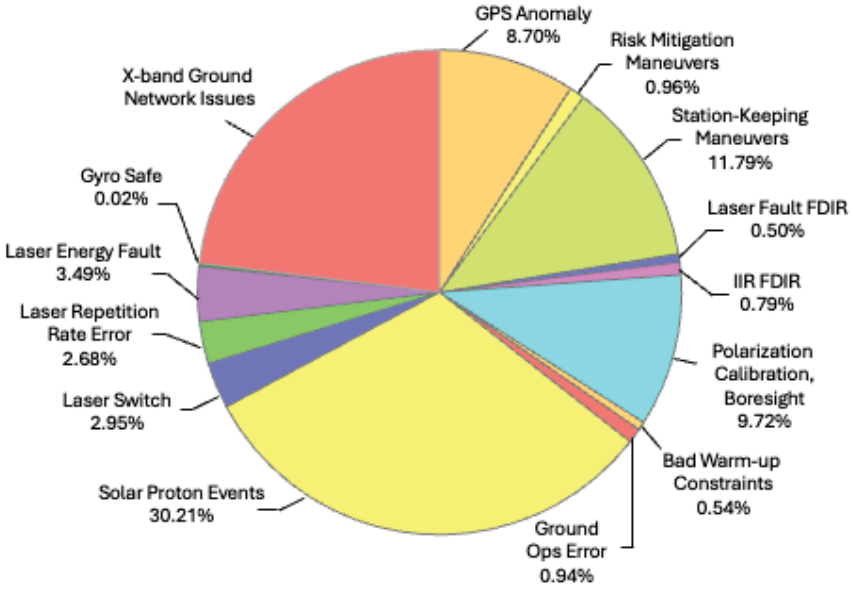

Figure 4-20. Payload, Platform and Ground System issues that impacted mission operations and the acquisition of the science data (Source credit: NASA).

The MOCC also conducted over-flight analysis for the Hubble Space Telescope and Landsat 5 satellite to identify situations when lasing operations should be temporarily halted for a few seconds. Over the mission more than 100 commands were successfully issued to inhibit laser operations.

4.4.3. Solar Flare Operational Procedure

The CALIPSO mission operations concept was designed to minimize on-console operator presence and take advantage of the autonomous FDIR systems on the platform and payload to monitor critical subsystems and, if appropriate, take immediate action. During the mission, the routine workload for both teams remained steady, and activities were designed for a normal 40-hour work week. For abnormal situations, such as during the instrument checkout or during an anomaly investigation, the teams worked outside their usual hours.

One issue that occasionally impacted off-duty operations was the need to issue commands to protect the payload during significant solar flare events. A flux of heavy ions could have damaged the high voltage laser Q-switch driver MOSFETs or, for more extreme conditions, the PLC memory. The MOCC had a staff member on-call around the clock with a mobile device to receive NOAA space weather warnings. For events that were predicted to exceed established thresholds for extended periods, a request was issued by phone to the on-call SOCC representative to send commands at the earliest transmission opportunity to power off the laser and, possibly, the PLC. The threshold for depowering the laser was set at 10 MeV integrated proton flux levels above 10 particles cm^{-2} s^{-1} sr^{-1} (10 proton flux units), and the threshold for the depowering the PLC was set at 100 MeV integrated proton flux levels above 1 pfu. During the mission 32 solar events occurred that required a command

to be uplinked to the platform (see the mission timeline shown in Figure 3-1), and of these, 8 events were during off-normal duty hours for the SOCC and 23 for the MOCC. This procedure likely contributed to the prolonged period of service by backup laser and PLC.

4.4.4. CALIPSO Orbit and A-Train/C-Train Constellation Coordination

The formation of the A-Train was initially motivated by the desire to match CALIPSO lidar observations within the CloudSat cloud profiling radar's 1-km field of view (FOV) footprint and to co-locate these observations within the Aqua MODIS and CERES instrument's measurement swath (Stephens et al., 2002). An added desire was to minimize the time separation between satellite observations to capture the same state of cloud development across all the instrument measurements. Other missions in formulation (i.e., PARASOL, OCO, Glory, GCOM-W, and OCO-2) recognized the added value of flying their passive sensors with CALIPSO and CloudSat and, hence, modified their mission plans to join the A-Train.

A coordinated flight strategy was developed by the A-Train Mission Operations Working Group that defined individual spacecraft control boxes stationed along the Aqua orbit. Each mission was responsible for station-keeping within its phased zone and for communicating on planned and executed maneuvers to all members. The A-Train was formed with Aqua (2002) leading the constellation and Aura (2004) following. The PARASOL mission entered the A-Train in 2004 and was followed by the addition of CALIPSO and CloudSat in 2006. Because of the tighter matching constraints between CALIPSO and CloudSat (C-C) satellites, the CloudSat mission took on the responsibility of flying their spacecraft in response to CALIPSO's position. The C-C team held a goal for 50% of possible match opportunities, and achieved >90% coincidences, within a time separation of 15 seconds or less. A battery anomaly with CloudSat's platform prompted the mission to temporarily leave the A-Train in September 2011. CloudSat returned to the A-Train in 2012; however, out of abundance of caution for the safety of the other missions, the time separation between the CALIPSO and CloudSat satellites was increased, and CloudSat was positioned behind CALIPSO. The GCOM-W (2012-present) and OCO-2 (2014-present) missions also joined the A-Train constellation. The Aura mission was already in orbit before C-C launched and flew in the same orbit as Aqua but trailed it by 15 minutes. Aura moved its control box closer in time to Aqua in 2008 to reduce time separation and align its limb measurements with the other A-Train observations.

In 2018, CALIPSO and CloudSat descended out of the A-Train because of low fuel reserves for the CALIPSO spacecraft and concerns with the reliability of a reaction wheel for the CloudSat platform. These two missions subsequently formed the C-Train constellation (~40 sec separation with a revised ±4 km ground track overlap goal) and continued coordinated operations until December 2023. Figure 4-21 depicts the A-Train constellation in the mid-life of CALIPSO's operation (2014-2018).

While in the A-Train, CALIPSO maintained an ascending node crossing bias relative to Aqua of 215 km to the East to minimize the impact of sun glint in the coincident Aqua-CALIPSO measurements. The orbit apogee (732 km), perigee (715 km), and inclination (98.2º) were tuned to a sun-synchronous frozen orbit configuration with a mean local time of about 13:41 at the ascending node. These parameters yielded an orbit mean altitude of 705 km, and an orbit repeat cycle of 16 days. Following the descent of CALIPSO into the C-Train, the mean orbit altitude decreased to 688 km and the other orbital parameters changed. Figure 4-9 shows the CALIPSO orbit's MLT over the duration of the mission and how it drifted to later crossing times once CALIPSO moved into the C-Train. The C-Train's eastward orbital precession across the Aqua MODIS swath addressed an original CALIPSO mission objective by providing long-sought validation of MODIS cloud products as a function of MODIS view angle.

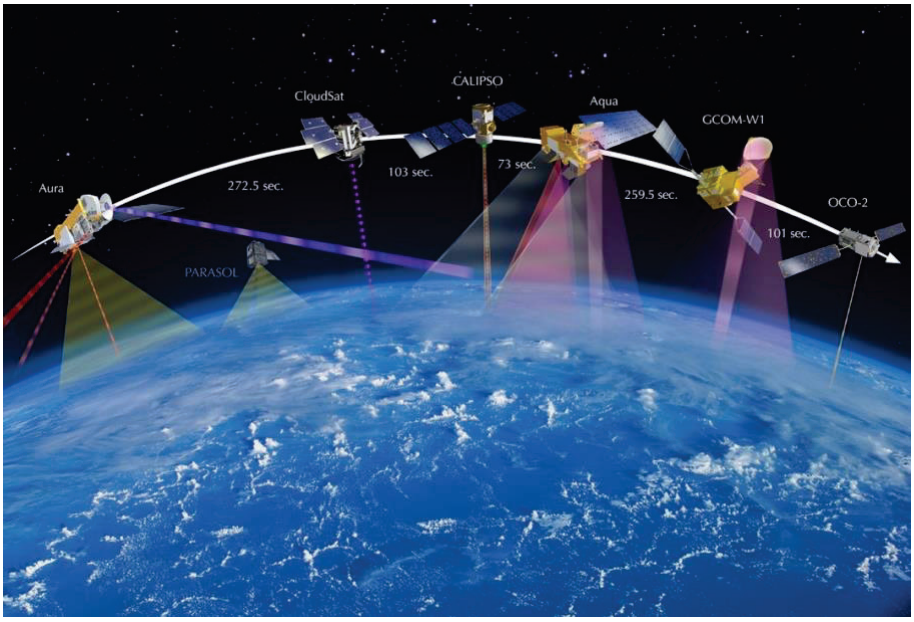

Figure 4-21. The A-Train constellation between 2014 and 2018. The PARASOL mission ended operations in 2013 and is included in the figure at a lower altitude as one of the original members, but that it had descended out of the constellation. The position of CloudSat is also noted behind CALIPSO. Prior to 2012, CloudSat flew ahead of CALIPSO (Source credit: NASA).

The international A-Train was the first time that Earth Science satellite missions were organized into a coordinated constellation and successfully conducted sustained operations within a tight set of control constraints. The measurement synergies enabled through the A-Train were unprecedented and yielded significant new insights into Earth's radiation budget and the hydrological cycle among many other discoveries. The MOWG developed protocols for communicating and exchanging orbital information between members and procedures for planning and executing routine as well as unexpected risk mitigation maneuvers. The A-Train community's *esprit de corps* furthered the development of joint measurement retrievals, encouraged greater transparency in scientific analysis, and inspired an exchange of information that significantly helped to advance Earth System Science. The joint CALIPSO mission operations team was a key player in the MOWG and helped it shape policies that are still in use today.

4.4.5. Payload and Platform Decommissioning

During the mission, the spacecraft was operated to comply with the French Space Act Law, which required atmospheric re-entry of the platform within 25 years following cessation of operations. The descent of the platform out of the A-Train to form the C-Train in September 2018 at a mean orbit altitude of 688 km was designed, in part, to satisfy the disposal requirement. Following approval of the maneuver plan by the CNES Loi sur les Opérations Spatiales (LOS) office, the maneuver was successfully conducted.

The payload operations ended on 1 July 2023 and all systems were powered off. The PLC was powered on one last time on 11 December 2023 to verify communications with the platform and to verify the integrity of the payload controller as a final query for the DHU anomaly investigation.

The SOCC completed the passivation of the platform on 15 December 2023. Remaining fuel was depleted and the power relays opened. No further communication with the platform has occurred.

4.4.6. Data Production, Archive, and Distribution

The CALIPSO L0 data were downlinked daily and processed into standard and expedited L1, L2 and level 3 (L3) data products. All CALIPSO data products and their associated browse images were transferred to the ASDC for archive and distribution. Expedited data products generated for all three instruments (CALIOP, IIR and WFC) were typically available within 24 hours of data downlink and were used by a variety of customers for near-real-time applications and to support field campaigns. Earlier in the mission, standard data products were typically generated within 2-3 days of downlink. Starting around 2015, the data latency increased to 8 to 10 weeks because of the delay in the readiness of the Goddard Earth Observing System (GEOS) assimilated meteorological products used to support the CALIOP calibration procedure.

In collaboration with the French AERIS project (https://en.aeris-data.fr/), CALIPSO maintained a mirror of the CALIPSO data sets at the ICARE data facility in Lille (https://www.icare.univ-lille.fr/), France. ICARE additionally supports online data search and order tools and provides a full complement of browse images. Data were transferred between ASDC and ICARE using both SFTP and SCP file transfer protocols. Daily file comparisons were made to ensure that each site maintains a full and complete set of all orderable data products.

Regular communication between ASDC and ICARE project leaders and data management team members from NASA and CNES ensured consistent product availability across all distribution sites. During monthly teleconferences and through regular email communication, the teams shared daily product generation, ingest, and feedback reports, discuss current development efforts, and kept abreast of all topics involved with the production, archive and distribution of data.

The French data archive contains a duplicate copy of all the L1, L2, and L3 data products produced by the CALIPSO mission and appropriate data user documentation. At the time this Final Report was submitted, data from the final reprocessing were still being transferred from ASDC to ICARE. The project will complete the transfers within the coming months.

4.4.6.1. Documentation Repository

The CALIPSO project archived its extensive catalogue of project data and documentation at three NASA repositories, each with different capabilities and objectives. A separate French CALIPSO documentation archive is maintained at AERIS/ICARE in Lille, France.

The repository at ASDC complies with the NASA Earth Science Data Preservation Content Specification 423-SPC-00 guideline and contains copies of the following project data products and documentation:

- Mission description and science objectives
- A complete catalogue of all raw (level 0) and derived science data products (level 1, 2, and 3) produced by the CALIPSO mission
- A complete record of payload status and health data for the mission
- Science data product requirements and design
- Processing and algorithm version history
- Product generation algorithms (Algorithm Theoretical Basis Documents)
- Product data description and quality summaries
- Instrument calibration and validation
- Science data processing software
- List of all science data product algorithm inputs

Documents that are publicly available through ASDC were reviewed by the LaRC Export and ITAR control office and hold no restrictions for public dissemination. These products, software, and documents are available for use under NASA's Earth Science Data System Open-Source Software Policy (SPD-41a).

A second CALIPSO documentation repository was constructed on the NASA SharePoint system. This archive includes a large selection of project documentation spanning mission formulation activities, project reviews, official correspondence, mission operation reports, instrument anomaly investigations, and budgets. The archive requires permission for access and the contents may contain restricted information that should be reviewed prior to its public dissemination. https://nasa.sharepoint.com/sites/CALIPSO/Repository1/Forms/AllItems.aspx

A third NASA archive contains a complete copy of all documentation, including science team and working group presentations, as well as data and documentation that could not fit within storage allocation limits on the NASA SharePoint system. These documents and data should also be reviewed by Export Control and ITAR office prior to their public release.

4.4.6.2. CALIPSO Website

During the mission, NASA's CALIPSO team maintained a mission website (https://www-calipso.larc.nasa.gov) that provided mission content for the public and science community. In the few months following the end of the project, the project website will be restructured with relevant content split between ASDC (https://asdc.larc.nasa.gov/project/CALIPSO) and the LaRC Science Directorate site. The latter URL is tailored more for public affairs rather than a source on data content. The ASDC website will contain information needed to order and use CALIPSO data.

4.4.6.3. CALIOP Lidar Simulator Tools

During the CALIPSO mission, two pioneering high-fidelity lidar instrument simulator tools (FREESIM and LidarSim) were developed by CALIPSO at LaRC and used to generate synthetic data to support performance trade studies with BAE Systems, science algorithm development, and scientific investigations. The FREESIM tool is a sophisticated radiometric engineering model and contains parameter specifications for the individual components within the transmitter and the receiver, including all detectors and post-detector gain amplification subsystems.

The LidarSim model tool is an extension of FREESIM with additional options to generate simulated signals for a single profile or a series of profiles along an orbit track. LidarSim was a critical resource for algorithm development by providing highly realistic CALIOP L1 attenuated backscatter profiles for all three measurement channels. These synthetic data include the noise characteristics inherent to analog detection using both PMTs and APDs and incorporate uncertainties related to the measurement environment. This capability enabled the team to explore algorithm designs, and it proved to be an invaluable tool for understanding the subtle and complex intricacies of the algorithm system with the CALIOP observations.

Figure 4-22 displays an example of a simulated lidar scene created by LidarSim that was used to investigate the sensitivity of the CALIOP feature finding algorithm to random noise. The scene illustrates the versatility of the simulator model with providing stepwise changes in the introduction of noise and its impact to the detection of two aerosol layers. Prior to CALIPSO, there were no such tools, and the evolution of these simulators leaves a valuable contribution to lidar remote sensing science and development of future spaceborne lidar missions. The software for these models is archived in the CALIPSO repository.

DOI: 10.64631/LIZS5968

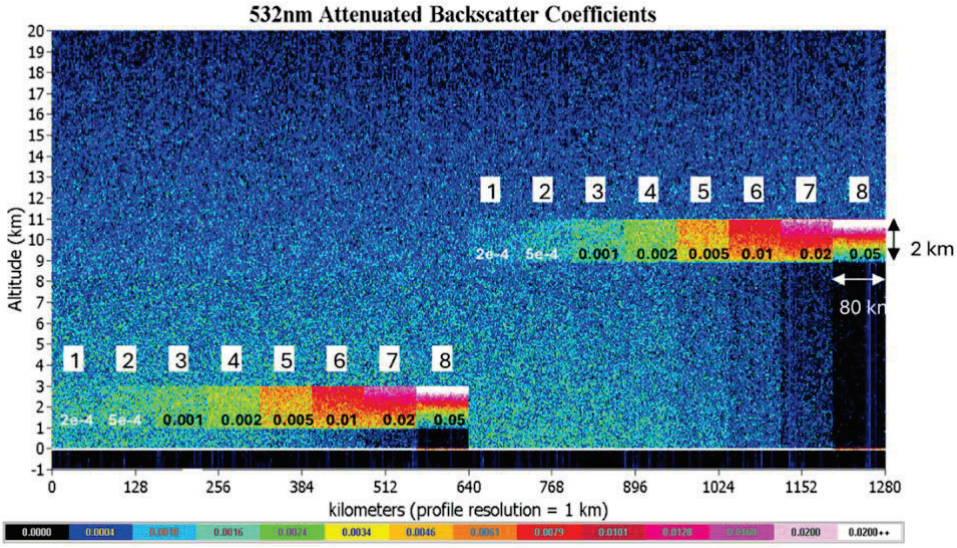

Figure 4-22. Simulation of CALIOP 532 nm nighttime attenuated backscatter coefficients (km-1 sr-1) showing two particulate layers, each of which is constructed of 8 contiguous subsections that extend horizontally for 240 consecutive laser pulses (~80 km). Both layers are 2 km thick and a lidar ratio of 20 sr is assigned in all 16 subsections (Source credit: NASA).

4.4.6.4. Calibration/Validation Activities

Throughout the mission, the CALIPSO team and greater scientific community used ground-based, airborne, and satellite observations of aerosol and clouds over the globe to evaluate CALIOP, IIR, and WFC instrument performance, verify assumptions with the data retrieval algorithms, and assess the accuracy of the data products. Findings were often reported at meetings and in publications, which significantly influenced improvements to CALIPSO data products that appeared in the series of data releases. Although a detailed summary of these investigations is beyond the scope this report, it is noteworthy to report that many of the ~5000 publications citing CALIPSO data included feedback on the quality of CALIPSO's data products.

Aircraft under-flights were found to be the most beneficial for seeking validation comparisons with CALIOP because of the need to obtain coincident observations of aerosol and/or cloud features before their properties changed. Over the course of the CALIPSO mission, HSRL flights (>125 opportunities) were conducted in a variety of aerosol and cloud environments. These profile measurements were indispensable for assessing CALIPSO calibration accuracy and aerosol/cloud retrieval uncertainties. The CALIPSO team placed considerable value in the HSRL data and often stated that it would have been exceedingly difficult to assess CALIOP's calibration performance, let alone diagnosis issues with retrieval assumptions, without matched HSRL comparisons.

The CALIPSO project also acquired extensive validation data sets through active participation in national and international field measurements campaigns. Multi-sensor validation measurements were obtained during many campaigns highlighted in the mission timeline shown in Figure 3-1, such as AEROCLO-SA (Africa), ORACLES (Africa), NAAMES (North America), REThinC (USA), ACEPOL (USA), and CAMP^{2}Ex (Philippines) to name a few. (A full list of the field missions listed in the Mission Timeline is provided in Appendix F.). While the value of direct comparisons cannot be understated, an equally valuable aspect is the inclusion of CALIOPS's observations into the science mission plan for each of the field campaigns. Ultimately the ability to answer science questions

provides a final level of confidence. The number and diversity of field campaigns that CALIPSO engaged is a testament to the value of the CALIPSO instrument suite to the community.

The calibration assessment previously conducted for the V1 IIR L1 products (Garnier et al., 2017) were repeated for the V2 products. Comparisons with MODIS since launch show that the revised calibration scheme successfully eliminates the systematic seasonal and regional biases that were found previously (Garnier et al., 2018). In the IIR L2 cloud microphysical retrievals, the key pieces of information are the inter-channel microphysical indices inferred from the effective emissivities. Mitchell et al. (2018) compared IIR indices, which are very sensitive to the presence of small particles, with indices reconstructed from *in situ* observations in cold cirrus clouds. The authors found a general agreement within IIR estimated uncertainties, but larger discrepancies were related to the processing of the *in situ* observations, which can produce ambiguous results for very small particles.

4.4.6.5. Mission Level 1 Measurement Requirements

The CALIPSO mission satisfied all of its Level 1 measurement requirements as specified in the CALIPSO Level 1 Requirements document (2003, 2005) and summarized in Table 5. Studies that reported on the validation of these requirements are included in the last column of the table.

Table 5. CALIPSO Level 1 Measurement Requirements

Data Product	Measurement Capabilities and Uncertainties	Relevant References
Aerosol height, thickness	For layers with $\tau > 0.005$	Kim S.-W. et al., 2008; Wu D. et al., 2011; Solanki and Singh, 2014; Wu Y. et al., 2014
Aerosol optical depth, τ and extinction, σ (z)	40 %	Mamouri et al., 2009; Omar et al., 2010; Kittaka et al., 2011; Campbell et al., 2012; Schuster et al., 2012; Omar et al., 2013; Kim M.-H. et al., 2013; Rogers et al., 2014; Zong et al., 2015; Kim M.-H. et al., 2017; Toth et al., 2018; Young et al., 2018; Thorsen et al., 2025
Cloud Height	For layers with $\tau > 0.01$	McGill et al., 2007; Kim S.-W. et al., 2008, 2011; Dupont et al., 2010; Yorks et al., 2011; Thorsen et al., 2011; Blanchard et al., 2014; Balmes and Fu, 2018
Cloud Thickness	For layers with $\tau < 5$	Dupont et al., 2010; Thorsen et al., 2011; Kim S.-W. et al., 2011; Yorks et al., 2011
Cloud τ, σ (z)	Within a factor of 2 for $\tau < 5$	Mioche et al., 2010; Dupont et al., 2010; Thorsen et al., 2011; Hlavka et al., 2012; Holz et al., 2016 ; Young et al., 2018; Balmes et al., 2019
Ice/water phase	Layer by layer	Avery et al., 2020; Cesana et al., 2016; Wang, D. et al., 2024
Ice cloud emissivity, ε	$\pm$ 0.03	Garnier et al., 2012, 2015.
Ice particle size	$\pm$ 50% for $\varepsilon > 0.2$	Sourdeval et al., 2013; Garnier et al., 2021b

5. Appendix A: Summary of the CALIPSO Data Products

Appendix A presents an overview of the many data products generated from the downlinked CALIPSO measurements. Section A1 and Table A3 give concise summaries of all data products developed jointly by the LSWG and the Data Management Team (DMT) and distributed by the DMT and ASDC. Similarly, data products created and distributed by external organizations and/or independent researchers are described in section A2 and summarized in Table A4.

5.1. CALIPSO Standard Data Products

The CALIPSO project routinely produced and distributed both standard and expedited versions of the CALIOP, IIR, and WFC data products. Standard products were designed for use in the most rigorous science investigations and laid the foundation for the publication of over 5,000 peer-reviewed journal papers that use CALIPSO data. The expedited products were tailored for near-real-time use by operational forecast centers and field measurements campaigns. Due to latency in the delivery of required meteorological model data, standard products were typically not available until approximately 8–10 weeks after data acquisition. Because the expedited products used historical meteorological data, they were generally available within 24 hours after downlink. However, this earlier delivery came at the expense of a slight degradation of geolocation knowledge and some loss of calibration accuracy, both of which affected the quality of the science retrievals. Users were strongly cautioned against using expedited data products as the basis for research findings or journal publications. With the cessation of active data acquisition in June 2023, distribution of the expedited data products was permanently halted.

CALIPSO standard data products are publicly available for the full mission, from June 2006 through June 2023. These data are distributed to the scientific community by both the ASDC and AERIS/ICARE in version 4 Hierarchical Data Format (HDF4) files. For L1, L1.5, and L2 processing, each standard data file (granule) contains approximately 45 minutes (i.e., ½ orbit) of continuous data spanning a full daytime or nighttime orbit segment. L3 data files contain globally gridded monthly averages derived from the L1 and L2 products. All files were produced using algorithms and source code developed jointly by CNES, IPSL/LATMOS, AERIS/ICARE, the joint French-American CALIPSO LSWG, and the NASA-LaRC DMT. The correspondences between NASA's standard Earth Observing System Data and Information System (EOSDIS) data processing levels and the CALIPSO data products are given by Table A1 (EOSDIS definitions) and Table A2 (CALIPSO descriptions).

Table A1: NASA's Earth Observing System Data and Information System (EOSDIS) data processing levels; quoted text is from https://www.earthdata.nasa.gov/learn/earth-observation-data-basics/data-processing-levels

Level	EOSDIS Description
0	"Reconstructed, unprocessed instrument and payload data at full resolution, with any and all communications artifacts (e.g., synchronization frames, communications headers, duplicate data) removed."
1A	"Level 1A (L1A) data are reconstructed, unprocessed instrument data at full resolution, time-referenced, and annotated with ancillary information. This ancillary information can include radiometric and geometric calibration coefficients and georeferencing parameters (e.g., platform ephemeris)."

Level	EOSDIS Description
1B	"L1B data are L1A data that have been processed to instrument units (not all instruments have L1B source data)."
2	"Derived geophysical variables at the same resolution and location as L1 source data."
2A	"L2A data contains information derived from the geolocated instrument data, such as ground elevation, highest and lowest surface return elevations, energy quantile heights ("relative height" metrics), and other waveform-derived metrics describing the intercepted surface."
2B	"L2B data are L2A data that have been processed to instrument units (not all instruments will have a L2B equivalent)."
3	"Variables mapped on uniform space-time grid scales, usually with some completeness and consistency."
3A	"L3A data are generally periodic summaries (weekly, 10-day, monthly) of L2 products."

Table A2: Relationships between the CALIPSO data product offerings and the formal EOSDIS product definitions

Level	Description
0	Science and engineering data downlinked from the CALIPSO satellite; CALIPSO level 0 data conforms to the EOSDIS definition of level 0 data
1B	CALIPSO level 1B data is similar to EOSDIS level 1A data. The primary difference is that signal corrections and calibration coefficients are applied to the CALIPSO level 1B data. The CALIPSO level 1B files contain all science and engineering parameters required to reproduce the EOSDIS level 1A "reconstructed, unprocessed instrument data at full resolution"
1.5	The CALIPSO level 1.5 data product is generated by using CALIPSO level 2 data to 'cloud clear' the matching level 1B profiles before averaging those profiles to a 20 km along track resolution. It does not have an analog in the EOSDIS classification scheme.
2	CALIPSO level 2 data is a combination of EOSDIS level 2 and level 2A data
3	CALIPSO level 3 data is

5.1.1. Algorithm Maturity

CALIOP

The CALIOP data processing software was built around a tightly integrated family of peer-reviewed science algorithms that defined the state-of-the-art for lidar retrieval techniques during the period immediately prior to launch. In the years following, these algorithms were modified, upgraded, or replaced, as required, to reliably and automatically accommodate the tremendous diversity of meteorological conditions observed while acquiring a near-continuous global data set. Announcements of major upgrades were routinely reported in the peer-reviewed literature. That the CALIPSO software architecture retained this degree of flexibility after over ~25 years of continuous development is a major tribute to skill and foresight of the original designers.

The fundamental paradigm implemented in the CALIOP software is the concept of 'layer properties'. Layer boundaries are determined within fully calibrated L1 profiles based on the magnitude of the 532 nm attenuated backscatter intensity relative to the expected molecular background (Vaughan et al., 2009). Layer properties are then derived from the attenuated backscatter coefficients within the

identified layer boundaries, most often by integration. In subsequent analyses, decisions about layer type (e.g., Cloud-Aerosol Discrimination (CAD), aerosol subtyping, lidar ratio selection, etc.) are made on the basis of these layer properties, together with ancillary information such as temperature and geographic location. Layer type and subtype then dictated the extinction-to-backscatter ratio (i.e., lidar ratio) that was used to retrieved profiles of altitude-resolved within each layer.

IIR

The IIR L1 calibration algorithm was considered fully mature for the release of the V2 data release. The IIR L2 algorithm used selected range-resolved CALIOP inputs in a standard split-window technique to provide fast retrievals of effective emissivities, optical depths, and microphysical properties. This innovative algorithm also evolved over the course of the mission to optimize the information reported in the CALIOP L2 cloud and aerosol products in the automated IIR scene classification procedures. Internal IIR consistency checks and extensive comparisons with CALIOP cirrus optical depths were conducted throughout the mission to assess the quality of the retrievals down to very small optical depths. The V5 IIR L2 algorithm is fully mature for single-layered semi-transparent clouds overlying ocean surfaces and showed significant improvement for dense opaque clouds, for high clouds overlying low opaque water clouds, and over land. Retrievals over land used a surface emissivity database derived from prior IIR observations. Cloud microphysical properties were retrieved from Look-Up Tables (LUTs) built from pre-computed optical properties derived from either theory or in situ measurements. These LUTs were regularly updated as the knowledge of ice crystal properties advanced within the scientific community.

WFC

The analysis algorithms used to derive science parameters from the CALIPSO WFC measurements are fully mature.

Data Validation Levels

The following validation levels were assigned, as warranted, to the full suite of CALIPSO V5 data products:

- Beta: the data product contains parameters that have not yet been fully validated and hence may include undiscovered artifacts. The CALIOP L2 5 km merged layer diagnostic product, which contains several previously unreleased 1064 nm retrievals, is the only product in the CALIPSO V5 release that is designated as 'beta'.
- Standard: Parameter retrievals and associated uncertainty estimates have been compared to accurate, collocated, and independent measurements.

For L1 and L2 products, data validation levels are included in the CALIPSO V5 filenames.

5.1.2. CALIOP Level 0 Data Products

The CALIOP L0 products translate the raw binary data downlinked from the satellite into the more universally accessible HDF4 format. These data are the raw lidar profile measurements from the 1064 nm channel and the 532 nm parallel and perpendicular channels, along with instrument status parameters needed to interpret the profile data. Unlike the binary data, information for all three channels is packaged in single files.

5.1.3. CALIOP Level 1 Data Products

The following paragraphs describe the principal parameters included in the CALIOP L1 data product. The CALIOP L1 files were specifically designed to serve as a comprehensive, stand-alone product

that provides all of the fundamental inputs required to derive the entire suite of CALIOP L2 products. Examples illustrating the CALIOP L1 data products are shown in Figure A-1.

CAL_LID_L1_Attenuated backscatter profiles

The primary geophysical data products generated by the CALIOP L1 analyses are altitude-resolved, geolocated, and calibrated profiles of attenuated backscatter coefficients at 532 nm (total and perpendicular component) and 1064 nm (total only). Profiles extend from ~40 km above local mean sea level to ~2 km below. The vertical resolution of the data varies according to altitude, with coarser spatial resolutions being reported at higher altitudes, and the finest resolutions (30 m vertically) in the lower troposphere between ~8.2 km and the surface. The horizontal resolution is fixed by the laser pulse rate of 20.16 Hz, corresponding to a footprint spacing of ~335 meters (Hunt et al., 2009).

CAL_LID_L1_Calibration coefficients

Calibration coefficients and their associated uncertainties are reported for each attenuated backscatter profile. The ancillary meteorological data required to calculate the calibration coefficients are also provided. These data include profiles of atmospheric pressure, temperature, and molecular number density, all obtained from the MERRA-2 reanalysis data distributed by GMAO. The molecular and ozone scattering and absorption cross sections needed to convert number densities into molecular backscatter and extinction coefficients are also included.

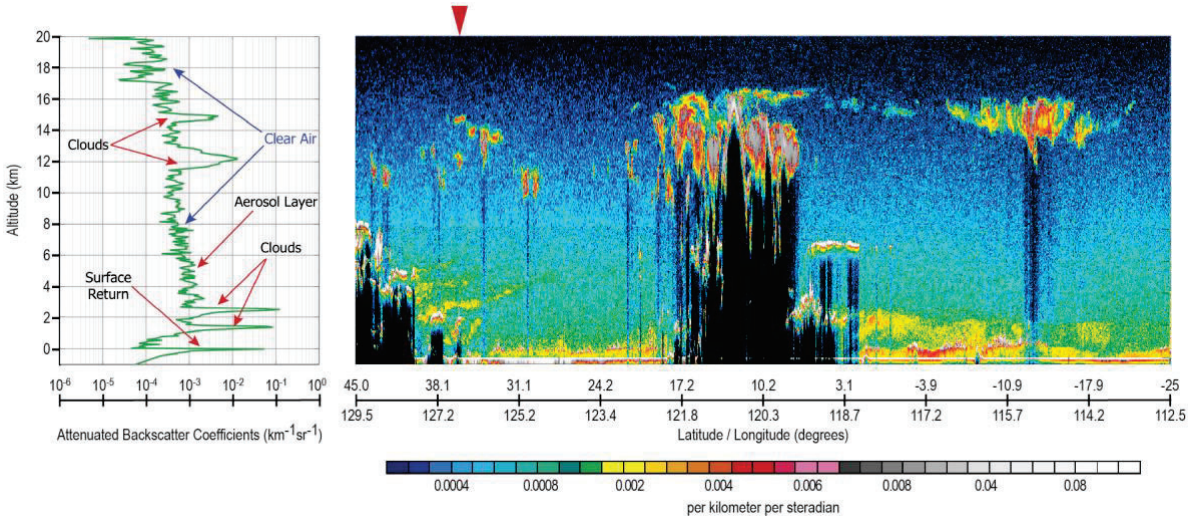

Figure A-1: Left panel: profile of CALIOP 532 nm attenuated backscatter coefficients measured over the Yellow Sea (36.1° N, 126.6° E) on 13 August 2006 at 17:41:18 UTC. For this profile, single-shot measurements have been averaged to a 5 km horizontal resolution (15 laser pulses). Clouds, aerosols, and the ocean surface return all appear as signal enhancements rising above the ambient molecular backscatter intensity. Right panel: time history of CALIOP backscatter measurements acquired on 13 August 2006 from 17:38:49 to 17:58:15 UTC, illustrating the wide range of feature locations and backscatter intensities that can be encountered during a single orbit segment. The red arrow at the top of the image denotes the location of the profile data shown in the left panel. (Image adapted from Vaughan et al., 2009; Used under CC BY 4.0.)

CAL_LID_L1_Level 1 Ancillary data

These data include time stamps; satellite position and attitude information; lidar footprint latitude, longitude, and surface characterization; meteorological data such as tropopause heights and temperatures; instrument operational state parameters (e.g., laser energy); additional on-board measurements of background light levels and the Root Mean Square (RMS) variation of the baseline

signal; and quality assurance (QA) flags that provide a synopsis of various instrument health and status parameters. External sources for these ancillary data include the International Geosphere-Biosphere Program (IGBP) the Air Force Weather Agency, and the CloudSat science and data management teams, creators of the Digital Elevation Model (DEM) used in CALIPSO's V5 data products.

5.1.4. IIR Level 1 Data Products

CAL_IIR_L1_CALIIR calibration images and gains

New in the final Version 3 (V3) data release, the IIR L1 CAL products contain the blackbody and deep space calibration images used to produce the initial gains at 8.65, 10.6 and 12.05 μm, which are also reported. These products cover one full orbit.

CAL_IIR_L1_COR__IIR gain corrections

New in the final (V3) data release, the IIR L1 COR products contain semi-empirical corrections of the initial gains at 8.65, 10.6 and 12.05 μm reported in CAL_IIR_L1_CAL. These products cover one full orbit.

CAL_IIR_L1__IIR Level 1b Radiances

L1 IIR products are organized in daytime and night-time orbit segments (granules) to match the CALIOP L1 definition.

The primary IIR L1b products are calibrated radiances at 8.65, 10.6 and 12.05 μm re-sampled and registered on a 1 km × 1 km resolution grid centered on the CALIOP lidar track, at mean sea level, with a cross-track swath width of 69 km. Each row of pixels lies perpendicular to the lidar track and is centered on a lidar footprint. The distance between two successive rows is exactly 3 lidar footprints. An IIR quality flag is provided to alert data users to potential noise problems and calibration difficulties.

5.1.5. WFC Level 1 Data Product

L1 WFC products are reported during daytime only, with file names synchronized with the lidar and IIR L1 file names. In all products, calibrated radiances and bidirectional reflectances for the WFC spectral bandwidth of 620-670 nm are registered to an Earth-based grid centered on the CALIOP ground track. The data products include swath and track homogeneity parameters that quantify the homogeneity of the cross-track image frames.

CAL_WFC_L1_125m_WFC Level 1b Scans

The 125 m Native Science grid contains only the central 5 km wide high-resolution portion of the WFC swath.

CAL_WFC_L1_1Km_WFC Level 1b Scans

The 1 km Native Science grid covers the full 61 km swath. The 125 m data in the central 5 km swath have been averaged to 1 km resolution to fill in this portion of the WFC swath.

CAL_WFC_L1_IIR_WFC Level 1b Radiances Registered to IIR Grid

To facilitate the use of the WFC data in IIR retrievals, the WFC radiometric data are registered to the same Earth-based geometric grid as the IIR data.

Table A3: CALIPSO data products produced by the CALIPSO DMT

Data Product Name	Description	Comments (e.g., validation status, user community served)
CAL_LID_L0	Raw lidar profile data converted from binary to HDF4 and repackaged to include all measurement channels in a single file	
CAL_LID_L1	CALIOP attenuated backscatter profiles: 532 nm total and perpendicular, 1064 total, calibration coefficients, ancillary data	532 nm: fully validated (Rogers et al., 2011; Kar et al., 2018; Getzewich et al., 2018) 1064 nm: fully validated (Vaughan et al., 2019)
CAL_LID_L1.5	Cloud-cleared CALIOP attenuated backscatter profiles averaged to 20 km horizontally, ancillary data	Primary users were operational forecast centers and aerosol transport modelers
CAL_LID_L2_ VFM	CALIOP vertical feature mask: layer locations, cloud-aerosol discrimination, ice-water phase, aerosol typing	Fully validated; product used to construct value-added data products generated by other researchers (e.g., GEOPROF-LIDAR)
CAL_LID_L2_ 333mMLay	CALIOP 333 m layer boundaries and spatial and optical properties; the V3 products (333mCLay) report only clouds, whereas V4 also includes aerosol layers	Fully validated
CAL_LID_L2_ 01kmCLay	CALIOP 1 km cloud layer boundaries and layer spatial and optical properties	Fully validated
CAL_LID_L2_ 05kmALay	CALIOP 5 km aerosol layer boundaries; layer spatial and optical properties, aerosol typing, optical depth; includes single shot layer detection information	Typing: Fully validated (Schuster et al., 2012; Burton et al., 2013; Bibi et al., 2016; Zhao, Y. et al., 2024) AOD: Fully validated (Redemann et al., 2012; Kim M.-H. et al., 2013; Liu, C. et al., 2018)
CAL_LID_L2_ 05kmCLay	CALIOP 5 km cloud layer boundaries; layer spatial and optical properties, ice-water phase, ice water path, optical depth; includes single shot layer detection information	Boundaries: Fully validated (Yorks et al., 2011; Thorsen et al., 2011) IWP: Fully validated (Avery et al., 2012; Cesana et al., 2016) Optical depths: Fully validated (Holz et al., 2016; Balmes et al., 2019)
CAL_LID_L2_ 05kmMLay	CALIOP 5 km cloud and aerosol layer boundaries; layer spatial and optical properties, ice-water phase and ice water path (clouds only), optical depths at 532 nm (clouds, aerosols, and total column) and 1064 nm (aerosols only); includes single shot layer detection information	See remarks for 05kmALay and 05kmCLay

Data Product Name	Description	Comments (e.g., validation status, user community served)
CAL_LID_L2_ MLay_ Diagnostic	An enhanced version of the 05kmMLay product that also includes cloud and total column optical depths at 1064 nm	Cloud and column optical depths at 1064 nm are beta parameters. All other parameters are fully validated
CAL_LID_L2_ 5kmCPro	CALIOP cloud backscatter, extinction and ice water content profiles; uncertainties; QA parameters	Fully validated (Hlavka et al., 2012; Thornberry et al., 2017)
CAL_LID_L2_ 5kmAPro	CALIOP aerosol backscatter and extinction profiles; uncertainties; QA parameters	Fully validated (Tian et al., 2017)
CAL_LID_L2_ PSCMask	CALIOP polar stratospheric cloud (PSC) product; layer locations, optical properties and composition	Fully validated (Snels et al., 2021; Lavy et al., 2024)
CAL_LID_L2_ BlowingSnow_ Antarctica	CALIOP blowing snow over Antarctica; snow layer heights and optical properties at single shot horizontal resolution	Fully validated (e.g., Yang et al., 2021)
CAL_LID_L3_ Tropospheric_ APro_AllSky	Gridded monthly averages of CALIOP tropospheric aerosol extinction profiles in all sky conditions (i.e., cloudy and clear); sample counts, ancillary data	Fully validated
CAL_LID_L3_ Tropospheric_ APro_ CloudFree	Gridded monthly averages of CALIOP tropospheric aerosol extinction profiles in cloud-free skies; sample counts, ancillary data	Fully validated
CAL_LID_L3_ Tropospheric_ APro_CloudySky-Transparent	Gridded monthly averages of CALIOP tropospheric aerosol extinction profiles above and below semi-transparent clouds; sample counts, ancillary data	Fully validated
CAL_LID_L3_ Tropospheric_ APro_CloudySky-Opaque	Gridded monthly averages of CALIOP tropospheric aerosol extinction profiles above opaque clouds; sample counts, ancillary data	Fully validated
CAL_LID_L3_ Stratospheric_APro	Gridded monthly averages of CALIOP stratospheric aerosol extinction profiles above opaque clouds; sample counts, ancillary data	Fully validated (Kar et al., 2019; Chouza et al., 2020)
CAL_LID_L3_ Ice_Cloud	Gridded monthly averages and histograms of CALIOP ice-water content and ice cloud extinction coefficients, ancillary data	Fully validated (Winker et al., 2024)
CAL_LID_L3_ Cloud_Occurrence	Gridded monthly counts of CALIOP cloud occurrence partitioned by thermodynamic phase and opacity; ice clouds also binned by layer optical depth, ancillary data	Fully validated

Data Product Name	Description	Comments (e.g., validation status, user community served)
CAL_LID_L3_ GEWEX_Cloud	Gridded monthly counts of CALIOP cloud amounts and cloud top heights and temperatures reported for high, middle and low altitude regions	Fully validated; target users are data analysts and modelers who are familiar with the GEWEX cloud assessment project (Stubenrauch et al., 2024)
CAL_IIR_L1_CAL	IIR calibration images and uncorrected gains	Target users are infrared instruments experts.
CAL_IIR_L1_ COR	IIR gain corrections	Target users are infrared instruments experts.
CAL_IIR_L1	IIR calibrated and geo-located radiances at 08.65 μm, 10.6 μm and 12.05 μm	Fully validated (Garnier et al., 2017, 2018)
CAL_IIR_L2_ Track	IIR track data: emissivity and cloud properties	Single-layer cloud over ocean: • Optical depth: Fully validated (Garnier et al., 2012, 2015) • Effective diameter: Fully validated (Sourdeval et al., 2013; Garnier et al., 2021b) • Cirrus microphysics: Fully validated (Mitchell et al., 2025)
CAL_IIR_L2_ Swath	IIR Swath data: emissivity and cloud properties	Fully validated for cloud-free scenes over oceans (Garnier et al., 2017)
CAL_IIR_L3_ GEWEX_Cloud	Gridded monthly averages and histograms of IIR optical and microphysical properties of selected ice and water clouds	Target users are data analysts who are familiar with the GEWEX cloud assessment project (Stubenrauch et al., 2024)
CAL_WFC_L1_ 125m	WFC at 125 m: radiances and reflectances across 5 km center swath	Fully validated
CAL_WFC_L1_ 1Km	WFC at 1 km: radiances and reflectances across 61 km swath	Fully validated
CAL_WFC_L1_ IIR	WFC radiances and reflectances registered to IIR grid	Fully validated
Standard browse images	CALIOP attenuated backscatter, color ratio, depolarization ratio, layer type and subtype; IIR brightness temperatures and inter-channel differences; WFC radiances	Reproduced in numerous peer-reviewed publications by non-LaRC researchers

5.1.6. CALIOP Level 2 Data Products

The fundamental data products generated in the CALIOP L2 analyses are (i) layer top and base altitudes, reported in the vertical feature mask and cloud and aerosol layer products; and (ii) range-resolved profiles of particulate backscatter and extinction coefficients, reported in the cloud and aerosol profile products.

CAL_LID_L2_05kmALay_5 km aerosol layer boundaries

Complete spatial and optical descriptions of all aerosol layers detected within the CALIOP backscatter profiles are reported in the 5 km aerosol layer products. Information provided for each layer includes base and top altitudes; aerosol type; directly measured optical parameters such as integrated attenuated backscatter at 532 nm and 1064 nm, layer-integrated volume depolarization and attenuated backscatter color ratios; and derived optical parameters, including estimates of optical depth at both wavelengths. Layers are reported at a horizontal resolution of 5 km with provisions made for reporting up to 8 layers within each 5 km column. Also included are complete geospatial information for each column, full diagnostic information for each layer detected, and a comprehensive subset of the single shot layer detection results within each 5 km column.

CAL_LID_L2_05kmCLay_5 km cloud layer boundaries

Complete spatial and optical descriptions of all cloud layers detected are reported in the 5 km cloud layer products. Information provided for each layer includes base and top altitudes; ice-water phase determination; ice-water path; integrated attenuated backscatter at 532 nm; layer-integrated volume depolarization ratio; and estimates of optical depth at 532 nm. Layers are reported at a horizontal resolution of 5 km, with provisions made for up to 10 layers within each 5 km column. Also included are complete geospatial information for each column, full diagnostic information for each layer detected, and comprehensive subset of the single shot layer detection results within each 5 km column.

CAL_LID_L2_05kmMLay_5 km cloud and aerosol layer boundaries

Introduced in the V4 data release, the 5 km merged layer product combines the information reported separately in the 5 km aerosol layer product and the 5 km cloud layer product into a single, merged HDF file. Layers are reported at a horizontal resolution of 5 km, with provisions made for up to 15 layers within each 5 km column. Also included are complete geospatial information for each column, full diagnostic information for each layer detected, and comprehensive subset of the single shot layer detection results within each 5 km column.

CAL_LID_L2_MLay_Diagnostic_5 km cloud and aerosol layer boundaries

New in the V5 data release, the merged diagnostic layer product contains all the information in the 05kmMLay product. It also reports a number of diagnostic parameters used in algorithm development and verification but not normally included in publicly released products. To augment the single shot layer detection results, the MLay Diagnostic files contain a comprehensive subset of features reported in the 1 km resolution layer product, so that layers detected at all CALIOP averaging resolutions are reported in a single product. Several yet-to-be-validated parameters are also included, with the most prominent being 1064 nm cloud optical depths and 1064 nm ODCOD retrievals.

CAL_LID_L2_01kmCLay_1 km cloud layer boundaries

The 1 km cloud product is a higher resolution subset of the 5 km cloud product designed specifically to match the 1 km pixel resolution of the IIR. The requirement for higher spatial resolution limits the amount of averaging that can be done in the detection phase, hence fainter layers requiring more averaging (e.g., subvisible cirrus) are not consistently reported in the 1 km product. While the 1 km product reports a full catalog of directly measured spatial and optical properties (e.g., layer boundaries and 532 nm integrated attenuated backscatter), it does not provide derived optical properties such as optical depths.

CAL_LID_L2_333mMLay single shot (1/3 km) cloud and aerosol layer boundaries

The 1/3 km cloud product is a subset of the 1 km product. Layers are detected and reported at single-shot resolution. Due to CALIOP's on-board data averaging scheme, single shot data is only available between ~8.2 km and the surface. Because the detection of these layers is done using single shot data, only the most robust layers can be confidently identified, thus some layers identified at 1 km will not appear in the 1/3 km product. The 1/3 km product reports the same layer parameters and ancillary information that are provided in the 1 km product.

CAL_LID_L2_VFM

The Vertical Feature Mask (VFM) is a concise distillation of the CALIOP layer products that provides researchers with simple but comprehensive 'where' and 'what' information about the cloud/aerosol content of any region in the vertical swath. The VFM data consists of an array of bit-mapped integers provided at the full CALIOP downlink resolution, with each value conveying information about a single range resolution element. These integers are interpreted as a set of scene classification flags that provide a first-order characterization of the corresponding spatial region in terms of layer detection and layer type. VFM examples are shown in Figure A-2.

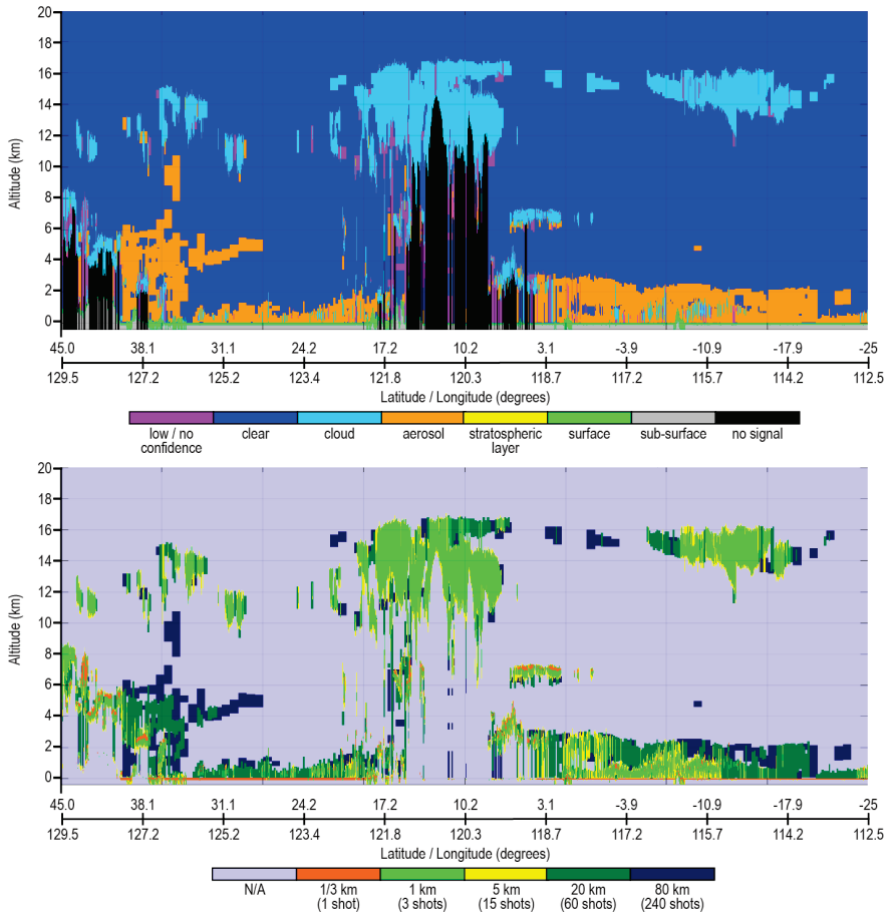

Figure A-2: Images derived from the vertical feature mask product for the 13 August 2006 data segment shown in Figure A-1. The upper panel shows V4 layer classifications for all features detected within the scene. The lower panel shows V4 layer boundaries for all layers detected, color coded according to the amount of horizontal averaging required to detect each layer. The lower panel thus provides a coarse contour plot of layer backscatter intensity (Source credit: NASA).

CAL_LID_L2_05kmCPro_Cloud backscatter and extinction profiles

The 5 km cloud profile product contains the range-resolved extinction coefficients used to compute the layer optical depths reported in the 5 km cloud layer product. Profiles of cloud backscatter and extinction coefficients at 532 nm (e.g., see Figure A-3) are reported at 60 m vertical resolution between -0.5 km and 20.2 km and at 180 m vertical resolution between 20.2 km and 30 km. The horizontal resolution is fixed at 5 km. Ancillary information reported with each set of profiles includes time and position data and surface elevation statistics. Meteorological context is provided by GMAO profiles of temperature, atmospheric pressure, relative humidity, and ozone and molecular number densities, which are interpolated spatially and temporally to the CALIPSO orbit track and time.

CAL_LID_L2_5kmAPro_Aerosol backscatter and extinction profiles

The 5 km aerosol profile product reports profiles of aerosol backscatter and extinction coefficients at 532 nm and 1064 nm (e.g., see Figure A-4). Data are reported from 30 km to -0.5 km vertically at a horizontal spatial resolution of 5 km. The vertical resolution is 60 m vertically below 20.2 km, and 180 m above. The meteorological and ancillary data provided in the cloud profile product are also reported in the aerosol profile product. A full set of diagnostic and QA parameters is provided in both the aerosol and cloud profile products.

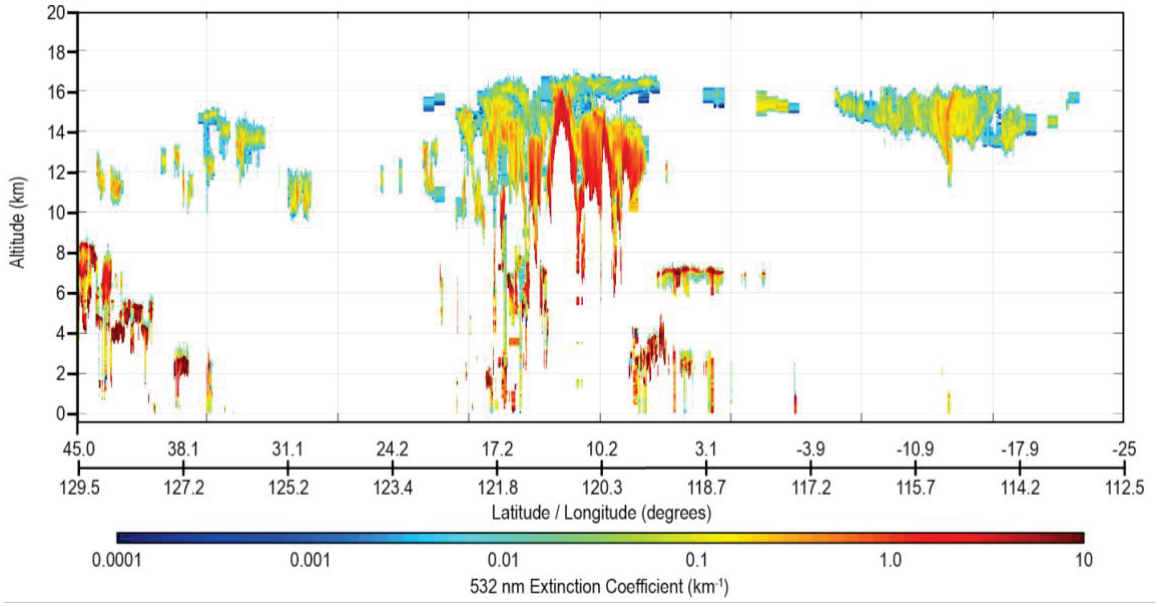

Figure A-3: Cloud extinction coefficients at 532 nm for the 13 August 2006 scene depicted in Figure A-1. In those cases where extended averaging is required for layer detection, profile data is replicated as necessary to span the full horizontal width of the layer. An example of this is seen in the faint, trailing edge of the cirrus layer at ~22° S between 14 km and 16 km. As seen in Figure A-2, detecting this portion of the cloud required averaging to 80 km horizontally, and this coarser resolution is reflected in the horizontal uniformity of the extinction coefficients reported in the cloud profile product. The white portions of the image indicate those places where no retrieval was attempted (e.g., in clear air regions and layers identified as aerosols) Source credit: NASA.

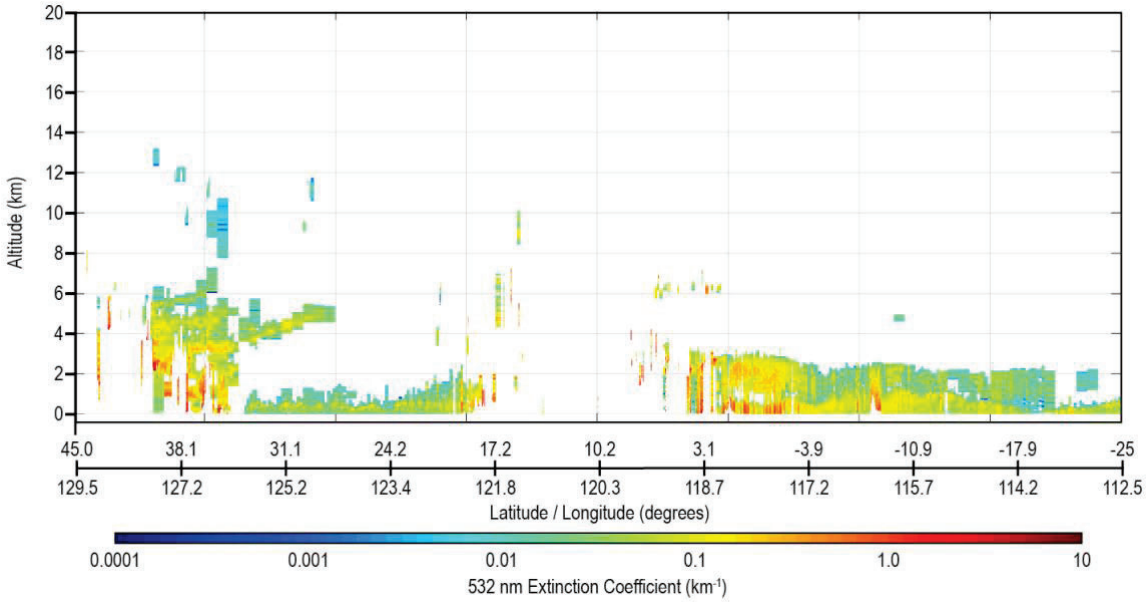

Figure A-4: V4 532 nm aerosol extinction coefficients for the 13 August 2006 scene depicted in Figure A-1. The white portions of the image indicate those places where no aerosol extinction retrieval was attempted (e.g., in clouds and in clear air regions) (Source credit: NASA).

CAL_LID_L2_PSCMask_Polar stratospheric cloud backscatter and composition profiles

The CALIPSO lidar L2 PSC data product ensemble describes the spatial distribution, optical properties, and composition of PSC layers observed by the CALIPSO lidar on a uniform 5 km horizontal by 180 m vertical grid. The PSC data ensemble is derived from the nighttime CALIPSO lidar L1B data products using the PSC detection and composition classification algorithm described in Pitts et al. (2018). The PSC processing algorithm includes retrievals of backscatter and extinction coefficients that enable estimates of PSC particle surface area density and volume density. An example of the unique PSC data obtained from CALIOP is given in Figure A-5, which shows the time series of the 2006-2018 mean, standard deviation, and range of daily PSC spatial volume in the Antarctic (Figure A-5a) and Arctic (Figure A-5b), with maximum and minimum values color-coded according to the year in which they occurred. At the peak of the season in July, the relative standard deviation in Antarctic PSC spatial volume is about ±25%. In contrast, the relative year-to-year variability in Arctic PSC spatial volume is much larger, with the relative standard deviations exceeding 100% for most days.

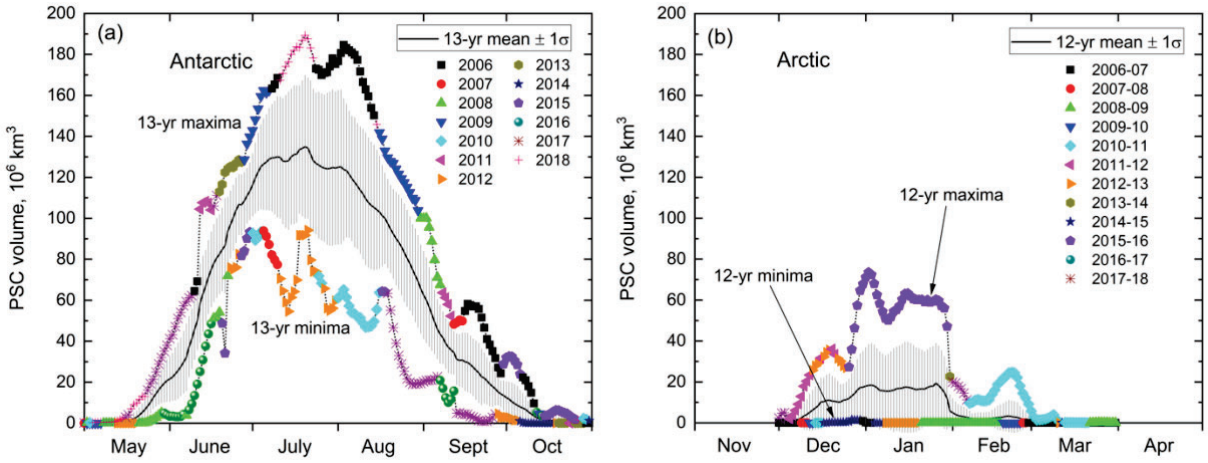

Figure A-5: Time series of 2006-2018 mean, standard deviation, and range of daily values of CALIOP (a) Antarctic and (b) Arctic PSC spatial volume (daily areal coverage integrated over altitude). Maxima and minima are color-coded by the year in which they occurred. (Updated from Pitts et al., 2018; Used under CC BY 4.0).

CAL_LID_L2_Blowing Snow: Antarctica

The CALIPSO L2 Blowing Snow (Antarctica) data product reports the spatial and temporal frequencies, layer heights, and optical depths of blowing snow detected over Antarctica from 2006 to the present. The product also includes relevant meteorological parameters and a monthly 1 × 1 degree blowing snow frequency grid. The monthly data is derived from the CALIOP L1B profile products and L2 333 m merged layer data products using code and algorithms developed by Steve Palm (Palm et al., 2011). Figure A-6 shows the monthly mean spatial distributions of blowing snow frequencies composited over data acquired between 2006 and 2017. Minimum blowing snow frequencies are seen to occur in Austral summer, coinciding with the maximum occurrence frequencies of PSCs (Figure A-5). When combined with model re-analysis fields of temperature and moisture, the estimates of sublimation magnitudes derived from the CALIPSO blowing snow retrievals are considerably larger than model estimates (Palm et al., 2017).

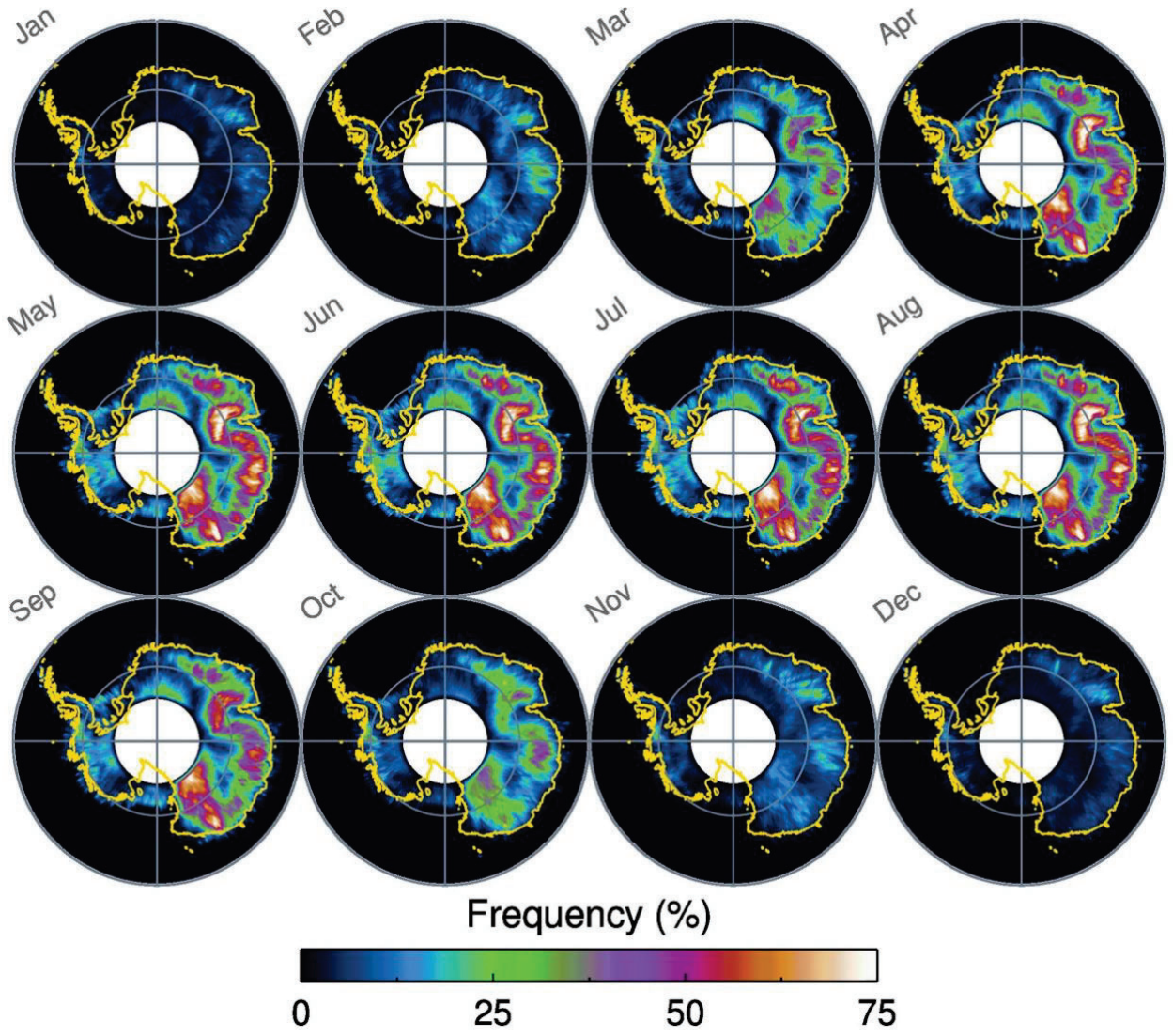

Figure A-6: Average monthly blowing snow frequency over Antarctica for the period of 2006-2017 (Source credit: NASA).

5.1.7. CALIOP Level 1.5 Data Products

The CALIOP L1.5 product is a cloud-cleared, highly averaged (20 km horizontally by 60 m vertically) version of the CALIOP L1 data. The L2 VFM is used to identify and exclude cloud-contaminated regions prior to the averaging process. The L1.5 product contains the means, medians, and standard deviations of cloud-cleared L1 attenuated backscatter coefficients averaged horizontally over 20 km (i.e., 60 laser pulses). A full complement of meteorological and diagnostic information is also included. An L1.5 expedited product distributed during the on-orbit phase of the mission was designed specifically to support near-real time operational needs, and thus was constructed from expedited L1 and L2 products. In order to support retrospective analyses to be conducted by the aerosol modeling community, L1.5 standard products derived from the standard versions of the L1 and L2 data products were released beginning in April 2019. Figure A-7 compares the CALIOP L1B data (upper panel) to its cloud-cleared and averaged L1.5 standard counterpart (lower panel).

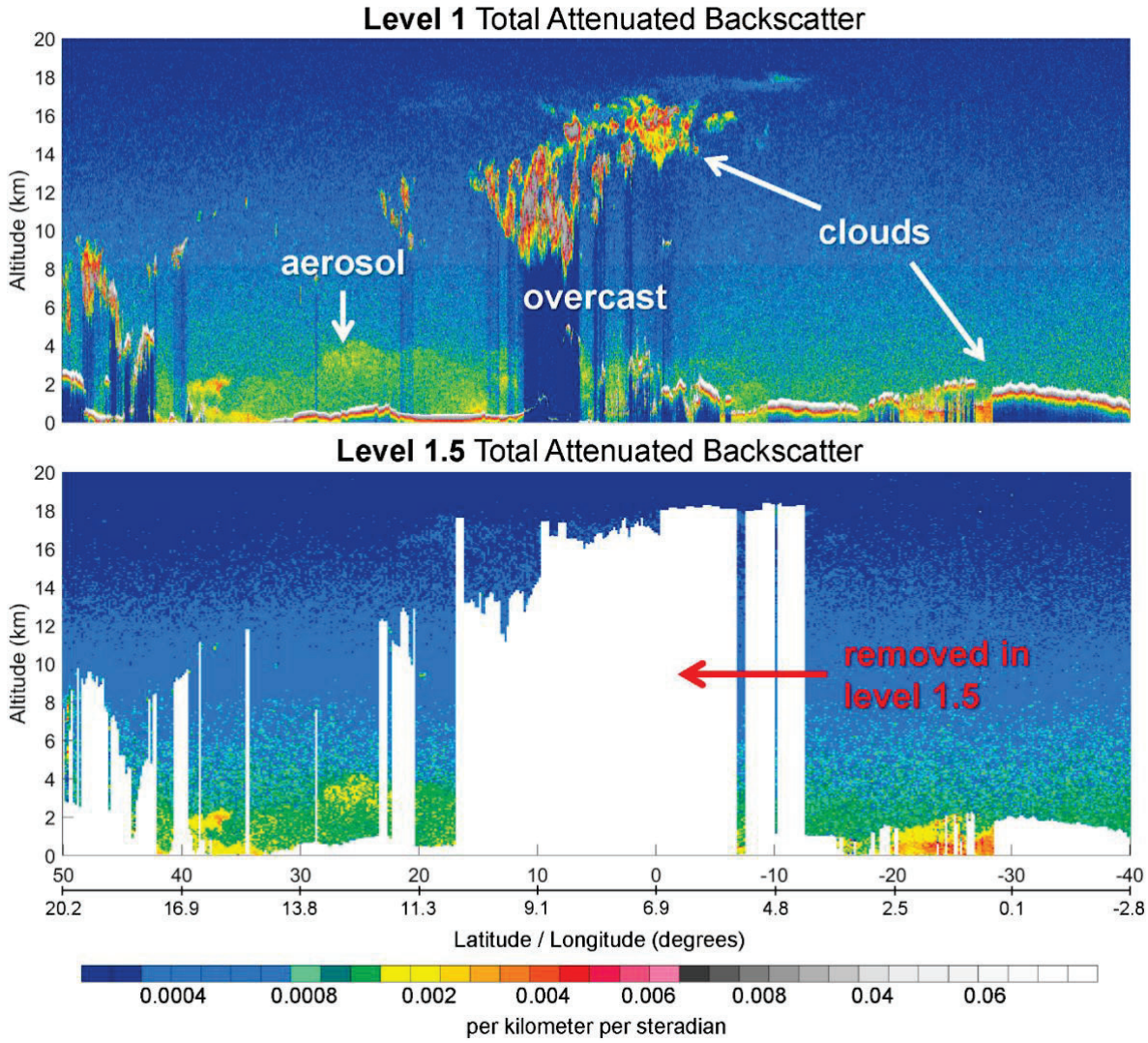

Figure A-7: CALIOP level 1 (top) and level 1.5 (bottom) 532 nm total attenuated backscatter coefficients for a subset of an individual granule measured on November 21st, 2010 (Source credit: NASA).

5.1.8. CALIOP Level 3 Data Products

The CALIOP L3 data products are spatially gridded monthly statistics of the spatial, optical, and morphological properties of clouds and aerosols reported on equal-angle latitude/longitude grids. The L3 products are derived from the L1 and L2 products following the application of rigorous quality assurance screening processes. The CALIOP L3 data products include separate tropospheric and stratospheric aerosol profile products and three cloud products: a cloud vertical occurrence frequency product, and an ice-cloud only product that profiles of cloud extinction and ice water contents. Though grid structures are different among these various L3 products, they are all congruent and can be easily combined if desired. Lastly, CALIOP also created a special L3 product specifically for the GEWEX Cloud Assessment.

CALIOP Level 3 Tropospheric Aerosol Data Products

The fundamental data reported in the CALIOP L3 tropospheric aerosol profile products are gridded (2° latitude by 5° longitude) monthly averages of aerosol extinction coefficient profiles, together with

aerosol optical depths, sampling statistics, and meteorological data. The L3 data are derived from the L2 layer and aerosol profile products. Quality screened profiles are reported between -0.5 km and 12 km above mean sea level with a vertical resolution of 60 m, with extinction coefficients reported for all aerosols, regardless of type, and separately for each of the seven aerosol subtypes identified in the L2 analyses. Four types of the level 3 tropospheric aerosol profile products are distributed, delineated by cloud cover (Tackett et al., 2018). In order to mitigate the influence of low energy laser pulses, the L3 tropospheric aerosol enforces a minimum sample size of 80 valid profiles in each grid cell. Data in grid cells not meeting this threshold are reported as fill values.

CAL_LID_L3_Tropospheric_APro_AllSky_Aerosol extinction profiles

The all sky L3 tropospheric aerosol product reports gridded monthly averages of quality-screened CALIOP L2 aerosol extinction profiles wherever aerosols are detected, irrespective of cloud presence. Monthly mean pressure, temperature, and relative humidity profiles derived from GMAO meteorological data are reported for each grid cell, as are mean surface altitudes and composition (i.e., land vs. water). Aerosol type and spatial distribution statistics are also included, as are gridded monthly averages of total column AOD and its uncertainty. Figure A-8a shows examples of the 3D distribution of mean AOD from June 2006 through December 2011 reported in the "All Sky" product. Figure A-8b, also derived from the "All Sky" product, shows the regional variability in aerosol extinction profiles for all nighttime data acquired during June, July, and August 2007–2012.

CAL_LID_L3_Tropospheric_APro_Cloud-Free Aerosol extinction profiles

The cloud-free L3 tropospheric aerosol product reports gridded monthly averages of CALIOP L2 aerosol extinction profiles for only those cases where the L2 input profiles were entirely cloud-free. The cloud-free product reports the same set of optical, spatial, and morphological parameters that are given in the "All Sky" product.

CAL_LID_L3_Tropospheric_APro_CloudSky-Transparent_Aerosol extinction profiles

The cloudy sky transparent L3 tropospheric aerosol product reports gridded monthly averages of CALIOP L2 aerosol extinction profiles for only those cases where the L2 input profiles contained one or more semi-transparent clouds. The cloudy sky transparent product reports the same set of optical, spatial, and morphological parameters that are given in the "All Sky" product.

CAL_LID_L3_Tropospheric_APro_CloudySky-Opaque_Aerosol extinction profiles

The cloudy sky opaque L3 tropospheric aerosol product reports gridded monthly averages of CALIOP L2 aerosol extinction profiles for only those cases where the L2 input profiles contained an opaque cloud. The cloudy sky opaque product reports the same set of optical, spatial, and morphological parameters that are given in the "All Sky" product. Note that summing the information reported in the cloud-free, cloudy sky transparent and cloudy sky opaque products will generate the same data set reported in the "All Sky" product.

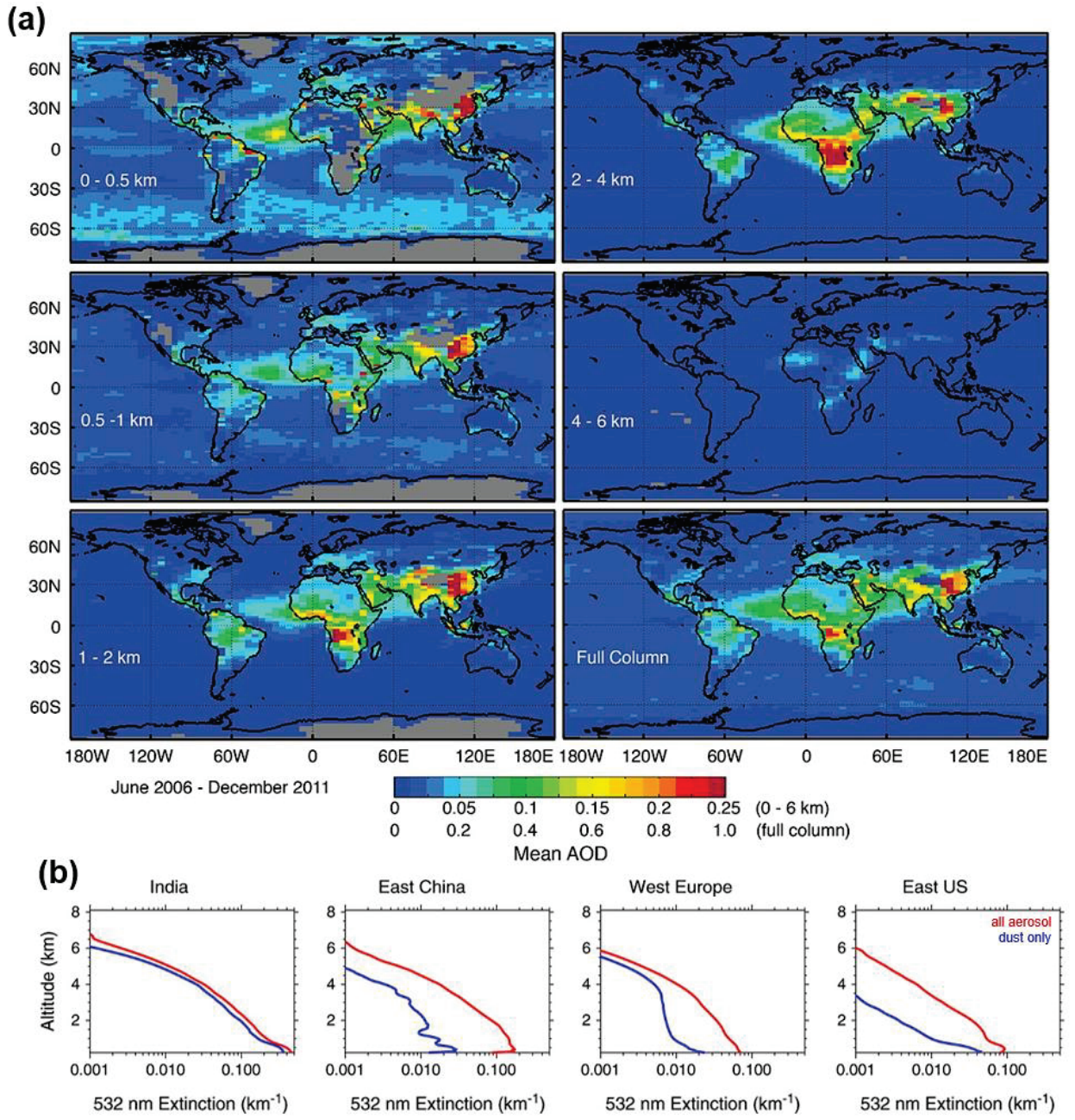

Figure A-8: (a) Maps of the 3D distribution of aerosol optical depths reported in the CALIPSO level 3 aerosol profile product. The lower right map shows the global distribution of total column AOD. The remaining panels show AOD distributions for selected vertical slices through the total column (Bond et al., 2013). (b) Profiles of mean aerosol extinction coefficients reported by the CALIPSO level 3 aerosol profile product for all aerosol species and for dust-only, aggregated by region (adapted from Huang, L. et al., 2013; Used under CC BY 4.0).

5.1.9. CALIOP Level 3 Stratospheric Aerosol Data Products

The primary data products reported in CALIOP level 3 stratospheric aerosol profile products are monthly mean gridded profiles of 532 nm aerosol extinction, particulate backscatter, attenuated scattering ratio and stratospheric aerosol optical depth, along with estimated uncertainties for all parameters. The corresponding profiles of total attenuated backscatter, molecular backscatter, and

ozone absorption, along with ancillary information on the tropopause altitude, potential temperature and sample statistics, are also included. The spatial grid is 5° in latitude, 20° in longitude and 900 m in altitude which is coarser than the CALIOP L3 tropospheric aerosol product because the SNR in the stratosphere is significantly lower and thus requires more extensive averaging. The L3 aerosol profiles are derived from CALIOP L1B nighttime 532 nm attenuated backscatter profiles with inputs from the L2 5 km merged layer and PSC mask products for cloud filtering. The stratospheric aerosol profile product has two components. In the "background" component, all layers reported in the CALIOP 5 km merged layer and PSC mask products are removed prior to averaging the calibrated L1B attenuated backscatter profiles, including clouds, aerosols, and PSCs. In the "all aerosol" component, only the clouds and PSCs are removed while retaining the backscatter from those layers classified as aerosols with good confidence scores (Kar et al., 2019). Figure A-9 shows time histories of injections of volcanic aerosols into the stratosphere, derived from the L3 stratospheric aerosol profile product for January 2007 through December 2017.

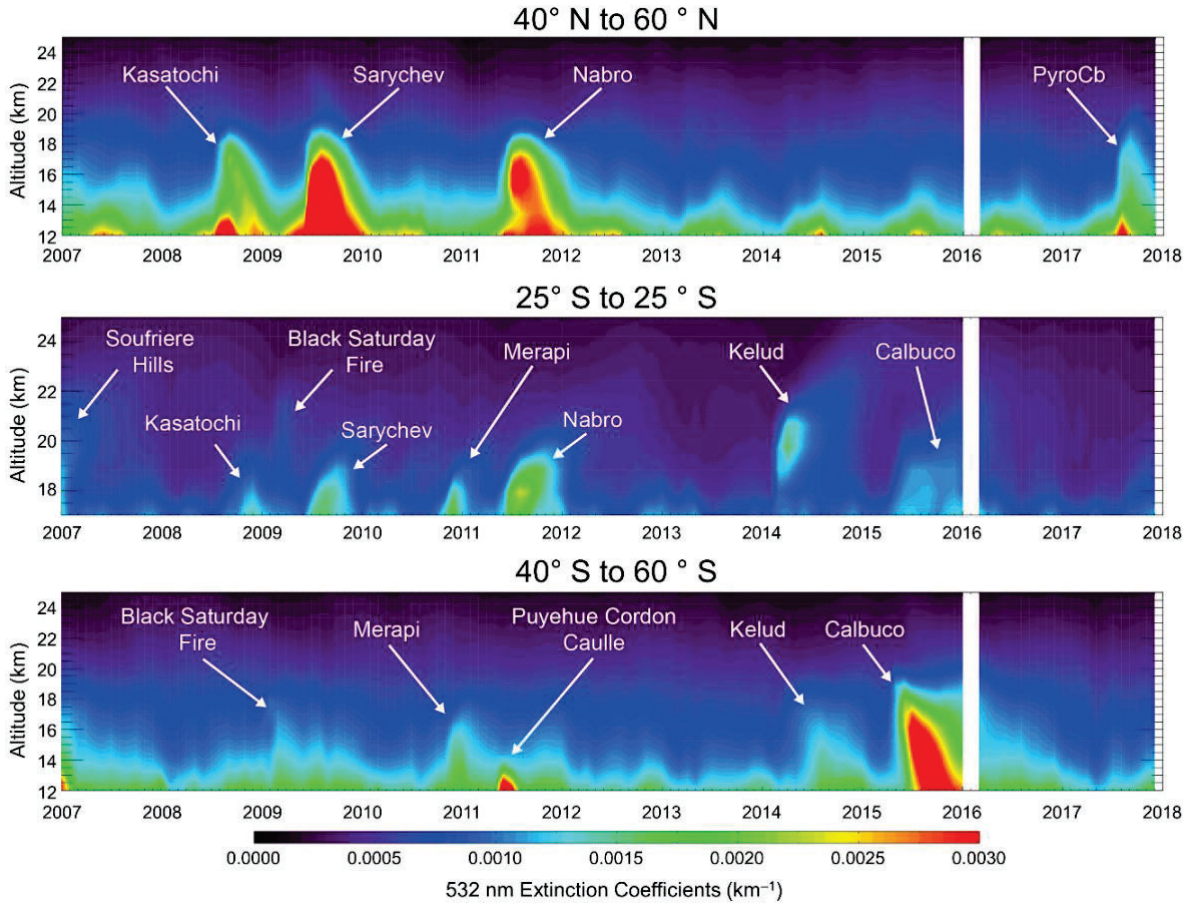

Figure A-9: Time-height cross sections of the retrieved extinction coefficients in the "all aerosol" mode of the CALIOP L3 stratospheric aerosol product from January 2007 through December 2017 for a) the middle to high northern latitudes, b) the tropics and c) the middle to high southern latitudes. The white areas indicate missing data (adapted from Kar et al., 2019; Used under CC BY 4.0).

5.1.10. CALIOP Level 3 Cloud Data Products

The CALIPSO project now distributes three L3 cloud products: an ice cloud product, a cloud occurrence product, and a special product created specifically to support the GEWEX Cloud Assessment project. The subsections below provide additional details about each.

CAL_LID_L3_Ice_Cloud Extinction and ice water content distributions

The L3 ice cloud product reports histograms of ice cloud extinction coefficients and ice water content on a global 3-D grid with cell dimensions extending horizontally over 2° of latitude and 2.5° of longitude and 120 m vertically. The statistics are harvested from the L2 cloud profile product, with quality filters applied to select high cloud phase confidence, reliable extinction coefficients, and only clouds composed of randomly orientated ice crystals (i.e., clouds containing horizontally oriented ice crystals are excluded). The use of histograms rather than averages allows users to isolate specific ranges when comparing parameters derived from instruments having different sensitivities. The product is augmented with ancillary data that includes monthly mean pressure, temperature, and relative humidity profiles for each grid cell, along with tropopause height, surface altitudes and surface type (i.e., land vs. water). Figure A-10 provides examples of the information contained in the L3 ice cloud product. The left panel shows zonally averaged ice cloud extinction coefficients for all data acquired during July 2008, while the right panel shows histograms of extinction coefficients at three altitude regions in the tropics for the same time period.

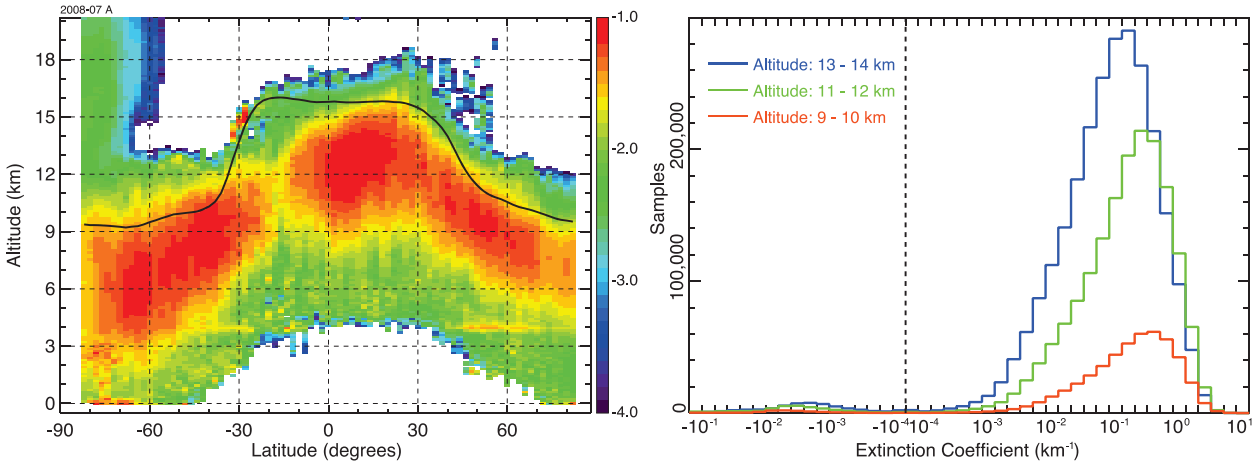

Figure A-10: Left panel: zonally averaged ice cloud extinction coefficients (km^{-1}) derived from 532 nm attenuated backscatter observations acquired during July 2008. The black line indicates the mean tropopause height. Right panel: histograms of ice cloud extinction coefficients at three altitude regions in the tropics (23.5° S to 23.5° N) (Source credit: NASA).

CAL_LID_L3_Cloud_Occurrence profiles

The CALIOP level 3 cloud occurrence product reports counts of clouds partitioned by their thermal phase and opacity on a global 3-D grid with cell dimensions extending horizontally over 2° of latitude and 2.5° of longitude and 60 m vertically. Ice clouds are further binned by their layer optical depths. The counts in each grid cell are accumulated using all clouds detected at all averaging resolutions reported in the L2 merged layer product. QA filters are applied to select only those layers classified as clouds with high confidence. Reporting sample counts rather than averages allows greatly increased flexibility in the aggregation of statistics.

Including ice cloud optical depth histograms provides a user a flexibility to examine cloud occurrence with a desired optical depth threshold when comparing with other instruments with different optical depth sensitivity. Figure A-11 illustrates an application of the optical depth histograms. The left panel shows the zonal mean occurrence frequency of all clouds detected in nighttime measurements acquired during July 2008. In the right panel, ice clouds with optical depths less than 0.3 are excluded from the aggregated statistics, resulting in marked occurrence frequency decreases at high altitudes, especially in the tropics and in the Antarctic polar stratospheric cloud region.

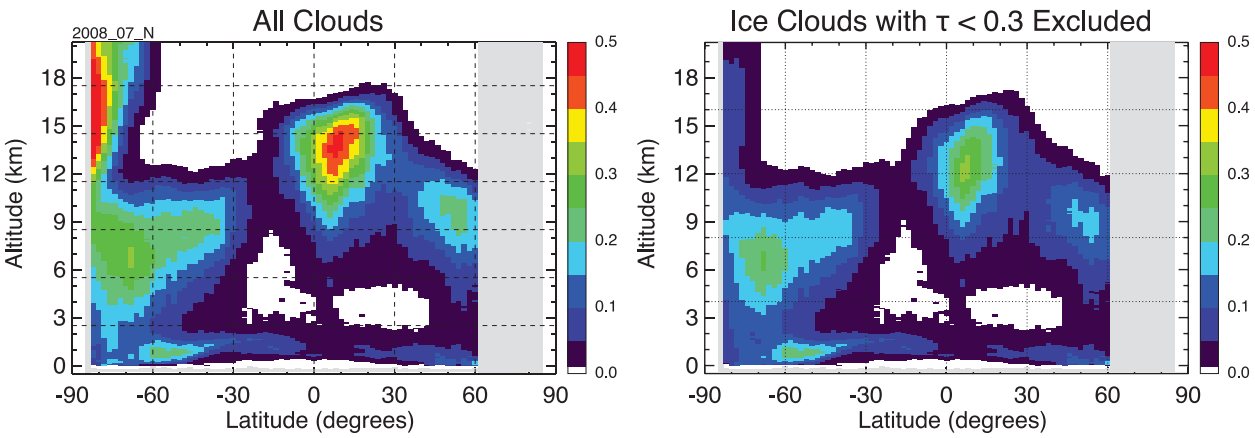

Figure A-11: Left panel: nighttime cloud occurrence frequency during July 2008 for all clouds, irrespective of cloud phase and optical depth. Right panel: same data as in the left panel, but with ice clouds having layer optical depths smaller than 0.3 excluded (Source credit: NASA).

CAL_LID_L3_GEWEX_Cloud

The CALIOP L3 GEWEX product reports cloud occurrence and cloud top at high, middle and low altitude regions according to specifications developed by the GEWEX Cloud Assessment component of the World Climate Research Programme (WCRP) (see https://climserv.ipsl.polytechnique.fr/gewexca/index.html). The contents of this product are identical to the yearly CALIPSO-ST GEWEX product described below; however, the file format and structure are different. The CALIOP L3 GEWEX product aggregates the 70 parameters reported separately on a yearly basis in the GEWEX netCDF files into monthly HDF4 files that contain all 70 quantities. An example of the information contained in the CALIOP L3 GEWEX product is given in Figure A-12, which shows zonal high cloud amount from 2006 through 2016.

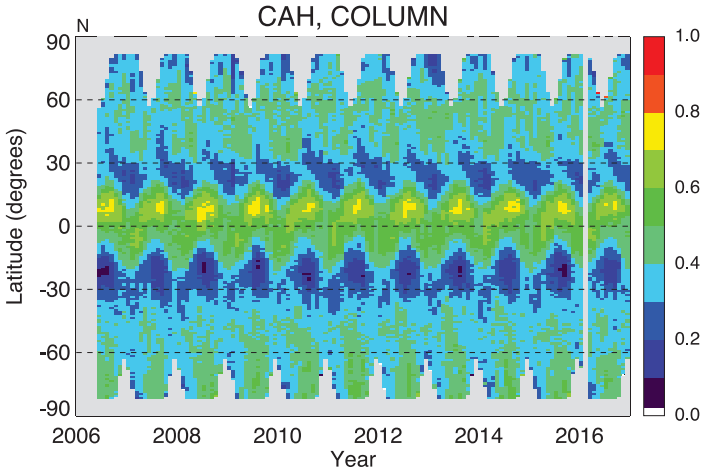

Figure A-12: Nighttime zonal high cloud amount from 2006 to 2016 illustrating the seasonal shift of intertropical convergence zone in the tropics. The GEWEX cloud assessment defines high clouds as those with cloud top pressures less than 440 mb (Source credit: NASA).

5.1.11. CALIOP Ancillary Data Products

Lidar browse images (web-based only)

Upon completion of each day's L1 and L2 processing, the CALIPSO automated processing system updates the CALIPSO public web site (https://www-calipso.larc.nasa.gov/products/lidar/browse_images/production/) with a complete set of height vs. time browse images of the L1 data. Parameters plotted include the attenuated backscatter coefficients at 1064 nm and 532 nm (e.g., as in Figure A-13a), 532 nm volume depolarization ratios, the attenuated total backscatter color ratio (1064/532), and several different vertical feature mask images (e.g., as in Figure A-13b) showing layer detection and classification results for each orbit segment. For the CALIOP's final data release, several key observables can be visualized with color maps specifically designed to improve the clarity of the data content in these images for individuals with Color Vision Deficiencies (CVD). Also included are the corresponding images for the IIR (brightness temperatures and inter-channel brightness temperature differences) and WFC (daytime only).

CALIPSO/CloudSat combined browse images (web-based only)

The CALIPSO web site displays combined CALIPSO+CloudSat browse images in which cloud mask and radar reflectivity parameters obtained from the CloudSat 2B-GEOPROF product are superimposed on the coincident CALIPSO 532 nm attenuated backscatter images. Panels (c) and (d) in Figure A-13 show examples from August 18th, 2008. The web versions of these images are dynamically displayed, so that as a user drags a mouse over an image, the CloudSat data will appear/disappear. From June 2006 to April 2011 there is ~92% agreement of data availability between CALIPSO and CloudSat. After November 2011, a battery anomaly cause CloudSat to change to Daylight Only OPerations (DOOP), so the combined images after this time are reported only during daylight.

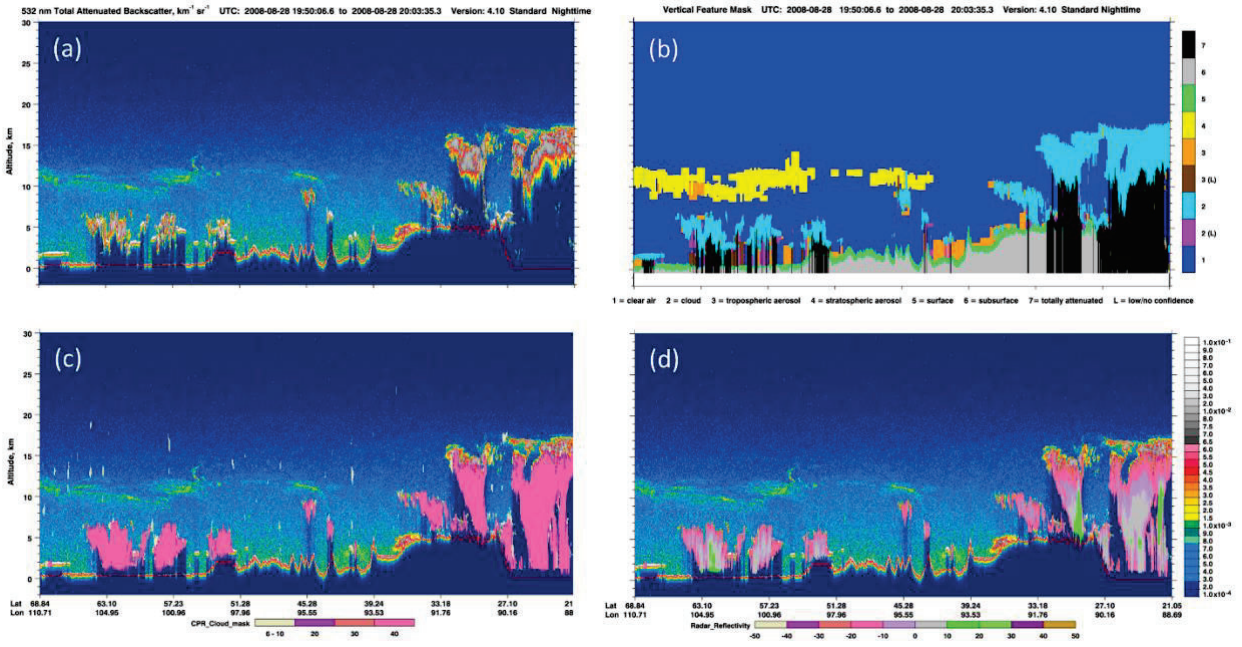

Figure A-13: (a) 532 nm total attenuated backscatter, (b) vertical feature mask, (c) 532 nm total attenuated backscatter with CloudSat cloud mask, and (d) with CloudSat radar reflectivity for a CALIPSO orbital segment from August 18th, 2008 between 19:50:06 to 20:03:35 UTC (Source credit: NASA).

5.1.12. IIR Level 2 Data Products

The following paragraphs describe the primary data products distributed as part of the IIR L2 data products. The fundamental data products generated in the IIR L2 are a scene classification and cloud (or aerosol) layer properties reported under the CALIOP ground track (IIR Track product) and over the IIR field-of-view (IIR Swath product). L2 IIR products are organized in daytime and night-time portions of the orbit to match CALIOP products definition.

CAL_IIR_L2_Track_Scene classification

The IIR scene classification product is based on 5 km CALIOP L2 cloud and aerosol products. It allows categorizing scenes to be further analyzed, where layers are located above or below 7 km in altitude. For each scene, up to 8 layers are considered. A total of 53 types of scenes are defined.

Three scenes are identified as reference scenes for further analysis. They are either the surface (cloud-free or aerosols only areas over land or sea), or a dense opaque layer, defined as high opaque when above 7 km, and low opaque otherwise.

CAL_IIR_L2_Track_Emissivity and microphysical properties

The IIR track product contains brightness temperatures in each IIR channel under the CALIOP track, upper multi-layer system's effective emissivities in each IIR channel, absorption optical depth at 12.05 μm, effective diameter for both ice only and water only cloud systems, and ice and liquid water paths (e.g., as shown in Figure A-14). New retrievals in cirrus clouds, including ice number concentration, were added in the final V5 release. Uncertainties for the effective emissivities, optical depths, effective diameters, ice and liquid water paths, and all the new cirrus retrievals are also reported. Full retrieval context is provided: vertical structure from CALIOP, upper multi-layer system's radiative temperature and height, equivalent blackbody temperatures, surface emissivities and temperatures, reference brightness temperatures, as well as a set of computation and quality flags. Parameters are reported with 1 km resolution.

CAL_IIR_L2_Swath_Horizontal cloud / aerosol mask

Scene classification over the IIR swath is derived from IIR Track classification and IIR radiances.

CAL_IIR_L2_Swath_Emissivity and microphysical properties

This product contains IIR brightness temperatures over the IIR swath, upper layer(s) effective emissivities in each IIR channel, absorption optical depths at 12.05 μm, ice and water cloud effective diameters, and ice and liquid water paths. Uncertainties are reported for effective emissivities, optical depths, effective diameters, and ice and liquid water paths. WFC reflectance and homogeneity indices are used to provide context for the track-to-swath extension. Several quality flags are also included. All parameters are reported with 1 km × 1 km resolution.

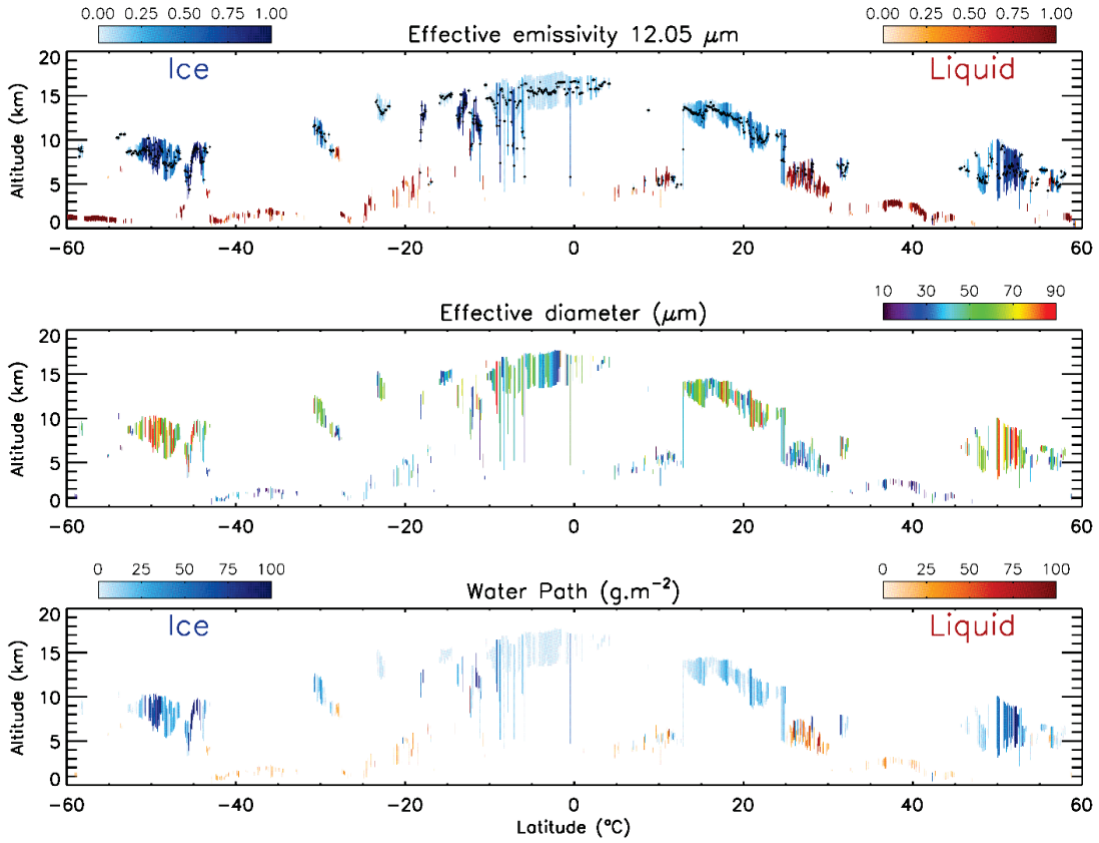

Figure A-14: Example of emissivities at 12.05 μm of ice (blue) and liquid (red) cloud systems (top panel), effective diameters (middle panel) and ice (blue) and liquid (red) water path (bottom panel) as retrieved at mid- and low latitudes by the IIR V5 algorithm for a daytime semi-orbit on 10 January 2008 (10:25:23 ZD). The vertical lines are between the bottom and top altitudes of the multi-layer cloud system, and the black crosses in the top panel indicate its radiative altitude (Source credit: NASA).

5.1.13. IIR Level 3 Data Product

CAL_IIR_L3_GEWEX_Cloud

This product, created specifically to support the GEWEX Cloud Assessment (see https://climserv.ipsl.polytechnique.fr/gewexca/index.html), reports cloud amount, radiative temperature, effective emissivity, optical depth, effective radius and water path for cloud samples for which IIR standard microphysical retrievals are successful. Cloud properties are reported over ocean and land surface for pseudo mono-layer ice clouds, liquid water clouds, and high ice clouds of layer pressure lower than 440 hPa. The IIR L3 GEWEX Cloud product aggregates separate GEWEX-style netCDF yearly files into 12 monthly HDF4 files per year. An example of the information contained in the product is given in Figure A-15, which shows maps of ice clouds mean effective radius and corresponding optical depth for all the months of July from 2006 through 2016.

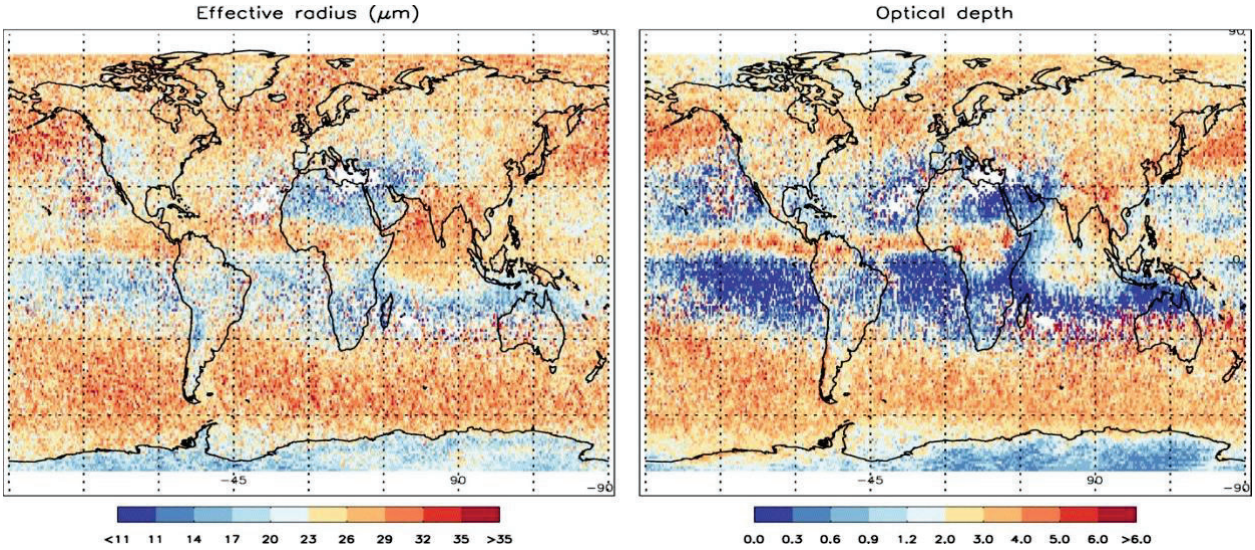

Figure A-15: Mean effective radius (left) and corresponding optical depth (right) for all ice clouds observed during the month of July in the years from 2006 through 2016 (Source credit: NASA).

5.2. Additional CALIPSO Data Products

5.2.1. SODA: Synergized Optical Depths of Aerosols

The SODA product uses simultaneous ocean surface echoes measured by CALIPSO and CloudSat to derive total column aerosol optical depths at both CALIOP wavelengths for cloud-free scenes over oceans (Josset et al., 2008). For reference, collocated MODIS optical depth estimates are also provided, as are AOD estimates computed using CALIOP and AMSR-E combined. Data is distributed in HDF files via AERIS/ICARE at CALIOP single shot resolution (333 m horizontal) and for 5 km horizontal averages. Monthly averages of the 5 km product are also available at 2.5° latitude by 2.5° longitude resolution. The most recent version of SODA (V2) is based on the CALIOP V4.2 and CloudSat R5 data releases. Figure A-16 compares the optical depths retrieved using SODA to coincident optical depths reported by MODIS.

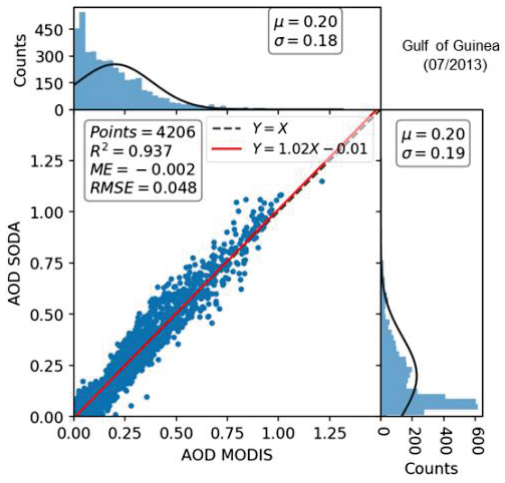

Figure A-16: Daytime SODA AOD as a function of MODIS AOD over the Gulf of Guinea for July and August 2013. Histograms on the top and right of the figure display, respectively, the statistical distributions of the MODIS and SODA values (Source credit: NASA).

5.2.2. DARDAR: raDAR+liDAR

The DARDAR project combines CloudSat radar measurements with CALIPSO lidar measurements to derive cloud properties using multi-sensor data fusion techniques. Among the data products provided by the DARDAR project are (a) DARDAR-MASK, which integrates retrievals from CALIOP, the IIR, CloudSat, and MODIS to generate a family of enhanced scene classification products; and (b) DARDAR-CLOUD, which uses the variational algorithm described in Delanoë and Hogan (2010) to retrieve profiles of cloud extinction coefficients, ice-water content, and effective radius (see Figure A-17) from combined CALIPSO and CloudSat data. DARDAR data is distributed in HDF files via AERIS/ICARE.

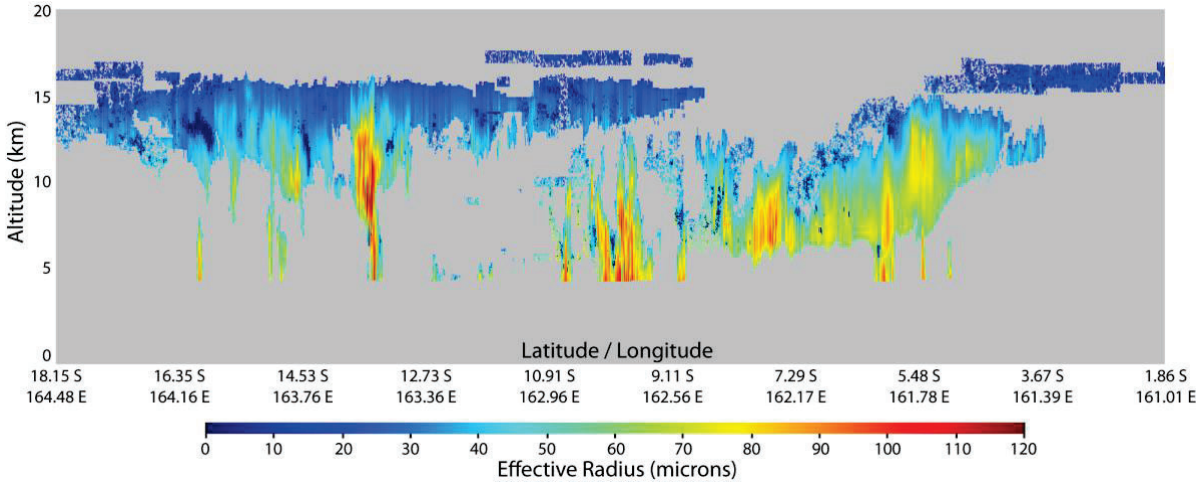

Figure A-17: DARDAR effective radius retrieved from combined CALIPSO+CloudSat measurements (adapted from the image at http://www.icare.univ-lille1.fr/projects/dardar/ documentation_dardar_cloud, Source credit: AERIS/ICARE, Used with permission).

5.2.3. C3M: CALIPSO-CloudSat-CERES-MODIS

CERES project team members, supported by the NASA Energy Water Cycle Study, developed and distribute the integrated CALIPSO, CloudSat, CERES, and MODIS merged product (C3M). This product contains cloud and aerosol properties retrieved from the CALIPSO, CloudSat and MODIS sensors over their ground tracks, collocated with the near nadir view of CERES instrument footprints. The product also contains CERES derived top-of-atmosphere irradiances, vertical profiles of shortwave, longwave, and window region modeled irradiances (Kato et al., 2011). C3M data fusion examples are shown in Figure A-18. The product is distributed by the LaRC ASDC in daily files written in HDF format.

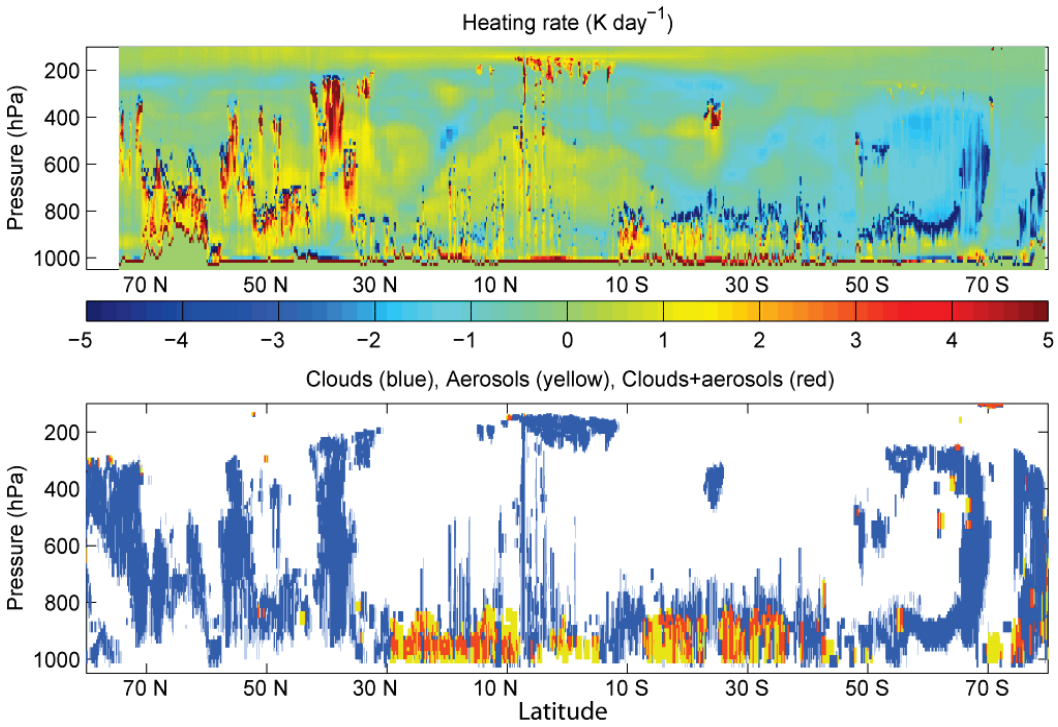

Figure A-18: Upper panel: heating rates for data acquired 1 July 2006 computed from the C3M data product; lower panel: vertical curtain of atmospheric composition derived from CALIPSO and CloudSat retrievals and used to calculate heating rate profile (Source credit: NASA).

5.2.4. CALTRACK

Created and distributed by the AERIS/ICARE data center in Lille, France, the Caltrack family of data products aggregates selected parameters from the CALIPSO L1 (333 m horizontal resolution) and L2 files (5 km horizontal resolution) with collocated parameters measured and/or retrieved by other A-Train sensors. The current generation of Caltrack products collocates CALIPSO measurements with data acquired by CloudSat, POLDER, OMI, and MODIS.

Table A4: CALIPSO Data Products from external (non-CALIPSO) archive sites.

Data Product	Description	Comments
SODA	Synergized Optical Depths of Aerosols derived from simultaneous ocean surface echoes measured by CALIPSO and CloudSat: https://www.icare.univ-lille.fr/soda/	Collaborators: LATMOS/IPSL (France), NASA-LaRC (USA) and the AERIS/ICARE data center (France)
DARDAR	Feature mask and cloud properties derived using a variational algorithm from collocated raDAR (CloudSat) and liDAR (CALIPSO) measurements: https://www.icare.univ-lille.fr/dardar/	A collaboration between the University of Reading Department of Meteorology (UK) and LATMOS/IPSL (France)
Caltrack	CALIPSO measurement subsets collocated with retrieved parameters from other A-Train sensors (e.g., CloudSat, MODIS, POLDER, etc.) distributed at 1/3 km and 5 km horizontal resolutions: https://www.icare.univ-lille.fr/calxtract/	Created and distributed by the AERIS/ICARE data center (France)

Data Product	Description	Comments
C3M	Integrated CERES-CALIPSO-CloudSat-MODIS data set: https://asdc.larc.nasa.gov/news/release-announcement-for-ceres-level-2-cccm-c3m-product-version-d2	Developed by CERES science investigators for use in process studies
CALIPSO-GOCCP	GCM Oriented CALIPSO Cloud Product produced by LMD/ IPSL: CALIOP profiles and cloud climatology at resolutions used in GCMs: http://climserv.ipsl.polytechnique.fr/cfmip-obs/Calipso_goccp.html	Collaborators: LMD/IPSL, IPSL ClimServ data center, CNES, AERIS/ICARE data center (France), and NASA LaRC (USA).
CALIPSO-ST GEWEX	Gridded cloud amount and top height statistics at high, middle and low altitude regions produced according to GEWEX Cloud Assessment specifications and distributed via the GEWEX web pages: http://climserv.ipsl.polytechnique.fr/gewexca/index.html	Collaborators: NASA LaRC, GEWEX.
IIR_CALIPSO-ST GEWEX	Gridded ice and water cloud optical and microphysical properties statistics produced according to GEWEX Cloud Assessment specifications and distributed via the GEWEX web pages: http://climserv.ipsl.polytechnique.fr/gewexca/index.html	Collaborators: NASA LaRC, GEWEX.
2B-CLDCLASS-LIDAR	combines CloudSat CALIOP measurements to determine meteorological cloud type (e.g., stratus, cirrus, etc.): https://www.cloudsat.cira.colostate.edu/data-products/2b-cldclass-lidar	Produced by the CloudSat Data Processing Center at Colorado State University's Cooperative Institute for Research in the Atmosphere
2B-FLXHR-LIDAR	CloudSat, CALIPSO and MODIS data combined to generate estimates of broadband fluxes and heating rates: https://www.cloudsat.cira.colostate.edu/data-products/2b-flxhr-lidar	
GEOPROF-LIDAR	vertical occurrence and classification of hydrometeors derived by combining the CALIPSO VFM and the CloudSat cloud mask: https://www.cloudsat.cira.colostate.edu/data-products/2b-geoprof-lidar	
2C-ICE	Ice water content, effective radius and extinction coefficients derived from the synthesis of CALIPSO and CloudSat data: https://www.cloudsat.cira.colostate.edu/data-products/2c-ice	
CIMSS PBL	PBL heights derived from CALIPSO backscatter profiles: http://cimss.ssec.wisc.edu/calipso/	Produced by the Cooperative Institute for Meteorological Satellite Studies (CIMSS) at the University of Wisconsin

Data Product	Description	Comments
LIVAS	LIdar climatology of Vertical Aerosol Structure for space-based lidar simulation studies: https://dust.aemet.es/research/livas	Collaborators: NOA, TROPOS, ACTRIS, ESA and EARLINET
3S-GEOPROF-COMB	A Global Gridded Dataset for Cloud Vertical Structure from combined CloudSat and CALIPSO observations https://doi.org/10.5281/zenodo.8057790	Created by researchers from the University of Colorado Boulder and Colorado State University
Combined browse images	Combined CALIOP/IIR/WFC images: https://www.icare.univ-lille.fr/asd-content/calipso/	AERIS/ICARE data center (France)

5.2.5. 2B-FLXHR-LIDAR

The 2B-FLXHR-LIDAR product combines CloudSat radar profiles with CALIPSO lidar backscatter profiles, MODIS radiances, and ECMWF temperature and humidity profiles to calculate altitude-dependent estimates of the upwelling and downwelling longwave and shortwave fluxes. The associated heating rates are subsequently derived from these flux estimates (Henderson, 2011; Henderson et al., 2013). The 2B-FLXHR-LIDAR data product is distributed in HDF format by the CloudSat Data Processing Center at Colorado State University.

5.2.6. GEOPROF-LIDAR

GEOPROF-LIDAR is a straightforward fusion of the CloudSat cloud mask and the CALIPSO vertical feature mask accomplished using the techniques as described in Mace et al. (2009a). An illustration of the GEOPROF-LIDAR output, including both CloudSat and CALIOP source data is provided in Figure A-19. GEOPROF-LIDAR files are distributed in HDF format by the CloudSat Data Processing Center at Colorado State University.

5.2.7. 2C-ICE

Using the optimal estimation algorithm described in Deng et al. (2010), the 2C-ICE product uses CloudSat radar reflectivity profiles and CALIPSO 532 nm total attenuated backscatter profiles to generate estimates of cloud extinction, ice water content and effective radius for ice clouds identified in the combined CALIPSO-CloudSat data set. The temperature information required for the analysis is obtained from ECMWF meteorological data. The 2C-ICE data product is distributed in HDF format by the CloudSat Data Processing Center at Colorado State University.

5.2.8. CALIPSO-GOCCP: GCM Oriented CALIPSO Cloud Product

CALIPSO-GOCCP uses the CALIOP L1 products to build a cloud climatology adapted to evaluating cloudiness predictions by GCMs (Chepfer et al., 2010, 2013). The product includes vertical profiles of scattering ratio, color ratio and depolarization ratio at the vertical resolution used in current GCMs. A specific cloud detection algorithm is used to provide vertical distributions and maps of cloud fractions (e.g., Chepfer et al., 2018). The product is written in netCDF format and is processed and available at the ClimServ data center and is also available via AERIS/ICARE.

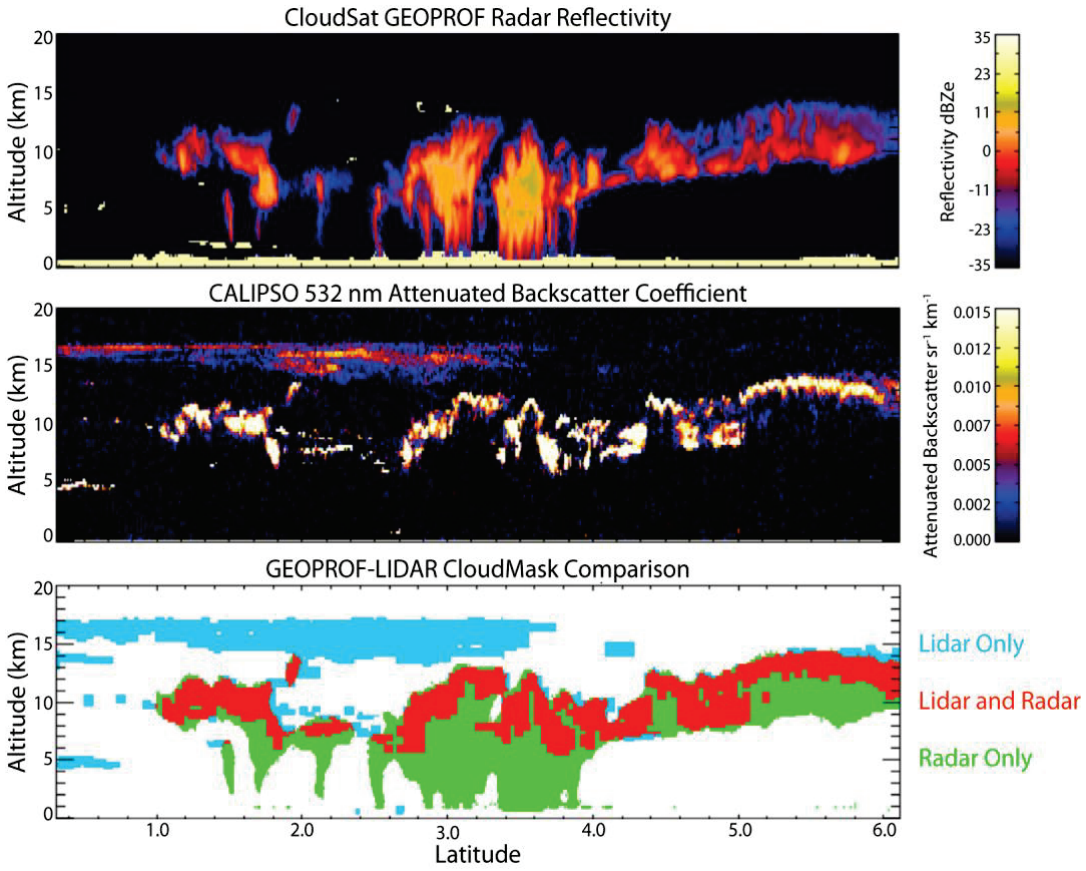

Figure A-19: Upper panel shows CloudSat radar reflectivity; middle panel shows CALIOP 532 nm attenuated backscatter coefficients; lower panel show the corresponding GEOPROF-LIDAR image, creating by combining the CloudSat cloud mask with the CALIOP VFM; data acquired 08 January 2007 between 03:26:25 and 03:28:01 UTC (Source credit: NASA).

5.2.9. CIMSS SAAL Heights

The Cooperative Institute for Meteorological Satellite Studies (CIMSS) at the University of Wisconsin uses an iterated Haar wavelet technique to produce a Surface-Attached Aerosol Layer (SAAL) data product that provides a proxy for PBL heights. These data are distributed in HDF format (http://cimss.ssec.wisc.edu/calipso/) and are available for daytime granules. The CIMSS SAAL retrieval is fully automated and specifically designed to accommodate CALIOP's low SNR daytime measurements. Seasonal averages of SAAL heights for the 2006-2012 time period are shown in Figure A-20. The CIMSS SAAL heights are validated through comparison with TAMDAR observations and HSRL observations from aircraft platforms.

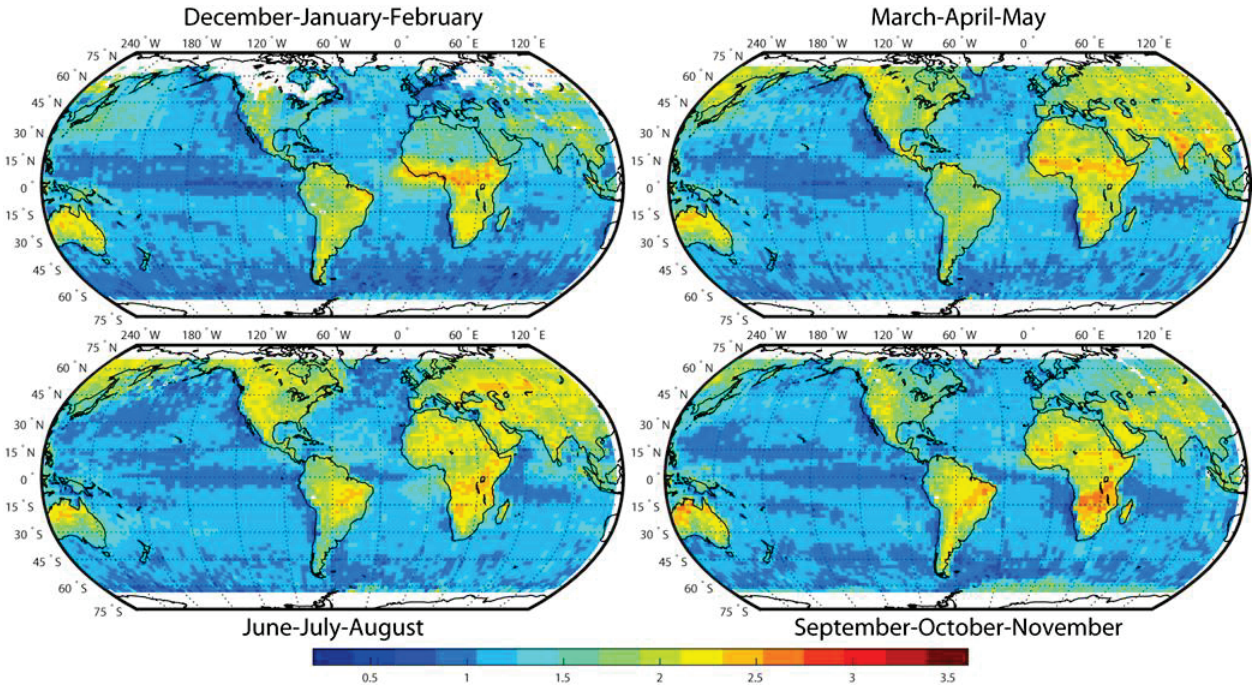

Figure A-20: Seasonal averages of SAAL heights retrieved from daytime CALIOP measurements from 2006 through 2012; colors represent SAAL heights in kilometers above mean sea level (Source credit: NASA).

5.2.10. LIVAS

LIVAS is a multi-wavelength database of aerosol and cloud optical properties developed jointly by the National Observatory of Athens (NOA, Greece), the Leibniz Institute for Tropospheric Research (TROPOS, Germany), the Italian National Research Council and the ACTRIS and EARLINET observing networks, under a grant from ESA. LIVAS uses conversion coefficients from an extensive database of ground-based measurements to derive extinction coefficient profiles at 355 nm, 1.57 μm, and 2.05 μm from the 532 nm and 1064 nm extinction profiles reported in the CALIOP profile products. As an example, Figure A-21 shows a LIVAS image of 355 nm extinction coefficients derived from CALIPSO measurements of dust and cirrus acquired 30 January 2008. The LIVAS data products are distributed in netCDF4 format.

5.2.11. 3S-GEOPROF-COMB

3S-GEOPROF-COMB, developed by researchers from the University of Colorado Boulder and Colorado State University, is a global gridded dataset that describes cloud vertical structure obtained by combining the active remote sensing measurements from the CloudSat radar and the CALIPSO lidar. The vertical resolution of the 3S-GEOPROF-COMB data set is 240 m. Figure A-22 shows a 3S-GEOPROF-COMB example for a complex cloud scene measured 2010-09-01 over the southern oceans and Antarctica.

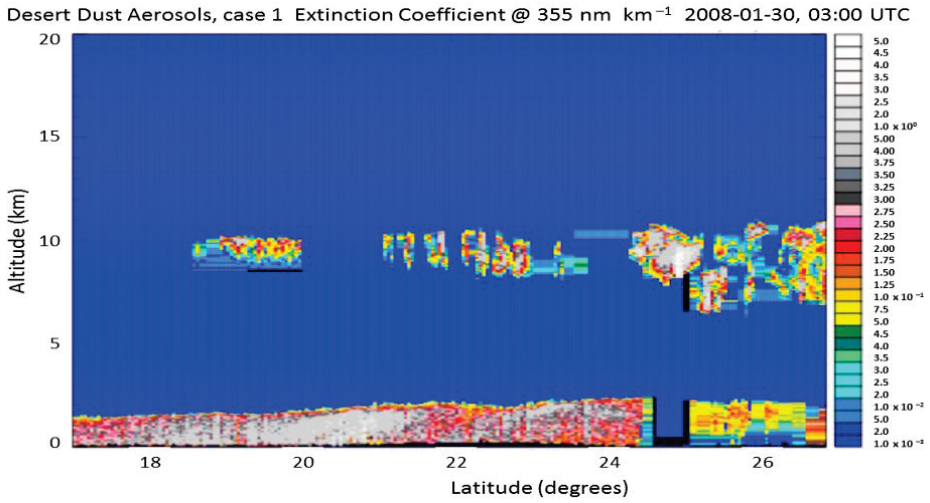

Figure A-21: LIVAS image of 355 nm extinction coefficients derived from CALIPSO measurements of dust and cirrus acquired 30 January 2008 (Source Credit: V. Amaridis, Used with permission).

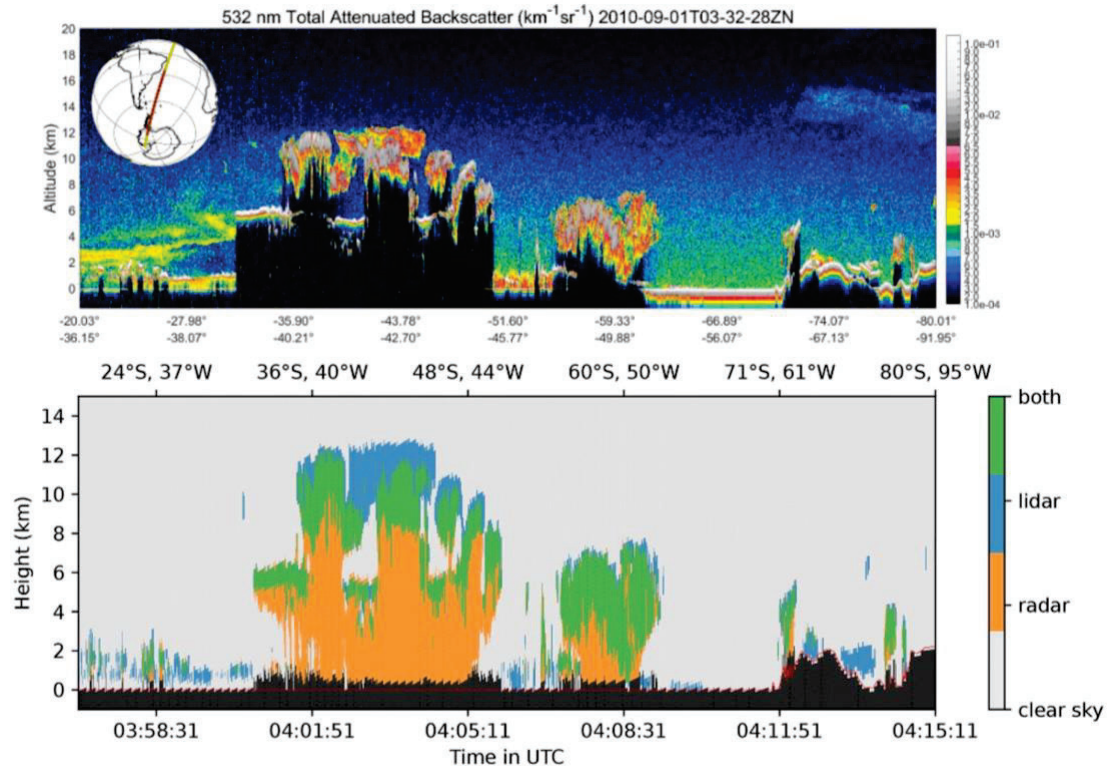

Figure A-22: Upper panel shows CALIOP 532 nm attenuated backscatter coefficients measured September 1, 2010. Lower panel shows a quick-look image "collocated radar and lidar cloud masks, indicating regions detected by lidar only (blue), radar only (orange), or lidar and radar (green)". Top image Source credit: NASA. Lower image and description from Bertrand et al., 2024 (Used under CC BY 4.0).

5.2.12. Combined Lidar/IIR/WFC Browse Images (web-based only)

Upon reception of CALIPSO L1 data, AERIS/ICARE in France updates the CALIPSO public web site (https://www.icare.univ-lille.fr/asd-content/calipso/) with a series of height vs. time browse images of L1 and L2 data. Parameters plotted include the CALIOP total attenuated backscatter

coefficient at 532 nm, IIR brightness temperatures at 8.65 μm, 10.6 μm and 12.05 μm, IIR brightness temperature differences 8.65-12.05 μm and 10.6-12.05 μm and WFC reflectance (daytime only).

6. Appendix B: Acronyms

Table of Acronyms

Acronym	Definition
2B-FLXHR-LIDAR	CloudSat Level 2B Fluxes and Heating Rates with Lidar
2D	two-Dimensional/three-Dimensional
3D	Three-Dimensional
AAC	Aerosols Above Clouds
ABI	Advanced Baseline Imager
ABM	Automated Boresight Mechanism
ACCESS	Advancing Collaborative Connections for Earth System Science
ACEPOL	Aerosol Characterization from Polarimeter and LIDAR
ACP	Atmospheric Chemistry and Physics
ACTRIS	The Aerosol, Clouds, and Trace gases Research InfraStructure
AERIS	A collective of data centers for atmospheric science
AERIS/ICARE	ICARE is a data center within AERIS
AEROCLO-SA	AErosols, RadiatiOn and CLOuds in Southern Africa
AERONET	AErosol RObotic NETwork
AHI	Advanced Himawari Imager
AIRS	Atmospheric Infrared Sounder
AMSR	Advanced Microwave Scanning Radiometer
AMSR-E	Advanced Microwave Scanning Radiometer for the Earth Observing System
AMV	Atmospheric Motion Vector
AOCS	Attitude and Orbit Control System
AOD	Aerosol Optical Depth
APD	Avalanche Photodiode
AR5	5th Assessment Report
ASDC	Atmospheric Science Data Center
ASI	Agenzia Spaziale Italiana
ATBD	Algorithm Theoretical Basis Document
ATLID	Atmospheric LIDAR
AVHRR	Advanced Very High Resolution Radiometer
BAE	British Aerospace
BATC	Ball Aerospace and Technologies Corporation

Acronym	Definition
b_{bp}	subsurface particulate backscattering coefficients
BEU	Battery Electronic Unit
BOL	Begin of Life
BSC-DREAM8b	regional atmospheric model developed by the Barcelona Supercomputing Center (BSC) for simulating and forecasting mineral dust aerosols
C3M	CERES, CALIPSO, CloudSat, and MODIS observations
C5	MODIS data Collection 5
C6	MODIS data Collection 6
CAD	Cloud-Aerosol Discrimination
CAESAR	Conjunction Analysis and Evaluation Service, Alerts and Recommendations
CALIOP	Cloud-Aerosol LIdar with Orthogonal Polarization
CALIPSO	Cloud-Aerosol Lidar and Infrared Pathfinder Satellite Observation
CAMP2Ex	Cloud, Aerosol and Monsoon Processes Philippines Experiment
CARA	Conjunction Assessment Risk Analysis
CATS	Cloud-Aerosol Transport System
CC	Creative Commons (https://creativecommons.org/licenses/by/4.0)
C-C	CALIPSO-CloudSat
CCD	Charge-Coupled Device
CCS	Constellation Coordination System
CCSTM	CALIPSO-CloudSat Science Team
CC-VEX	The CALIPSO-CloudSat Validation Experiment
CERES	Clouds and the Earth's Radiant Energy System
CFMIP	Cloud Feedback Model Intercomparison Project
CIMSS	Cooperative Institute for Meteorological Satellite Studies
CloudSat	Satellite carrying the Cloud Profiling Radar (CPR)
CM2.1	Global Climate Model Version 2.1
CM3	Global Climate Model Version 3
CMAQ	Community Multi-scale Air Quality
CMIP	Coupled Model Intercomparison Project
CNES	Centre National d'Etudes Spatiales
CNES-led	Centre National d'Etudes Spatiales leadership
CoRoT	Convection, Rotation and planetary Transits
CPL	Cloud Physics Lidar

Acronym	Definition
CPR	Cloud Profiling Radar
CRE	Cloud Radiative Effects
CSS	Coarse Sun Sensors
CTH	Cloud-Top Height
CVD	Color Vision Deficiencies
DARDAR	raDAR/liDAR
DARE	Direct Aerosol Radiative Effects
De	Effective Diameter
DEM	Digital Elevation Model
DHS	Data Handling System
DHU	Data Handling Unit
DLR	Deutsches zentrum für Luft und Raumfahrt
DOOP	Daylight Only OPerations
DRE	Direct Radiative Effect
EARLINET	European Aerosol Research LIdar NETwork
EarthCARE	Earth Clouds Aerosols and Radiation Explorer
ECMWF	European Center for Medium-range Weather Forecasting
EDAC	Error Detection and Correction
ENSO	El Nino Southern Oscillation
EOS	Earth Observing System
EOSDIS	Earth Observing System Data and Information System
EPA	Environmental Protection Agency
EPS	Electronic Power System
ESA	European Space Agency
ESD	Earth Science Division
ESSP	Earth System Science Pathfinder
EUNADICS-AV	EUropean Natural Airborne Disaster Information and Coordination System for AViation
FDIR	Fault Detection Isolation and Recovery
FOV	Field Of View
FREESIM	Radiometric Engineering Model
GCM	General Circulation Models
GCOM-W	Global Change Observation Mission-Water

Acronym	Definition
GEO-KOMPSAT-2A	Geostationary Korea Multipurpose Satellite
GEOS	Goddard Earth Observing System
GFDL	Geophysical Fluid Dynamics Laboratory
GISS	Goddard Institute for Space Studies
GMAO	Global Modeling and Assimilation Office
GNSS	Global Navigation Satellite System
GOCCP	GCM-Oriented Cloud-Aerosol Lidar and Infrared Pathfinder Satellite Observation
GOES	Geostationary Operational Environmental Satellite
GPS	Global Positioning System
GSFC	Goddard Space Flight Center
GYR	Gyrometers
H&S	Health and Status
HDF	Hierarchical Data Format
HQ	HeadQuarters
HSRL	High Spectral Resolution Lidar
HYSPLIT	Hybrid Single-Particle Lagrangian Integrated Trajectory
IAB	Integrated Attenuated Backscatter
IAGOS-CARIBIC	In-service Aircraft for a Global Observing System Civil Aircraft for the Regular Investigation of the Atmosphere Based on an Instrument Container
IASI	Infrared Atmospheric Sounding Interferometer
ICARE	Cloud-Aerosol-Water-Radiation Interactions
ICESat	Ice, Cloud, and land Elevation Satellite
ICESat-2	Ice, Cloud, and Land Elevation Satellite-2
IFOV	Instantaneous Field Of View
IFS	Integrated Forecast System
IGBP	International Geosphere-Biosphere Program
IIR	Infrared Imaging Radiometer
IPCC	Intergovernmental Panel on Climate Change
IPSL	Institute Pierre-Simon Laplace
IR	Infrared
ISCCP	International Satellite Cloud Climatology Project
ISS	International Space Station
ITAR	International Traffic in Arms Regulations

Acronym	Definition
IWC	Ice Water Content
JPSS-1	Joint Polar Satellite System-1
JSG	Joint Steering Group
L0	Level 0
L1	Level 1
L1.5	Level 1.5
L2	Level 2
L3	Level 3
LaRC	Langley Research Center
LATMOS	Laboratoire ATMosphères et Observations Spatiales
LEO	Low Earth Orbit
LidarSim	high-fidelity lidar instrument simulator developed at LaRC
LIRAD	LIdar+RADiometer
LITE	Lidar In-space Technology Experiment
LIVAS	LIdar climatology of Vertical Aerosol Structure
LMD	Laboratoire de Météorologie Dynamique
LOS	Loi sur les Opérations Spatiales
LSWG	Lidar Science Working Group
LUT	Look-Up Table
LVPS	Low Voltage Power Supply
LW	Longwave
LWCRE	LW Cloud Radiative Effects
MACC-II	Monitoring Atmospheric Composition and Climate, phase 2
MAG	Magnetometer
MAM	March, April and May
MDR	Mission Design Review
MEASURES	Making Earth System Data Records for Use in Research Environments
MERLIN	MEthane Remote sensing LIdar missioN
MISR	Multi-angle Imaging SpectroRadiometer
MJO	Madden-Julian Oscillation
MLI	Multi-Layer Insulation
MLT	Mean Local Time
MOCC	Mission Operations Control Center

Acronym	Definition
MODIS	Moderate Resolution Imaging Spectroradiometer
MOSFET	Metal-Oxide-Semiconductor Field-Effect Transistor
MOWG	Mission Operations Working Group
MTB	Magneto-Torques Bars
NAAMES	North Atlantic Aerosols and Marine Ecosystems Study
NASA	National Aeronautics and Space Administration
NAT	Nitric Acid Trihydrate
NCEP	National Center for Environmental Prediction
Nd:YAG	Neodymium-doped Yttrium Aluminum Garnet
NETD	Noise-Equivalent Temperature Difference
Ni	Ice Crystal Number Concentration
NICAM-SPRINTARS	Nonhydrostatic Icosahedral Atmospheric Model - Spectral Radiation-Transport Model for Aerosol Species
NOA	National Observatory of Athens
NOAA	National Oceanic and Atmospheric Administration
NRL	Naval Research Laboratory
NWP	Numerical Weather Prediction
NWS	National Weather Service
OCO	Orbiting Carbon Observatory
OD	Optical Depth
ODCOD	Ocean Derived Column Optical Depths
OMI	Ozone Monitoring Instrument
ORACLES	ObseRvations of Aerosols above CLouds and their intEractionS
PARASOL	Polarization & Anisotropy of Reflectances for Atmospheric Sciences coupled with Observations from a Lidar
PBL	Planetary Boundary Layer
PGR	Polarization Gain Ratio
PI	Principal Investigator
PLC	Payload Controller
PMA	Processor Module A
PMB	Processor Module B
PMT	Photomultiplier Tube
PROTEUS	Plateforme Reconfigurable pour l'Observation, les Telecommunications et les Usages Scientifiques

Acronym	Definition
PSC	Polar Stratospheric Cloud
PSCi	Polar Stratospheric Cloud initiative
QA	Quality Assurance
RAMS-CMAQ	Regional Atmospheric Modeling System - Community Multiscale Air Quality
REDEM	REvue D'Extension de Mission
REED	Small electromagnetic switching device
REThinC	Radiative Effects of Thin Cirrus Clouds
REVEX	REVue d'EXploitation
RMM	Risk Mitigation Maneuver
RMS	Root Mean Square
RSIG	Remote Sensing Information Gateway
RW	Reaction Wheel
Rx	Spacecraft Receiver
SAA	South Atlantic Anomaly
SAAL	Surface-Attached Aerosol Layer
SADM	Solar Array Drive Mechanisms
SAGE	Stratospheric Aerosol and Gas Experiment
SatCORPS	Satellite Cloud and Radiation Property Retrieval System
SBC	Single-Board Computer
SDRAM	Synchronous Dynamic Random Access Memory
SEU	Single Event Upset
SEVIRI	Spinning Enhanced Visible and Infrared Imager
SHG	Second Harmonic Generator
SLSTR	Sea and Land Surface Temperature Radiometer
SMD	Science Mission Directorate
SMOS	Soil Moisture and Ocean Salinity
SNR	Signal-to-Noise Ratio
SOCC	Science Operations Control Center
SODA	Synergized Optical Depth of Aerosols
SON	September, October and November
SOW	Statement Of Work
SSC	Swedish Space Corporation
SST	Sea Surface Temperature

Acronym	Definition
STR	Star Tracker
STS	Supercooled Ternary Solution
SW	Shortwave
TAMDAR	Tropospheric Airborne Meteorological Data Reporting
TAS	Thales Alenia Space
THR	Thruster
TM/TC	TeleMetry/TeleCommand
TOA	Top-Of-Atmosphere
TOMS	Total Ozone Mapping Spectrometer
TROPOMI	TROPOspheric Monitoring Instrument
TROPOS	Leibniz Institute for Tropospheric Research
TTCS	Telemetry, Tracking, and Command System
Tx	Spacecraft Transmitter
USA	United States of America
V1	Version 1
V2	Version 2
V3	Version 3
V4	Version 4
V5	Version 5
VAAC	Volcanic Ash Advisory Center
VFM	Vertical Feature Mask
VIIRS	Visible Infrared Imaging Radiometer Suite
WCRP	World Climate Research Programme
WFC	Wide Field-of-view Camera
WMO	World Meteorological Organization
WRF-Chem	Weather Research and Forecasting (WRF) model coupled with Chemistry

7. Appendix C: References

Abel, S. J., P. A. Barrett, P. Zuidema, J. Zhang, M. Christensen, F. Peers, J. W. Taylor, I. Crawford, K. N. Bower, and M. Flynn, 2020: "Open cells can decrease the mixing of free-tropospheric biomass burning aerosol into the south-east Atlantic boundary layer", *Atmos. Chem. Phys.*, **20**, 4059–4084, https://doi.org/10.5194/acp-20-4059-2020.

Abshire, J. B., X. Sun, H. Riris, J. M. Sirota, J. F. McGarry, S. Palm, D. Yi, and P. Liiva, 2005: "Geoscience Laser Altimeter System (GLAS) on the ICESat Mission: On-orbit measurement performance", *Geophys. Res. Lett.*, **32**, L21S02, https://doi.org/10.1029/2005GL024028.

Ackerman, S. A., R. E. Holz, R. Frey, E. W. Eloranta, B. Maddux, and M. McGill, 2008: "Cloud Detection with MODIS: Part II Validation", *J. Atmos. Oceanic Technol.*, **25**, 1073-1086, https://doi.org/10.1175/2007JTECHA1053.1.

Ahlgrimm, M., R. Forbes, R. J. Hogan, and I. Sandu, 2018: "Understanding global model systematic shortwave radiation errors in subtropical marine boundary layer cloud regimes", *J. Adv. Model. Earth Syst.*, **10**, 2042–2060, https://doi.org/10.1029/2018MS001346.

Allan R. P. and C. J. Merchant, 2025: "Reconciling Earth's growing energy imbalance with ocean warming", *Environ. Res. Lett.*, **20** 044002, https://doi.org/10.1088/1748-9326/adb448.

Allen, R. J., A. Amiri-Farahani, J.-F. Lamarque, C. Smith, D. Shindell, T. Hassan, and C. E. Chung, 2019: "Observationally constrained aerosol–cloud semi-direct effects", *npj Clim. Atmos. Sci.*, **2**, 16, https://doi.org/10.1038/s41612-019-0073-9.

Amiridis, V., E. Marinou, A. Tsekeri, U. Wandinger, A. Schwarz, E. Giannakaki, R. Mamouri, P. Kokkalis, I. Binietoglou, S. Solomos, T. Herekakis, S. Kazadzis, E. Gerasopoulos, D. Balis, A. Papayannis, C. Kontoes, K. Kourtidis, N. Papagiannopoulos, L. Mona, G. Pappalardo, O. Le Rille, and A. Ansmann, 2015: "LIVAS: a 3-D multi-wavelength aerosol/cloud climatology based on CALIPSO and EARLINET", *Atmos. Chem. Phys.*, **15**, 7127–7153, https://doi.org/10.5194/acp-15-7127-2015

Amiri-Farahani, A., R. J. Allen, D. Neubauer, and U. Lohmann, 2017: "Impact of Saharan dust on North Atlantic marine stratocumulus clouds: importance of the semidirect effect", *Atmos. Chem. Phys.*, **17**, 6305–6322, https://doi.org/10.5194/acp-17-6305-2017.

Ancellet, G., J. Pelon, J. Totems, P. Chazette, A. Bazureau, M. Sicard, T. Di Iorio, F. Dulac, and M. Mallet, 2016: "Long-range transport and mixing of aerosol sources during the 2013 North American biomass burning episode: analysis of multiple lidar observations in the western Mediterranean basin", *Atmos. Chem. Phys.*, **16**, 4725–4742, https://doi.org/10.5194/acp-16-4725-2016.

Arouf, A., H. Chepfer, T. Vaillant de Guélis, M. Chiriaco, M. D. Shupe, R. Guzman, A. Feofilov, P. Raberanto, T. S. L'Ecuyer, S. Kato, and M. R. Gallagher, 2022: "The Surface Longwave Cloud Radiative Effect derived from Space Lidar Observations", *Atmos. Meas. Tech.*, **15**, 3893-3923, https://doi.org/10.5194/amt-15-3893-2022.

Avery, M., D. Winker, A. Heymsfield, M. Vaughan, S. Young, Y. Hu and C. Trepte, 2012: "Cloud Ice Water Content Measured by the CALIOP Space-based Lidar", *Geophys. Res. Lett.*, **39**, L05808, https://doi.org/10.1029/2011GL050545.

Avery, M. A., R. A. Ryan, B. J. Getzewich, M. A. Vaughan, D. M. Winker, Y. Hu, A. Garnier, J. Pelon and C. A. Verhappen, 2020: "CALIOP V4 Cloud Thermodynamic Phase Assignment and the Impact of Near-Nadir Viewing Angles", *Atmos. Meas. Tech.*, **13**, 4539-4563, https://doi.org/10.5194/amt-13-4539-2020.

Bagtasa, G., M. G. Cayetano, C.-S. Yuan, O. Uchino, T. Sakai, T. Izumi, I. Morino, T. Nagai, R. C. Macatangay, and V. A. Velazco, 2019: "Long-range transport of aerosols from East and Southeast Asia to northern Philippines and its direct radiative forcing effect", *Atmos. Environ.*, **218**, 117007, https://doi.org/10.1016/j.atmosenv.2019.117007.

Baker, K. R., M. C. Woody, L. Valin, J. Szykman, E. L. Yates, L. T. Iraci, H. D. Choi, A. J. Soja, S. N. Koplitz, L. Zhou, P. Campuzano-Jost, J. L. Jimenez, and J. W. Hair, 2018: "Photochemical model evaluation of 2013 California wild fire air quality impacts using surface, aircraft, and satellite data", *Sci. Total Environ.*, **637–638**, 1137–1149, https://doi.org/10.1016/j.scitotenv.2018.05.048.

Bali, K., A. K. Mishra and S. Singh, 2017: "Impact of anomalous forest fire on aerosol radiative forcing and snow cover over Himalayan region", *Atmos. Environ.*, **150**, 264–275, https://doi.org/10.1016/j.atmosenv.2016.11.061

Balmes, K. A. and Q. Fu, 2018: "An Investigation of Optically Very Thin Ice Clouds from Ground-Based ARM Raman Lidars", *Atmosphere*, **445**; https://doi.org/10.3390/atmos9110445.

Balmes, K. A., Q. Fu and T. J. Thorsen, 2019: "Differences in Ice Cloud Optical Depth from CALIPSO and Ground-Based Raman Lidar at the ARM SGP and TWP Sites", *J. Geophys. Res. Atmos.*, **124**, 1755-1778, https://doi.org/10.1029/2018JD028321.

Banks, R., H.E. Brindley, C. Flamant, M.J. Garay, N.C. Hsu, O.V. Kalashnikova, L. Klüser, and A.M. Sayer, 2013: "Intercomparison of satellite dust retrieval products over the west African Sahara during the Fennec campaign in June 2011", *Remote Sens. Environ.*, **136**, 99-116, https://doi.org/10.1016/j.rse.2013.05.003.

Barker, H. W., 2008a: "Overlap of Fractional Cloud for Radiation Calculations in GCMs: A Global Analysis using CloudSat and CALIPSO Data", *J. Geophys. Res.*, **113**, D00A01, https://doi.org/10.1029/2007JD009677.

Barker, H. W., 2008b: "Representing Cloud Overlap with an Effective Decorrelation Length: An assessment using CloudSat and CALIPSO Data", *J. Geophys. Res.*, **113**, D24205, https://doi.org/10.1029/2008JD010391.

Barkley, A. E., J. M. Prospero, N. Mahowald, D. S. Hamilton, K. J. Popendorf, A. M. Oehlert, A. Pourmand, A. Gatineau, K. Panechou-Pulcherie, P. Blackwelder, and C. J. Gaston, 2019: "African biomass burning is a substantial source of phosphorus deposition to the Amazon, Tropical Atlantic Ocean, and Southern Ocean", *PNAS*, https://doi.org/10.1073/pnas.1906091116.

Barth, M. C., C. A. Cantrell, W. H. Brune, S. A. Rutledge, J. H. Crawford, H. Huntrieser, L. D. Carey, D. MacGorman, M. Weisman, K. E. Pickering, E. Bruning, B. Anderson, E. Apel, M. Biggerstaff, T. Campos, P. Campuzano-Jost, R. Cohen, J. Crounse, D. A. Day, G. Diskin, F. Flocke, A. Fried, C. Garland, B. Heikes, S. Honomichl, R. Hornbrook, L. G. Huey, J. L. Jimenez, T. Lang, M. Lichtenstern, T. Mikoviny, B. Nault, D. O'Sullivan, L. L. Pan, J. Peischl, I. Pollack, D. Richter, D. Riemer, T. Ryerson, H. Schlager, .J. St. Clair, J. Walega, P. Weibring, A. Weinheimer, P. Wennberg, A. Wisthaler, P. J. Wooldridge, and C. Ziegler, 2015: "The Deep Convective Clouds and Chemistry (DC3) Field Campaign", *Bull. Amer. Meteor. Soc.*, **96**, 1281-1309, https://doi.org/10.1175/BAMS-D-13-00290.1201.

Bauer, S. E., U. Im, K. Mezuman, and C. Y. Gao, 2019: "Desert dust, industrialization and agricultural fires: Health impacts of outdoor air pollution in Africa", *J. Geophys. Res. Atmos.*, **124**, 4104–4120, https://doi.org/10.1029/2018JD029336.

Behrenfeld, M. J., Y. Hu, C. A. Hostetler, G. Dall'Olmo, S. D. Rodier, J. W. Hair and C. R. Trepte, 2013: "Space-based LIDAR measurements of global ocean carbon stocks", *Geophys. Res. Lett.*, **40**, 4355–4360, https://doi.org/10.1002/grl.50816.

Behrenfeld, M. J., Y. Hu, R. T. O'Malley, E. S. Boss, C. A. Hostetler, D. A. Siegel, J. L. Sarmiento, J. Schulien, J. W. Hair, X. Lu, S. Rodier and A. J. Scarino, 2017: "Annual boom–bust cycles of polar phytoplankton biomass revealed by space-based lidar", *Nat. Geosci.*, **10**, 118–122, https://doi.org/10.1038/ngeo2861.

Behrenfeld, M. J., P. Gaube, A. Della Penna, R. T. O'Malley, W. J. Burt, Y. Hu, P. S. Bontempi, D. K. Steinberg, E. S. Boss, D. A. Siegel, C. A. Hostetler, P. D. Tortell and S. C. Doney, 2019a: "Global satellite-observed daily vertical migrations of ocean animals", *Nature*, **576**, 257–261, https://doi.org/10.1038/s41586-019-1796-9.

Behrenfeld, M. J., R. H. Moore, C. A. Hostetler, J. Graff, P. Gaube, L. M. Russell, G. Chen, S. C. Doney, S. Giovannon, H. Liu, C. Proctor, L. M. Bolaños, N. Baetge, C. Davie-Martin, T. K. Westberry, T. S. Bates, T. G. Bell, K. D. Bidle, E. S. Boss, S. D. Brooks, B. Cairns, C. Carlson, K. Halsey, E. L. Harvey, C. Hu, L. Karp-Boss, M. Kleb, S. Menden-Deuer, F. Morison, P. K. Quinn, A. J. Scarino, B. Anderson, J. Chowdhary, E. Crosbie, R. Ferrare, J. W. Hair, Y. Hu, S. Janz, J. Redemann, E. Saltzman, M. Shook, D. A. Siegel, A. Wisthaler, M. Yang Martin, and L. Ziemba, 2019b: "The North Atlantic Aerosol and Marine Ecosystem Study (NAAMES): Science Motive and Mission Overview", *Front. Mar. Sci,* **6**, https://doi.org/10.3389/fmars.2019.00122.

Behrenfeld, M. J., L. Lorenzoni, Y. Hu, K. M. Bisson, C. A. Hostetler, P. Di Girolamo, D. Dionisi, F. Longo and S. Zoffoli, 2023: "Satellite Lidar Measurements as a Critical New Global Ocean Climate Record", *Remote Sens.*, **15**, 5567, https://doi.org/10.3390/rs15235567.

Beig, G., R. Srinivas, N. S. Parkhi, G. R. Carmichael, S. Singh, S. K. Sahu, A. Rathod, and S. Maji, 2019: "Anatomy of the winter 2017 air quality emergency in Delhi", *Sci. Total Environ.*, **681**, 305–311, https://doi.org/10.1016/j.scitotenv.2019.04.347.

Bellouin, N., J. Quaas, E. Gryspeerdt, S. Kinne, P. Stier, D. Watson-Parris, O. Boucher, K. S. Carslaw, M. Christensen, A. L. Daniau, J. L. Dufresne, G. Feingold, S. Fiedler, P. Forster, A. Gettelman, J. M. Haywood, U. Lohmann, F. Malavelle, T. Mauritsen, D. T. McCoy, G. Myhre, J. Mülmenstädt, D. Neubauer, A. Possner, M. Rugenstein, Y. Sato, M. Schulz, S. E. Schwartz, O. Sourdeval, T. Storelvmo, V. Toll, D. Winker, and B. Stevens, 2020: "Bounding global aerosol radiative forcing of climate change", *Rev. Geophys.*, **58**, e2019RG000660, https://doi.org/10.1029/2019RG000660.

Benedetti, A., J. S. Reid, P. Knippertz, J. H. Marsham, F. Di Giuseppe, S. Rémy, S. Basart, O. Boucher, I. M. Brooks, L. Menut, L. Mona, P. Laj, G. Pappalardo, A. Wiedensohler, A. Baklanov, M. Brooks, P. R. Colarco, E. Cuevas, A. da Silva, J. Escribano, J. Flemming, N. Huneeus, O. Jorba, S. Kazadzis, S. Kinne, T. Popp, P. K. Quinn, T. T. Sekiyama, T. Tanaka, and E. Terradellas, 2018: "Status and future of numerical atmospheric aerosol prediction with a focus on data requirements", *Atmos. Chem. Phys.*, **18**, 10615–10643, https://doi.org/10.5194/acp-18-10615-2018.

Bertrand, L., J. E. Kay, J. Haynes, and G. de Boer, 2024: "A Global Gridded Dataset for Cloud Vertical Structure from Combined CloudSat and CALIPSO Observations", *Earth Syst. Sci. Data*, **16**, 1301–1316, https://doi.org/10.5194/essd-16-1301-2024.

Bessagnet, B., L. Menut, A. Colette, F. Couvidat, M. Dan, S. Mailler, L. Létinois, V. Pont, and L. Rouïl, 2017: "An Evaluation of the CHIMERE Chemistry Transport Model to Simulate Dust Outbreaks across the Northern Hemisphere in March 2014", *Atmosphere*, **8**, 251, https://doi.org/10.3390/atmos8120251.

Bian, J., D. Li, Z. Bai, Q. Li, D. Lyu, and X. Zhou, 2020: "Transport of Asian surface pollutants to the global stratosphere from the Tibetan Plateau region during the Asian summer monsoon", *Natl. Sci. Rev.*, **7**, 516-533, https://doi.org/10.1093/nsr/nwaa005.

Bibi, H., K. Alam and S. Bibi, 2016: "In-depth discrimination of aerosol types using multiple clustering techniques over four locations in Indo-Gangetic plains", *Atmos. Res.*, **181**, 106–114, https://doi.org/10.1016/j.atmosres.2016.06.017.

Biondi, R., A. K. Steiner, G. Kirchengast, H. Brenot, and T. Rieckh, 2017: "Supporting the detection and monitoring of volcanic clouds: a promising new application of Global Navigation Satellite System radio occultation", *Adv. Space Res.*, **60**, 2707–2722, https://doi.org/10.1016/j.asr.2017.06.039.

Bisson, K. M., P. J. Werdell, A. P. Chase, S. J. Kramer, B. B. Cael, E. Boss, L. I. W. McKinna and M. J. Behrenfeld, 2023: "Informing ocean color inversion products by seeding with ancillary observations", *Opt. Express*, **31**, 40557-40572, https://doi.org/10.1364/OE.503496.

Blanchard, Y., J. Pelon, E. W. Eloranta, K. P. Moran, J. Delanoë, and G. Sèze, 2014: "A Synergistic Analysis of Cloud Cover and Vertical Distribution from A-Train and Ground-Based Sensors over the High Arctic Station Eureka from 2006 to 2010", *J. Appl. Meteor. Climatol.*, **53**, 2553-2570, https://doi.org/10.1175/JAMC-D-14-0021.1.

Bodas-Salcedo, A., M. J. Webb, S. Bony, H. Chepfer, J.-L. Dufresne, S. A. Klein, Y. Zhang, R. Marchand, J. M. Haynes, R. Pincus, and V. O. John, 2011: "COSP: satellite simulation software for model assessment", *B. Am. Meteorol. Soc.*, **92**, 1023–1043, https://doi.org/10.1175/2011BAMS2856.1.

Bodas-Salcedo, A., P. G. Hill, K. Furtado, K. D. Williams, P. R. Field, J. C. Manners, P. Hyder, and S. Kato, 2016: "Large contribution of supercooled liquid clouds to the solar radiation budget of the Southern Ocean", *J. Climate*, **29**, 4213–4228, https://doi.org/10.1175/JCLI-D-15-0564.1.

Bodas-Salcedo, A., J. P. Mulcahy, T. Andrews, K. D. Williams, M. A. Ringer, P. R. Field, and G. S. Elsaesser, 2019: "Strong dependence of atmospheric feedbacks on mixed-phase microphysics and aerosol-cloud interactions in HadGEM3", *JAMES*, **11**, 1735-1758, https://doi.org/10.1029/2019MS001688.

Bond, T. C., S. J. Doherty, D. W. Fahey, P. M. Forster, T. Berntsen, B. J. DeAngelo, M. G. Flanner, S. Ghan, B. Kärcher, D. Koch, S. Kinne, Y. Kondo, P. K. Quinn, M. C. Sarofim, M. G. Schultz, M. Schulz, C. Venkataraman, H. Zhang, S. Zhang, N. Bellouin, S. K. Guttikunda, P. K. Hopke, M. Z. Jacobson, J. W. Kaiser, Z. Klimont, U. Lohmann, J. P. Schwarz, D. Shindell, T. Storelvmo, S. G. Warren, and C. S. Zender, 2013: "Bounding the role of black carbon in the climate system: A scientific assessment", *J. Geophys. Res.*, **118**, 5380–5552, https://doi.org/10.1002/jgrd.50171.

Bou Karam-Francis, D., C. Flamant, J.-P. Chaboureau, J. Banks, J. Cuesta, H. Brindley, and L. Oolman, 2017: "Dust emission and transport over Iraq associated with the summer Shamal winds", *Aeolian Research*, **24**, 15–31, https://doi.org/10.1016/j.aeolia.2016.11.001.

Burton, S. P., R. A. Ferrare, M. A. Vaughan, A. H. Omar, R. R. Rogers, C. A. Hostetler, and J. W. Hair, 2013: "Aerosol Classification from Airborne HSRL and Comparisons with the CALIPSO

Vertical Feature Mask", *Atmos. Meas. Tech.*, **6**, 1397–1412, https://doi.org/10.5194/amt-6-1397-2013.

Cai, X., D. M. Winker, M. Vaughan, B. Magill, B. J. Getzewich, C. R. Trepte, and P. Lucker, 2018: "Introduction of the CALIOP Level 3 3-dimensional Cloud Occurrence Product," American Geophysical Union Fall Meeting 2018, abstract #A11I-2353, Washington, DC, 10–14 December 2018; see https://agu.confex.com/agu/fm18/mediafile/Handout/Paper345072/2018AGU_poster_xcai_final.pdf.

Cairo, F., J. P. Pommereau, K. S. Law, H. Schlager, A. Garnier, F. Fierli, M. Ern, M. Streibel, S. Arabas, S. Borrmann, J. J. Berthelier, C. Blom, T. Christensen, F. D'Amato, G. Di Donfrancesco, T. Deshler, A. Diedhiou, G. Durry, O. Engelsen, F. Goutail, N. R. P. Harris, E. R. T. Kerstel, S. Khaykin, P. Konopka, A. Kylling, N. Larsen, T. Lebel, X. Liu, A. R. MacKenzie, J. Nielsen, A. Oulanowski, D. J. Parker, J. Pelon, J. Polcher, J. A. Pyle, F. Ravegnani, E. D. Rivière, A. D. Robinson, T. Röckmann, C. Schiller, F. Simões, L. Stefanutti, F. Stroh, L. Some, P. Siegmund, N. Sitnikov, J. P. Vernier, C. M. Volk, C. Voigt, M. von Hobe, S. Viciani, and V. Yushkov, 2010: "An introduction to the SCOUT-AMMA stratospheric aircraft, balloons and sondes campaign in West Africa, August 2006: rationale and roadmap", *Atmos. Chem. Phys.*, **10**, 2237–2256, https://doi.org/10.5194/acp-10-2237-2010.

Campbell, J. R., J. L. Tackett, J. S. Reid, J. Zhang, C. A. Curtis, E. J. Hyer, W. R. Sessions, D. L. Westphal, J. M. Prospero, E. J. Welton, A. H. Omar, M. A. Vaughan, and D. M. Winker, 2012: "Evaluating nighttime CALIOP 0.532 μm aerosol optical depth and extinction coefficient retrievals", *Atmos. Meas. Tech.*, **5**, 2143-2160, https://doi.org/10.5194/amt-5-2143-2012.

Casadevall, 1994: "The 1989-1990 eruption of Redoubt volcano, Alaska: impacts on aircraft operations", *J. Volcanol. Geoth. Res.*, **62**, 301–316, https://doi.org/10.1016/0377-0273(94)90038-8.

Cazenave, Q., M. Ceccaldi, J. Delanoë, J. Pelon, S. Groß, and A. Heymsfield, 2019: "Evolution of DARDAR-CLOUD ice cloud retrieval: new parameters and impacts on the retrieved microphysical properties", *Atmos. Meas. Tech.*, **12**, 2819–2835, https://doi.org/10.5194/amt-12-2819-2019.

Cesana, G., H. Chepfer, D. Winker, B. Getzewich, X. Cai, O. Jourdan, G. Mioche, H. Okamoto, Y. Hagihara, V. Noel, and M. Reverdy, 2016: "Using in-situ airborne measurements to evaluate three cloud phase products derived from CALIPSO", *J. Geophys. Res. Atmos.*, **121**, 5788-5808, https://doi.org/10.1002/2015JD024334.

Cesana, G., A. D. Del Genio, A. S. Ackerman, M. Kelley, G. Elsaesser, A. M. Fridlind, Y. Cheng, and M.-S. Yao, 2019a: "Evaluating Models' Response of Tropical Low Clouds to SST Forcings Using CALIPSO Observations", *Atmos. Chem. Phys.*, **19**, 2813–2832, https://doi.org/10.5194/acp-19-2813-2019.

Cesana, G., D. Waliser, D. Henderson, T. L'Ecuyer, X. Jiang, and J. Li, 2019b: "The Vertical Structure of Radiative Heating Rates: A Multimodel Evaluation Using A-Train Satellite Observations", *J. Climate*, **32**, 1573–1590, https://doi.org/10.1175/JCLI-D-17-0136.1.

Cesana, G., A. D. Del Genio, and H. Chepfer, 2019c: "The Cumulus and Stratocumulus CloudSat-CALIPSO Dataset (CASCCAD)", *Earth Syst. Sci. Data*, **11**, 1745–1764, https://doi.org/10.5194/essd-11-1745-2019.

Cesana, G. V., A. S. Ackerman, A. M. Fridlind, I. Silber, A. D. Del Genio, M. D. Zelinka, H. Chepfer, T. Khadir, and R. Roehrig, 2024: "Observational constraint on a feedback from supercooled clouds reduces projected warming uncertainty", *Commun Earth Environ*, **5**, 181, https://doi.org/10.1038/s43247-024-01339-1.

Chazette, P., J.-C. Raut, F. Dulac, S. Berthier, S.-W. Kim, P. Royer, J. Sanak, S. Loaec, and H. Grigaut-Desbrosses, 2010: "Simultaneous observations of lower tropospheric continental aerosols with a ground-based, an airborne, and the spaceborne CALIOP lidar systems", *J. Geophys. Res.*, **115**, D00H3, https://doi.org/10.1029/2009JD012341.

Chazette, P., C. Flamant, J. Totems, M. Gaetani, G. Smith, A. Baron, X. Landsheere, K. Desboeufs, J.-F. Doussin, and P. Formenti, 2019: "Evidence of the complexity of aerosol transport in the lower troposphere on the Namibian coast during AEROCLO-sA", *Atmos. Chem. Phys.*, **19**, 14979–15005, https://doi.org/10.5194/acp-19-14979-2019.

Chazette, P., A. Baron, and C. Flamant, 2022: "Mesoscale spatio-temporal variability of airborne lidar-derived aerosol properties in the Barbados region during EUREC^{4}A", *Atmos. Chem. Phys.*, **22**, 1271–1292, https://doi.org/10.5194/acp-22-1271-2022.

Chen, D., Z. Liu, C. Davis, and Y. Gu, 2017: "Dust Radiative Effects on Atmospheric Thermodynamics and Tropical Cyclogenesis over the Atlantic Ocean Using WRF/Chem Coupled with an AOD Data Assimilation System", *Atmos. Chem. Phys.*, **17**, 7917–7939, https://doi.org/10.5194/acp-17-7917-2017.

Cheng, Y., T. Dai, D. Goto, N. A. J. Schutgens, G. Shi, and T. Nakajima, 2019: "Investigating the assimilation of CALIPSO global aerosol vertical observations using a four-dimensional ensemble Kalman filter", *Atmos. Chem. Phys.*, **19**, 13445–13467, https://doi.org/10.5194/acp-19-13445-2019.

Chepfer, H., S. Bony, D. M. Winker, M. Chiriaco, J.-L. Dufresne, and G. Seze, 2008: "Use of CALIPSO lidar observations to evaluate the cloudiness simulated by a climate model", *Geophys. Res. Lett.*, **35**, L15704, https://doi.org/10.1029/2008GL034207.

Chepfer, H., S. Bony, D. Winker, G. Cesana, J. L. Dufresne, P. Minnis, C. J. Stubenrauch, and S. Zeng, 2010: "The GCM Oriented CALIPSO Cloud Product (CALIPSO-GOCCP)", *J. Geophys. Res.*, **115**, D00H16, https://doi.org/10.1029/2009JD012251.

Chepfer, H., G. Cesana, D. Winker, B. Getzewich, M. Vaughan, and Z. Liu, 2013: "Comparison of two different cloud climatologies derived from CALIOP attenuated backscattered measurements (Level 1): the CALIPSO-ST and the CALIPSO-GOCCP", *J. Atmos. Oceanic Technol.*, **30**, 725–744, https://doi.org/10.1175/JTECH-D-12-00057.1.

Chepfer, H., V. Noel, M. Chiriaco, B. Wielicki, D. Winker, N. Loeb, and R. Wood, 2018: "The Potential of a Multidecade Spaceborne Lidar Record to Constrain Cloud Feedback", *J. Geophys. Res. Atmos.*, **123**, 5433–5454, https://doi.org/10.1002/2017JD027742.

Chiriaco, M., H. Chepfer, P. Minnis, M. Haeffelin, S. Platnick, D. Baumgardner, P. Dubuisson, M. McGill, V. Noël, J. Pelon, D. Spangenberg, S. Sun-Mack, and G. Wind, 2007: "Comparison of CALIPSO-Like, LaRC, and MODIS Retrievals of Ice-Cloud Properties over SIRTA in France and Florida during CRYSTAL-FACE", *J. Appl. Met. Climat.*, **46**, 249-272, https://doi.org/10.1175/JAM2435.1.

Chouza, F., T. Leblanc, J. Barnes, M. Brewer, P. Wang, and D. Koon, 2020: "Long-term (1999–2019) variability of stratospheric aerosol over Mauna Loa, Hawaii, as seen by two co-located lidars and satellite measurements", *Atmos. Chem. Phys.*, **20**, 6821–6839, https://doi.org/10.5194/acp-20-6821-2020.

Chowdhury, S., S. Dey, and K. R. Smith, 2018: "Ambient PM2.5 exposure and expected premature mortality to 2100 in India under climate change scenarios", *Nat. Commun.*, **9**, 318, https://doi.org/10.1038/s41467-017-02755-y.

Christian, K., J. Wang, C. Ge, D. Peterson, E. Hyer, J. Yorks, and M. McGill, 2019: "Radiative forcing and stratospheric warming of pyrocumulonimbus smoke aerosols: first modeling results with multi-sensor (EPIC, CALIPSO, CATS) views from space", *Geophys. Res. Lett.*, **46**, 10061–10071, https://doi.org/10.1029/2019GL082360.

Cigala, V., R. Biondi, A. J. Prata, A. K. Steiner, G. Kirchengast, and H. Brenot, 2019: "GNSS Radio Occultation Advances the Monitoring of Volcanic Clouds: The Case of the 2008 Kasatochi Eruption", *Remote Sens.*, **11**, 2199, https://doi.org/10.3390/rs11192199.

Clarisse, L., C. Clerbaux, B. Franco, J. Hadji-Lazaro, S. Whitburn, A. K. Kopp, D. Hurtmans, and P. F. Coheur, 2019: "A decadal dataset of global atmospheric dust retrieved from IASI satellite measurements", *J. Geophys. Res. Atmos.*, **124**, 1618–1647, https://doi.org/10.1029/2018JD029701.

Crawford, A. M., B. Stunder, F. Ngan, and M. Pavolonis, 2016: "Initializing HYSPLIT with satellite observations of volcanic ash: A case study of the 2008 Kasatochi eruption", *J. Geophys. Res.*, **121**, 10, 786–10,803, https://doi.org/10.1002/2016JD024779.

Crawford, J. H., J.-Y. Ahn, J. Al-Saadi, L. Chang, L. K. Emmons, J. Kim, G. Lee, J.-H. Park, R. J. Park, J. H. Woo, C.-K. Song, J.-H. Hong, Y.-D. Hong, B. L. Lefer, M. Lee, T. Lee, S. Kim, K.-E. Min, S. S. Yum, H. J. Shin, Y.-W. Kim, J.-S. Choi, J.-S. Park, J. J. Szykman, R. W. Long, C. E. Jordan, I. J. Simpson, A. Fried, J. E. Dibb, S.Y. Cho, and Y. P. Kim, 2021: "The Korea–United States Air Quality (KORUS-AQ) field study", *Elem. Sci. Anth.*, **9**, https://doi.org/10.1525/elementa.2020.00163.

Cuevas, E., C. Camino, A. Benedetti, S. Basart, E. Terradellas, J. M. Baldasano, J.-J. Morcrette, B. Marticorena, P. Goloub, A. Mortier, A. Berjón, Y. Hernández, M. Gil-Ojeda, and M. Schulz, 2015: "The MACC-II 2007-2008 reanalysis: atmospheric dust evaluation and characterization over Northern Africa and Middle East", *Atmos. Chem. Phys.*, **15**, 3991-4024, https://doi.org/10.5194/acp-15-3991-2015.

Davis, S. M., L. M. Avallone, B. H. Kahn, K. G. Meyer, and D. Baumgardner, 2009: "Comparison of airborne in situ measurements and Moderate Resolution Imaging Spectroradiometer (MODIS) retrievals of cirrus cloud optical and microphysical properties during the Midlatitude Cirrus Experiment (MidCiX)", *J. Geophys. Res.*, **114**, D02203, https://doi.org/10.1029/2008JD010284.

Dawson, K. W., N. Meskhidze, D. Josset and S. Gassó, 2015: "A new study of sea spray optical properties from multi-sensor spaceborne observations", *Atmos. Chem. Phys.*, **15**, 3241–3255, https://doi.org/10.5194/acp-15-3241-2015.

de Laat, A., E. Defer, J. Delanoë, F. Dezitter, A. Gounou, A. Grandin, A. Guignard, J. F. Meirink, J.-M. Moisselin, and F. Parol, 2017: "Analysis of geostationary satellite derived cloud parameters associated with high ice water content environments", *Atmos. Meas. Tech.*, **10**, 1359–1371, https://doi.org/10.5194/amt-10-1359-2017.

Deng, M., G. G. Mace, Z. Wang and H. Okamoto, 2010: "Tropical Composition, Cloud and Climate Coupling Experiment Validation for Cirrus Cloud Profiling Retrieval Using CloudSat Radar and CALIPSO Lidar", *J. Geophys. Res.*, **115**, D00J15, https://doi.org/10.1029/2009JD013104.

Deng, M., G. G. Mace, Z. Wang, and R. P. Lawson, 2013: "Evaluation of Several A-Train Ice Cloud Retrieval Products with in situ Measurements Collected during the SPartICus Campaign", *J. Appl. Meteor. Climatol.*, **52**, 1014-1030, https://doi.org/10.1175/JAMC-D-12-054.1.

Deng, M., G. G. Mace, Z. Wang, and E. Berry, 2015: "CloudSat 2C-ICE Product Update with a New Ze Parameterization in Lidar-only Region", *J. Geophys. Res. Atmos.*, **120**, 12,198–12,208, https://doi.org/10.1002/2015JD023600.

de Villiers, R. A., G. Ancellet, J. Pelon, B. Quennehen, A. Schwarzenboeck, J.F. Gayet, and K. S. Law, 2010: "Airborne measurements of aerosol optical properties related to early spring transport of mid-latitude sources into the Arctic", *Atmos. Chem. Phys.*, **10**, 5011–5030, https://doi.org/10.5194/acp-10-5011-2010.

Di Biagio, C., J. Pelon, G. Ancellet, A. Bazureau, A., and V. Mariage, 2018: "Sources, load, vertical distribution, and fate of wintertime aerosols north of Svalbard from combined V4 CALIOP data, ground-based IAOOS lidar observations and trajectory analysis", *J. Geophys. Res. Atmos.*, **123**, 1363–1383, https://doi.org/10.1002/2017JD027530.

Ding, K., X. Huang, A. Ding, M. Wang, H. Su, V.-M. Kerminen, T. Petäjä, Z. Tan, Z. Wang, D. Zhou, J. Sun, H. Liao, H. Wang, K. Carslaw, R. Wood, P. Zuidema, D. Rosenfeld, M. Kulmala, C. Fu, U. Pösch, Y. Cheng, and M. O. Andreae, 2021: "Aerosol-boundary-layer-monsoon interactions amplify semi-direct effect of biomass smoke on low cloud formation in Southeast Asia", *Nat. Commun.*, **12**, 6416, https://doi.org/10.1038/s41467-021-26728-4.

Dionisi, D., V. E. Brando, G. Volpe, S. Colella and R. Santoleri, 2020: "Seasonal distributions of ocean particulate optical properties from spaceborne lidar measurements in Mediterranean and Black sea", *Remote Sens. Environ.*, **247**, 111889, https://doi.org/10.1016/j.rse.2020.111889.

Douglas, A. and T. L'Ecuyer, 2020: "Quantifying Cloud Adjustments and the Radiative Forcing due to Aerosol-Cloud Interactions in Satellite Observations of Warm Marine Clouds", *Atmos. Chem. Phys.*, **20**, 6225–6241, https://doi.org/10.5194/acp-20-6225-2020.

Dupont, J.-C., M. Haeffelin, Y. Morille, V. Noel, P. Keckhut, D. Winker, J. Comstock, P. Chervet, and A. Roblin, 2010: "Macrophysical and optical properties of midlatitude cirrus clouds from 4 ground-based lidars and collocated CALIOP observations", *J. Geophys. Res.*, **115**, D00H24, https://doi.org/10.1029/2009JD011943.

El Amraoui, L., B. Sič, A. Piacentini, V. Marécal, N. Frebourg, and J.-L. Attié, 2020: "Aerosol data assimilation in the MOCAGE chemical transport model during the TRAQA/ChArMEx campaign: Lidar observations", *Atmos. Meas. Tech.*, **13**, 4645–4667, https://doi.org/10.5194/amt-13-4645-2020.

Etherton, B. J., M. S. Wandishin, J. E. Hart, G. J. Layne, M. H. Leon, and M. A. Petty, 2014: "Assessment of the Current Icing Product (CIP) and Forecast Icing Product (FIP) Version 1.1", NOAA technical memorandum OAR GSD-52, https://doi.org/10.7289/V5/TM-OAR-GSD-52.

Fadnavis, S., G. Kalita, M. Rowlinson, A. Rap, J.-L. F. Li, B. Gasparini, A. Laakso, and R. Müller, 2019: "The impact of recent changes in Asian anthropogenic emissions of SO2 on sulfate loading

in the upper troposphere and lower stratosphere and the associated radiative changes", *Atmos. Chem. Phys.*, **19**, 9989–10008, https://doi.org/10.5194/acp-19-9989-2019.

Fiooco, G., and L. D. Smullins, 1963,"Detection of Scattering Layers in the Upper Atmosphere (60-140 km) by Optical Radar," *Nature*, **199**, 1275-1276, http://doi.org/10.1038/1991275a0.

Forbes, R. M., A. Geer, K. Lonitz, and M. Ahlgrimm, 2016: "Reducing systematic errors in cold-air outbreaks", ECMWF, Reading, United Kingdom, 16–22, https://doi.org/10.21957/s41h7q7l.

Formenti, P., B. D'Anna, C. Flamant, M. Mallet, S. John Piketh, K. Schepanski, F. Waquet, F. Auriol, G. Brogniez, F. Burnet, J.-P. Chaboureau, A. Chauvigné, P. Chazette, C. Denjean, K. Desboeufs, J.-F. Doussin, N. Elguindi, S. Feuerstein, M. Gaetani, C. Giorio, D. Klopper, M. D. Mallet, P. Nabat, A. Monod, F. Solmon, A. Namwoonde, C. Chikwililwa, R. Mushi, E. J. Welton, and B. Holben, 2019: "The Aerosols, Radiation and Clouds in Southern Africa Field Campaign in Namibia: Overview, Illustrative Observations, and Way Forward", *Bull. Amer. Meteor. Soc.*, **100**, 1277-1298, https://doi.org/10.1175/BAMS-D-17-0278.1.

Frey, W. R., A. L. Morrison, J. E. Kay, R. Guzman, and H. Chepfer, 2018: "The combined influence of observed Southern Ocean clouds and sea ice on top-of-atmosphere albedo", *J. Geophys. Res. Atmos.*, **123**, 4461–4475, https://doi.org/10.1029/2018JD028505.

Friberg, J., B. G. Martinsson, S. M. Andersson, and O. S. Sandvik, 2018: "Volcanic impact on the climate – the stratospheric aerosol load in the period 2006–2015", *Atmos. Chem. Phys.*, **18**, 11149–11169, https://doi.org/10.5194/acp-18-11149-2018.

Friberg, J., B. G. Martinsson and M. K. Sporre, 2023: "Short and long-term stratospheric impact of smoke from the 2019/2020 Australian wildfires", *Atmos. Chem. Phys.*, **23**, 12557–12570, https://doi.org/10.5194/acp-23-12557-2023.

Fromm, M., D. Peterson, and L. Di Girolamo, 2019: "The primary convective pathway for observed wildfire emissions in the upper troposphere and lower stratosphere: a targeted reinterpretation", *J. Geophys. Res. Atmos.*, **124**, 13254-13272, https://doi.org/10.1029/2019JD031006.

Froyd, K. D., D. M. Murphy, T. J. Sanford, D. S. Thomson, J. C. Wilson, L. Pfister, and L. Lait, 2009: "Aerosol composition of the tropical upper troposphere", *Atmos. Chem. Phys.*, **9**, 4363–4385, https://doi.org/10.5194/acp-9-4363-2009.

Gao, M., P. E. Saide, J. Xin, Y. Wang, Z. Liu, Y. Wang, Z. Wang, M. Pagowski, S. K. Guttikunda, and G. R. Carmichael, 2017: "Estimates of Health Impacts and Radiative Forcing in Winter Haze in Eastern China through Constraints of Surface PM2.5 Predictions", *Environ. Sci. Technol.*, **51**, 2178–2185, https://doi.org/10.1021/acs.est.6b03745.

Garnier A., J. Pelon, P. Dubuisson, M. Faivre, O. Chomette, N. Pascal, and D. P. Kratz, 2012: "Retrieval of cloud properties using CALIPSO Imaging Infrared Radiometer. Part I: effective emissivity and optical depth", *J. Appl. Meteor. Climatol.*, **51**, 1407-1425, https://doi.org/10.1175/JAMC-D-11-0220.1.

Garnier, A., J. Pelon, P. Dubuisson, P. Yang, M. Faivre, O. Chomette, N. Pascal, P. Lucker, and T. Murray, 2013: "Retrieval of cloud properties using CALIPSO Imaging Infrared Radiometer. Part II: effective diameter and ice water path", *J. Appl. Meteor. Climatol.,* **52**, 2582–2599, https://doi.org/10.1175/JAMC-D-12-0328.1.

Garnier, A., J. Pelon, M. A. Vaughan, D. M. Winker, C. R. Trepte, and P. Dubuisson, 2015 : "Lidar multiple scattering factors inferred from CALIPSO lidar and IIR retrievals of semi-transparent

cirrus cloud optical depths over oceans", *Atmos. Meas. Tech.*, **8**, 2759–2774, https://doi.org/10.5194/amt-8-2759-2015.

Garnier, A., N. A. Scott, J. Pelon, R. Armante, L. Crépeau, B. Six, and N. Pascal, 2017: "Long-term assessment of the CALIPSO Imaging Infrared Radiometer (IIR) calibration and stability through simulated and observed comparisons with MODIS/Aqua and SEVIRI/Meteosat", *Atmos. Meas. Tech.*, **10**, 1403–1424, https://doi.org/10.5194/amt-10-1403-2017.

Garnier, A., T. Trémas, J. Pelon, K.-P. Lee, D. Nobileau, L. Gross-Colzy, N. Pascal, P. Ferrage, P., and N. A. Scott, 2018: "CALIPSO IIR Version 2 Level 1b calibrated radiances: analysis and reduction of residual biases in the Northern Hemisphere," *Atmos. Meas. Tech.*, **11**, 2485–2500, https://doi.org/10.5194/amt-11-2485-2018.

Garnier, A., J. Pelon, N. Pascal, M. A. Vaughan, P. Dubuisson, P. Yang, and D. L. Mitchell, 2021a: "Version 4 CALIPSO IIR ice and liquid water cloud microphysical properties, Part I: the retrieval algorithms", *Atmos. Meas. Tech.*, **14**, 3253–3276, https://doi.org/10.5194/amt-14-3253-2021.

Garnier, A., J. Pelon, N. Pascal, M. A. Vaughan, P. Dubuisson, P. Yang, and D. L. Mitchell, 2021b: "Version 4 CALIPSO IIR ice and liquid water cloud microphysical properties, Part II: results over oceans", *Atmos. Meas. Tech.*, **14**, 3277–3299, https://doi.org/10.5194/amt-14-3277-2021.

Gasparini, B., A. Meyer, D. Neubauer, S. Münch, and U. Lohmann, 2018: "Cirrus cloud properties as seen by the CALIPSO satellite and ECHAM-HAM global climate model", *J. Climate*, **31**, 1983–2003, https://doi.org/10.1175/JCLI-D-16-0608.1.

Gasteiger**,** J., S. Groß, B. Weinzierl, D. Sauer, and V. Freudenthaler, 2017: "Particle settling and convective mixing in the Saharan Air Layer as seen from an integrated model, lidar, and in-situ perspective", *Atmos. Chem. Phys.*, **17**, 297–311, https://doi.org/10.5194/acp-17-297-2017.

Gayet, J.-F., G. Mioche, A. Dörnbrack, A. Ehrlich, A. Lampert, and M. Wendisch, 2009: "Microphysical and optical properties of Arctic mixed-phase clouds. The 9 April 2007 case study", *Atmos. Chem. Phys.*, **9**, 6581–6595, https://doi.org/10.5194/acp-9-6581-2009.

Getzewich, B. J., M. A. Vaughan, W. H. Hunt, M. A. Avery, K. A. Powell, J. L. Tackett, D. M. Winker, J. Kar, K.-P. Lee, and T. Toth, 2018: "CALIPSO Lidar Calibration at 532-nm: Version 4 Daytime Algorithm", *Atmos. Meas. Tech.*, **11**, 6309-6326, https://doi.org/10.5194/amt-11-6309-2018.

Goldberg, D. L., B. de Foy, M. O. Nawaz, J. Johnson, G. Yarwood, and L. Judd, 2024: "Quantifying NOx Emission Sources in Houston, Texas Using Remote Sensing Aircraft Measurements and Source Apportionment Regression Models", *ACS ES&T Air*, **1**, 1391−1401, https://doi.org/10.1021/acsestair.4c00097.

Gong, W., Y. Huang, T. Zhang, Z. Zhu, Y. Ji, and H. Xiang, 2017: "Impact and Suggestion of Column to-Surface Vertical Correction Scheme on the Relationship between Satellite AOD and Ground-Level PM2.5 in China", *Remote Sens.*, **9**, 1038, https://doi.org/10.3390/rs9101038.

Govardhan, G., S. K. Satheesh, R. Nanjundiah, K. K. Moorthy, and S. S. Babu, 2017: "Possible climatic implications of high altitude emissions of black carbon", *Atmos. Chem. Phys.*, 17, 9623-9644, https://doi.org/10.5194/acp-17-9623-2017.

Gryspeerdt, E., Sourdeval, O., Quaas, J., Delanoë, J., Krämer, M., and Kühne, P., 2018: "Ice crystal number concentration estimates from lidar-radar satellite remote sensing – Part 2: Controls on the ice crystal number concentration", *Atmos. Chem. Phys.*, **18**, 14351–14370, https://doi.org/10.5194/acp-18-14351-2018.

Guffanti, M., T. J. Casadevall, and K. Budding, 2010: "Encounters of aircraft with volcanic ash cloud; A compilation of known incidents, 1953-2009", in U.S. Geological Survey Data Series, USGS, https://pubs.usgs.gov/ds/545.

Guzman, R., H. Chepfer, V. Noel, T. V. de Guélis, J. E. Kay, P. Raberanto, G. Cesana, M. A. Vaughan, and D. M. Winker, 2017: "Direct atmosphere opacity observations from CALIPSO provide new constraints on cloud-radiation interactions", *J. Geophys. Res. Atmos.*, **122**, 1066–1085, https://doi.org/10.1002/2016JD025946.

Haarig, M., R. Engelmann, A. Ansmann, I. Veselovskii, D. N. Whiteman and D. Althausen, 2016: "1064 nm rotational Raman lidar for particle extinction and lidar-ratio profiling: cirrus case study", *Atmos. Meas. Tech.*, **9**, 4269–4278, https://doi.org/10.5194/amt-9-4269-2016.

Hakuba, M. Z., S. Fourest, T. Boyer, B. Meyssignac, J. A. Carton, G. Forget, L. Cheng, D. Giglio, G. C. Johnson, S. Kato, R. E. Killick, N. Kolodziejczyk, M. Kuusela, F. Landerer, W. Llovel, R. Locarnini, N. Loeb, J. M. Lyman, A. Mishonov, P. Pilewskie, J. Reagan, A. Storto, T. Sukianto, and K. von Schuckmann, 2024: "Trends and Variability in Earth's Energy Imbalance and Ocean Heat Uptake Since 2005", *Surv. Geophys.*, **45**, 1721–1756, https://doi.org/10.1007/s10712-024-09849-5.

Haggerty, J., E. Defer, A. de Laat, K. Bedka, J. Moisselin, R. Potts, J. Delanoë, F. Parol, A. Grandin, and S. DiVito, 2019: "Detecting Clouds Associated with Jet Engine Ice Crystal Icing", *B. Am. Meteorol. Soc.*, **100**, 31–40, https://doi.org/10.1175/BAMS-D-17-0252.1.

Hansen J. E., P. Kharecha, M. Sato, G. Tselioudis, J. Kelly, S. E. Bauer, R. Ruedy, E. Jeong, Q. Jin, E. Rignot, I. Velicogna, M. R. Schoeberl, K. von Schuckmann, J. Amponsem, J. Cao, A. Keskinen, J. Li, and A. Pokela, 2025: "Global Warming Has Accelerated: Are the United Nations and the Public Well-Informed?", *Environment: Science and Policy for Sustainable Development*, **67:1**, 6-44, https://doi.org/10.1080/00139157.2025.2434494.

Haynes, J. M., Y.-J. Noh, S. D. Miller, K. D. Haynes, I. Ebert-Uphoff and A. Heidinger, 2022: "Low Cloud Detection in Multilayer Scenes using Satellite Imagery with Machine Learning Methods", *J. Atmos. Oceanic Technol.*, **39**, 319–334, https://doi.org/10.1175/JTECH-D-21-0084.1.

He, M., Y. Hu, N. Chen, D. Wang, J. Huang, and K. Stamnes, 2019: "High cloud coverage over melted areas dominates the impact of clouds on the albedo feedback in the Arctic", *Sci. Rep.*, **9**, 9529, https://doi.org/10.1038/s41598-019-44155-w.

Heidinger, A. K., A. T. Evan, M. J., Foster and A. Walther, 2012: "A naïve bayesian cloud detection scheme derived from CALIPSO and applied within PATMOS-x", *J. Appl. Meteorol. Clim.*, **51**, 1129–1144, https://doi.org/10.1175/JAMC-D-11-02.1.

Heidinger, A. K., N. Bearson, M. J. Foster, Y. Li, S. Wanzong, S. Ackerman, R. E. Holz, S. Platnick, and K. Meyer, 2019: "Using Sounder Data to Improve Cirrus Cloud Height Estimation from Satellite Imagers", *J. Atmos. Oceanic Technol.*, **36**, 1331–1342, https://doi.org/10.1175/JTECH-D-18-0079.1.

Hedelt, P., D. S. Efremenko, D. G. Loyola, R. Spurr, and L. Clarisse, 2019: "Sulfur dioxide layer height retrieval from Sentinel-5 Precursor/TROPOMI using FP_ILM", *Atmos. Meas. Tech.*, **12**, 5503–5517, https://doi.org/10.5194/amt-12-5503-2019.

Henderson, D. S., 2011: "A new look at the Earth's radiation balance from an A-train observational perspective", M.S. Thesis, Department of Atmospheric Science, Colorado State University, 135 pp.; see http://gradworks.umi.com/14/83/1483924.html.

Henderson, D., T. L'Ecuyer, G. Stephens, P. Partain and M. Sekiguchi, 2013: "A Multi-sensor Perspective on the Radiative Impacts of Clouds and Aerosols", *J. Appl. Meteor. Climatol.*, **52**, 853–871, https://doi.org/10.1175/JAMC-D-12-025.1.

Herzfeld, U. C., T. Trantow, M. Vaughan, S. Palm, C. Opfer and E. Rodriguez, 2025: "High-Resolution Detection of Stratospheric Aerosols in CALIPSO Atmospheric Lidar Data Facilitated by the CALIOP-Density-Dimension Algorithm", *IEEE Trans. Geosci. Remote Sens.*, **63**, 5703821, https://doi.org/10.1109/TGRS.2025.3569546.

Heymsfield, A., and P. Willis, 2014: "Cloud Conditions Favoring Secondary Ice Particle Production in Tropical Maritime Convection", *J. Atmos. Sci.*, **71**, 4500–4526, https://doi.org/10.1175/JAS-D-14-0093.1.

Hlavka, D., J. Yorks, S. Young, M. Vaughan, R. Kuehn, M. McGill, and S. Rodier, 2012: "Airborne Validation of Cirrus Cloud Properties Derived from CALIPSO Lidar Measurements: Optical Properties", *J. Geophys. Res.*, **117**, D09207, https://doi.org/10.1029/2011JD017053.

Holz, R., S. Ackerman, F. Nagle, R. Frey, S. Dutcher, R. Kuehn, M. Vaughan, and B. Baum. 2008: "Global MODIS Cloud Detection and Height Evaluation Using CALIOP", *J. Geophys. Res.*, **113**, D00A19, https://doi.org/10.1029/2008JD009837.

Holz, R. E., S. Platnick, K. Meyer, M. Vaughan, A. Heidinger, P. Yang, G. Wind, S. Dutcher, S. Ackerman, N. Amarasinghe, F. Nagle and C. Wang, 2016: "Resolving ice cloud optical thickness biases between CALIOP and MODIS using infrared retrievals", *Atmos. Chem. Phys.*, **16**, 5075-5090, https://doi.org/10.5194/acp-16-5075-2016.

Hu, Y., D. Winker, Z. Liu, M. Vaughan, K. Powell and B. Hunt, 2006: "The lidar sub-surface perpendicular polarization returns: Creating a value-added CALIPSO ocean profile product", 36th COSPAR Scientific Assembly, Beijing, China, 16–23 July 2006 [see https://ui.adsabs.harvard.edu/abs/2006cosp...36....4H/abstract].

Hu, Y., 2007: "Depolarization ratio–effective lidar ratio relation: Theoretical basis for space lidar cloud phase discrimination", *Geophys. Res. Lett.*, **34**, L11812, https://doi.org/10.1029/2007GL029584.

Hu, Y., Z. Liu, D. Winker, M. Vaughan, V. Noel, L. Bissonnette, G. Roy, and M. McGill, 2006: "A simple relation between depolarization and multiple scattering of water clouds and its application for lidar calibration", *Optics Letters*, **31**, 1809–1811, https://doi.org/10.1364/OL.31.001809.

Hu, Y. M. Vaughan, Z. Liu, B. Lin, P. Yang, D. Flittner, W. Hunt, R. Kuehn, J. Huang, D. Wu, S. Rodier, K. Powell, C. Trepte, and D. Winker, 2007a: "The depolarization-attenuated backscatter relation: CALIPSO lidar measurements vs. theory", *Opt. Express*, **15**, 5327–5332, https://doi.org/10.1364/OE.15.005327.

Hu, Y., M. Vaughan, Z. Liu, K. Powell, and S. Rodier, 2007b: "Retrieving Optical Depths and Lidar Ratios for Transparent Layers Above Opaque Water Clouds from CALIPSO Lidar Measurements", *IEEE Geosci. Remote Sens. Lett.*, **4**, 523–526, https://doi.org/10.1109/LGRS.2007.901085.

Hu, Y., K. Powell, M. Vaughan, C. Trepte, C. Weimer, M. Beherenfeld, S. Young, D. Winker, C. Hostetler, W. Hunt, R. Kuehn, D. Flittner, M. Cisewski, G. Gibson, B. Lin, and D. MacDonnell, 2007c: Elevation information in tail (EIT) technique for lidar altimetry, *Opt. Express*, **15**, 14504–14515, https://doi.org/10.1364/OE.15.014504.

Hu, Y., K. Stamnes, M. Vaughan, J. Pelon, C. Weimer, D. Wu, M. Cisewski, W. Sun, P. Yang, B. Lin, A. Omar, D. Flittner, C. Hostetler, C. Trepte, D. Winker, G. Gibson, and M. Santa-Maria, 2008: "Sea surface wind speed estimation from space-based lidar measurements", *Atmos. Chem. Phys.*, **8**, 3593–3601, https://doi.org/10.5194/acp-8-3593-2008.

Hu, Y., 2009: "Ocean, Land and Meteorology Studies Using Space-Based Lidar Measurements", 5th WSEAS International Conference on Remote Sensing, Genova, Italy, 17–19 October 2009, https://ntrs.nasa.gov/citations/20090037431.

Hu, Y., S. Rodier, K. Xu, W. Sun, J. Huang, B. Lin, P. Zhai and D. Josset, 2010: Occurrence, Liquid Water Content, and Fraction of Supercooled Water Clouds from Combined CALIOP/IIR/MODIS Measurements, *J. Geophys. Res.*, **115**, D00H34, https://doi.org/10.1029/2009JD012384.

Huang, H., K. Zhang, Z. Zhang, W. Smith Jr., J. He, N. Liu and C. Le, 2024: "Revisiting Winter Southern Ocean CO_2 Uptake Based on CALIPSO Observations", *Geophys. Res. Lett.*, **51**, e2024GL108335, https://doi.org/10.1029/2024GL108335.

Huang, L., J. H. Jiang, J. L. Tackett, H. Su, and R. Fu, 2013: Seasonal and diurnal variations of aerosol extinction profile and type distribution from CALIPSO 5-year observations, *J. Geophys. Res.*, **118**, 4572–4596, https://doi.org/10.1002/jgrd.50407.

Huang, Y., S. Siems, M. Manton, A. Protat, L. Majewski, and H. Nguyen, 2019: "Evaluating Himawari-8 Cloud Products Using Shipborne and CALIPSO Observations: Cloud top Height and Cloud top Temperature", *J. Atmos. Oceanic Technol.*, **36**, 2327–2347, https://doi.org/10.1175/JTECH-D-18-0231.1.

Hunt, W. H, D. M. Winker, M. A. Vaughan, K. A. Powell, P. L. Lucker, and C. Weimer, 2009: "CALIPSO Lidar Description and Performance Assessment", *J. Atmos. Oceanic Technol.*, **26**, 1214–1228, https://doi.org/10.1175/2009JTECHA1223.1.

IPCC, 1995: *Climate Change 1995: The science of climate change. Contribution of Working Group I to the SecondAssessment Report of the Intergovernmental Panel on Climate Change*, Houghton, J. T., L.G. Meira Filho, B. A. Callender, N. Harris, A. Kattenberg, and K. Maskel, Eds., Cambridge University Press, Cambridge, United Kingdom, New York, NY, USA, and Melbourne, Australia, 574 pp. Report available at https://www.ipcc.ch/report/ar2/wg1/.

IPCC, 2013: *Climate Change 2013: The Physical Science Basis. Contribution of Working Group I to the Fifth Assessment Report of the Intergovernmental Panel on Climate Change*, Stocker, T. F., D. Qin, G.-K. Plattner, M. Tignor, S. K. Allen, J. Boschung, A. Nauels, Y. Xia, V. Bex and P.M. Midgley, Eds., Cambridge University Press, Cambridge, United Kingdom and New York, NY, USA, 1535 pp, https://doi.org/10.1017/CBO9781107415324, Report available at https://www.ipcc.ch/report/ar5/wg1/.

Jacob, D. J., J. H. Crawford, H. Maring, A. D. Clarke, J. E. Dibb, L. K. Emmons, R. A. Ferrare, C. A. Hostetler, P. B. Russell, H. B. Singh, A. M. Thompson, G. E. Shaw, E. McCauley, J. R. Pederson, and J. A. Fisher, 2010: "The Arctic Research of the Composition of the Troposphere from Aircraft and Satellites (ARCTAS) mission: design, execution, and first results", *Atmos. Chem. Phys.*, **10**, 5191–5212, https://doi.org/10.5194/acp-10-5191-2010.

Jensen, E. J., R. P. Lawson, J. W. Bergman, L. Pfister, T. P. Bui, and C. G. Schmitt, 2013: "Physical processes controlling ice concentrations in synoptically forced, midlatitude cirrus", *J. Geophys. Res. Atmos.*, **118**, 5348-5360, https://doi.org/10.1002/jgrd.50421.

Jensen, E. J., L. Pfister, D. E. Jordan, T. V. Bui, R. Ueyama, H. B. Singh, T. D. Thornberry, A. W. Rollins, R.-S. Gao, D. W. Fahey, K. H. Rosenlof, J. W. Elkins, G. S. Diskin, J. P. DiGangi, R. P. Lawson, S. Woods, E. L. Atlas, M. A. Navarro Rodriguez, S. C. Wofsy, J. Pittman, C. G. Bardeen, O. B. Toon, B. C. Kindel, P. A. Newman, M. J. McGill, D. L. Hlavka, L. R. Lait, M. R. Schoeberl, J. W. Bergman, H. B. Selkirk, M. J. Alexander, J.-E. Kim, B. H. Lim, J. Stutz, and K. Pfeilsticker, 2017: "The NASA Airborne Tropical Tropopause Experiment: High-Altitude Aircraft Measurements in the Tropical Western Pacific", *Bull. Amer. Meteor. Soc.,* **98**, 129-143, https://doi.org/10.1175/BAMS-D-14-00263.1.

Jia, R., M. Luo, Y. Liu, Q. Zhu, S. Hua, C. Wu, and T. Shao, 2019: "Anthropogenic Aerosol Pollution over the Eastern Slope of the Tibetan Plateau", *Adv. Atmos. Sci.*, **36**, 847–862, https://doi.org/10.1007/s00376-019-8212-0.

Johansson, E., A. Devasthale, A. M. L. Ekman, M. Tjernström, and T. L'Ecuyer, 2019: "How does cloud overlap affect the radiative heating in the tropical upper troposphere/lower stratosphere?", *Geophys. Res. Lett.*, **46**, 5623–5631, https://doi.org/10.1029/2019GL082602.

Josset, D., J. Pelon, A. Protat, and C. Flamant, 2008: "New approach to determine aerosol optical depth from combined CALIPSO and CloudSat ocean surface echoes", *Geophys. Res. Lett.*, **35**, L10805, https://doi.org/10.1029/2008GL033442.

Josset, D., R. Rogers, J. Pelon, Y. Hu, Z. Liu, A. Omar and P-W. Zhai, 2011: "CALIPSO lidar ratio retrieval over the ocean", *Opt. Express*, **19**, 18696–18706, https://doi.org/10.1364/OE.19.018696.

Josset, D., J. Pelon, A. Garnier, Y-X. Hu, M. Vaughan, P. Zhai, R. Kuehn and P. Lucker, 2012: "Cirrus optical depth and lidar ratio retrieval from combined CALIPSO-CloudSat observations using ocean surface echo", *J. Geophys. Res.*, **117**, D05207, https://doi.org/10.1029/2011JD016959.

Jung, J., A. H. Souri, D. C. Wong, S. Lee, W. Jeon, J. Kim, and Y. Choi, 2019: "The impact of the direct effect of aerosols on meteorology and air quality using aerosol optical depth assimilation during the KORUS-AQ campaign", *J. Geophys. Res. Atmos.*, **124**, 8303–8319, https://doi.org/10.1029/2019JD030641.

Kacenelenbogen, M., M. Vaughan, J. Redemann, S. Young, Z. Liu, Y. Hu, A. Omar, S. LeBlanc, Y. Shinozuka, J. Livingston, Q. Zhang, and K. Powell, 2019: "Estimations of Global Shortwave Direct Aerosol Radiative Effects Above Opaque Water Clouds Using a Combination of A-Train Satellite Sensors", *Atmos. Chem. Phys.*, **19**, 4933–4962, https://doi.org/10.5194/acp-19-4933-2019.

Kacenelenbogen, M. S. F., R. Kuehn, N. D. Amarasinghe, K. G. Meyer, E. P. Nowottnick, M. A. Vaughan, H. Chen, S. Schmidt, R. A. Ferrare, J. W. Hair, R. C. Levy, H. Yu, P. Zuidema, R. Holz, and W. Marais, 2025: "All-Sky Direct Aerosol Radiative Effects Estimated from Integrated A-Train Satellite Measurements", *Atmos. Chem. Phys.*, **25**, 15875–15911, https://doi.org/10.5194/acp-25-15875-2025.

Kalluri, R. O. R., X. Zhang, L. Bi, J. Zhao, L. Yu, and K. R. Gopal, 2019: "Carbonaceous aerosol emission reduction over Shandong province and the impact of air pollution control as observed from synthetic satellite data", *Atmos. Environ.*, 117150, **222**, https://doi.org/10.1016/j.atmosenv.2019.117150.

Kar, J., M. A. Vaughan, K. P. Lee, J. Tackett, M. Avery, A. Garnier, B. Getzewich, W. Hunt, D. Josset, Z. Liu, P. Lucker, B. Magill, A. Omar, J. Pelon, R. Rogers, T. D. Toth, C. Trepte, J-P. Vernier, D. Winker and S. Young, 2018: "CALIPSO Lidar Calibration at 532 nm: Version 4 Nighttime Algorithm", *Atmos. Meas. Tech.*, **11**, 1459-1479, https://doi.org/10.5194/amt-11-1459-2018.

Kar, J., K.-P. Lee, M. A. Vaughan, J. L. Tackett, C. R. Trepte, D. M. Winker, P. L. Lucker, and B. J. Getzewich, 2019: "CALIPSO Level 3 Stratospheric Aerosol Product: Version 1.00 Algorithm Description and Initial Assessment", *Atmos. Meas. Tech.*, **12**, 6173–6191, https://doi.org/10.5194/amt-12-6173-2019.

Kato, S., S. Sun-Mack, W. F. Miller, F. G. Rose, Y. Chen, P. Minnis, and B. A. Wielicki, 2010: "Relation of cloud occurrence frequency, overlap, and effective thickness derived from CALIPSO and CloudSat merged cloud vertical profiles", *J. Geophys. Res.*, **115**, D00H28, https://doi.org/10.1029/2009JD012277.

Kato, S., F. G. Rose, S. Sun-Mack, W. F. Miller, Y. Chen, D. A. Rutan, G. L. Stephens, N. G. Loeb, P. Minnis, B. Wielicki, D. M. Winker, T. P. Charlock, P. W. Stackhouse, K.-M. Xu, and W. D. Collins, 2011: "Improvements of top-of-atmosphere and surface irradiance computations with CALIPSO, CloudSat, and MODIS-derived cloud and aerosol properties", *J. Geophys. Res.*, **116**, D19209, https://doi.org/10.1029/2011JD016050.

Kato, S., N. G. Loeb, D. A. Rutan, F. G. Rose, S. Sun-Mack, W. F. Miller and Y. Chen, 2012: "Uncertainty Estimate of Surface Irradiances Computed with MODIS-, CALIPSO-, and CloudSat-Derived Cloud and Aerosol Properties", *Surv. Geophys.*, **33**, 395–412, https://doi.org/10.1007/s10712-012-9179-x.

Kato, S., F. G. Rose, S. H. Ham, D. A. Rutan, A. Radkevich, T. E. Caldwell, S. Sun-Mack, W. F. Miller, and Y. Chen, 2019: "Radiative Heating Rates Computed with Clouds Derived from Satellite-based Passive and Active Sensors and their Effects on Generation of Available Potential Energy", *J. Geophys. Res. Atmos.*, **124**, 1720–1740, https://doi.org/10.1029/2018JD028878.

Khaykin, S. M., S. Godin-Beekman, P. Keckhut, A. Hauchecorne, J. Jumelet, J.-P. Vernier, A. Bourassa, D. A. Degenstein, L. A. Rieger, C. Bingen, F. Vanhellemont, C. Robert, M. Deland, and P. K. Bhartia, 2017: "Variability and evolution of the midlatitude stratospheric aerosol budget from 22 years of ground-based lidar and satellite observations", *Atmos. Chem. Phys.*, **17**, 1829–1845, https://doi.org/10.5194/acp-17-1829-2017.

Kichak, R. A., 2003: "Independent GLAS Anomaly Review Board Executive Summary", Goddard Space Flight Cent., Greenbelt, Md., available at https://icesat.gsfc.nasa.gov/icesat/docs/IGARB.pdf.

Kim, M.-H., S.-W. Kim, S.-C. Yoon, and A. H. Omar, 2013: "Comparison of Aerosol Optical Depth between CALIOP and MODIS-Aqua for CALIOP Aerosol Subtypes over the Ocean", *J. Geophys. Res.*, **118**, 13,241-13,252, https://doi.org/10.1002/2013JD019527.

Kim, M.-H., A. H. Omar, M. A. Vaughan, D. M. Winker, C. R. Trepte, Y. Hu, Z. Liu, and S.-W. Kim, 2017: "Quantifying the low bias of CALIPSO's column aerosol optical depth due to undetected aerosol layers", *J. Geophys. Res. Atmos.*, **122**, 1098-1113, https://doi.org/10.1002/2016JD025797.

Kim, M.-H., A. H. Omar, J. L. Tackett, M. A. Vaughan, D. M. Winker, C. R. Trepte, Y. Hu, Z. Liu, L. R. Poole, M. C. Pitts, J. Kar, and B. E. Magill, 2018: "The CALIPSO Version 4 Automated Aerosol Classification and Lidar Ratio Selection Algorithm", *Atmos. Meas. Tech.*, **11**, 6107-6135, https://doi.org/10.5194/amt-11-6107-2018.

Kim, S.-W., S. Berthier, P. Chazette, J.-C. Raut, F. Dulac, and S.-C. Yoon, 2008: "Validation of aerosol and cloud layer structures from the space-borne lidar CALIOP using Seoul National University ground-based lidar", *Atmos. Chem. Phys.*, **8**, 3705-3720, https://doi.org/10.5194/acp-8-3705-2008.

Kim, S.-W., E.-S. Chung, S.-C. Yoon, B.-J. Sohn, and N. Sugimoto, 2011: "Intercomparisons of cloud-top and cloud-base heights from ground-based Lidar, CloudSat and CALIPSO measurements", *Int. J. Remote Sens.*, **32**, 1179-1197, https://doi.org/10.1080/01431160903527439.

Kittaka, C., D. M. Winker, M. A. Vaughan, A. Omar, and L. A. Remer, 2011: "Intercomparison of column aerosol optical depths from CALIPSO and MODIS-Aqua", *Atmos. Meas. Tech.*, **4**, 131-141, https://doi.org/10.5194/amt-4-131-2011.

Knobelspiesse, K., H. M. J. Barbosa, C. Bradley, C. Bruegge, B. Cairns, G. Chen, J. Chowdhary, A. Cook, A. Di Noia, B. van Diedenhoven, D. J. Diner, R. Ferrare, G. Fu, M. Gao, M. Garay, J. Hair, D. Harper, G. van Harten, O. Hasekamp, M. Helmlinger, C. Hostetler, O. Kalashnikova, A. Kupchock, K. Longo De Freitas, H. Maring, J. V. Martins, B. McBride, M. McGill, K. Norlin, A. Puthukkudy, B. Rheingans, J. Rietjens, F. C. Seidel, A. da Silva, M. Smit, S. Stamnes, Q. Tan, S. Val, A. Wasilewski, F. Xu, X. Xu, and J. Yorks, 2020: "The Aerosol Characterization from Polarimeter and Lidar (ACEPOL) airborne field campaign", *Earth Syst. Sci. Data*, **12**, 2183–2208, https://doi.org/10.5194/essd-12-2183-2020.

Koffi, B., M. Schulz, F.-M. Bréon, F. Dentener, B. M. Steensen, J. Griesfeller, D. Winker, Y. Balkanski, S. E. Bauer, N. Bellouin, T. Berntsen, H. Bian, M. Chin, T. Diehl, R. Easter, S. Ghan, D. A. Hauglustaine, T. Iversen, A. Kirkevåg, X. Liu, U. Lohmann, G. Myhre, P. Rasch, Ø. Seland, R. B. Skeie, S. D. Steenrod, P. Stier, J. Tackett, T. Takemura, K. Tsigaridis, M. R. Vuolo, J. Yoon, and K. Zhang, 2016: "Evaluation of the aerosol vertical distribution in global aerosol models through comparison against CALIOP measurements: AeroCom phase II results", *J. Geophys. Res. Atmos.*, **121**, 7254–7283, https://doi.org/10.1002/2015JD024639.

Konsta, D., I. Binietoglou, A. Gkikas, S. Solomos, E. Marinou, E. Proestakis, S. Basart, C. P. García-Pando, H. El-Askary, and V. Amiridis, 2018: "Evaluation of the BSC-DREAM8b regional dust model using the 3D LIVAS-CALIPSO product", *Atmos. Environ.*, **195**, 46–62, https://doi.org/10.1016/j.atmosenv.2018.09.047.

Korras-Carraca, M., V. Pappas, N. Hatzianastassiou, I. Vardavas, and C. Matsoukas, 2019: "Global vertically resolved aerosol direct radiation effect from three years of CALIOP data using the FORTH radiation transfer model", *Atmos. Res.*, **224**, 138–156, https://doi.org/10.1016/j.atmosres.2019.03.024.

Koshiro, T., M. Shiotani, H. Kawai, and S. Yukimoto, 2018: "Evaluation of Relationships between Subtropical Marine Low Stratiform Cloudiness and Estimated Inversion Strength in CMIP5 Models Using the Satellite Simulator Package COSP", *SOLA*, **14**, 25–32, https://doi.org/10.2151/sola.2018-005.

Krämer, M., C. Rolf, A. Luebke, A. Afchine, N. Spelten, A. Costa, J. Meyer, M. Zöger, J. Smith, R. L. Herman, B. Buchholz, V. Ebert, D. Baumgardner, S. Borrmann, M. Klingebiel, and L. Avallone, 2016: "A microphysics guide to cirrus clouds – Part 1: Cirrus types", *Atmos. Chem. Phys.*, **16**, 3463–3483, https://doi.org/10.5194/acp-16-3463-2016.

Lavy, L., P. Bernath, M. Lecours and D. English, 2024: "Antarctic polar stratospheric cloud composition as observed by ACE, CALIPSO and MIPAS", *JQSRT*, **324**, 109061, https://doi.org/10.1016/j.jqsrt.2024.109061.

Law, K. S., A. Stohl, P. K. Quinn, C. A. Brock, J. F. Burkhart, J.-D. Paris, G. Ancellet, H. B. Singh, A. Roiger, H. Schlager, J. Dibb, D. J. Jacob, S. R. Arnold, J. Pelon, and J. L. Thomas, 2014: "Arctic air pollution: new insights from POLARCAT-IPY", *B. Am. Meteorol. Soc.*, **95**, 1873– 1895, https://doi.org/10.1175/BAMS-D-13-00017.1.

Lawson, R. P., B. Pilson, B. Baker, Q. Mo, E. Jensen, L. Pfister, and P. Bui, 2008: "Aircraft measurements of microphysical properties of subvisible cirrus in the tropical tropopause layer", *Atmos. Chem. Phys.*, **8**, 1609–1620, https://doi.org/10.5194/acp-8-1609-2008.

L'Ecuyer, T., H. Beaudoing, M. Rodell, W. Olson, B. Lin, S. Kato, C. Clayson, E. Wood, J. Sheffield, R. Adler, G. Huffman, M. Bosilovich, G. Gu, F. Roberston, P. Houser, D. Chambers, J. Famiglietti, E. Fetzer, W. Liu, X. Gao, C. Schlosser, E. Clark, D. Lettenmaier, and K. Hilburn, 2015: "The Observed State of the Energy Budget in the Early 21st Century", *J. Climate*, **28**, 8319–8346, https://doi.org/10.1175/JCLI-D-14-00556.1.

L'Ecuyer, T. S., Y. Hang, A. V. Matus, and Z. Wang, 2019: "Reassessing the effect of cloud type on Earth's energy balance in the age of active spaceborne observations. Part I: Top-of-atmosphere and surface", *J. Climate*, **32**, 6197–6217, https://doi.org/10.1175/JCLI-D-18-0753.1.

Lee H., S.-J. Jeong, O. V. Kalashnikova, M. G. Tosca, S.-W. Kim, and J.-S. Kug, 2018: "Characterization of wildfire-induced aerosol emissions from the Maritime Continent peatland and Central African dry savannah with MISR and CALIPSO aerosol products", *J. Geophys. Res. Atmos.*, **123**, 3116–3125, https://doi.org/10.1002/2017JD027415.

Lesigne, T., F. Ravetta, A. Podglajen, V. Mariage, and J. Pelon, 2024: "Extensive coverage of ultrathin tropical tropopause layer cirrus clouds revealed by balloon-borne lidar observations", *Atmos. Chem. Phys.*, **24**, 5935–5952, https://doi.org/10.5194/acp-24-5935-2024.

Li, W., L. Dong and S. Khan, 2019a: "Environmental Study on Contribution Rates of Aerosol Scale Height and Humidity in PM2.5 Inversion Based on Calipso Data", *Ekoloji*, **28**, 1185–1197 [see http://www.ekolojidergisi.com/article/environmental-study-on-contribution-rates-of-aerosolscale-height-and-humidity-in-pm25-inversion-5739].

Li, W., E. Ali, I. A. El-Magd, M. M. Mourad, and H. El-Askary, 2019b: "Studying the Impact on Urban Health over the Greater Delta Region in Egypt Due to Aerosol Variability Using Optical Characteristics from Satellite Observations and Ground-Based AERONET Measurements", *Remote Sens.*, **11**, 1998, https://doi.org/10.3390/rs11171998.

Li, X., P. Chen, Z. Zhang, Y. Li, and D. Pan, 2025: "Vertical structure observation from spaceborne lidar ICESat-2 in East China Sea", *Opt. Express*, **33**, 2847-2865, https://doi.org/10.1364/OE.540111.

Li, Y., Y. Xue, J. Guang, L. She, C. Fan, and G. Chen, 2018: "Ground-Level PM2.5 Concentration Estimation from Satellite Data in the Beijing Area Using a Specific Particle Swarm Extinction Mass Conversion Algorithm", *Remote Sens.*, **10**, 1906, https://doi.org/10.3390/rs10121906.

Li, Z., D. Painemal, G. Schuster, M. Clayton, R. Ferrare, M. Vaughan, D. Josset, J. Kar, and C. Trepte, 2022: "Assessment of tropospheric CALIPSO Version 4.2 aerosol types over the ocean using independent CALIPSO-SODA lidar ratios", *Atmos. Meas. Tech.*, **15**, 2745–2766, https://doi.org/10.5194/amt-15-2745-2022.

Listowski, C., J. Delanoë, A. Kirchgaessner, T. Lachlan-Cope, and J. King, 2019: "Antarctic clouds, supercooled liquid water and mixed phase, investigated with DARDAR: geographical and seasonal variations", *Atmos. Chem. Phys.*, **19**, 6771–6808, https://doi.org/10.5194/acp-19-6771-2019.

Liu, C., X. Shen, and W. Gao, 2018: "Intercomparison of CALIOP, MODIS, and AERONET aerosol optical depth over China during the past decade", *Int. J. Remote Sens.*, **39**, 7251–7275, https://doi.org/10.1080/01431161.2018.1466070.

Liu, D., Q. Liu, L. Qi and Y. Fu, 2016: "Oceanic single-layer warm clouds missed by the Cloud Profiling Radar as inferred from MODIS and CALIOP measurements", *J. Geophys. Res. Atmos.*, **121**, 12947–12965, https://doi.org/10.1002/2016JD025485.

Liu, Z., M. J. McGill, Y. Hu, C. A. Hostetler, M. Vaughan, and D. Winker, 2004: "Validating lidar depolarization calibration using solar radiation scattered by ice clouds", *IEEE Geosci. Remote Sens. Lett.*, **1**, 157–161, https://doi.org/10.1109/LGRS.2004.829613.

Liu, Z., M. A. Vaughan, D. M. Winker, C. Kittaka, R. E. Kuehn, B. J. Getzewich, C. R. Trepte, and C. A. Hostetler, 2009: "The CALIPSO Lidar Cloud and Aerosol Discrimination: Version 2 Algorithm and Initial Assessment of Performance", *J. Atmos. Oceanic Technol.*, **26**, 1198–1213, https://doi.org/10.1175/2009JTECHA1229.1.

Liu, Z., D. Winker, A. Omar, M. Vaughan, J. Kar, C. Trepte, Y. Hu, and G. Schuster, 2015: "Evaluation of CALIOP 532-nm AOD over Opaque Water Clouds", *Atmos. Chem. Phys.*, **15**, 1265–1288, https://doi.org/10.5194/acp-15-1265-2015.

Liu, Z., J. Kar, S. Zeng, J. Tackett, M. Vaughan, M. Avery, J. Pelon, B. Getzewich, K.-P. Lee, B. Magill, A. Omar, P. Lucker, C. Trepte, and D. Winker, 2019: "Discriminating Between Clouds and Aerosols in the CALIOP Version 4.1 Data Products", *Atmos. Meas. Tech.*, **12**, 703–734, https://doi.org/10.5194/amt-12-703-2019.

Loeb N., S.-H. Ham, R. P. Allan, T. J. Thorsen, B. Meyssignac, S. Kato, G. C. Johnson, and J. M. Lyman, 2024: "Observational Assessment of Changes in Earth's Energy Imbalance Since 2000", *Surv. Geophys*, **4**, 1757–1783, https://doi.org/10.1007/s10712-024-09838-8.

Lu, X. and Y.-X. Hu, 2014: "Accuracy of land surface elevation from CALIPSO mission data", *Opt. Eng.*, **54**, 031102, https://doi.org/10.1117/1.OE.54.3.031102.

Lu, X., Y. Hu, C. Trepte and Z. Liu, 2014: "A Super-Resolution Laser Altimetry Concept", *IEEE Geosci. Remote Sens. Lett.*, **11**, 298–302, https://doi.org/10.1109/LGRS.2013.2256876.

Lu, X., Y. Hu, J. Pelon, C. Trepte, K. Liu, S. Rodier, S. Zeng, P. Lucker, R. Verhappen, J. Wilson, C. Audouy, C. Ferrier, S. Haouchine, B. Hunt, and B. Getzewich, 2016: "Retrieval of ocean subsurface particulate backscattering coefficient from space-borne CALIOP lidar measurements", *Optics Express*, **24**, 29001-29008, https://doi.org/10.1364/OE.24.029001.

Lu, X., Y. Hu, Z. Liu, S. Rodier, M. Vaughan, P. Lucker, C. Trepte, and J. Pelon, 2017: "Observations of Arctic snow and sea ice cover from CALIOP lidar measurements", *Remote Sens. Environ.*, **194**, 248–263, https://doi.org/10.1016/j.rse.2017.03.046.

Lu, X., Y. Hu, Y. Yang, P. Bontempi, A. Omar and R. Baize, 2020: "Antarctic spring ice-edge blooms observed from space by ICESat-2", *Remote Sens. Environ.*, **245**, 111827, https://doi.org/10.1016/j.rse.2020.111827.

Lu, X., Y. Hu, Y. Yang, T. Neumann, A. Omar, R. Baize, M. Vaughan, S. Rodier, B. Getzewich, P. Lucker, C. Trepte, C. Hostetler, and D. Winker, 2021: "New ocean subsurface optical properties from space lidars: CALIOP/CALIPSO and ATLAS/ICESat-2", *Earth and Space Sciences*, **8**, e2021EA001839, https://doi.org/10.1029/2021EA001839.

Lu, X., Y. Hu, A. Omar, Y. Yang, M. Vaughan, S. Rodier, Z. Lee, A. Garnier, R. Ryan, B. Getzewich and C. Trepte, 2022: "Nearshore bathymetry and seafloor property studies from space lidars: CALIPSO and ICESat-2", *Opt. Express*, **30**, 36509–36525, https://doi.org/10.1364/OE.471444.

Ma, S., X. Zhang, C. Gao, D. Q. Tong, A. Xiu, G. Wu, X. Cao, L. Huang, H. Zhao, S. Zhang, S. Ibarra-Espinosa, X. Wang, X. Li, and M. Dan, 2019: "Multi-model simulations of springtime dust storms in East Asia: Implications of an evaluation of four commonly used air quality models (CMAQv5.2.1, CAMxv6.50, CHIMEREv2017r4, and WRF-Chem v3.9.1)", Geosci. Model Dev., 12, 4603–4625, https://doi.org/10.5194/gmd-12-4603-2019.

Mace, G., Q. Zhang, M. Vaughan, R. Marchand, G. Stephens, C. Trepte and D. Winker, 2009a: "A Description of Hydrometeor Layer Occurrence Statistics Derived from the First Year of Merged Cloudsat and CALIPSO Data", *J. Geophys. Res.*, **114**, D00A26, https://doi.org/10.1029/2007JD009755.

Mace, G. G, J. E. Jensen, G. McFarquhar, J. Comstock, T. Ackerman, D. L. Mitchell, X. Liu, and T. Garrett, 2009b: "SPARTICUS: Small Particles in Cirrus Science and Operations Plan", 1-22, available at https://oasis.library.unlv.edu/renew_pubs/33.

Mahapatra, P. S., S. P. Puppala, B. Adhikary, K. L. Shrestha, D. P. Dawadi, S. P. Paudel, and A. K. Panday, 2019: "Air quality trends of the Kathmandu Valley: A satellite, observation and modeling perspective", *Atmos. Environ.*, **201**, 334–347, https://doi.org/10.1016/j.atmosenv.2018.12.043.

Mailhe, L., C. Schiff, and J. H. Stadler, 2004: "Calipso's Mission Design: Sun-Glint Avoidance Strategies", AAS/AIAA Space Flight Mechanics Conference, 8-12 February 2004, Maui HI, https://ntrs.nasa.gov/citations/20040081137.

Mallet, M., F. Dulac, P. Formenti, P. Nabat, J. Sciare, G. Roberts, J. Pelon, G. Ancellet, D. Tanré, F. Parol, C. Denjean, G. Brogniez, A. di Sarra, L. Alados-Arboledas, J. Arndt, F. Auriol, L. Blarel, T. Bourrianne, P. Chazette, S. Chevaillier, M. Claeys, B. D'Anna, Y. Derimian, K. Desboeufs, T. Di Iorio, J.-F. Doussin, P. Durand, A. Féron, E. Freney, C. Gaimoz, P. Goloub, J. L. Gómez-Amo, M. J. Granados-Muñoz, N. Grand, E. Hamonou, I. Jankowiak, M. Jeannot, J.-F. Léon, M. Maillé, S. Mailler, D. Meloni, L. Menut, G. Momboisse, J. Nicolas, T. Podvin, V. Pont, G. Rea, J.-B. Renard, L. Roblou, K. Schepanski, A. Schwarzenboeck, K. Sellegri, M. Sicard, F. Solmon, S. Somot, B Torres, J. Totems, S. Triquet, N. Verdier, C. Verwaerde, F. Waquet, J. Wenger, and P. Zapf, 2016: "Overview of the Chemistry-Aerosol Mediterranean Experiment/Aerosol Direct Radiative Forcing on the Mediterranean Climate (ChArMEx/ADRIMED) summer 2013 campaign", *Atmos. Chem. Phys.*, **16**, 455–504, https://doi.org/10.5194/acp-16-455-2016.

Mallet, M., P. Nabat, B. Johnson, M. Michou, J. M. Haywood, C. Chen, and O. Dubovik, 2021: "Climate models generally underrepresent the warming by Central Africa biomass-burning aerosols over the Southeast Atlantic", *Sci. Adv.*, **7**, eabg9998, https://www.science.org/doi/10.1126/sciadv.abg9998.

Mamouri, R. E., V. Amiridis, A. Papayannis, E. Giannakaki, G. Tsaknakis, and D. S. Balis, 2009: "Validation of CALIPSO space-borne-derived attenuated backscatter coefficient profiles using a ground-based lidar in Athens, Greece", *Atmos. Meas. Tech.*, **2**, 513-522, https://doi.org/10.5194/amt-2-513-2009.

Mao, F., Z. Liang, Z. Pan, W. Gong, J. Sun, T. Zhang, X. Huang, L. Zang, X. Lu and J. Hong, 2021: "A simple multiscale layer detection algorithm for CALIPSO measurements", *Remote Sens. Environ.*, **266**, 112687, https://doi.org/10.1016/j.rse.2021.112687.

Maring, H., 2007: "Overview of A-Train Satellite Cloud Measurements", American Geophysical Union, Fall Meeting 2007, Abstract ID A42C-01, 10-14 December 2007, San Francisco, CA; see https://ui.adsabs.harvard.edu/abs/2007AGUFM.A42C..01M/abstract.

Marquis, J. W., A. S. Bogdanoff, J. R. Campbell, J. A. Cummings, D. L. Westphal, N. J. Smith, and J. Zhang, 2017: "Estimating Infrared Radiometric Satellite Sea Surface Temperature Retrieval Cold Biases in the Tropics due to Unscreened Optically-Thin Cirrus Clouds", *J. Atmos. Oceanic Technol.*, **34**, 355–373, https://doi.org/10.1175/JTECH-D-15-0226.1.

Martinsson, B. G., J. Friberg, O. S. Sandvik, M. Hermann, P. F. J. van Velthoven, and A. Zahn, 2017: "Particulate sulfur in the upper troposphere and lowermost stratosphere – sources and climate forcing", *Atmos. Chem. Phys.*, **17**, 10937–10953, https://doi.org/10.5194/acp-17-10937-2017.

Masunaga, H. and S. Bony, 2018: "Radiative Invigoration of Tropical Convection by Preceding Cirrus Clouds", *J. Atmos. Sci.*, **75**, 1327–1342, https://doi.org/10.1175/JAS-D-17-0355.1.

Matus A., and T. L'Ecuyer, 2017: "The role of cloud phase in Earth's radiation budget", *J. Geophys. Res. Atmos.*, 122, 2559–2578, https://doi.org/10.1002/2016JD025951.

Matus, A. V., T. S. L'Ecuyer, and D. S. Henderson, 2019: "New Estimates of Aerosol Direct Radiative Effects and Forcing From A-Train Satellite Observations", *Geophys. Res. Lett.*, **46** (14), 8338–8346, https://doi.org/10.1029/2019gl083656.

McCormick, M. P. and T. J. Swissler, 1983: "Stratospheric aerosol mass and latitudinal distribution of El Chicon eruption cloud for October 1982", *Geophys. Res. Lett.*, **10**(9), 877-880, https://doi.org/10.1029/GL010i009p00877.

McCormick, M. P., T. J. Swissler, W. P. Chu and W. H. Fuller Jr, 1978: "Post-Volcanic Stratospheric Aerosol Decay as Measured by Lidar", *J. Atmos. Sci.,* **35**, 1296-1303, https://doi.org/10.1175/1520-0469(1978)035<1296:PVSADA>2.0.CO;2.

McGill, M. J., M. A. Vaughan, C. R. Trepte, W. D. Hart, D. L. Hlavka, D. M. Winker, and R. Kuehn, 2007: "Airborne validation of spatial properties measured by the CALIPSO lidar", *J. Geophys. Res.*, **112**, D20201, https://doi.org/10.1029/2007JD008768.

McKim, B., S. Bony and J. L. Dufresne, 2024: "Weak anvil cloud area feedback suggested by physical and observational constraints", *Nat. Geosci.*, https://doi.org/10.1038/s41561-024-01414-4.

Megie, G., F. Bos, J. E. Blamont, and M. L. Chanin, 1978: "Simultaneous nighttime Lidar measurements of atmospheric sodium and potassium", *Planetary and Space Science*, **26**, 27-35, https://doi.org/10.1016/0032-0633(78)90034-X.

Miller, S. D. and G. L. Stephens, 1999: "Multiple scattering effects in the lidar pulse stretching problem", *J. Geophys. Res. Atmos.*, **104**, 22205-22219, https://doi.org/10.1029/1999JD900481.

Min, M., J. Li, F. Wang, Z. Liu, and W. P. Menzel, 2020: "Retrieval of cloud top properties from advanced geostationary satellite imager measurements based on machine learning algorithms", *Remote Sens. Environ.*, **239**, 111616, https://doi.org/10.1016/j.rse.2019.111616.

Minnis, P., S. Sun-Mack, W. L. Smith Jr., G. Hong, and Y. Chen, 2019: "Advances in neural network detection and retrieval of multilayer clouds for CERES using multispectral satellite data," Proc. SPIE 11152, Remote Sensing of Clouds and the Atmosphere XXIV, 1115202 (9 October 2019), https://doi.org/10.1117/12.2532931.

Minnis, P., S. Sun-Mack, Y. Chen, F.-L. Chang, C. R. Yost, W. L. Smith, Jr., P. W. Heck, R. F. Arduini, Q. Z. Trepte, K. Ayers, K. Bedka, S. Bedka, R. R. Brown, D. R. Doelling, A. Gopalan, E. Heckert, G. Hong, Z. Jin, R. Palikonda, R. Smith, B. Scarino, D. A. Spangenberg, P. Yang, Y. Xie, and Y. Yi, 2021: "CERES MODIS cloud product retrievals for Edition 4, Part 1: Algorithm changes", *IEEE Trans. Geosci. Remote Sens.*, **59**, 2744-2780, https://doi.org/10.1109/TGRS.2020.3008866.

Mioche, G., D. Josset, J.-F. Gayet, J. Pelon, A. Garnier, A. Minikin and A. Schwarzenboeck, 2010: "Validation of the CALIPSO/CALIOP extinction coefficients from in situ observations in mid-latitude cirrus clouds during CIRCLE-2 experiment", *J. Geophys. Res.*, **115**, D00H25, https://doi.org/10.1029/2009JD012376.

Mioche, G. and O. Jourdan, 2018: "Spaceborne Remote Sensing and Airborne In Situ Observations of Arctic Mixed-Phase Clouds", in Mixed-Phase Clouds: Observations and Modeling, C. Andronache, Ed., Elsevier, ISBN: 978-0-12-810549-8, pp. 121–150, https://doi.org/10.1016/B978-0-12-810549-8.00006-4.

Mitchell, D. L., A. Garnier, J. Pelon and E. Erfani, 2018: "CALIPSO (IIR-CALIOP) Retrievals of Cirrus Cloud Ice Particle Concentrations", *Atmos. Chem. Phys.*, **18**, 17325–17354, https://doi.org/10.5194/acp-18-17325-2018.

Mitchell, D. L., A. Garnier and S. Woods, 2025: "Advances in CALIPSO (IIR) cirrus cloud property retrievals – Part 1: Methods and testing", *Atmos. Chem. Phys.*, **25**, 14071–14098, https://doi.org/10.5194/acp-25-14071-2025.

Mitchell, D. L. and A. Garnier, 2025: "Advances in CALIPSO (IIR) cirrus cloud property retrievals – Part 2: Global estimates of the fraction of cirrus clouds affected by homogeneous ice nucleation", *Atmos. Chem. Phys.*, **25**, 14099–14129, https://doi.org/10.5194/acp-25-14099-2025.

Molina, L. T., S. Madronich, J. S. Gaffney, E. Apel, B. de Foy, J. Fast, R. Ferrare, S. Herndon, J. L. Jimenez, B. Lamb, A. R. Osornio-Vargas, P. Russell, J. J. Schauer, P. S. Stevens, R. Volkamer, and M. Zavala, 2010: "An overview of the MILAGRO 2006 Campaign: Mexico City emissions and their transport and transformation", *Atmos. Chem. Phys.*, **10**, 8697–8760, https://doi.org/10.5194/acp-10-8697-2010.

Morrison, A. L., J. E. Kay, H. Chepfer, R. Guzman and V. Yettella, 2018: "Isolating the liquid cloud response to recent Arctic sea ice variability using spaceborne lidar observations", *J. Geophys. Res. Atmos.*, **123**, 473–490, https://doi.org/10.1002/2017JD027248.

Nabavi, S. O., L. Haimberger and C. Samimi, 2017: "Sensitivity of WRF-chem predictions to dust source function specification in West Asia", *Aeolian Research*, **24**, 115-131, https://doi.org/10.1016/j.aeolia.2016.12.005.

Nam, C. , S. Bony, J.-L. Dufresne, and H. Chepfer, 2012: "The 'too few, too bright' tropical low cloud problem in CMIP5 models", *Geophys. Res. Lett.*, **39**, L21801, https://doi.org/10.1029/2012GL053421.

Nam, J., S.-W. Kim, R. J. Park, J.-S. Park and S. S. Park, 2018: "Changes in column aerosol optical depth and ground-level particulate matter concentration over East Asia", *Air. Qual. Atmos. Health*, **11**, 49–60, https://doi.org/10.1007/s11869-017-0517-5.

National Academies of Sciences, Engineering, and Medicine, 2018: "Thriving on Our Changing Planet: A Decadal Strategy for Earth Observation from Space", The National Academies Press, Washington, DC, https://doi.org/10.17226/24938

National Research Council, 1996: "A Plan for a Research Program on Aerosol Radiative Forcing and Climate Change", The National Academies Press, Washington, DC, https://doi.org/10.17226/5107.

Nayak, M., M. Witkowski, D. Vane, T. Livermore, M. Rokey, M. Barthuli, I. J. Gravseth, B. Pieper, A. Rodzinak, S. Silva and P. Woznick, 2012: "CloudSat Anomaly Recovery and Operational Lessons

Learned", SpaceOps 2012, Stockholm, Sweden, 11–15 June 2012, https://ntrs.nasa.gov/citations/20130009146.

Neukermans, G., T. Harmel, M. Galí, N. Rudorff, J. Chowdhary, O. Dubovik, C. Hostetler, Y. Hu, C. Jamet, K. Knobelspiesse, Y. Lehahn, P. Litvinov, A. M. Sayer, B. Ward, E. Boss, I. Koren and L. A. Miller, 2018: "Harnessing remote sensing to address critical science questions on ocean-atmosphere interactions", *Elem. Sci. Anth.*, **6**, 71, https://doi.org/10.1525/elementa.331.

Noh, Y.-J., J. M. Forsythe, S. D. Miller, C. J. Seaman, Y. Li, A. K. Heidinger, D. T. Lindsey, M. A. Rogers, and P. T. Partain, 2017: "Cloud Base Height Estimation from VIIRS. Part II: A Statistical Algorithm Based on A-Train Satellite Data", *J. Atmos. Oceanic Technol.*, **34**, 585–598, https://doi.org/10.1175/JTECH-D-16-0110.1.

Nowottnick, E. P. A. K. Rowe, A. R. Nehrir, J. A. Zawislak, A. J. Piña, W. McCarty, R. A. Barton-Grimley, K. M. Bedka, J. R. Bennett, A. Brammer, M. E. Buzanowicz, G. Chen, S.-H. Chen, S. S. Chen, P. R. Colarco, J. W. Cooney, E. Crosbie, J. Doyle, T. Fehr, R. A. Ferrare, S. D. Harrah, S. M. Hristova-Veleva, B. H. Lambrigtsen, Q. A. Lawton, A. Lee, E. Marinou, E. R. Martin, G. Močnik, E. Mazza, R. Rodriguez Monje, K. M. Núñez Ocasio, Z. Pu, M. Rajagopal, J. S. Reid, C. E. Robinson, R. Rios-Berrios, B. D. Rodenkirch, N. Sakaeda, V. Salazar, M. A. Shook, L. Sinclair, G. M. Skofronick-Jackson, K. L. Thornhill, R. D. Torn, D. P. Van Gilst, P. G. Veals, H. Vömel, S. Wong, S.-N. Wu, L. D. Ziemba, and E. J. Zipser, 2024: "Dust, convection, winds and waves: The 2022 NASA CPEX-CV campaign", *Bull. Amer. Meteor. Soc.*, **105**, E2097-E2125, https://doi.org/10.1175/BAMS-D-23-0201.1.

O, K.-T., R. Wood, and H.-H. Tseng, 2018: "Deeper, precipitating PBLs associated with optically thin veil clouds in the Sc-Cu transition", *Geophys. Res. Lett.*, **45**, 5177–5184, https://doi.org/10.1029/2018GL077084.

Ocko, I. B. and P. A. Ginoux**,** 2017: "Comparing multiple model-derived aerosol optical properties to collocated ground-based and satellite measurements", *Atmos. Chem. Phys.*, **17**, 4451–4475, https://doi.org/10.5194/acp-17-4451-2017.

Oh, S. M., R. Borde, M. Carranza, and I.-C. Shin, 2019: "Development and Intercomparison Study of an Atmospheric Motion Vector Retrieval Algorithm for GEO-KOMPSAT-2A", *Remote Sens.*, **11**, 2054, https://doi.org/10.3390/rs11172054.

Oikawa, E., T. Nakajima, and D. Winker, 2018: "An Evaluation of the Shortwave Direct Aerosol Radiative Forcing Using CALIOP and MODIS Observations", *J. Geophys. Res.*, **123** (2), 1211–1233, https://doi.org/10.1002/2017jd027247.

Omar, A., D. Winker, C. Kittaka, M. Vaughan, Z. Liu, Y. Hu, C. Trepte, R. Rogers, R. Ferrare, R. Kuehn, and C. Hostetler, 2009: "The CALIPSO Automated Aerosol Classification and Lidar Ratio Selection Algorithm", *J. Atmos. Oceanic Technol.*, **26**, 1994–2014, https://doi.org/10.1175/2009JTECHA1231.1.

Omar, A., Z. Liu, M. Vaughan, K. L. Thornhill, C. Kittaka, S. Ismail, Y. Hu, G. Chen, D. Winker, C. Trepte, E. L. Winstead, and B. E Anderson, 2010: "Extinction-to-backscatter ratios of Saharan dust layers derived from in situ measurements and CALIPSO overflights during NAMMA", *J. Geophys. Res.*, **115**, D24217, https://doi.org/10.1029/2010JD014223.

Omar, A. H., D. M. Winker, J. Tackett, D. Giles, J. Kar, Z. Liu, M. Vaughan, K. Powell, and C. Trepte, 2013: "CALIOP and AERONET Aerosol Optical Depth Comparisons: One Size Fits None", *J. Geophys. Res.*, **118**, 4748-4766, https://doi.org/10.1002/jgrd.50330.

Osborn, M. T., 1998: "Calibration of LITE data", in: Proceedings of the 19th International Laser Radar Conference, NASA/CP-19980227633, 245–247, Annapolis, MD, USA, 6–10 July 1998.

Painemal, D., M. Clayton, R. Ferrare, S. Burton, D. Josset, and M. Vaughan, 2019: "Novel aerosol extinction coefficients and lidar ratios over the ocean from CALIPSO–CloudSat: evaluation and global statistics", *Atmos. Meas. Tech.*, **12**, 2201–2217, https://doi.org/10.5194/amt-12-2201-2019.

Painemal, D., F.-L. Chang, R. Ferrare, S. Burton, Z. Li, W. L. Smith Jr., P. Minnis, Y. Feng, and M. Clayton, 2020: "Reducing uncertainties in satellite estimates of aerosol-cloud interactions over the subtropical ocean by integrating vertically resolved aerosol observations", *Atmos. Chem. Phys.*, **20**, 7167-7177, https://doi.org/10.5194/acp-20-7167-2020.

Palm, S., D. Hlavka, W. Hart, J. Spinhirne, and M. McGill, 2004: "Calibration of the Geoscience Laser Altimeter System (GLAS) atmospheric channels", in: Proceedings of the 22nd International Laser Radar Conference, ESA SP-561, 1003–1006, Matera, Italy, 12–16 July 2004.

Palm, S., Y. Yang, J. Spinhirne and A. Marshak, 2011: "Satellite Remote Sensing of Blowing Snow Properties over Antarctica", *J. Geophys. Res.*, **116**, D16123, https://doi.org/10.1029/2011JD015828.

Palm, S. P., V. Kayetha, Y. Yang and R. Pauly, 2017: "Blowing snow sublimation and transport over Antarctica from 11 years of CALIPSO observations", *The Cryosphere*, **11**, 2555–2569, https://doi.org/10.5194/tc-11-2555-2017.

Pan, Z., F. Mao, X. Lu, W. Gong, H. Shen, and Q. Mao, 2019: "Enhancement of vertical cloud-induced radiative heating in East Asian monsoon circulation derived from CloudSat-CALIPSO observations", *Int. J. Remote Sens.*, **41**, 595–614, https://doi.org/10.1080/01431161.2019.1646935.

Parish, D. D., D. T. Allen, T. S. Bates, M. Estes, F. C. Fehsenfeld, G. Feingold, R. Ferrare, R. M. Hardesty, J. F. Meagher, J. W. Nielsen-Gammon, R. B. Pierce, T. B. Ryerson, J. H. Seinfeld, and E. J. Williams, 2009: "Overview of the Second Texas Air Quality Study (TexAQS II) and the Gulf of Mexico Atmospheric Composition and Climate Study (GoMACCS)", *J. Geophys. Res.*, **114**, D7, https://doi.org/10.1029/2009JD011842.

Pelon, J., D. Winker, G. Ancellet, M. Vaughan, D. Josset, A. Bazureau, and N. Pascal, 2017: "Space observation of aerosols from satellite over China during pollution episodes: status and perspectives", in Air Pollution in Eastern Asia: An Integrated Perspective, I. Bouarar, X. Wang and G. P. Brasseur, Eds., Springer-Verlag GmbH, ISBN 978-3319594880.

Peng, N., J. Su, X. Han, X. Deng, W. Lan, and Jinyan Wang, 2023: "Distributions and Direct Radiative Effects of Different Aerosol Types in North China", *Remote Sens.*, **15**, 5511, https://doi.org/10.3390/rs15235511.

Penner, J. E., C. Zhou, A. Garnier, and D. L. Mitchell, 2018: "Anthropogenic Aerosol Indirect Effects in Cirrus Clouds", *J. Geophys. Res. Atmos.*, **123**, 11,652–11,677, https://doi.org/10.1029/2018JD029204.

Petersen, W. A., D. Hudak, V. N. Bringi, P. Siqueira, A. Tokay, V. Chandrasekar, L. F. Bliven, R. Cifelli, T. Lang, S. Rutledge, G. Skofronick-Jackson, and M. Schwaller, 2007: "NASA GPM/PMM participation in the Canadian CloudSat/CALIPSO Validation Project (C3VP): Physical process studies in snow", 33rd International Conference on Radar Meteorology, American Meteorological Society, 6-10 August 2007, Cairns, Australia, available at https://gpm.nasa.gov/sites/default/files/document_files/petersenetal_C3VP.pdf.

Peterson, D., E. Hyer, and J. Wang, 2014: "Quantifying the potential for high-altitude smoke injection in the North American boreal forest using the standard MODIS fire products and subpixel-based methods", *J. Geophys. Res. Atmos.*, **119**, 3401– 3419, https://doi.org/10.1002/2013JD021067.

Peterson, D. A., J. R. Campbell, E. J. Hyer, M. D. Fromm, G. P. Kablick III, J. H. Cossuth, and M. T. Deland, 2018: "Wildfire-driven thunderstorms cause a volcano-like stratospheric injection of smoke", *npj Clim. Atmos. Sci.*, **1**, 30, https://doi.org/10.1038/s41612-018-0039-3.

Pitts, M. C., L. R. Poole and R. Gonzalez, 2018: "Polar stratospheric cloud climatology based on CALIPSO spaceborne lidar measurements from 2006–2017", *Atmos. Chem. Phys.*, **18**, 10881–10913, https://doi.org/10.5194/acp-18-10881-2018.

Platnick, S., K. G. Meyer, M. D. King, G. Wind, N. Amarasinghe, B. Marchant, G. T. Arnold, Z. Zhang, P. A. Hubanks, R. E. Holz, P. Yang, W. L. Ridgway, and J. Riedi, 2017: "The MODIS Cloud Optical and Microphysical Products: Collection 6 Updates and Examples from Terra and Aqua", *IEEE Trans. Geosci. Remote Sens.*, **55**, 502–525, https://doi.org/10.1109/TGRS.2016.2610522.

Platt, C. M. R., 1973: "Lidar and Radiometric Observations of Cirrus Clouds", *J. Atmos. Sci.*, **6**, 1191–1204 , https://doi.org/10.1175/1520-0469(1973)030<1191:LAROOC>2.0.CO;2.

Po-Chedley, S., M. D. Zelinka, N. Jeevanjee, T. J. Thorsen, and B. D. Santer, 2019: "Climatology explains intermodel spread in tropical upper tropospheric cloud and relative humidity response to greenhouse warming", *Geophys. Res. Lett.*, **46**, 13399–13409, https://doi.org/10.1029/2019GL084786.

Powell, K. A., C. A. Hostetler, Z. Liu, M. A. Vaughan, R. E. Kuehn, W. H. Hunt, K. Lee, C. R. Trepte, R. R. Rogers, S. A. Young, and D. M. Winker, 2009: "CALIPSO Lidar Calibration Algorithms: Part I - Nighttime 532 nm Parallel Channel and 532 nm Perpendicular Channel", *J. Atmos. Oceanic Technol.*, **26**, 2015-2033, https://doi.org/10.1175/2009-JTECHA1242.1.

Prospero, J. M., P. Ginoux, O. Torres, S. E. Nicholson, and T. E. Gill, 2002: "Environmental Characterization of Global Sources of Atmospheric Soil Dust Identified with the NIMBUS 7 Total Ozone Mapping Spectrometer (TOMS) Absorbing Aerosol Product", *Rev. Geophys.*, **40**(1), 1002, https://doi.org/10.1029/2000RG000095.

Qin, Y., A. D. Steven, T. Schroeder, T. R. McVicar, J. Huang, M. Cope, and S. Zhou, 2019: "Cloud Cover in the Australian Region: Development and Validation of a Cloud Masking, Classification and Optical Depth Retrieval Algorithm for the Advanced Himawari Imager", *Front. Environ. Sci.*, **7**, https://doi.org/10.3389/fenvs.2019.00020.

Quennehen, B., J.-C. Raut, K. S. Law, N. Daskalakis, G. Ancellet, C. Clerbaux, S.-W. Kim, M. T. Lund, G. Myhre, D. J. L. Olivié, S. Safieddine, R. B. Skeie, J. L. Thomas, S. Tsyro, J. Bazureau, A., Bellouin, N., Hu, M., Kanakidou, M., Klimont, Z., Kupiainen, K., Myriokefalitakis, S., Quaas, S. T. Rumbold, M. Schulz, R. Cherian, A. Shimizu, J. Wang, S.-C. Yoon, and T. Zhu, 2016: "Multimodel evaluation of short-lived pollutant distributions over east Asia during summer 2008", *Atmos. Chem. Phys.*, **16**, 10765–10792, https://doi.org/10.5194/acp-16-10765-2016.

Ray, D., A. Ghosh, A. Chatterjee, S. K. Ghosh, and S. Raha, 2019: "Size-specific PAHs and Associated Health Risks over a Tropical Urban Metropolis: Role of Long-range Transport and Meteorology", *Aerosol Air. Qual. Res.*, **19**, 2446–2463, https://doi.org/10.4209/aaqr.2019.06.0312.

Raymond, D. J., 2000: "The Hadley circulation as a radiative-convective instability", *J. Atmos. Sci.*, **57**, 1286–1297, https://doi.org/10.1175/1520-0469(2000)057<1286:THCAAR>2.0.CO;2.

Reagan, J. A. and D. A. Zielinskie, 1991: "Spaceborne lidar remote sensing techniques aided by surface returns", Opt. Eng., 30, 96–102, https://doi.org/10.1117/12.55776.

Redemann, J., M. A. Vaughan, Q. Zhang, Y. Shinozuka, P. B. Russell, J. M. Livingston, M. Kacenelenbogen and L. A. Remer, 2012: "The comparison of MODIS-Aqua (C5) and CALIOP (V2 & V3) aerosol optical depth", *Atmos. Chem. Phys.*, **12**, 3025–3043, https://doi.org/10.5194/acp-12-3025-2012.

Redemann, J., R. Wood, P. Zuidema, S. J. Doherty, B. Luna, S. E. LeBlanc, M. S. Diamond, Y. Shinozuka, I. Y. Chang, R. Ueyama, L. Pfister, J.-M. Ryoo, A. N. Dobracki, A. M. da Silva, K. M. Longo, M. S. Kacenelenbogen, C. J. Flynn, K. Pistone, N. M. Knox, S. J. Piketh, J. M. Haywood, P. Formenti, M. Mallet, P. Stier, A. S. Ackerman, S. E. Bauer, A. M. Fridlind, G. R. Carmichael, P. E. Saide, G. A. Ferrada, S. G. Howell, S. Freitag, B. Cairns, B. N. Holben, K. D. Knobelspiesse, S. Tanelli, T. S. L'Ecuyer, A. M. Dzambo, O. O. Sy, G. M. McFarquhar, M. R. Poellot, S. Gupta, J. R. O'Brien, A. Nenes, M. Kacarab, J. P. S. Wong, J. D. Small-Griswold, K. L. Thornhill, D. Noone, J. R. Podolske, K. S. Schmidt, P. Pilewskie, H. Chen, S. P. Cochrane, A. J. Sedlacek, T. J. Lang, E. Stith, M. Segal-Rozenhaimer, R. A. Ferrare, S. P. Burton, C. A. Hostetler, D. J. Diner, F. C. Seidel, S. E. Platnick, J. S. Myers, K. G. Meyer, D. A. Spangenberg, H. Maring, and L. Gao, 2021: "An overview of the ORACLES (ObseRvations of Aerosols above CLouds and their intEractionS) project: aerosol–cloud–radiation interactions in the southeast Atlantic basin", *Atmos. Chem. Phys.*, **21**, 1507–1563, https://doi.org/10.5194/acp-21-1507-2021.

Reid, J. S. H. B. Maring, G. T. Narisma, S. van den Heever, L. Di Girolamo, R. Ferrare, P. Lawson, G. G. Mace, J. B. Simpas, S. Tanelli, L. Ziemba, B. van Diedenhoven, R. Bruintjes, A. Bucholtz, B. Cairns, M. O. Cambaliza, G. Chen, G. S. Diskin, J. H. Flynn, C. A. Hostetler, R. E. Holz, T. J. Lang, K. S. Schmidt, G. Smith, A. Sorooshian, E. J. Thompson, K. L. Thornhill, C. Trepte, J. Wang, S. Woods, S. Yoon, M. Alexandrov, S. Alvarez, C. G. Amiot, J. R. Bennett, M. Brooks, S. P. Burton, E. Cayanan, H. Chen, A. Collow, E. Crosbie, A. DaSilva, J. P. DiGangi, D. D. Flagg, S. W. Freeman, D. Fu, E. Fukada, M. R. A. Hilario, Y. Hong, S. M. Hristova-Veleva, R. Kuehn, R. S. Kowch, G. R. Leung, J. Loveridge, K. Meyer, R. M. Miller, M. J. Montes, J. N. Moum, A. Nenes, S. W. Nesbitt, M. Norgren, E. P. Nowottnick, R. M. Rauber, E. A. Reid, S. Rutledge, J. S. Schlosser, T. T. Sekiyama, M. A. Shook, G. A. Sokolowsky, S. A. Stamnes, T. Y. Tanaka, A. Wasilewski, P. Xian, Q. Xiao, Zhuocan Xu, and J. Zavaleta, 2023: "The Coupling Between Tropical Meteorology, Aerosol Lifecycle, Convection, and Radiation during the Cloud, Aerosol and Monsoon Processes Philippines Experiment (CAMP^{2}Ex)", *Bull. Amer. Meteor. Soc.*, **104**, E1179–E1205, https://doi.org/10.1175/BAMS-D-21-0285.1.

Rodenkirch, B. D. and A. K., Rowe, 2024: "Near-Storm Environmental Relationships With Tropical Oceanic Convective Structure Observed During NASA CPEX and CPEX-AW", *J. Geophys. Res. Atmos.*, **129**, e2023JD039632, https://doi.org/10.1029/2023JD039632.

Rodriguez, J. V., R. C. Verhappen, C. Weimer, C. R. Trepte, and T. E. Cayton, 2022: "Charged Particle Fluxes Associated With CALIPSO Low Laser Energy Shots," *IEEE Transactions on Nuclear Science*, **69**(10), 2146-2153, https://doi.org/10.1109/TNS.2022.3204715.

Rogers, R. R., C. A. Hostetler, J. W. Hair, R. A. Ferrare, Z. Liu, M. D. Obland, D. B. Harper, A. L. Cook, K. A. Powell, M. A. Vaughan, and D. M. Winker, 2011: "Assessment of the CALIPSO

Lidar 532 nm Attenuated Backscatter Calibration Using the NASA LaRC Airborne High Spectral Resolution Lidar", *Atmos. Chem. Phys.*, **11**, 1295-1311, https://doi.org/10.5194/acp-11-1295-2011.

Rogers, R. R., M. A. Vaughan, C. A. Hostetler, S. P. Burton, R. A. Ferrare, S. A. Young, J. W. Hair, M. D. Obland, D. B. Harper, A. L. Cook, and D. M. Winker, 2014: "Looking Through the Haze: Evaluating the CALIPSO Level 2 Aerosol Optical Depth using Airborne High Spectral Resolution Lidar Data", *Atmos. Meas. Tech.*, **7**, 4317-4340, https://doi.org/10.5194/amt-7-4317-2014.

Rollins, A. W., T. D. Thornberry, E. Atlas, M. Navarro, S. Schauffler, F. Moore, J. W. Elkins, E. Ray, K. Rosenlof, V. Aquila, and R.-S. Gao, 2018: "SO2 Observations and Sources in the Western Pacific Tropical Tropopause Region", *J. Geophys. Res. Atmos.*, **123**, 13,549-13,559, https://doi.org/10.1029/2018JD029635.

Ryan, R. A., M. A. Vaughan, S. D. Rodier, J. L. Tackett, J. A. Reagan, R. A. Ferrare, J. W. Hair, and B. J. Getzewich, 2024: "Total Column Optical Depths Retrieved from CALIPSO Lidar Ocean Surface Backscatter", *Atmos. Meas. Tech.*, **17**, 6517–6545, https://doi.org/10.5194/amt-17-6517-2024.

Ryder, C. L., J. B. McQuaid, C. Flamant, P. D. Rosenberg, R. Washington, H. E. Brindley, E. J. Highwood, J. H. Marsham, D. J. Parker, M. C. Todd, J. R. Banks, J. K. Brooke, S. Engelstaedter, V. Estelles, P. Formenti, L. Garcia-Carreras, C. Kocha, F. Marenco, H. Sodemann, C. J. T. Allen, A. Bourdon, M. Bart, C. Cavazos-Guerra, S. Chevaillier, J. Crosier, E. Darbyshire, A. R. Dean, J. R. Dorsey, J. Kent, D. O'Sullivan, K. Schepanski, K. Szpek, J. Trembath, and A. Woolley, 2015: "Advances in understanding mineral dust and boundary layer processes over the Sahara from Fennec aircraft observations", *Atmos. Chem. Phys.*, **15**, 8479–8520, http://doi.org/10.5194/acp-15-8479-2015.

Ryder, C. L., C. Bézier, H. F. Dacre, R. Clarkson, V. Amiridis, E. Marinou, E. Proestakis, Z. Kipling, A. Benedetti, M. Parrington, S. Rémy and M. Vaughan, 2024: "Aircraft engine dust ingestion at global airports", *Nat. Hazards Earth Syst. Sci.*, **24**, 2263–2284, https://doi.org/10.5194/nhess-24-2263-2024.

Saint-Lu, M., S. Bony and J.-L. Dufresne, 2020: "Observational Evidence for a Stability Iris Effect in the Tropics", *Geophys. Res. Lett.*, **47**, e2020GL089059, https://doi.org/10.1029/2020GL089059.

Santek, D. R. Dworak, S. Nebuda, S. Wanzong, R. Borde, I. Genkova, J. García-Pereda, R. Galante Negri, M. Carranza, K. Nonaka, K. Shimoji, S. M. Oh, B.-I. Lee, S.-R. Chung, J. Daniels, W. Bresky, 2019: "2018 Atmospheric Motion Vector (AMV) Intercomparison Study", *Remote Sens.*, **11**, 2240, https://doi.org/10.3390/rs11192240.

Šavli, M., J. de Kloe, G.-J. Marseille, M. Rennie, N. Žagar and N. Wedi, 2019: "The prospects for increasing the horizontal resolution of the Aeolus horizontal line-of-sight wind profiles", *Q. J. Roy. Meteorol. Soc.*, **145**, 3499–3515, https://doi.org/10.1002/qj.3634.

Schafler, A., G. Craig, H. Wernli, P. Arbogast, J. D. Doyle, R. McTaggart-Cowan, J. Methven, G. Rivière, F. Ament, M. Boettcher, M. Bramberger, Q. Cazenave, R. Cotton, S. Crewell, J. Delanoë, A. Dörnbrack, A. Ehrlich, F. Ewald, A. Fix, C. M. Grams, S. L. Gray, H. Grob, S. Groß, M. Hagen, B. Harvey, L. Hirsch, M. Jacob, T. Kölling, H. Konow, C. Lemmerz, O. Lux, L. Magnusson, B. Mayer, M. Mech, R. Moore, J. Pelon, J. Quinting, S. Rahm, M. Rapp, M. Rautenhaus, O. Reitebuch, C. A. Reynolds, H. Sodemann, T. Spengler, G. Vaughan, M. Wendisch, M. Wirth, B. Witschas, K. Wolf, and T. Zinner, 2018: "The North Atlantic Waveguide and Downstream Impact Experiment", *Bull. Amer. Meteor. Soc.*, **99**, 1607-1637, https://doi.org/10.1175/BAMS-D-17-0003.1.

Schoeberl, M. R., E. J. Jensen, L. Pfister, R. Ueyama, T. Wang, H. Selkirk, M. Avery, T. Thornberry, and A. E. Dessler, 2019: "Water vapor, clouds, and saturation in the tropical tropopause layer", *J. Geophys. Res. Atmos.*, **124**, 3984–4003, https://doi.org/10.1029/2018JD029849.

Schoeberl, M. R., E. J. Jensen, L. Pfister, R. Ueyama, M. Avery, and A. E. Dessler, 2018: "Convective Hydration of the Upper Troposphere and Lower Stratosphere", *J. Geophys. Res. Atmos.*, **123**, 4583–4593, https://doi.org/10.1029/2018JD028286.

Schulte, R. M., M. D. Lebsock, J. M. Haynes and Y. Hu, 2024: "A random forest algorithm for the prediction of cloud liquid water content from combined CloudSat–CALIPSO observations", *Atmos. Meas. Tech.*, **17**, 3583–3596, https://doi.org/10.5194/amt-17-3583-2024.

Schuster, G. L., M. Vaughan, D. MacDonnell, W. Su, D. Winker, O. Dubovik, T. Lapyonok, and C. Trepte, 2012: "Comparison of CALIPSO aerosol optical depth retrievals to AERONET measurements, and a climatology for the lidar ratio of dust", *Atmos. Chem. Phys.*, **12**, 7431-7452, https://doi.org/10.5194/acp-12-7431-2012.

Sekiyama, T. T., Tanaka, T. Y., Shimizu, A., and Miyoshi, T., 2010: "Data assimilation of CALIPSO aerosol observations", *Atmos. Chem. Phys.*, **10**, 39-49, https://doi.org/10.5194/acp-10-39-2010.

Shea, Y. L., B. A. Wielicki, S. Sun-Mack, and P. Minnis, 2017: "Quantifying the dependence of satellite cloud retrievals on instrument uncertainty", *J. Climate*, https://doi.org/10.1175/JCLI-D-16-0429.1.

Shi, Z., Z. Zhang, W. Chen, and Y. Lin, 2022: "Global estimation of clear-sky shortwave aerosol direct radiative effects based on CALIPSO observations", *Int. J. Remote Sens.*, **43**, 1514-1548, https://doi.org/10.1080/01431161.2022.2045042.

Shukurov, K. A., D. V. Simonenkov, A. V. Nevzorov, A. Rashki, N. H. Hamzeh, S. F. Abdullaev, L. M. Shukurova, and O. G. Chkhetiani, 2023: "CALIOP-Based Evaluation of Dust Emissions and Long-Range Transport of the Dust from the Aral−Caspian Arid Region by 3D-Source Potential Impact (3D-SPI) Method", *Remote Sens.*, **15**, 2819, https://doi.org/10.3390/rs15112819.

Slingo, A. and J. M. Slingo, 1988: "The response of a general circulation model to cloud longwave radiative forcing. 1. Introduction and initial experiments", *Q. J. R. Meteorolog. Soc.*, **114**, 1027–1062, https://doi.org/10.1002/qj.49711448209.

Slingo, J. M. and A. Slingo, 1991: "The response of a general circulation model to cloud longwave radiative forcing. 2. Further studies", *Q. J. R. Meteorolog. Soc.*, **117**, 333–364, https://doi.org/10.1002/qj.49711749805.

Smalley, M., K. Suselj, M. Lebsock, and J. Teixeira, 2019: "A novel framework for evaluating and improving parameterized subtropical marine boundary layer cloudiness", *Mon. Wea. Rev.*, **147**, 3241–3260, https://doi.org/10.1175/MWR-D-18-0394.1.

Smith, W. L., P. Minnis, C. Fleeger, D. Spangenberg, R. Palikonda, and L. Nguyen, 2012: "Determining the Flight Icing Threat to Aircraft with Single-Layer Cloud Parameters Derived from Operational Satellite Data", *J. Appl. Meteor. Climatol.*, **51**, 1794–1810, https://doi.org/10.1175/JAMC-D-12-057.1.

Snels, M., A. Scoccione, L. Di Liberto, F. Colao, M. Pitts, L. Poole, T. Deshler, F. Cairo, C. Cagnazzo, and F. Fierli, 2019: "Comparison of Antarctic polar stratospheric cloud observations by groundbased and spaceborne lidars and relevance for Chemistry Climate Models", *Atmos. Chem. Phys.*, **19**, 955–972, https://doi.org/10.5194/acp-19-955-2019.

Snels, F. Colao, I. Shuli, A. Scoccione, M. De Muro, M. Pitts, L. Poole and L. di Liberto, 2021: "Quasi-coincident observations of polar stratospheric clouds by ground-based lidar and CALIOP at Concordia (Dome C, Antarctica) from 2014 to 2018", *Atmos. Chem. Phys.*, **21**, 2165–2178, https://doi.org/10.5194/acp-21-2165-2021.

Sokol, A. B., C. J. Wall and D. L. Hartmann, 2024: "Greater climate sensitivity implied by anvil cloud thinning", *Nat. Geosci.*, https://doi.org/10.1038/s41561-024-01420-6.

Sokolik, I. N., A. J. Soja, P. J. DeMott, and D. Winker, 2019: "Progress and challenges in quantifying wildfire smoke emissions, their properties, transport and atmospheric impacts", *J. Geophys. Res. Atmos.*, **124**, 13005–13025, https://doi.org/10.1029/2018JD029878.

Solanki, R. and N. Singh, 2014: "LiDAR Observations of the vertical distribution of Aerosols in free troposphere: Comparison with CALIPSO level-2 data over the central Himalayas", *Atmos. Environ.*, **99**, 227-238, https://doi.org/10.1016/j.atmosenv.2014.09.083.

Sorooshian, A., L. Wai Siu, K. Butler, M. A. Brunke, B. Cairns, S. Chellappan, J. Chen, Y. Choi, E. C. Crosbie, L. Cutler, J. P. DiGangi, G. S. Diskin, R. A. Ferrare, J. W. Hair, C. A. Hostetler, S. Kirschler, M. M. Kleb, X.-Y. Li, H. Liu, A. McComiskey, S. Namdari, D. Painemal, J. S. Schlosser, T. Shingler, M. A. Shook, S. Silva, K. Sinclair, W. L. Smith, Jr., C. Soloff, S. Stamnes, S. Tang, K. L. Thornhill, F. Tornow, G. Tselioudis, B. Van Diedenhoven, C. Voigt, H. Vömel, H. Wang, E. L. Winstead, Y. Xu, X. Zeng, B. Zhang, L. Ziemba, and P. Zuidema, 2025: "The NASA ACTIVATE mission", *Bull. Amer. Meteor. Soc.,* **106**, E1517–E1538, https://doi.org/10.1175/BAMS-D-24-0136.s1.

Sourdeval, O., G. Brogniez, J. Pelon, L. C. Labonnote, P. Dubuisson, F. Parol, D. Josset, A. Garnier, M. Faivre, and A. Minikin, 2012: "Validation of IIR/CALIPSO Level 1 measurements by comparison with collocated airborne observations during 'CIRCLE-2' and 'BISCAY 08' campaigns", *J. Atmos. Oceanic Technol.*, **29**, 653–667, https://doi.org/10.1175/JTECH-D-11-00143.1.

Sourdeval, O., L. C. Labonnote, G. Brogniez, O. Jourdan, J. Pelon and A. Garnier, 2013: "A Variational Approach for Retrieving Ice Cloud Properties from Infrared Measurements: Application in the Context of Two IIR Validation Campaigns", *Atmos. Chem. Phys.*, **13**, 8229-8244, https://doi.org/10.5194/acp-13-8229-2013.

Sourdeval, O., E. Gryspeerdt, M. Krämer, T. Goren, J. Delanoë, A. Afchine, F. Hemmer, and J. Quaas, 2018: "Ice crystal number concentration estimates from lidar-radar satellite remote sensing. Part 1: Method and evaluation", Atmos. Chem. Phys., 18, 14327-14350, https://doi.org/10.5194/acp-18-14327-2018.

Stamnes, S., C. Hostetler, R. Ferrare, S. Burton, X. Liu, J. Hair, Y. Hu, A. Wasilewski, W. Martin, B. van Diedenhoven, J. Chowdhary, I. Cetinić, L. K. Berg, K. Stamnes, and B. Cairns, 2018: "Simultaneous polarimeter retrievals of microphysical aerosol and ocean color parameters from the 'MAPP' algorithm with comparison to high-spectral-resolution lidar aerosol and ocean products", *Appl. Opt.*, **57**, 2394-2413, https://doi.org/10.1364/AO.57.002394.

Stengel, M., S. Stapelberg, O. Sus, S. Finkensieper, B. Würzler, D. Philipp, R. Hollmann, C. Poulsen, M. Christensen, and G. McGarragh, 2020: "Cloud_cci Advanced Very High Resolution Radiometer post meridiem (AVHRR-PM) dataset version 3: 35-year climatology of global cloud and radiation properties", *Earth Syst. Sci. Data*, **12**, 41–60, https://doi.org/10.5194/essd-12-41-2020.

Stephens, G. L. and T. L'Ecuyer, 2015: "The Earth's energy balance", *Atmos. Res.*, **166**, 195–203, https://doi.org/10.1016/j.atmosres.2015.06.024.

Stephens, G. L., D. G. Vane, R. J. Boain, G. G. Mace, K. Sassen, Z. Wang, A. J. Illingworth, E. J. O'Connor, W. B. Rossow, S. L. Durden, S. D. Miller, R. T. Austin, A. Benedetti, C. Mitrescu, and the CloudSat Team, 2002: "The CloudSat mission and the A-Train: A new dimension of space-based observations of clouds and precipitation", *Bull. Amer. Meteor. Soc.*, **83**, 1771-1790, https://doi.org/10.1175/BAMS-83-12-1771.

Stephens, G., D. Winker, J. Pelon, C. Trepte, D. Vane, C. Yuhas, T. L'Ecuyer, and M. Lebsock, 2018: "CloudSat and CALIPSO within the A-Train: Ten years of actively observing the Earth system", *B. Am. Meteorol. Soc.*, 99, 583–603, https://doi.org/10.1175/BAMS-D-16-0324.1.

Stevens, B., S. Bony, D. Farrell, F. Ament, A. Blyth, C. Fairall, J. Karstensen, P. K. Quinn, S. Speich, C. Acquistapace, F. Aemisegger, A. L. Albright, H. Bellenger, E. Bodenschatz, K.-A. Caesar, R. Chewitt-Lucas, G. de Boer, J. Delanoë, L. Denby, F. Ewald, B. Fildier, M. Forde, G. George, S. Gross, M. Hagen, A. Hausold, K. J. Heywood, L. Hirsch, M. Jacob, F. Jansen, S. Kinne, D. Klocke, T. Kölling, H. Konow, M. Lothon, W. Mohr, A. K. Naumann, L. Nuijens, L. Olivier, R. Pincus, M. Pöhlker, G. Reverdin, G. Roberts, S. Schnitt, H. Schulz, A. P. Siebesma, C. C. Stephan, P. Sullivan, L. Touzé-Peiffer, J. Vial, R. Vogel, P. Zuidema, and Coauthors, 2021, "EUREC^{4}A", *Earth Syst. Sci. Data*, **13**, 4067–4119, https://doi.org/10.5194/essd-13-4067-2021.

Stubenrauch, C. J., S. Kinne, G. Mandorli, W. B. Rossow, D. M. Winker, S. A. Ackerman, H. Chepfer, L. Di Girolamo, A. Garnier, A. Heidinger, K.-G. Karlsson, K. Meyer, P. Minnis, S. Platnick, M. Stengel, S. Sun-Mack, P. Veglio, A. Walther, X. Cai, A. H. Young and G. Zhao, 2024: "Lessons Learned from the Updated GEWEX Cloud Assessment Database", *Surv. Geophys.*, **45**, 1999-2048, https://doi.org/10.1007/s10712-024-09824-0.

Su, T., Z. Li and R. Kahn, 2018: "Relationships between the planetary boundary layer height and surface pollutants derived from lidar observations over China: regional pattern and influencing factors", *Atmos. Chem. Phys.*, **18**, 15921–15935, https://doi.org/10.5194/acp-18-15921-2018.

Sun, T., H. Che, B. Qi, Y. Wang, Y. Dong, X. Xia, H. Wang, K. Gui, Y. Zheng, H. Zhao, Q. Ma, R. Du, and X. Zhang, 2018: "Aerosol optical characteristics and their vertical distributions under enhanced haze pollution events: effect of the regional transport of different aerosol types over eastern China", *Atmos. Chem. Phys.*, **18**, 2949–2971, https://doi.org/10.5194/acp-18-2949-2018.

Tackett, J. L., D. M. Winker, B. J. Getzewich, M. A. Vaughan, S. A. Young, and J. Kar, 2018: "CALIPSO lidar level 3 aerosol profile product: version 3 algorithm design", *Atmos. Meas. Tech.*, **11**, 4129-4152, https://doi.org/10.5194/amt-11-4129-2018.

Tackett, J. L., J. Kar, M. A. Vaughan, B. Getzewich, M.-H. Kim, J.-P. Vernier, A. H. Omar, B. Magill, M. C. Pitts, and D. Winker, 2023: "The CALIPSO version 4.5 stratospheric aerosol subtyping algorithm", *Atmos. Meas. Tech.*, **16**, 745–768, https://doi.org/10.5194/amt-16-745-2023.

Tackett, J. L., R. A. Ryan, A. E. Garnier, J. Kar, B. Getzewich, X. Cai, M. A. Vaughan, C. R. Trepte, R. Verhappen, D. M. Winker and K.-P. A. Lee, 2025: "Mitigating Impacts of Low Energy Laser Pulses on CALIOP Data Products", *Atmos. Meas. Tech.*, **18**, 6211–6231, https://doi.org/10.5194/amt-18-6211-2025.

Tan, I. and T. Storelvmo, 2019: "Evidence of Strong Contributions from Mixed-Phase Clouds to Arctic Climate Change", *Geophys. Res. Lett.*, **46**, 2894–2902, https://doi.org/10.1029/2018GL081871.

Tan, I., C. Zhou A. Lamy, and C. L. Stauffer, 2025: "Moderate climate sensitivity due to opposing mixed-phase cloud feedbacks", *npj Clim Atmos Sci.*, **8**, 86, https://doi.org/10.1038/s41612-025-00948-7.

Tan, S., X. Zhang and G. Shi, 2019: "MODIS Cloud Detection Evaluation Using CALIOP over Polluted Eastern China", *Atmosphere*, **10**, 333, https://doi.org/10.3390/atmos10060333.

Tan, Z., C. Liu, S. Ma, X. Wang, J. Shang, J. Wang, W. Ai and W. Yan, 2022: "Detecting Multilayer Clouds from the Geostationary Advanced Himawari Imager Using Machine Learning Techniques", *IEEE Trans. Geosci. Remote Sens.*, **60**, 4103112, https://doi.org/10.1109/TGRS.2021.3087714.

Tesche, M., U. Wandinger, A. Ansmann, D. Althausen, D. Müller, and A. H. Omar, 2013: "Ground-based validation of CALIPSO observations of dust and smoke in the Cape Verde region", *J. Geophys. Res. Atmos.*, **118**, 2889-2902, https://doi.org/10.1002/jgrd.50248.

Thomas J. L., C. M. Polashenski, A. J. Soja, L. Marelle, K. Casey, H. D. Choi, J.-C. Raut, C. Wiedinmyer, L. K. Emmons, J. Fast, J. Pelon, K. S. Law, M. G. Flanner, and J. E. Dibb, 2017: "Quantifying black carbon deposition over the Greenland ice sheet from forest fires in Canada", *Geophys. Res. Lett.*, 44, 7965–7974, https://doi.org/10.1002/2017GL073701.

Thomason, L. W., N. Ernest, L. Millán, L. Rieger, A. Bourassa, J.-P. Vernier, G. Manney, B. Luo, F. Arfeuille, and T. Peter, 2018: "A global, space-based stratospheric aerosol climatology: 1979 to 2016", *Earth Syst. Sci. Data*, **10**, 469–492, https://doi.org/10.5194/essd-10-469-2018.

Thompson, D. W. J., S. Bony, and Y. Li, 2017: "Thermodynamic constraint on the depth of the global tropospheric circulation", *PNAS*, **114**, 8181–8186, https://doi.org/10.1073/pnas.1620493114.

Thornberry, T. D., A. W. Rollins, M. A. Avery, S. Woods, R. P. Lawson, T. V. Bui and R.-S. Gao, 2017: "Ice water content-extinction relationships and effective diameter for TTL cirrus derived from in situ measurements during ATTREX 2014", *J. Geophys. Res. Atmos.*, **122**, 4494–4507, http://dx.doi.org/10.1002/2016JD025948.

Thorsen, T. J., Q. Fu, and J. M. Comstock, 2011: "Comparison of the CALIPSO satellite and ground-based observations of cirrus clouds at the ARM TWP sites", *J. Geophys. Res.*, **116**, D21203, https://doi.org/10.1029/2011JD015970.

Thorsen, T. J., S. Kato, N. G. Loeb, and F. G. Rose, 2018: "Observation-Based Decomposition of Radiative Perturbations and Radiative Kernels". *J. Climate*, **31**, 10039–10058, https://doi.org/10.1175/JCLI-D-18-0045.1

Thorsen, T. J., R. A. Ryan, and M. A. Vaughan, 2025: "Validation of aerosol optical depth retrieved from CALIPSO lidar ocean surface backscatter", *J. Geophys. Res. Atmos.*, **130**, e2024JD042416, https://doi.org/10.1029/2024JD042416.

Tian, P., X. Cao, L. Zhang, N. Sun, L. Sun, T. Logan, J. Shi, Y. Wang, Y. Ji, Y. Lin, Z. Huang, T. Zhou, Y. Shi and R. Zhang, 2017: "Aerosol vertical distribution and optical properties over China from long-term satellite and ground-based remote sensing", *Atmos. Chem. Phys.*, **17**, 2509–2523, https://doi.org/10.5194/acp-17-2509-2017.

Todd, M. C. and C. Cavazos-Guerra, 2016: "Dust aerosol emission over the Sahara during summertime from Cloud-Aerosol Lidar with Orthogonal Polarization (CALIOP) observations", *Atmos. Environ.*, **128**, 147-157, https://doi.org/10.1016/j.atmosenv.2015.12.037.

Toon, O. B., D. O. Starr, E. J. Jensen, P. A. Newman, S. Platnick, M. R. Schoeberl, P. O. Wennberg, S. C. Wofsy, M. J. Kurylo, H. Maring, K. W. Jucks, M. S. Craig, M. F. Vasques, L. Pfister, K. H. Rosenlof, H. B. Selkirk, P. R. Colarco, S. R. Kawa, G. G. Mace, P. Minnis, and K. E. Pickering, 2010: "Planning, implementation, and first results of the Tropical Composition, Cloud and Climate Coupling Experiment (TC4)", *J. Geophys. Res.,* **115**, D00J04, https://doi.org/10.1029/2009JD013073.

Toon, O. B., H. Maring, J. Dibb, R. Ferrare, D. J. Jacob, E. J. Jensen, Z. J. Luo, G. G. Mace, L. L. Pan, L. Pfister, K. H. Rosenlof, J. Redemann, J. S. Reid, H. B. Singh, A. M. Thompson, R. Yokelson, P. Minnis, G. Chen, K. W. Jucks, and A. Pszenny, 2015: "Planning, implementation, and scientific goals of the Studies of Emissions and Atmospheric Composition, Clouds and Climate Coupling by Regional Surveys (SEAC^{4}RS) field mission", *J. Geophys. Res. Atmos.*, **121**, 4967-5009, https://doi.org/10.1002/2015JD024297.

Toth, T. D., J. R. Campbell, J. S. Reid, J. L. Tackett, M. A. Vaughan, J. Zhang and J. W. Marquis, 2018: "Minimum Aerosol Layer Detection Sensitivities and their Subsequent Impacts on Aerosol Optical Thickness Retrievals in CALIPSO Level 2 Data Products", *Atmos. Meas. Tech.*, **11**, 499–514, https://doi.org/10.5194/amt-11-499-2018.

Toth, T. D., J. Zhang, J. S. Reid and M. A. Vaughan, 2019: "A bulk-mass-modeling-based method for retrieving Particulate Matter Pollution using CALIOP observations", *Atmos. Meas. Tech.*, **12**, 1739–1754, https://doi.org/10.5194/amt-12-1739-2019.

Toth, T. D., J. Zhang, M. A. Vaughan, J. S. Reid, and J. R. Campbell, 2022: "Retrieving Particulate Matter Concentrations over the Contiguous United States through the Use of CALIOP Observations", *Atmos. Environ.*, **274**, 118979, https://doi.org/10.1016/j.atmosenv.2022.118979.

Toth, T. D., M. B. Clayton, Z. Li, D. Painemal, S. D. Rodier, J. Kar, T. J. Thorsen, R. A. Ferrare, M. A. Vaughan, J. L. Tackett, H. Bian, M. Chin, A. E. Garnier, E. J. Welton, R. A. Ryan, C. R. Trepte and D. M. Winker, 2025: "Mapping CALIPSO Marine and Dusty Marine Aerosol Lidar Ratios using MODIS AOD Constrained Retrievals and GOCART Model Simulations", *Atmos. Meas. Tech.*, **18**, 6765–6793, https://doi.org/10.5194/amt-18-6765-2025.

Trepte, Q. Z., P. Minnis, S. Sun-Mack, C. R. Yost, Y. Chen, Z. Jin, F.-L. Chang, W. L. Smith Jr., K. M. Bedka, and T. L. Chee, 2019: "Global cloud detection for CERES Edition 4 using Terra and Aqua MODIS data", *IEEE Trans. Geosci. Remote Sens.*, **57**, 9410–9449, https://doi.org/10.1109/TGRS.2019.2926620.

Tsikerdekis, A., P. Zanis, A. L. Steiner, F. Solmon, V. Amiridis, E. Marinou, E. Katragkou, T. Karacostas, and G. Foret, 2017: "Impact of dust size parameterizations on aerosol burden and radiative forcing in RegCM4", *Atmos. Chem. Phys.*, **17**, 769–791, https://doi.org/10.5194/acp-17-769-2017.

Ueyama, R., E. J. Jensen, and L. Pfister, 2018: "Convective influence on the humidity and clouds in the tropical tropopause layer during boreal summer", *J. Geophys. Res. Atmos.*, **123**, 7576–7593, https://doi.org/10.1029/2018JD028674.

Vaillant de Guélis, T., H. Chepfer, V. Noel, R. Guzman, P. Dubuisson, D. M. Winker, and S. Kato, 2017a: "The link between outgoing longwave radiation and the altitude at which a spaceborne lidar beam is fully attenuated", *Atmos. Meas. Tech.*, **10**, 4659–4685, https://doi.org/10.5194/amt-10-4659-2017.

Vaillant de Guélis, T., H. Chepfer, V. Noel, R. Guzman, D. M. Winker, and R. Plougonven, 2017b: "Using Space Lidar Observations to Decompose Longwave Cloud Radiative Effect Variations Over the Last Decade", *Geophys. Res. Lett.*, **44**, 11,994–12,003, https://doi.org/10.1002/2017GL074628.

Vaillant de Guélis, T., H. Chepfer, R. Guzman, M. Bonazzola, D. M. Winker, and V. Noel, 2018: "Space lidar observations constrain longwave cloud feedback", *Sci. Rep.*, **8**, 16570, https://doi.org/10.1038/s41598-018-34943-1.

Vaillant de Guélis, T., M. A. Vaughan, D. M. Winker, and Z. Liu, 2021: "Two-dimensional and multi-channel feature detection algorithm for the CALIPSO lidar measurements", *Atmos. Meas. Tech.*, **14**, 1593–1613, https://doi.org/10.5194/amt-14-1593-2021.

Vaughan, M., K. Powell, R. Kuehn, S. Young, D. Winker, C. Hostetler, W. Hunt, Z. Liu, M. McGill, and B. Getzewich, 2009: "Fully Automated Detection of Cloud and Aerosol Layers in the CALIPSO Lidar Measurements", *J. Atmos. Oceanic Technol.*, **26**, 2034–2050, https://doi.org/10.1175/2009JTECHA1228.1.

Vaughan, M. A., Z. Liu, M. J. McGill, Y. Hu, and M. D. Obland, 2010: "On the Spectral Dependence of Backscatter from Cirrus Clouds: Assessing CALIOP's 1064 nm Calibration Assumptions Using Cloud Physics Lidar Measurements", *J. Geophys. Res.*, **115**, D14206, https://doi.org/10.1029/2009JD013086.

Vaughan, M., A. Garnier, D. Josset, M. Avery, K.-P. Lee, Z. Liu, W. Hunt, J. Pelon, Y. Hu, S. Burton, J. Hair, J. Tackett, B. Getzewich, J. Kar, and S. Rodier, 2019: "CALIPSO Lidar Calibration at 1064 nm: Version 4 Algorithm", *Atmos. Meas. Tech.*, **12**, 51–82, https://doi.org/10.5194/amt-12-51-2019.

Vaughan, M., S. D. Rodier, Z. Liu, A. Garnier, K.-P. Lee, B. Getzewich, and S. Zeng, 2023a: "Correcting CALIOP Polarization Gain Ratios for Diurnal Variations", in Proceedings of the 30th International Laser Radar Conference, Sullivan, J. T., T. Leblanc, S. Tucker, B. Demoz, E. Eloranta, C. Hostetler, S. Ishii, L. Mona, F. Moshary, A. Papayannis and K. Rupavatharam, Eds., pp. 691–697, Springer Atmospheric Sciences, Springer, Cham., https://doi.org/10.1007/978-3-031-37818-8_89.

Vaughan, M., L. Rupert, R. Verhappen, C. Trepte, C. Weimer, A. Garnier, B. Getzewich, K.-P. Lee, S. Rodier, T. Murray, and K. Beaumont, 2023b: "Optimizing CALIOP's Boresight Position", CloudSat/CALIPSO Science Team Meeting, 10–12 October 2023, Washington D.C., https://ntrs.nasa.gov/citations/20230014042.

Venkata, S. L. and J. A. Reagan, 2016: "Aerosol Retrievals from CALIPSO Lidar Ocean Surface Returns", *Remote Sens.*, **8**, 1006, https://doi.org/10.3390/rs8121006.

Vérèmes, H., C. Listowski, J. Delanoë, C. Barthe, P. Tulet, F. Bonnardot, and D. Roy, 2019: "Spatial and seasonal variability of clouds over the South-West Indian Ocean based on the DARDAR mask product", *Q. J. Roy. Meteorol. Soc.*, **145**, 3561–3576, https://doi.org/10.1002/qj.3640.

Verlinde, J., J. Y. Harrington, G. M. McFarquhar, V. T. Yannuzzi, A. Avramov, S. Greenberg, N. Johnson, G. Zhang, M. R. Poellot, J. H. Mather, D. D. Turner, E. W. Eloranta, B. D. Zak, A. J. Prenni, J. S. Daniel, G. L. Kok, D. C. Tobin, R. Holz, K. Sassen, D. Spangenberg, P. Minnis, T. P. Tooman, M. D. Ivey, S. J. Richardson, C. P. Bahrmann, M. Shupe, P. J. DeMott, A. J. Heymsfield, and R. Schofield, 2007: "The mixed-phase arctic cloud experiment", *Bull. Amer. Meteor. Soc.*, **88**, 205-222, https://doi.org/10.1175/BAMS-88-2-205.

Vernier, J. P., J. P. Pommereau, A. Garnier, J. Pelon, N. Larsen, J. Nielsen, T. Christensen, F. Cairo, L. W. Thomason, T. Leblanc, and I. S. McDermid, 2009: "Tropical stratospheric aerosol layer from CALIPSO lidar observations", *J. Geophys. Res.*, **114**, D00H10, https://doi.org/10.1029/2009JD011946.

Vescovini, T., P. Nabat, M. Mallet, and F. Solmon, 2024: "Aerosol direct radiative effects from extreme fire events in Australia, California and Siberia occurring in 2019–2020", *J. Geophys. Res. Atmos.*, **129**, e2024JD041002, https://doi.org/10.1029/2024JD041002.

Virtanen, T.H., Bugliaro, L., Clarisse, L., de Laat, J., Hedelt, P., Marchese, F., Rüfenacht, R., Theys, N., Vandenbussche, S., Vazquez, M., 2019: "EUNADICS-AV DELIVERABLE (D -N°: D14): Validation of tailored satellite products", 64 pp.; see https://ec.europa.eu/research/participants/documents/downloadPublic?documentIds=080166e5c11f3b14&appId=PPGMS.

Voigt, A., N. Albern, and G. Papavasileiou, 2019: "The atmospheric pathway of the cloud-radiative impact on the circulation response to global warming: important and uncertain", *J. Climate*, **32**, 3051–3067, https://doi.org/10.1175/JCLI-D-18-0810.1.

Voigt, A., S. North, B. Gasparini and S.-H. Ham, 2024: "Atmospheric cloud-radiative heating in CMIP6 and observations, and its response to surface warming", *Atmos. Chem. Phys.*, **24**, 9749–9775, https://doi.org/10.5194/acp-24-9749-2024.

Wall, C. J., T. Kohyama, and D. L. Hartmann, 2017: "Low-cloud, boundary layer, and sea ice interactions over the Southern Ocean during winter", *J. Climate*, **30**, 4857–4871, https://doi.org/10.1175/JCLI-D-16-0483.1.

Wall, C. J., N. J. Lutsko and D. N. Vishny, 2022: "Revisiting Cloud Radiative Heating and the Southern Annular Mode", *Geophys. Res. Lett.*, e2022GL100463, https://doi.org/10.1029/2022GL100463.

Wang, C., S. Platnick, K. Meyer, Z. Zhang and Y. Zhou, 2020: "A Machine Learning-Based Cloud Detection and Thermodynamic Phase Classification Algorithm using Passive Spectral Observations", *Atmos. Meas. Tech.*, **13**, 2257–2277, https://doi.org/10.5194/amt-13-2257-2020.

Wang, D., C. A. Yang and M. Diao, 2024: "Validation of satellite-based cloud phase distributions using global-scale in situ airborne observations", *Earth and Space Science*, **11**, e2023EA003355. https://doi.org/10.1029/2023EA003355.

Wang, L., B. Lyu, and Y. Bai, 2020: "Aerosol vertical profile variations with seasons, air mass movements and local PM2.5 levels in three large China cities", *Atmos. Environ.*, **224**, 117329, https://doi.org/10.1016/j.atmosenv.2020.117329.

Wang, S.-C., Y. Wang, M. Estes, R. Lei, R. Talbot, L. Zhu, and P. Hou, 2018: "Transport of Central American fire emissions to the U.S. Gulf Coast: Climatological pathways and impacts on ozone and PM2.5", *J. Geophys. Res. Atmos.*, **123**, 8344–8361, https://doi.org/10.1029/2018JD028684.

Wang, X., H. Miao, Y. Liu, Q. Bao, B. He, J. Li, and Y. Zhao, 2022: "The use of satellite data-based 'critical relative humidity' in cloud parameterization and its role in modulating cloud feedback", *JAMES*, **14**, e2022MS003213, https://doi.org/10.1029/2022MS003213.

Warneke, C., J. P. Schwarz, J. Dibb, O. Kalashnikova, G. Frost, J. Al-Saad, S. S. Brown, W. A. Brewer, A. Soja, F. C. Seidel, R. A. Washenfelder, E. B. Wiggins, R. H. Moore, B. E. Anderson, C. Jordan, T. I. Yacovitch, S. C. Herndon, S. Liu, T. Kuwayama, D. Jaffe, N. Johnston, V. Selimovic, R. Yokelson, D. M. Giles, B. N. Holben, P. Goloub, I. Popovici, M. Trainer, A. Kumar, R. B. Pierce,

D. Fahey, J. Roberts, E. M. Gargulinski, D. A. Peterson, X. Ye, L. H. Thapa, P. E. Saide, C. H. Fite, C. D. Holmes, S. Wang, M. M. Coggon, Z. C. J. Decker, C. E. Stockwell, L. Xu, G. Gkatzelis, K. Aikin, B. Lefer, J. Kaspari, D. Griffin, L. Zeng, R. Weber, M. Hastings, J. Chai, G. M. Wolfe, T. F. Hanisco, J. Liao, P. Campuzano Jost, H. Guo, J. L. Jimenez, J. Crawford, The FIREX-AQ Science Team, 2022: "Fire Influence on Regional to Global Environments and Air Quality (FIREX-AQ)", *J. Geophys. Res. Atmos.*, **128**, e2022JD037758, https://doi.org/10.1029/2022JD037758.

Weinzierl, B., A. Ansmann, J. M. Prospero, D. Althausen, N. Benker, F. Chouza, M. Dollner, D. Farrell, W. K. Fomba, V. Freudenthaler, J. Gasteiger, S. Groß, M. Haarig, B. Heinold, K. Kandler, T. B. Kristensen, O. L. Mayol-Bracero, T. Müller, O. Reitebuch, D. Sauer, A. Schäfler, K. Schepanski, A. Spanu, I. Tegen, C. Toledano, and A. Walser, 2017: "The Saharan Aerosol Long-Range Transport and Aerosol–Cloud-Interaction Experiment: Overview and Selected Highlights", *Bull. Amer. Meteor. Soc.*, **98**, 1427-1451, https://doi.org/10.1175/BAMS-D-15-00142.1.

Winker, D. M., R. H. Couch, and M. P. McCormick, 1996: "An overview of LITE: NASA's Lidar In-space Technology Experiment," in *Proceedings of the IEEE*, 84(2), 164-180, https://doi.org/10.1109/5.48222.

Winker, D. M., J. Pelon, J. A. Coakley, S. A. Ackerman, R. J. Charlson, P. R. Colarco, P. Flamant, Q.. Fu, R. M. Hoff, C. Kittaka, T. L. Kubar, H. Le Treut, M. P. McCormick, G. Megie, L. Poole, K. Powell, C. Trepte, M. A. Vaughan, and B. A. Wielicki, 2010: "The CALIPSO Mission: A Global 3d View of Aerosols and Clouds", *Bull Amer. Meteor. Soc.,* **91**, 1211-1230, https://doi.org/10.1175/2010BAMS3009.1.

Winker, D. M., J. L. Tackett, B. J. Getzewich, Z. Liu, M. A. Vaughan, and R. R. Rogers, 2013: "The global 3-D distribution of tropospheric aerosols as characterized by CALIOP", *Atmos. Chem. Phys.*, **13**, 3345–3361, https://doi.org/10.5194/acp-13-3345-2013.

Winker, D., H. Chepfer, V. Noel, and X. Cai, 2017: "Observational Constraints on Cloud Feedbacks: The Role of Active Satellite Sensors", *Surv. Geophys.*, **38**, 1483–1508, https://doi.org/10.1007/s10712-017-9452-0.

Winker, D., X. Cai, M. Vaughan, A. Garnier, B. McGill, M. Avery, and B. Getzewich, 2024: "A Level 3 monthly gridded ice cloud dataset derived from 12 years of CALIOP measurements", *Earth Syst. Sci. Data*, **16**, 2831–2855, https://doi.org/10.5194/essd-16-2831-2024.

Wood, R. and C.S. Bretherton, 2006: "On the Relationship between Stratiform Low Cloud Cover and Lower-Tropospheric Stability", *J. Climate,* **19**, 6425–6432, https://doi.org/10.1175/JCLI3988.1.

Wu, D., Z. Wang, B. Wang, J. Zhou and Y. Wang, 2011: "CALIPSO validation using ground-based lidar in Hefei (31.9°N, 117.2°E), China", *Appl. Phys. B*, **102**, 185-195, https://doi.org/10.1007/s00340-010-4243-z.

Wu, T., M, Fan, J. Tao, L. Su, P. Wang, D. Liu, M. Li, X. Han and L. Chen, 2017: "Aerosol Optical Properties over China from RAMS-CMAQ Model Compared with CALIOP Observations", *Atmosphere*, **8**, 201, https://doi:10.3390/atmos810020.

Wu, Y., L. Cordero, B. Gross, F. Moshary and S. Ahmed, 2014: "Assessment of CALIPSO attenuated backscatter and aerosol retrievals with a combined ground-based multiwavelength lidar and sunphotometer measurement", *Atmos. Environ.*, **84**, 44-53, https://doi.org/10.1016/j.atmosenv.2013.11.016.

Xia, L., F. Zhao, L. Chen, R. Zhang, K. Mao, A. Kylling, and Y. Ma, 2018: "Performance comparison of the MODIS and the VIIRS 1.38 μm cirrus cloud channels using libRadtran and CALIOP data", *Remote Sens. Environ.*, **206**, 363-374, https://doi.org/10.1016/j.rse.2017.12.040.

Yang, Y., A. Anderson, D. Kiv, J. Germann, M. Fuchs, S. Palm and T. Wang, 2021: "Study of Antarctic blowing snow storms using MODIS and CALIOP observations with a machine learning model", *Earth and Space Science*, **8**, e2020EA001310, https://doi.org/10.1029/2020EA001310.

Yao, J., S. M. Raffuse, M. Brauer, G. J. Williamson, D. M. J. S. Bowman, F. H. Johnston, and S. B. Henderson, 2018: "Predicting the minimum height of forest fire smoke within the atmosphere using machine learning and data from the CALIPSO satellite", *Remote Sens. Environ.*, **206**, 98–106, https://doi.org/10.1016/j.rse.2017.12.02.

Yeom, J.-M., J.-L. Roujean, K.-S. Han, K.-S. Lee, and H.-W. Kim, 2020: "Thin cloud detection over land using background surface reflectance based on the BRDF model applied to Geostationary Ocean Color Imager (GOCI) satellite data sets", *Remote Sens. Environ.*, **239**, 111610, https://doi.org/10.1016/j.rse.2019.111610.

Yorks, J., D. Hlavka, M. Vaughan, M. McGill, W. Hart, S. Rodier, and R. Kuehn, 2011: "Airborne Validation of Cirrus Cloud Properties Derived from CALIPSO Lidar Measurements, Part I: Spatial Properties", *J. Geophys. Res.*, **116**, D19207, https://doi.org/10.1029/2011JD015942.

Yost, C., P. Minnis, S. Sun-Mack, Y.Chen, and W. L. Smith Jr., 2021: "CERES MODIS Cloud Product Retrievals for Edition 4, Part II: Comparisons to CloudSat and CALIPSO", *IEEE Trans. Geosci. Remote Sens.*, **59**, 3695-3724, http://doi.org/10.1109/TGRS.2020.3015155.

Young, S. A. and M. A. Vaughan, 2009: The retrieval of profiles of particulate extinction from Cloud Aerosol Lidar Infrared Pathfinder Satellite Observations (CALIPSO) data: Algorithm description, *J. Atmos. Oceanic Technol.*, **26**, 1105–1119, https://doi.org/10.1175/2008JTECHA1221.1.

Young, S. A., M. A. Vaughan, J. L. Tackett, A, Garnier, J. B. Lambeth and K. A. Powell, 2018: "Extinction and Optical Depth Retrievals for CALIPSO Version 4 Data Release", *Atmos. Meas. Tech.*, **11**, 5701-5727, https://doi.org/10.5194/amt-11-5701-2018.

Yu, H., Y. J. Kaufman, M. Chin, G. Feingold, L. A. Remer, T. L. Anderson, Y. Balkanski, N. Bellouin, O. Boucher, S. Christopher, P. DeCola, R. Kahn, D. Koch, N. Loeb, M. S. Reddy, M. Schulz, T. Takemura, and M. Zhou, 2006: "A review of measurement-based assessments of the aerosol direct radiative effect and forcing", *Atmos. Chem. Phys.*, **6**, 613–666, https://doi.org/10.5194/acp-6-613-2006.

Zamora, L. M., R. A. Kahn, S. Eckhardt, A. McComiskey, P. Sawamura, R. Moore and A. Stohl, 2017: "Arctic aerosol net indirect effects on thin, mid-altitude, liquid-bearing clouds", *Atmos. Chem. Phys.*, **17**, 7311–7332, https://doi.org/10.5194/acp-17-7311-2017.

Zelinka, M. D., S. A. Klein and D. L. Hartmann, 2012a: "Computing and partitioning cloud feedbacks using cloud property histograms. Part I: Cloud radiative kernels", *J. Climate*, **25**, 3715–3735, https://doi.org/10.1175/JCLI-D-11-00248.1.

Zelinka, M. D., S. A. Klein and D. L. Hartmann, 2012b "Computing and partitioning cloud feedbacks using cloud property histograms. Part II: Attribution to changes in cloud amount, altitude, and optical depth", *J. Climate*, **25**, 3736–3754, https://doi.org/10.1175/JCLI-D-11-00249.1.

Zelinka, M. D., C. Zhou and S. A. Klein, 2016: "Insights from a refined decomposition of cloud feedbacks", *Geophys. Res. Lett.*, **43**, 9259–9269, https://doi.org/10.1002/2016GL069917.

Zeng, S., Y. Hu, M. Vaughan, C. Trepte, Z. Liu, A. Omar, B. Getzewich, and S. Rodier 2025: "Identification of Precipitating Marine Low-Altitude Water Clouds by CALIPSO: Observations and Detections", *J. Geophys. Res. Atmos.*, **130**, e2025JD043401, https://doi.org/10.1029/2025JD043401.

Zhai, P., Y. Hu, C. R. Trepte, and P. L. Lucker, 2009: "A vector radiative transfer model for coupled atmosphere and ocean systems based on successive order of scattering method", *Opt. Express*, **17**, 2057–2079, https://doi.org/10.1364/OE.17.002057.

Zhang, J., B. Zhao, X. Liu, G. Lin, Z. Jiang, C. Wu, and X. Zhao, 2022: "Effects of different types of aerosols on deep convective clouds and anvil cirrus", *Geophys. Res. Lett.*, **49**, e2022GL099478, https://doi.org/10.1029/2022GL099478.

Zhang, K., Z. Zhang, J. He, W. O. Smith, N. Liu and C. Le, 2024: "Re-evaluating winter carbon sink in Southern Ocean by recovering MODIS-Aqua chlorophyll-a product at high solar zenith angles", *ISPRS J. Photogramm.*, **218 A**, 588-599, https://doi.org/10.1016/j.isprsjprs.2024.09.033.

Zhang, M., Y. Zhang, Y. Wang, J. Liang, Z. Yue, W. Song, and G. Han, 2025: "Optical Properties of Near-Surface Cloud Layers and Their Interactions with Aerosol Layers: A Case Study of Australia Based on CALIPSO", *Atmosphere*, **16**(7), 793, https://doi.org/10.3390/atmos16070793.

Zhang, S., P. Chen, Y. Hu, Z. Zhang, C. Jamet, X. Lu, D. Dionisi and D. Pana, 2024: "Research Report: Diurnal global ocean surface pCO_2 and air–sea CO_2 flux reconstructed from spaceborne LiDAR data", *PNAS Nexus*, **3**, pgad432, https://doi.org/10.1093/pnasnexus/pgad432.

Zhang, Y., S. Xie, W. Lin, S. A. Klein, M. Zelinka, P.-L. Ma, P. J. Rasch, Y. Qian, Q. Tang and H.-Y. Ma, 2019: "Evaluation of Clouds in Version 1 of the E3SM Atmosphere Model with Satellite Simulators", *JAMES*, **11**, 1253–1268, https://doi.org/10.1029/2018MS001562.

Zhang, Z., W. Zhou, M. Wenig and L. Yang, 2017: "Impact of long-range desert dust transport on coastal East Asia: analysis of urban dust concentration and wet deposition with model simulation", *Air. Qual. Atmos. Health*, **10**, 325–337, https://doi.org/10.1007/s11869-016-0440-1.

Zhao, B., Y. Wang, Y. Gu, K.-N. Liou, J. H. Jiang, J. Fan, X. Liu, L. Huang, and Y. L. Yung, 2019: "Ice nucleation by aerosols from anthropogenic pollution", *Nat. Geosci.*, **12**, 602–607, https://doi.org/10.1038/s41561-019-0389-4.

Zhao, Y., Q. Tang, Z. Hu, Q. Yu and T. Liang, 2024: "Comparison and Analysis of CALIPSO Aerosol Optical Depth and AERONET Aerosol Optical Depth Products in Asia from 2006 to 2023", *Remote Sens.*, **16**, 4359, https://doi.org/10.3390/rs16234359.

Zhong, C., P. Chen, Z. Zhang, C. Xie, S. Zhang, M. Sun and D. Wu, 2024: "The use of spaceborne Lidar to map Antarctic krill distributions and biomass in the Southern Ocean", *Front. Mar. Sci.*, **11**, https://doi.org/10.3389/fmars.2024.1287229.

Zhu, H., H. Zhao, S. Yang, R. Zhou, Y. Wang, Y. Zou, C. Zhao, and R. Li, 2025: Smoke aerosols elevate precipitation top and latent heat to the upper atmosphere globally, *npj Clim. Atmos. Sci.*, **8**, 170, https://doi.org/10.1038/s41612-025-01047-3.

Zhu, Z., M. Zhang, Y. Huang, B. Zhu, G. Han, T. Zhang, and B. Liu, 2018: "Characteristics of the planetary boundary layer above Wuhan, China based on CALIPSO", *Atmos. Res.*, **214**, 204–212, https://doi.org/10.1016/j.atmosres.2018.07.024.

Zidikheri, M. J., C. Lucas, and R. J. Potts, 2018: "Quantitative verification and calibration of volcanic ash ensemble forecasts using satellite data", *J. Geophys. Res. Atmos.*, **123**, 4135–4156, https://doi.org/10.1002/2017JD027740.

Zong, X., X. Xia and H. Che, 2015: "Validation of aerosol optical depth and climatology of aerosol vertical distribution in the Taklimakan Desert", *Atmos. Pollut. Res.*, **6**, 239-244, https://doi.org/10.5094/APR.2015.028.

8. Appendix D: Payload Trending Information

Calibration Stability for 532 nm Data Products

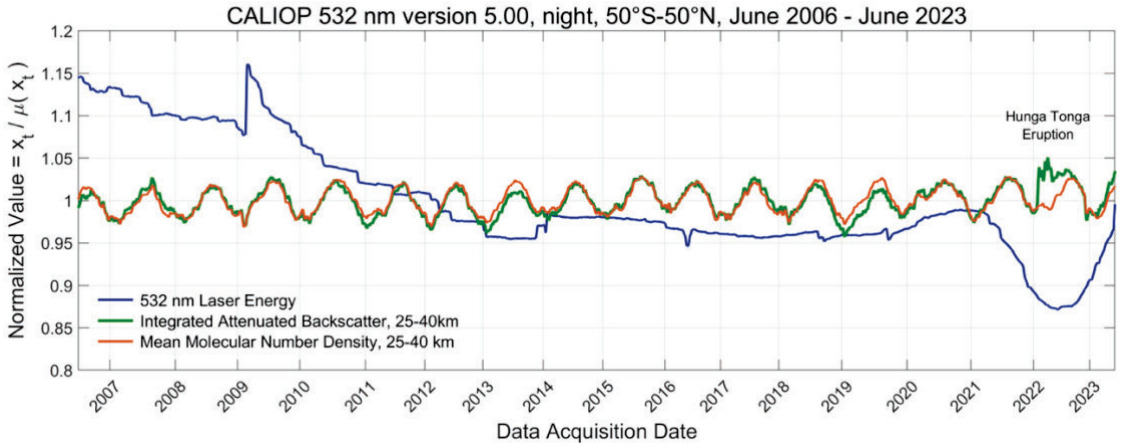

Figure D-1. The stability of CALIOP measurements and robustness of calibration procedures is evidenced by the time series of global 532 nm integrated attenuated backscatter (IAB) from 25-40 km over the course of the mission. In this largely aerosol-free region of the atmosphere, the seasonal trend in IAB tracks that of molecular number density as expected. Despite the reduction in 532 nm laser energy and increased occurrence of low energy shots within the SAA since 2017, the IAB remained well behaved. Each time series above is normalized by its respective mean (Source credit: NASA).

532 Channel SNR

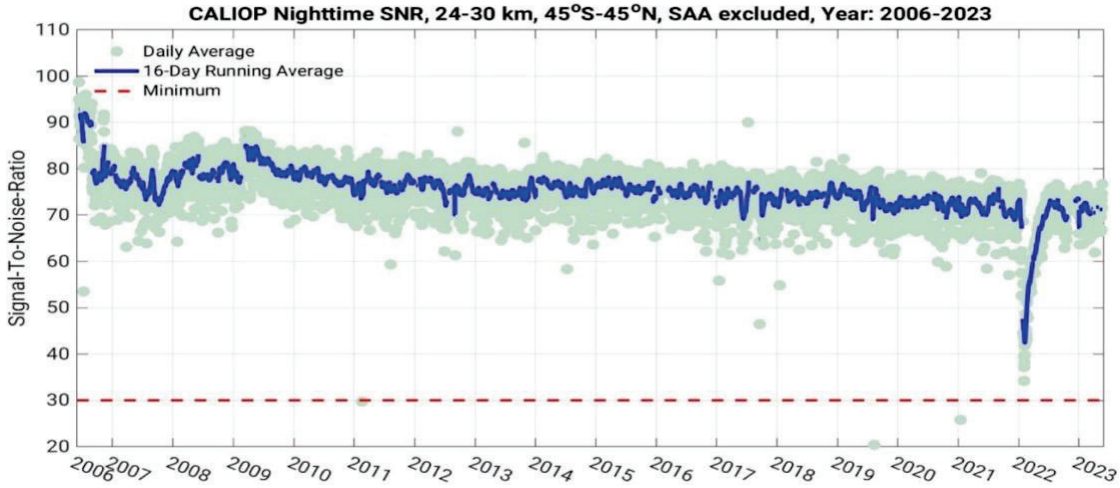

Figure D-2. Measured 532 nm channel nighttime signal-to-noise (SNR) computed from the nighttime total attenuated backscatter coefficients between 24 km and 30 km and 45º N to 45º S. Daily average values outside the SAA are displayed with a fitted 16-day running average curve overlaid. No noise filtering is applied to the data, meaning that radiation-induced noise and low energy laser shots are included in the SNR calculations. The SNR threshold of 30 was identified by the CALIPSO team as the minimum capability needed to satisfy Level 1 requirements. Nearly all of the decrease in SNR since switching to the backup laser in 2009 can be attributed to the decrease in laser energy. The perturbation in early 2022 was caused by volcanic aerosol injected by the eruption of Hunga Tonga that affected calibration and was not an instrument issue (Source credit: NASA).

Laser Energy

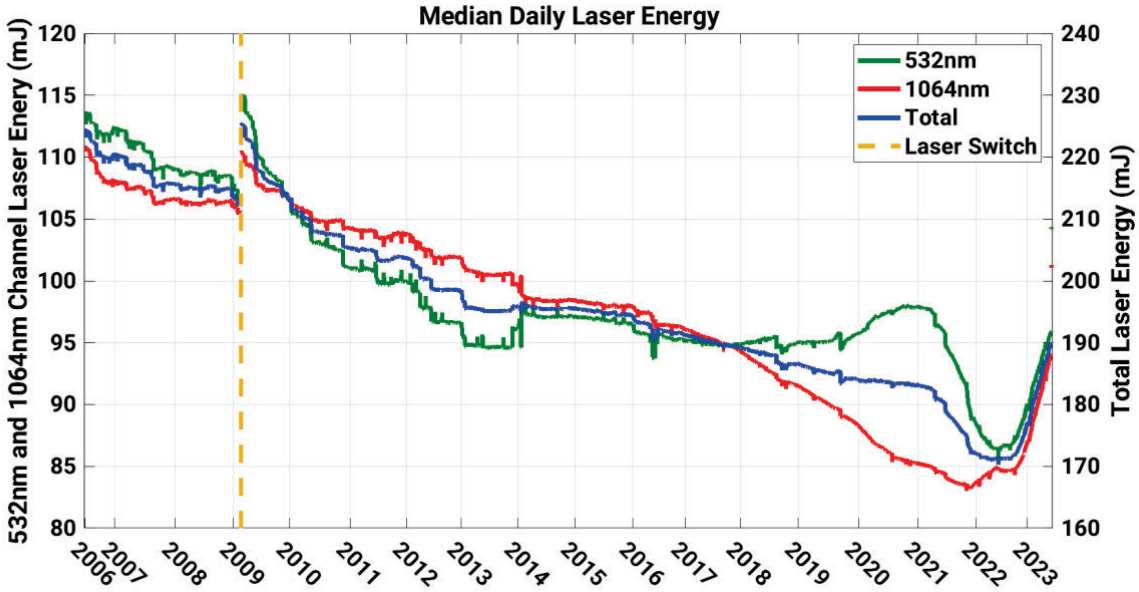

Figure D-3. The laser energy trends for the primary and backup lasers for the 1064 nm channel (red), the 532 nm channel (green) and the combined or total output energy (blue). The trends were constructed from daily median values. The output energy for 1064 nm and 532 nm are denoted on the left axes whereas the total energy is shown on the right axes. The primary laser showed a modest 10% degradation over more than 32 months of operations. The backup laser exhibited about a 20% drop over almost 14 years, nearly all of which occurred during the first 4 years of operation. Most of the decreases were due to failures of individual diode bars (an expected phenomenon), visible as discrete drops in energy. The smaller perturbations were likely caused by changes to the laser duty cycle during spacecraft maneuvers. The only adjustments to the backup laser since the initial tuning in 2009 were two temperature adjustments of the Second Harmonic Generator (SHG) to rebalance the energies between the two wavelengths. The primary laser had no temperature adjustments to the SHG. The output energy trends for the 532 nm and 1064 nm channels after 2017 remain unexplained (Source credit: NASA).

Laser Canister Pressure

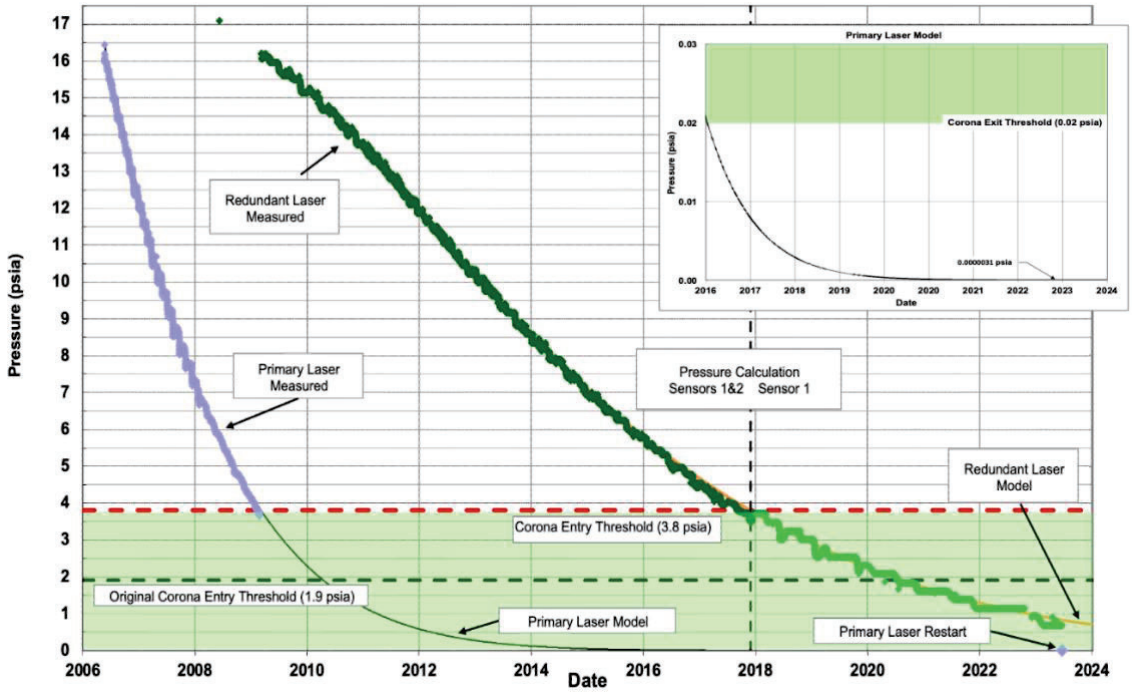

Figure D-4. Pressure trends for the primary and backup laser. Pressure readings on a given laser were made nearly continuously by two sensors while that laser was active. The values plotted are daily averages of the mean of the two sensor readings for the active laser. The highlighted green region indicates pressures at which corona discharges in the canister are likely below a value of 3.8 psia and above a value of 0.02 psia. This value is the pressure at which the primary and backup lasers began to exhibit symptoms of corona discharge across the Q-switch. The simple trend model provides a good fit to the measured data for both lasers and provided a credible basis for estimating the future behavior of the backup laser during the mission.

Figure D4 Inset**.** Predictions of the pressure trend for the primary laser at the end of the science phase of the mission and at the time of the restart of the primary laser. The model prediction indicated that the pressure for the primary laser pressure was well below 0.02 psia (the estimated lower limit of the corona region for the Q-switch) and continued operation of the primary laser was possible. The pressure sensor readings were known to be unreliable below 3.5 psia (Source credit: NASA).

Laser Low Energy Shot Trends

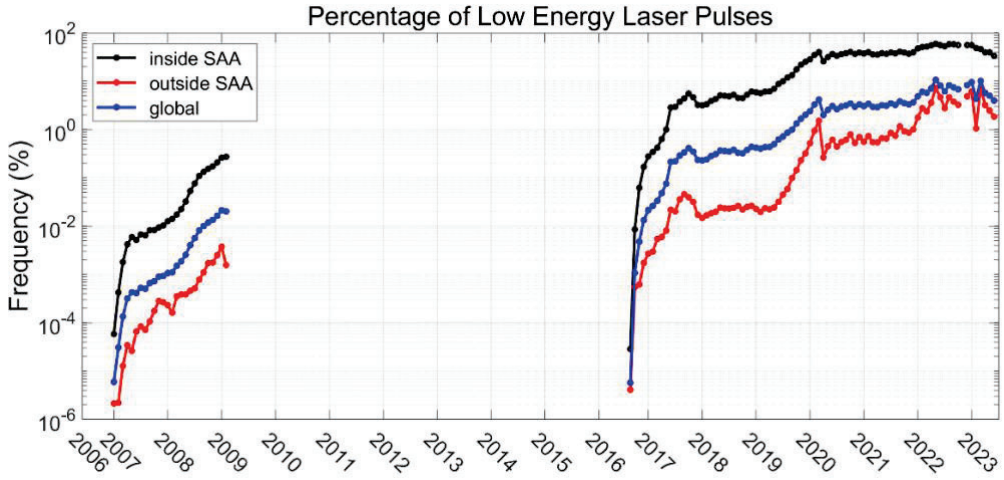

Figure D-5. The percentage of monthly averaged very low laser energy shots (E532 < 10 mJ) by the primary and backup lasers. The nominal laser energy for the 532-nm channel was between 115-90 mJ during the mission (see D3). Percent values are displayed for laser shots inside the South Atlantic Anomaly (SAA) (black), outside the SAA (red) and over the entire globe (blue). The trends clearly indicate that most low energy shots occurred within the SAA. For the primary laser, low energy shots were rare and still < 1% of possible monthly shots in early 2009 prior to its deactivation. For the backup laser, significantly more low energy shots were observed after mid-2017, and the frequency of these shots inside the SAA eventually exceeded 50% during the last years of the mission. Outside the SAA, backup low energy shots remained rather infrequent until 2020 when they became more prevalent. These very low energy shots affected the quality of the science data products and innovative algorithm techniques were developed to mitigate their impact. See section 4.3.4.2 for details on laser performance (Source credit: NASA).

Backup Laser Low Energy Drop Locations – October-December 2016-2022

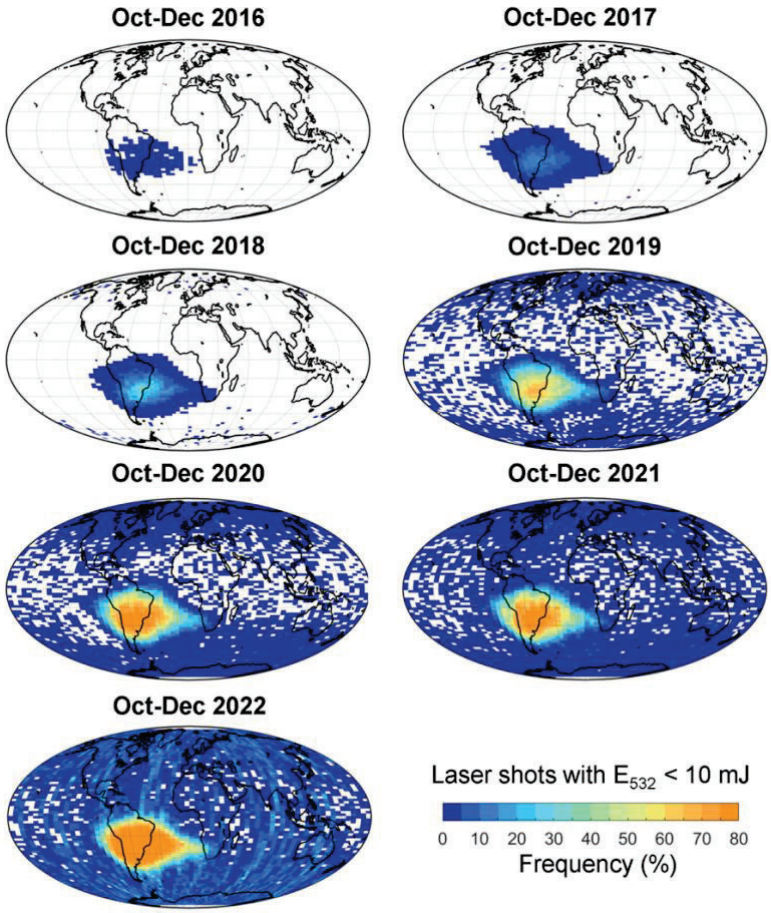

Figure D-6. Geographical distribution of low energy laser shot frequency (E_{532} < 10 mJ), October – December between 2016 and 2022 and averaged within bins 2º latitude and 5º longitude. Beginning in mid-2016, Type 2 low energy shots began occurring with the backup laser. The region having the highest frequency of low energy laser shots maps out the South Atlantic Anomaly (SAA) (Source credit: NASA).

APD Dark Noise

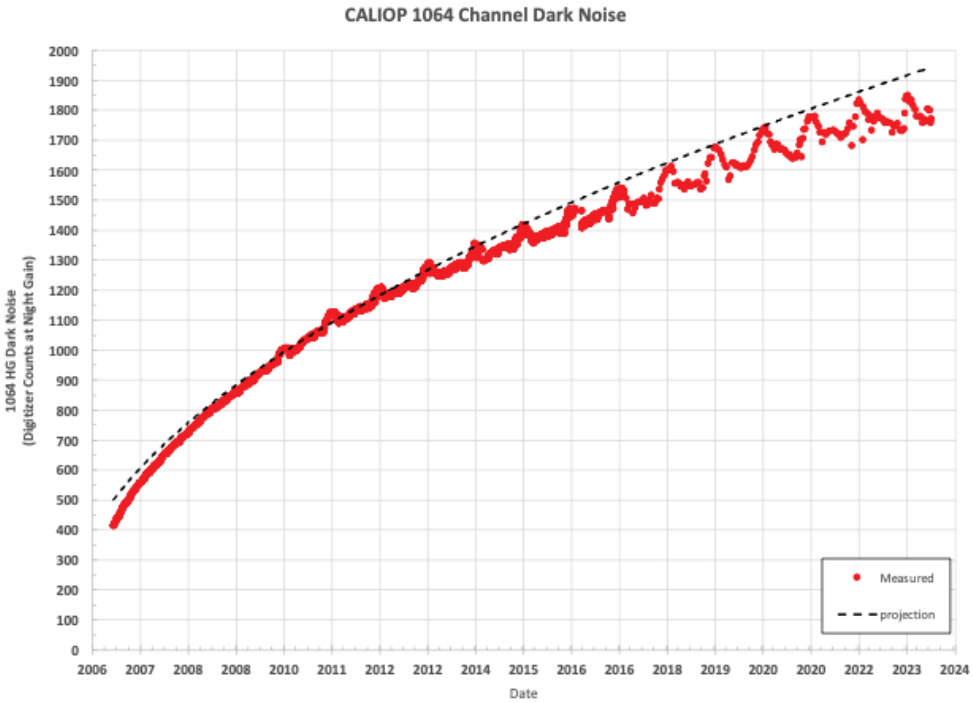

Figure D-7. Measured dark noise trend for the 1064 channel detector (APD). The dark noise increase is mostly due to cumulative radiation damage, with a small contribution from seasonal rises in the APD temperature above its regulated value. Both effects were expected behavior. The pre-launch prediction for the APD dark noise at the end of a 3-year mission was 1720 counts, based upon very limited information. The actual value after 17 years is only slightly above that value. The increase in dark noise contributes to a gradual and relatively insignificant decrease in the 1064 channel SNR (not displayed) (Source credit: NASA).

LVPS Temperature

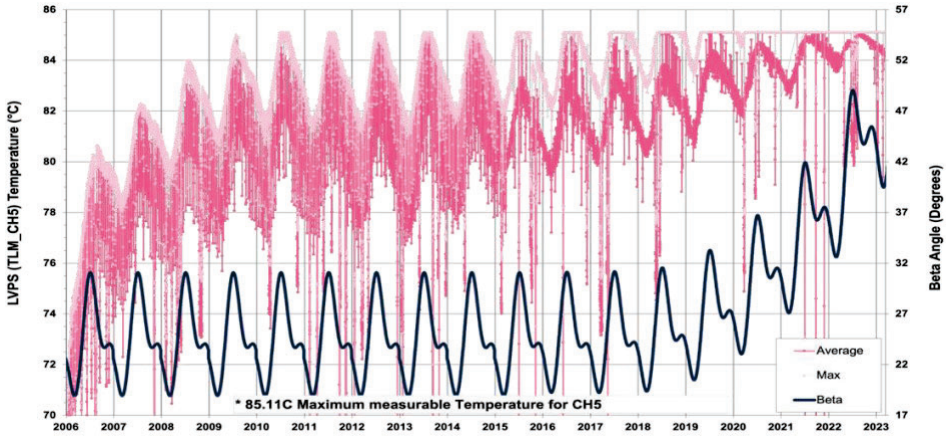

Figure D-8. LVPS Power Converter Temperature trend. The converter temperature was sensitive to heat sources in the rest of the payload, and the large variation reflects maximum heating that occurred during and after X-band transmissions. The seasonal variations resulted from changes in the solar beta angle. The long-term drift resulted from loss of cooling efficiency due to degradation of the radiator coating. Data from the period of high solar beta angles beginning in 2010 are clipped because of saturation of the Channel 5 digitizer. When that happened, an alternate measurement at a nearby location (Channel 4) was used as a surrogate. The black line is a prediction for the maximum and minimum LVPS temperatures for each year. The prediction was based on a thermal model that included estimates of radiator coating degradation, fine-tuned based upon the measured values. Measured data prior to 2019 indicated that the maximum temperature had stabilized at below 86°C. It rose afterwards because the orbit began drifting to later mean local crossing times for the ascending node at the equator. Although the peak temperatures were above the ground red limit, the remained below the manufacturer's rated maximum temperatures of 125ºC. The transmitter performed well and had no anomalies. More than 7000 transmits occurred over the mission (Source credit: NASA).

WFC Trending

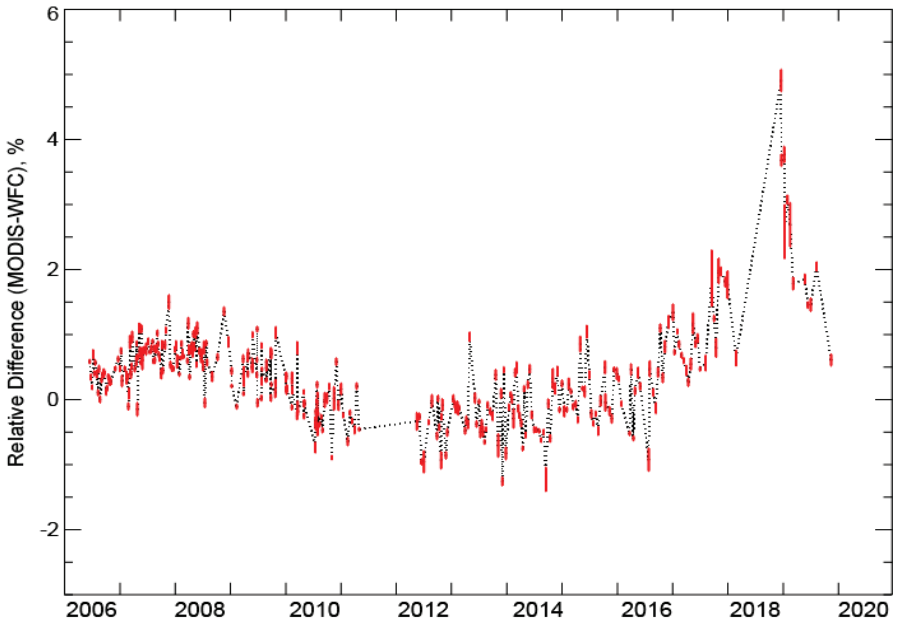

Figure D-9. Daily mean relative radiance differences (+/- 1s) over deep convective systems during the CALIPSO mission. The WFC was fully functional and operating nominally until April 2020. There was no on-orbit radiometric calibration capability for the WFC; instead, the project relied on vicarious approaches to verify and monitor the WFC radiometric calibration. Since the WFC bandpass was matched to the well-calibrated Aqua MODIS Channel 1, direct comparisons with nearly coincident MODIS Channel 1 measurements provided an excellent means of assessing the WFC radiometric performance. On-orbit performance assessments of the WFC radiometric products are regularly performed based on analysis of coincident WFC and MODIS data. Using deep convective clouds as vicarious calibration targets, direct comparisons of WFC and MODIS radiance measurements during the first 12 years of operation indicated that the WFC radiance tracked the MODIS data very closely with daily absolute mean differences never exceeding 1.5% and typically less than 1%. Analysis of WFC and MODIS deep convective cloud reflectance distributions also indicated that the WFC has exhibited very good radiometric stability during the ten plus years of operation with at most a < 1% drift relative to MODIS. The gap in MODIS/WFC comparison data between June 2011 and May 2012 is due to missing MODIS special product data (CloudSat subsets), which we used in these comparisons. This special MODIS product that had been subsetted to the CloudSat ground track was not produced during this period because CloudSat was not operational and not in formation with CALIPSO (Source credit: NASA).

IIR Trending

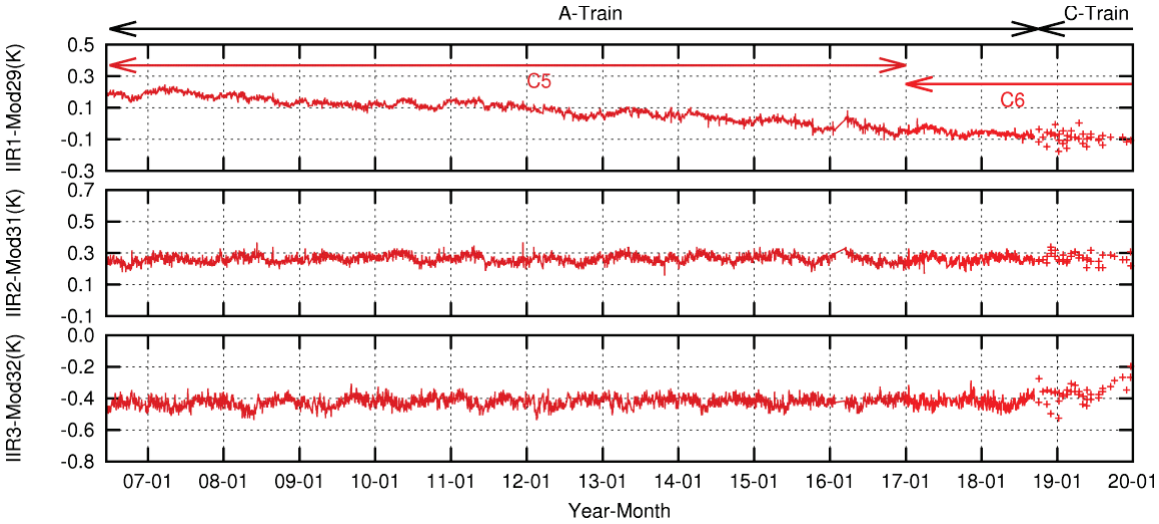

Figure D-10: IIR Calibration Trend Daily averaged brightness temperature differences between each IIR channel and a similar MODIS/Aqua band between launch and end 2019. Top, middle and bottom panels are for the pairs of channels (IIR 8.65 µm; MODIS29), (IIR 10.6 µm; MODIS31) and (IIR 12.05 µm; MODIS32), respectively. The analysis is applied to IIR V2 and MODIS co-located pixels after selecting homogeneous scenes over sea in the 60ºS-30ºS latitude band and in the 280-290 K brightness temperature range. The analysis uses MODIS Collection 5 (C5) until end 2016 and MODIS Collection 6 (C6) afterwards. Comparisons with simulations show that the slight trend of -0.02 K/year for IIR8.65-MODIS29 C5 (top) originates from MODIS29. No trend (less than ± 0.004 K/year) is evidenced for any of the IIR channels. Simulations for clear sky pixels in the tropics reproduce the differences between IIR1 and MODIS29 C5 within 0.02 K at the beginning of the mission. Differences between IIR2 and MODIS31 C5 are reproduced within 0.04 K, whereas IIR3-MODIS32 C5 is larger than simulated by 0.26 K (Garnier et al., 2017). In the A-Train, the standard deviations for each individual measurement are between 0.5 and 0.7 K. From October 2018 when CALIPSO is in the C-Train, co-located pixels are available about every 3 weeks for a time period of 2 to 3 days. For these collocated pixels, the acquisition time differences and the MODIS viewing angles are not as stable as in the A-Train, which explains the larger variability in the comparisons (Source credit: NASA).

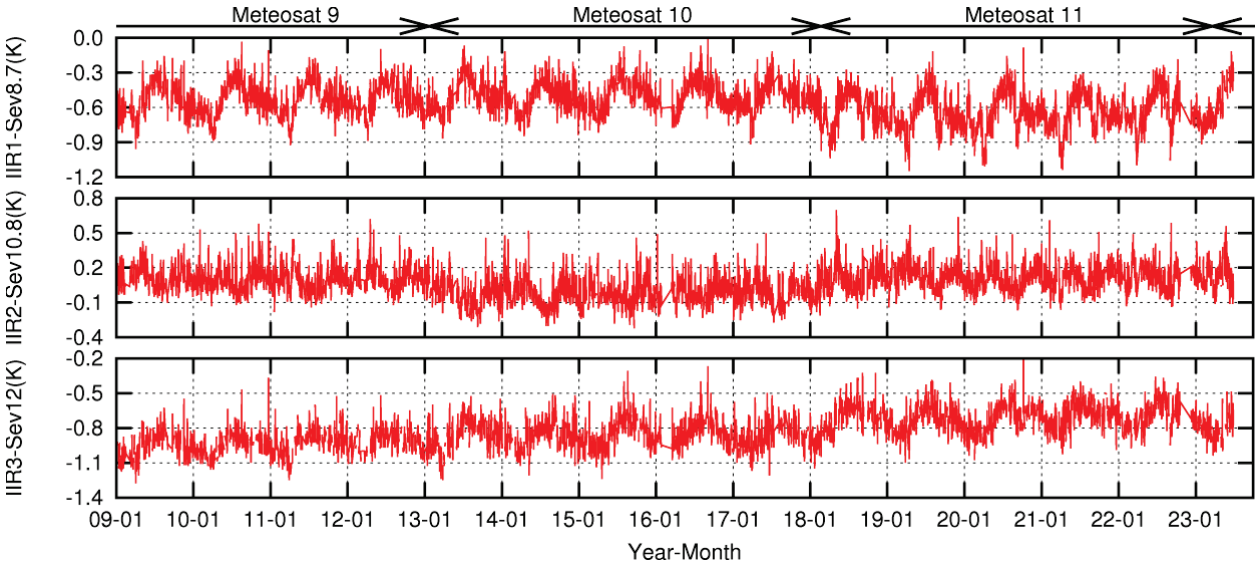

Figure D-11: Daily averaged brightness temperature differences between each IIR channel and a similar SEVIRI band from January 2009 until June 2023. Top, middle and bottom panels are for the pairs of channels (IIR8.65 µm; SEVIRI 8.7), (IIR10.6 µm; SEVIRI 10.8) and (IIR12.05 µm; SEVIRI 12), respectively. SEVIRI data are from the prime satellites with sub-satellite longitude at 0°, i.e. Meteosat 9 until 21 January 2013, then Meteosat 10 until 20 February 2018, Meteosat 11 until 20 March 2023, and Meteosat 10 again for the last months of the mission. The analysis is applied to IIR and SEVIRI co-located pixels over oceans after selecting homogeneous scenes where SEVIRI viewing angles are smaller than 10° to be close to IIR quasi-nadir observations, and brightness temperatures are chosen between 290 and 300 K. The same SEVIRI instrument response function is taken for the entire time-period, which contributes to the slight differences associated to the three SEVIRI instruments, thereby illustrating the sensitivity of the technique, notwithstanding the large variability. The seasonal variations are due to atmospheric and surface changes in the small geographical area selected for the analyses. No trend was detected, showing that IIR continued to be healthy until the end of the mission (Source credit: NASA).

9. Appendix E: Analysis of Publications

CALIPSO observations and data products produced by the CALIPSO project are highly valued by the international scientific community and are used in ~5000 publications. Scientific discoveries and advancements enabled by CALIPSO have been reported in Section 2. This appendix provides added insight into publication trends and the usage of the data products. The CALIPSO bibliography includes publications from international peer-reviewed journals as well as Master's Theses and Ph.D. dissertations written in English.

Publication Trends and Metrics

Figure E1 shows the number of CALIPSO publications by calendar year. The total number of peer-reviewed publications reported in Figure E1 is 4962. The trend showed a steady increase in publications, with only a modest reduction in the past year. It is fully expected that the total number will easily exceed 5000 before the end of 2025.

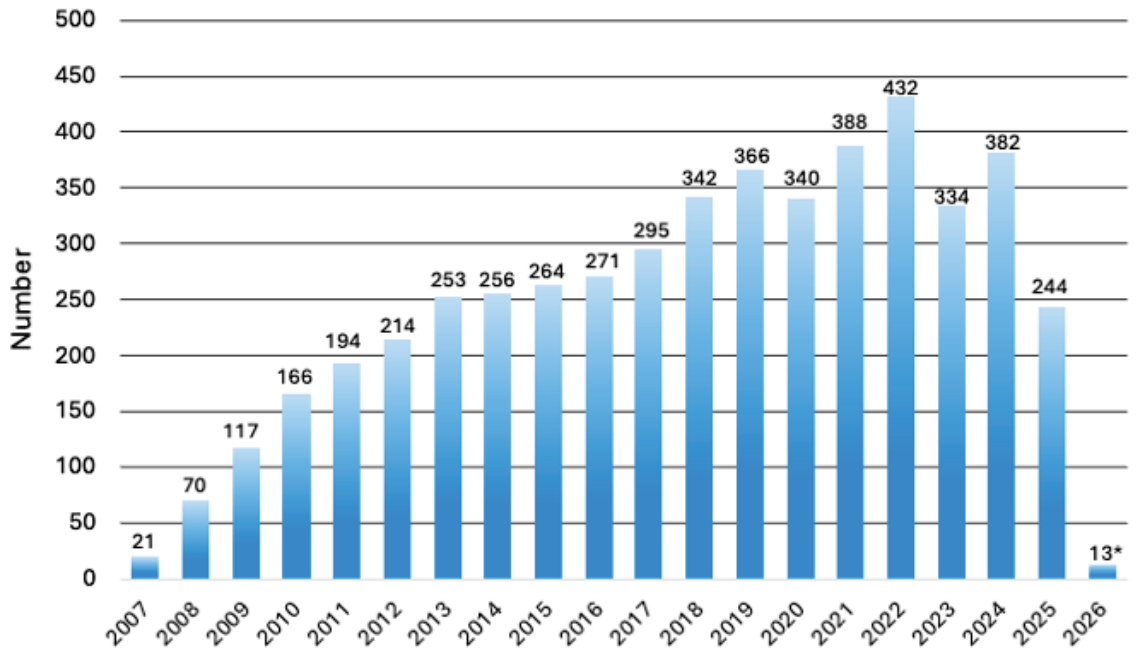

Figure E-1. Number of CALIPSO publications by year. The figure shows a healthy increase in their number during the early phase of the mission and shows a peak in 2022 at 432 publications. The publications identified for 2026 represent those accepted for publication but have not been formally published. The total number reported here is 4962, with more expected in 2025 (Source credit: NASA).

Publications by Journals

CALIPSO publications appear in over 80 journals. Table E1 lists the distribution by the ten leading journals. By a large margin, researchers have published in the Journal of Geophysical Research (Atmospheres) and Atmospheric Chemistry and Physics. The journal impact factor is a measure of the importance or rank of a journal based on the frequency with which an average article in a journal has been cited in a particular year or time period.

Table E1. Number of publications by the 10 leading journals.

Journal	Number	Impact Factor
Journal of Geophysical Research - Atmospheres	665	3.4
Atmospheric Chemistry and Physics	566	5.8
Geophysical Research Letters	225	8.4
Atmospheric Measurement Techniques	220	3.7
Remote Sensing	208	4.8
Atmospheric Environment	206	3.7
Journal of Climate	151	4.0
Atmospheric Research	141	4.4
Atmosphere	117	2.5
Remote Sensing of Environment	87	11.4

Master's Theses and Ph.D. Dissertations

CALIPSO has proven to be a fertile learning research resource for a developing the next generations of earth and atmospheric scientists. Over 330 Ph.D. dissertations and 135 Master's theses have been identified that are based, in whole or in part, on CALIPSO measurements. When trying to determine why there are more than twice as many more Ph.D. dissertations than Master's theses, it should be noted that it is more difficult to accurately account for the number of Master's theses, as they are not routinely tracked as closely as the Ph.D. dissertations.

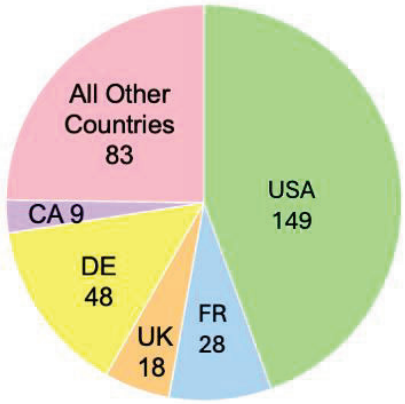

Figure E-2. Number of Ph.D. dissertations by country. Students from 18 countries are included in the 'other countries' category (Source credit: NASA).

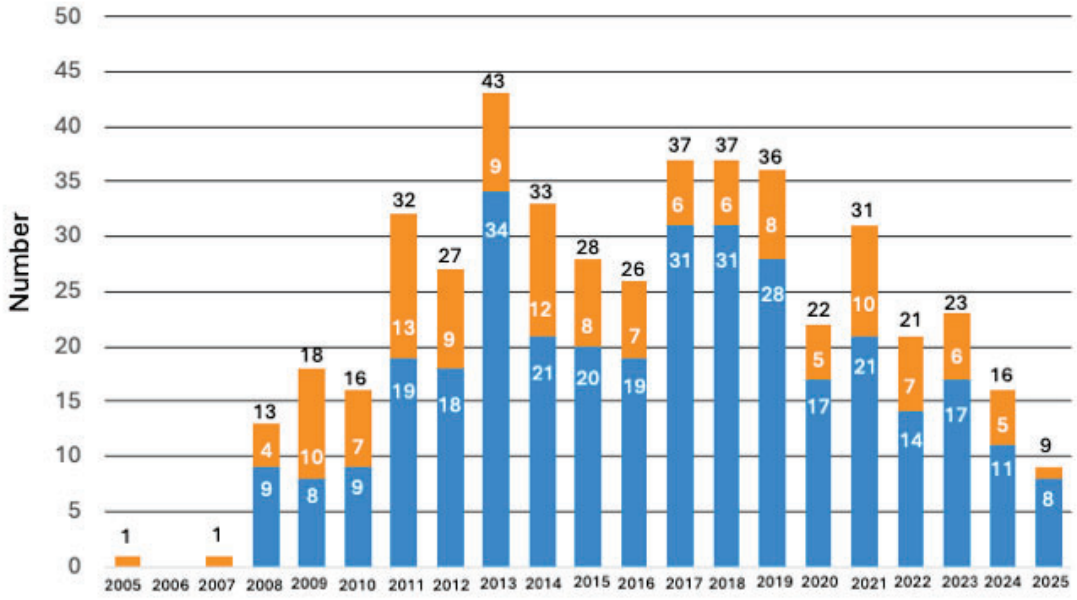

Figure E-3. Number of Ph.D. dissertations and Master's theses publications by year (335 Ph.D. (blue). dissertations and 135 Master's theses (orange). The total number of publications in a year is listed at the top of each bar) (Source credit: NASA).

10.Appendix F: International Field Campaigns

Campaigns	References
Atmospheric Radiation Measurement (ARM) 2000	https://www.arm.gov/research/campaigns/sgp2000sprcloud
Cirrus Regional Study of Tropical Anvils and Cirrus Layers–Florida Area Cirrus Experiment (CRYSTAL-FACE) 2002	Chiriaco et al., 2007
Midlatitude Cirrus Experiment (Mid-CIX) 2004	Davis et al., 2009
Pre-Aura Validation Experiment (Pre-AVE) 2004	Froyd et al., 2009
Mixed-Phase Arctic Cloud Experiment (MPACE) 2004	Verlinde et al., 2007
Costa Rica Aura Validation Experiment (CR_AVE) 2006	Lawson et al., 2008
CALIPSO-CloudSat Validation Experiment (CC-VEX) 2006	McGill et al., 2007
Megacity Initiative: Local And Global Research Observations (MILAGRO) 2006	Molina et al., 2010
Texas Air Quality Study (TEXAQS) 2006	Parish et al., 2009
NASA African Monsoon Multidisciplinary Analyses (NAMMA) 2006	Omar et al., 2010
Canadian CloudSat/CALIPSO Validation Project (C3VP) 2006	Petersen et al., 2007
African Monsoon Multidisciplinary Analysis (AMMA 2006)	Vernier et al., 2009
SCOUT-African Monsoon Multidisciplinary Analysis (SCOUT-AMMA 2006)	Cairo et al., 2010
Arctic Study of Tropospheric Aerosol, Clouds and Radiation (ASTAR) 2007	Gayet et al., 2009
Tropical Composition, Cloud and Climate Coupling Experiment (TC4) 2007	Toon et al., 2010
Ultra-light Motorized Campaign (ULM) 2007	Chazette et al., 2010
Cirrus Cloud Experiment-2 (CIRCLE-2) 2007	Mioche et al., 2010; Sourdeval et al., 2012, 2013
Arctic Research of the Composition of the Troposphere from Aircraft and Satellites (ARCTAS) 2008	Jacob et al., 2010
Biscay 08' (BISCAY) 2008	Sourdeval et al., 2012
Polar Study using Aircraft, Remote Sensing, Surface Measurements and Models, Climate, Chemistry, Aerosols and Transport (POLARCAT) 2008	de Villiers et al., 2010; Law et al., 2014
Saharan Mineral Dust Experiment (SAMUM-2) 2008	Tesche et al., 2013
Calibration Validation Campaigns (CALVAL) 2006-2011	Rogers et al., 2011, 2014
Small Particles In Cirrus (SPartiCus) 2010	Mace et al., 2009b; Deng et al., 2013; Jensen et al., 2013
Midlatitude Cirrus Properties Experiment (MACPEX) 2011	Jensen et al., 2013

Campaigns	References
Ice in Clouds Experiment-Tropical (ICE-T) 2011	Heymsfield and Willis, 2014
Deriving Information on Surface Conditions from COlumn and VERtically Resolved Observations Relevant to Air Quality (Discover AQ) (1,2,3)	https://science.larc.nasa.gov/discover-aq/ https://www.awma.org/content.asp?admin=Y&contentid=301
Development and Evaluation of satellite Validation Tools by Experimenters (DEVOTE) 2011	https://asdc.larc.nasa.gov/project/DEVOTE
FENNEC-The Saharan Climate System (FENNEC) 2011	Banks et al., 2013; Ryder et al., 2015
Deep Convective Clouds and Chemistry (DC3) 2012	Barth et al., 2015
Airborne Tropical Tropopause Experiment (ATTREX) 2012, 2014	Jensen et al., 2017; Schoeberl et al., 2019
Chemistry-Aerosol Mediterranean Experiment (CHARMEX) 2013	Mallet et al., 2016; Ancellet et al., 2016
Studies of Emissions and Atmospheric Composition, Clouds and Climate Coupling by Regional Surveys (SEAC^{4}RS) 2013	Toon et al., 2015
Saharan Aerosol Long-Range Transport and Aerosol–Cloud Interaction Experiment (SALTRACE) 2014	Weinzierl et al., 2017
Ship-Aircraft Bio-Optical Research (SABOR) 2014	Stamnes et al., 2018
North Atlantic Aerosol and Marine Ecosystem Study (NAAMES 1,2,3) 2015, 2016	Behrenfeld et al., 2019b
Korea–United States Air Quality (KORUS-AQ) 2016	Crawford et al., 2021
Pacific Oxidants Sulfur Ice and DehydratiON (POSIDON) 2016	Rollins et al., 2018; Schoeberl et al., 2019
ObseRvations of Aerosols above CLouds and their intEractionS (ORACLES 1, 2), 2016, 2017	Redemann et al., 2021
North Atlantic Waveguide and Downstream Impact Experiment (NAWDEX) 2016	Schafler et al., 2018
Aerosol Characterization from Polarimeter and Lidar (ACEPOL) 2017	Knobelspiesse et al., 2020
Aerosol, Radiation and Clouds in southern Africa (AEROCLO-SA) 2017	Formenti et al., 2019; Chazette et al., 2019
Ice-Atmosphere-Ocean Observing System (IAOOS) 2017-2020	Di Biagio et al., 2018
Cloud, Aerosol and Monsoon Processes Philippines Experiment (CAMP^{2}EX) 2019	Reid et al., 2023
Fire Influence on Regional to Global Environments and Air Quality (FIRE-X) 2019	Warneke et al., 2022
Elucidating the role of clouds-circulation coupling in climate (EUREC^{4}A) 2020	Stevens et al., 2021; Chazette et al., 2022

Campaigns	References
Aerosol Cloud Meteorology Interactions over the Western Atlantic Experiment (ACTIVATE) (1,2,3,4) 2020, 2021	Sorooshian et al., 2025
STRATEOLE-2 2021	Lesigne et al., 2024
Convective Processes Experiment-Aerosols and Winds (CPEX-AW), 2021	Rodenkirch and Rowe, 2024
Tracking Aerosol Convection ExpeRiment – Air Quality (TRACER-AQ) 2021	Goldberg et al., 2024
Convective Processes Experiment - Cabo Verde (CPEX-CV) 2022	Nowottnick et al., 2024
CALIPSO Night Validation Flights (CALIPSO-NVF) 2022	https://www.air.larc.nasa.gov/missions/calipso-nvf/index.html

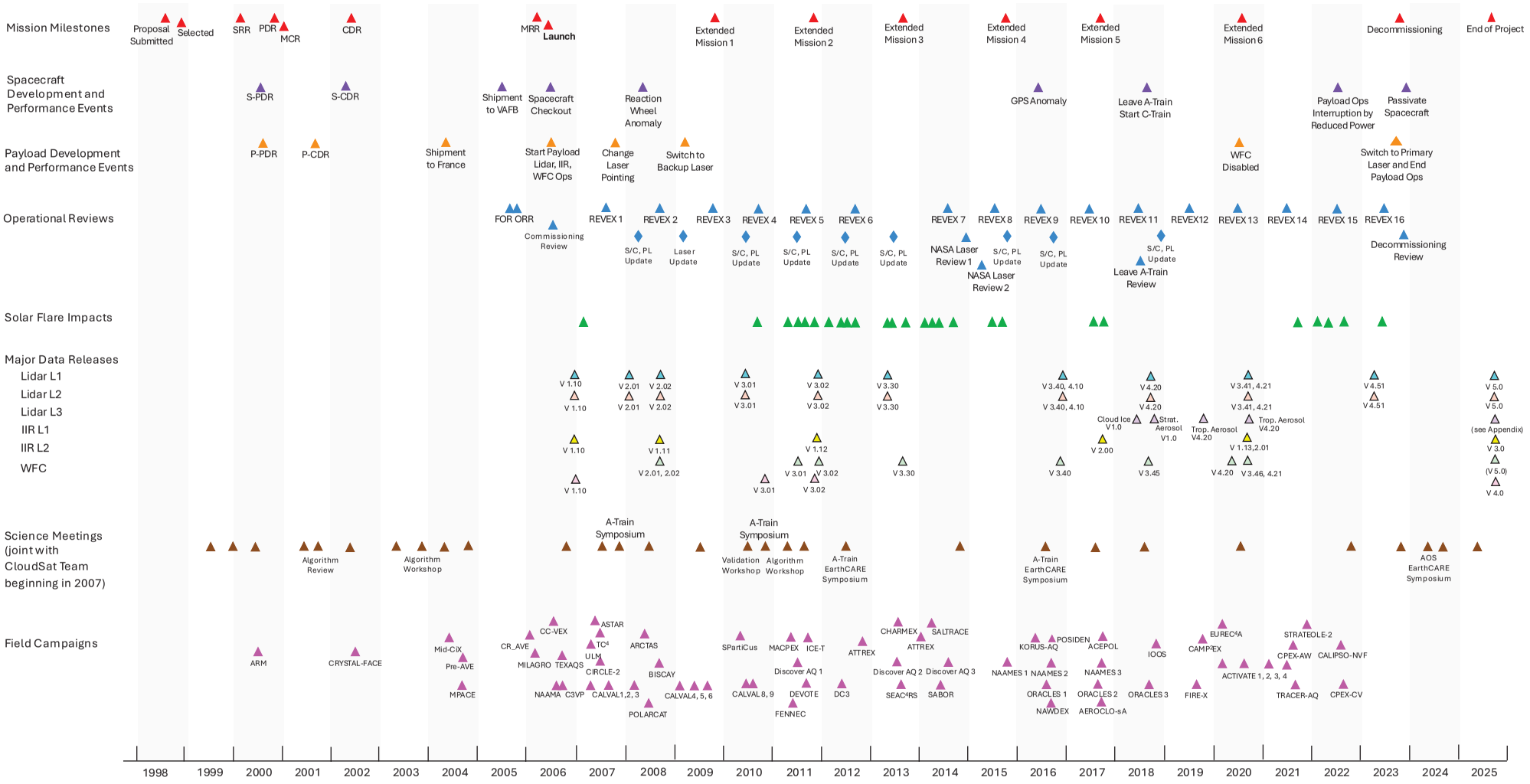
Mission Milestones
Proposal Submitted
Selected
SRR
PDR
MCR
CDR
MRR
Launch
Extended Mission 1
Extended Mission 2
Extended Mission 3
Extended Mission 4
Extended Mission 5
Extended Mission 6
Decommissioning
End of Project
Spacecraft Development and Performance Events
S-PDR
S-CDR
Shipment to VAFB
Spacecraft Checkout
Reaction Wheel Anomaly
GPS Anomaly
Leave A-Train Start C-Train
Payload Ops Interruption by Reduced Power
Passivate Spacecraft
Payload Development and Performance Events
P-PDR
P-CDR
Shipment to France
Start Payload Lidar, IIR, WFC Ops
Change Laser Pointing
Switch to Backup Laser
WFC Disabled
Switch to Primary Laser and End Payload Ops
Operational Reviews
FOR ORR
Commissioning Review
REVEX 1
REVEX 2
REVEX 3
REVEX 4
REVEX 5
REVEX 6
REVEX 7
REVEX 8
REVEX 9
REVEX 10
REVEX 11
REVEX12
REVEX 13
REVEX 14
REVEX 15
REVEX 16
S/C, PL Update
Laser Update
NASA Laser Review 1
NASA Laser Review 2
Leave A-Train Review
Decommissioning Review
Solar Flare Impacts
Major Data Releases
Lidar L1
Lidar L2
Lidar L3
IIR L1
IIR L2
WFC
V 1.10
V 2.01
V 2.02
V 3.01
V 3.02
V 3.30
V 3.40, 4.10
V 4.20
V 3.41, 4.21
V 4.51
V 5.0
Cloud Ice V1.0
Strat. Aerosol V1.0
Trop. Aerosol V4.20
V 2.00
V 1.11
V 1.12
V 1.13,2.01
V 2.01, 2.02
V 3.40
V 3.45
V 4.20
V 3.46, 4.21
(see Appendix)
V 3.0
(V 5.0)
V 4.0
Science Meetings (joint with CloudSat Team beginning in 2007)
A-Train Symposium
Algorithm Review
Algorithm Workshop
Validation Workshop
A-Train EarthCARE Symposium
AOS EarthCARE Symposium
Field Campaigns
ARM
CRYSTAL-FACE
Mid-CIX
Pre-AVE
MPACE
CC-VEX
CR_AVE
MILAGRO
TEXAQS
ASTAR
TC4
ULM
CIRCLE-2
NAAMA
C3VP
CALVAL1,2,3
ARCTAS
BISCAY
POLARCAT
CALVAL4, 5, 6
SPartiCus
CALVAL 8, 9
MACPEX
ICE-T
Discover AQ 1
DEVOTE
FENNEC
DC3
ATTREX
CHARMEX
SALTRACE
Discover AQ 2
Discover AQ 3
SEAC4RS
SABOR
KORUS-AQ
POSIDEN
ACEPOL
NAAMES 1
NAAMES 2
NAAMES 3
ORACLES 1
ORACLES 2
ORACLES 3
NAWDEX
AEROCLO-sA
IOOS
FIRE-X
EUREC4A
CAMP2EX
ACTIVATE 1, 2, 3, 4
STRATEOLE-2
CPEX-AW
TRACER-AQ
CALIPSO-NVF
CPEX-CV
1998
1999
2000
2001
2002
2003
2004
2005
2006
2007
2008
2009
2010
2011
2012
2013
2014
2015
2016
2017
2018
2019
2020
2021
2022
2023
2024
2025